Tomasz Hasek

Sub-THz systems for industrial inspection applications

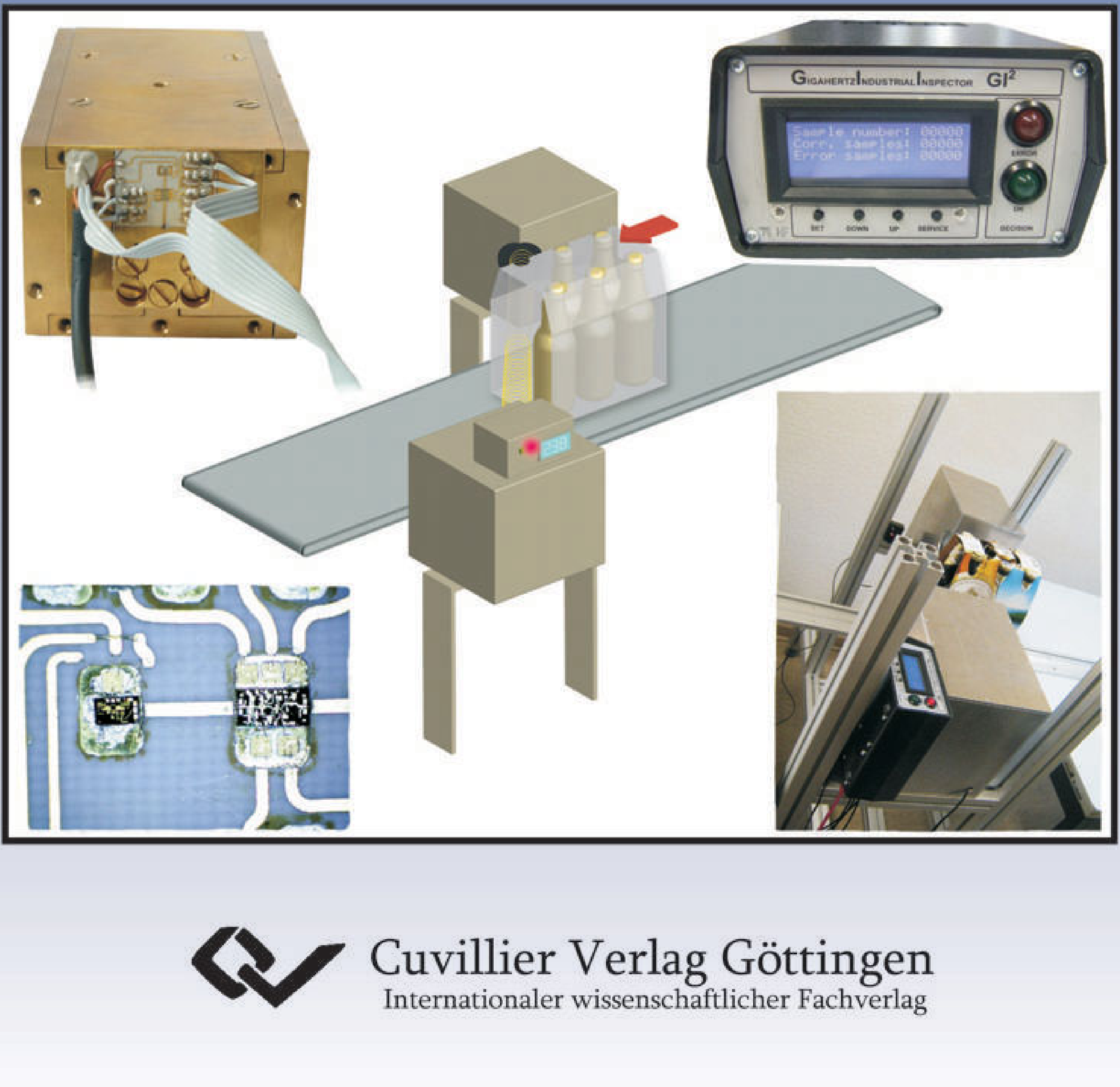

Cuvillier Verlag Göttingen
Internationaler wissenschaftlicher Fachverlag

Sub-THz systems for industrial inspection applications

Von der Fakultät für Elektrotechnik und Informationstechnik
der Technischen Universität Carolo-Wilhelmina zu Braunschweig

zur Erlangung der Würde

eines Doktor-Ingenieurs (Dr.-Ing.)

genehmigte Dissertation

von M. Sc. Tomasz Hasek
aus Ostrów Wielkopolski, Polen

eingereicht am:	28.01.2010
mündliche Prüfung am:	26.02.2010
Referenten:	Prof. Dr. rer. nat. Martin Koch Prof. Dr. rer. nat. Martin Hofmann

2010

Bibliografische Information der Deutschen Nationalbibliothek
Die Deutsche Nationalbibliothek verzeichnet diese Publikation in der Deutschen Nationalbibliografie; detaillierte bibliografische Daten sind im Internet über http://dnb.d-nb.de abrufbar.
1. Aufl. - Göttingen : Cuvillier, 2010
Zugl.: (TU) Braunschweig, Univ., Diss., 2010

978-3-86955-282-8

Nonnenstieg 8, 37075 Göttingen
Telefon: 0551-54724-0
Telefax: 0551-54724-21
www.cuvillier.de

1. Auflage, 2010
Gedruckt auf säurefreiem Papier

978-3-86955-282-8

To my wife Kasia and daughter Marta

“A rose by any other name would smell as sweet.”
- William Shakespeare

“A rose with a microcontroller would be a smart rose.”
- Randy Frank

Acknowledgements

This thesis is the result of my work at the Institut für Hochfrequenztechnik of the Technische Universität Braunschweig, Gemany in the years 2004 - 2009. Herewith I would like to thank all members of the Institute for their support.

First of all, I want to thank my supervisor, Prof. Dr. rer. nat. Martin Koch for providing me with the opportunity of working in the sub-terahertz and terahertz field. In particular, I want to thank him for the scientific, intellectual and financial support, and for offering me independence and confidence during my stay in the Institute. I would also like to thank Prof. Dr. Jörg Schöbel for the valuable discussions and sharing of the theoretical and practical knowledge in the microwave technology field. Simultaneously, I acknowledge Prof. Dr.-Ing. habil. Wolfgang Kowalsky, the chairman of the Examination committee and Prof. Dr. rer. nat. Martin Hofmann, the co-examinator.

I would also like to thank to all Ph. D. students who contributed to this work. In particular I acknowledge Dr.-Ing. Leif Stange, Dr.-Ing. Christian Jördens, Dr.-Ing. Rafał Wilk, Dr.-Ing. Ibraheem Al-Naib, Dipl.-Ing. Joachim Bonney, B.S. Dipl.-Ing. Pablo Herrero, Dipl.-Ing. Dennis Stanze, Dipl.-Ing. Ole Peters and Dipl. Des. Oliver Spieker.

I want to thank MS EE Kamran Ezdi and Dipl.-Ing. Christian Jansen for reading and editing this manuscript.

I owe special thanks to Dipl.-Ing. Carola Baaske, Dipl.-Ing. Kai Baaske, Dipl.-Wirtsch.-Ing. Norman Krumbholz, Dipl.-Ing. Christian Jansen, M. Sc. Nico Vieweg, Dipl.-Ing. Bernd Heinen and Dipl.-Ing Artur Hefczyc who were always ready to help me with the German language.

Serdecznie dziękuję mej żonie Katarzynie za wytrwałość i wsparcie, którego mi udzielała w trakcie realizacji tej pracy. Dziekuję za to, że przez 6 miesięcy potrafiła być wspaniałą mamą i “tatą” dla Martusi w momencie, gdy ja byłem pochłonięty pisaniem. W tym miejscu dziękuję Ci jeszcze raz Kasiu za zrozumienie mych dążeń, nawet wtedy, gdy oznaczało to odsunięcie niektórych Twoich planów na przyszłość. Za motywację słowa wdzięczności należą się mym najbliższym, t.j. rodzicom Halinie i Stanisławowi, bratu Przemkowi, oraz teściom Danucie i Wojciechowi. Dziekuję Wam wszystkim za dobre słowo i nieustanne wspieranie.

Braunschweig, January 2010 Tomasz Hasek

Introduction

For contemporary industry, quality assessment is of great concern. Depending on the manufactured product, quality control is compulsory or voluntary. However, in both cases, quality control leads to a decrease in detrimental costs and consequently, to the increase of the company's income. Since the food industry covers 20% of all manufactured goods worldwide, quality control systems for the food sector are of major interest. In general, the function of quality testing is to ensure that the properties of the product are consistent with the standards or baseline. As an example, in the food industry, the product has to have the proper net weight and it must not include foreign objects, like metal parts.

In the contemporary industry, there exist several systems that are employed for the quality evaluation of products. The most important are checkweighers, visible methods, radiographic methods, metal detectors and ultrasound systems. However, all of them have some disadvantages when employed in the food sector. By weighing the tested products, checkweighers can distinguish between conforming and nonconforming packages. However, the position of the missing item in a batch cannot be determined. Visible methods can be applied only to items that are transparent to visible light. Therefore, all products covered by paper or polyethylene packaging materials cannot be screened. Radiographic methods are widely applied because of the high spatial resolution and high penetration depth. However, for reasons of safety and ionisation concerns, their application in the food sector is limited. Metal detectors can scan the items for the presence of foreign objects. Unfortunately, the principle of operation of these devices limits their practical applications to the detection of metals. Ultrasound testing offers good spatial resolution, but this method usually requires a contact between the probe and the sample. Additionally, the use of a liquid couplant is needed. Therefore, this technique cannot be applied for nondestructive testing in the food industry. Further limitation arises from the fact that the items to be scanned are packaged. The space between the packaging material and the product may affect the coupling of the ultrasound to the evaluated items.

The goal of this thesis is to design a stand-alone, cost-effective and reliable scanner for the completeness testing of products in the food industry. To overcome the limitations of the previously described methods and to achieve a reasonable spatial resolution, the millimeter wave part of the electromagnetic spectrum has been chosen. In order to increase the spatial resolution of the system, lenses optimized for the target frequency have to be developed. The design of lenses for this particular frequency range requires the application of Gaussian optics, since the geometrical size of the components is comparable with the wavelength.

This thesis is structured as follows.

Chapter 1 explains the role and the need for industrial inspection. Additionally, existing and emerging techniques for the inspection of products are presented. For each method, the feasibility for the completeness testing is discussed.

In chapter 2, the fundamentals of microwave technique are presented. In particular, the principles of operation of microwave sources and detectors are explained. Additionally, the planar technology and antenna types that will be used for the design of the industrial scanner are presented.

In chapter 3 differences between geometrical and Gaussian optics are outlined. For both approaches, corresponding software is shortly described.

Chapter 4 shows the comparison of spherical and aspherical lenses. This chapter includes also the design procedure of the aspherical lenses using OpTaliX software. The simulations and measurements of beam profiles obtained with the developed lenses are shown.

Chapter 5 presents the feasibility study of millimeter wave systems for the new applications in the industry.

The design of a 35 GHz industrial inspector employing commercially available microwave components is described in chapter 6. Additionally, the results on completeness testing of drink bottles in a box obtained with the system are presented.

Chapter 7 includes the design of the cost-effective 38 GHz inspector based on the monolithic microwave integrated circuits. The ability to detect a missing bar packed in the container is evaluated.

Contents

1 Industrial inspection

This chapter describes the role and the need for industrial inspection of production lines. Additionally, existing and emerging nondestructive techniques for quality and completeness control are presented. The working principle, applications and the evaluation of various methods are shown.

1.1 The role of the industrial inspection

In order to be able to compete in the market and to enjoy customer confidence, companies must ensure that the product they offer fulfils the given standards. The function of determining the conformance of the product to the requirements is called industrial inspection. The inspection has two goals in the contemporary manufacturing industry: product specification and industrial process monitoring. These goals are attained by testing the final product, for example its weight, colour, appearance and presence in a batch.

Completeness inspection is a part of quality evaluation method. However, not the quality of a part, but its presence in a batch is checked. Completeness inspection is important for many branches of the industry, since there exist regulations requiring that the number of items in a package or its weight is defined [1]. In the USA, the Department of Commerce National Institute of Standards and Technology's (NIST) strictly defines net contents laws [2]. Similar directives are given by the United Kingdom [3] and other countries. The directives include detailed regulations on the testing methods. The number of underweight packages allowed and the number of packages to be inspected are specified. If one, or more packages are significantly underweighted, or an entire lot of packages has average negative weight error, then the legal requirements are violated. In this case, a company has to stop production, the products can be confiscated, or the orders have to be re-weighted. In order to avoid breaking the law, completeness control and quality control systems are needed.

Contemporary industry employs machines to a much bigger extent compared to the past. The trend towards automation of manufacturing processes requires the evaluation of control mechanisms to ensure the same end product quality, as achieved by hand-made production. Furthermore, it is desirable that a product is checked at every production stage to prevent unneeded expenses in subsequent manufacturing steps. For testing, often a statistical process control is involved. A repetitive fault in the product shows a malfunction of the manufacturing process.

The product examination can be carried out in two ways: destructive or nondestructive testing.

In the destructive testing method a mechanical test on the product is performed. The most commonly applied tests include stress tests, crash tests and metallographic tests. These tests give precise qualitative information about the ultimate tensile strength, fatigue life and hardness.

For destructive methods an additional process must be involved - the choice and extraction of the sample from the group. Destructive testing relies on the assumption that a chosen part is a good representative of the whole group. In reality it is not possible to guarantee that a specific part has exactly the same parameters as other products. It should be pointed out that the obtained data apply exclusively to the specimen being examined. In addition, destructive testing requires bulky laboratory environment systems and is relatively slow. Therefore, for industrial inspection, nondestructive testing is the most convenient way for product evaluation.

The definition of the word “nondestructive” according to American Heritage Dictionary is “Of, relating to, or being a process that does not result in damage to the material under investigation or testing”. The same source defines “testing” as “determination of presence or properties of the substance”. Since the words “testing”, “inspection”, “evaluation” have similar meaning in the aspect of industrial control process, the method of examination is called nondestructive testing (NDT), nondestructive inspection (NDI), or nondestructive evaluation (NDE), interchangeably. This method can be defined as “A process that does not result in any damage or change to the material or part under examination and through which the presence of conditions or discontinuities can be detected or measured, then evaluated.“ [4]. Nondestructive testing is a synergy of methods, instruments and intelligence [1]. Based on scientific knowledge, several methods for evaluation have been developed. The tests can be performed using the instrumentation. The development of a new testing method consists of three steps. In the first step, technical feasibility is checked. The outcome shows if the method can provide a desirable result in the laboratory. In the second step, factory feasibility is considered. Here, the working in harsh industrial conditions is examined. The machine intelligence is needed for correct interpretation of the instrument output. Therefore, in the third step, the decision rules are implemented into the machines.

Nondestructive testing has several advantages over destructive testing. The main advantage is that the part remains unchanged after the test. This means that in case it is required, even 100% parts can be tested, without a need for the sacrificing of samples. NDT methods are portable and easy to adopt in the production lines. In the end, NDT is more cost effective compared to destructive methods. Nondestructive examination has also some limitations: the tests usually do not deliver quantitative data; evaluation of some tests is controversial. Nevertheless, besides several disadvantages the NDT is preferred in contemporary production lines.

1.1.1 Manual inspection

Historically, NDT dates back to the time of the world creation. The book of Genesis says: “God said, »Let there be light«; and there was light. And God saw that the light was good; and God separated the light from the darkness”. This excerpt from the Old Testament describes a visual inspection performed by God. The human being is believed to be the most unique nondestructive testing instrument. Man is equipped with senses which enable him to perform several tests including visible inspection, determination of roughness, size etc. Also the senses of smell and hearing can point out some abnormalities in the production line. Historically, human inspection dates back to the Stone Age, where the craftsman work piece was visually examined during carving. Until the 1980s, an operator-performed manual, mainly visual inspection was

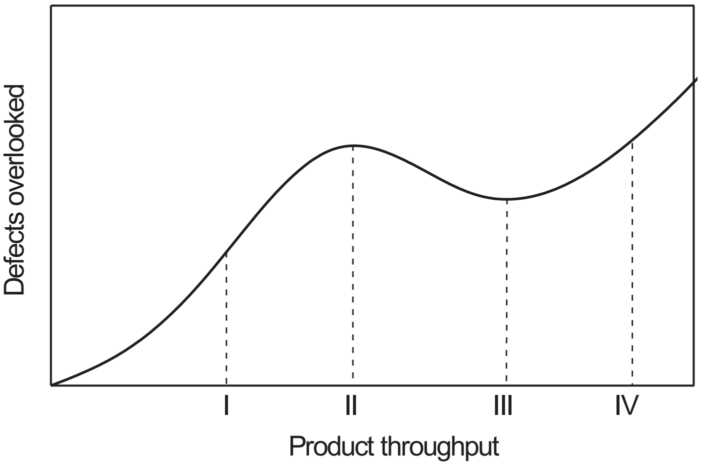

Figure 1.1: The influence of the task monotony and fatigue to the inspector efficiency.

executed. In comparison to the automated evaluation, human inspection is faster and easier to set-up. In contrast, machine inspection provides reliable results not affected by human fatigue or task monotony. Furthermore, the selection criteria remain unchanged, while decision criteria could vary from one inspector to the other. The influence of the task monotony and fatigue to the inspector efficiency has been studied by Kennedy, Andrews [5] and Wetherill [6]. The result of this investigation is shown in Fig. 1.1 [5]. The plot shows the percentage of overlooked defects versus the product throughput. The observation was focused on four different values of the product throughput. For very low production speed - range I in Fig. 1.1, the number of undetected defective items is very small. In range II, production the speed was increased. As a result, a bigger number of products has been overlooked. However, a further increase of the speed has increased the inspection efficiency, as shown in range III. This phenomenon can be attributed to the fact that the work in the range III is less monotonous, than in the range II. However, at very high speed rates (range IV), the percentage of missed defects grows up, since the fatigue of the inspector plays an important role. A further study has shown that the effect of the inspector's fatigue can be reduced, when the inspection is not continuous, as it is in the case of batch inspection.

The model of human inspection applies only for very small production throughputs. Still, it offers only a satisfactory effectiveness, not exceeding of 80% [7].

1.1.2 Automated inspection

In contrast, in modern industrial plants only automated inspection can satisfy the demand for contemporary production rates. Automated inspection results in lower laboratory costs and improved quality. Because of the dangers involved, automated inspection has no alternatives in testing of inflammable, explosive, or radioactive substances [8].

The automated inspection methods based on electronic devices are an extension of human senses. An automated industrial NDT gives the opportunity to examine raw materials prior to processing, evaluate the materials and semi products being in the production line, test complete products and evaluate serviced products [4]. However, even for automated examination, a hu-

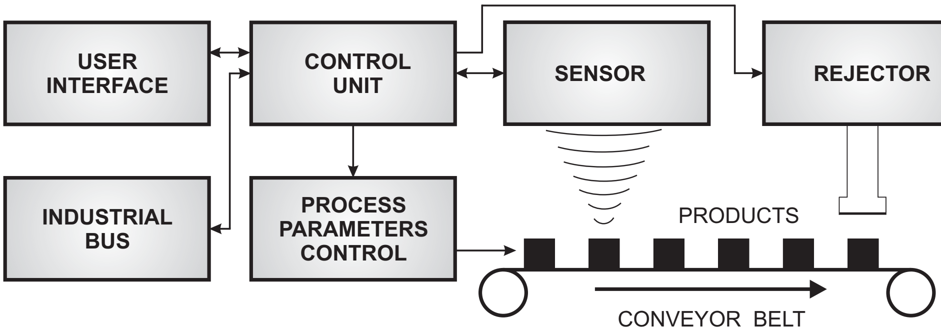

Figure 1.2: Automated inspection system.

man input is needed. Using electronics, it is possible to see more, better and faster, but in fact, the human has to make the final decision. The decision routines are often implemented in the instruments, but still the user has to adapt them to a specific application. Therefore, personnel must be qualified and certified, since the testing efficiency is determined by the individuals performing the examination.

The automatic inspection system is an integrated and complete quality control tool which uses various sensing methods to solve manufacturing problems [9]. A typical inspection system consists of a sensor, a control device including user interface and industrial communication bus, and a rejector as schematically shown in Fig. 1.2. The goal of a control device gathering the product parameter from the sensor is to decide whether or not that product follows given specification. The specification is defined in the control device, however it may adjusted by the user manually, or remotely using the industrial communication bus. Additionally, the control device may provide a feedback signal to the fabrication line system in case the product requirements are not fulfilled. The feedback signal should alter the fabrication parameters in such a way that the appropriate parameters are applied. If the product does not meet the requirements it should be removed from the conveyor belt, or marked for further selection. Many types of rejectors are in use; however the most popular are air blast rejector, push-off rejector, sweep-off rejector, parallel gate rejector, line divider rejector and drop-through rejector [10].

There exist four inspection and process control methods in the industry: off-line, at-line, on-line and in-line [11].

The off-line set-up is historically the oldest method. In this method, a sample of the product coming from the fabrication line is extracted as shown in Fig. 1.3 a) [11]. Then the sample is transported to the laboratory where it is prepared for analysis. Qualified personnel perform measurements on the sample. As the results are known, the information is forwarded to the production line to adjust the process parameters. Although the laboratory delivers data with highest level of conformance, a significant time period between sample extraction and the measurement results is needed. This makes off-line process control the least cost-effective, since the feedback information is delivered relatively late. In addition, during the evaluation process in the laboratory, faulty parts are still produced. In the worst case, all parts produced during the evaluation will go waste.

The at-line method is similar to the described off-line method. Here, the time for sample evaluation is decreased. This is achieved by placing the analyzing instrument in proximity to the production line as presented in Fig. 1.3 b) [11]. The sample extraction is manual or

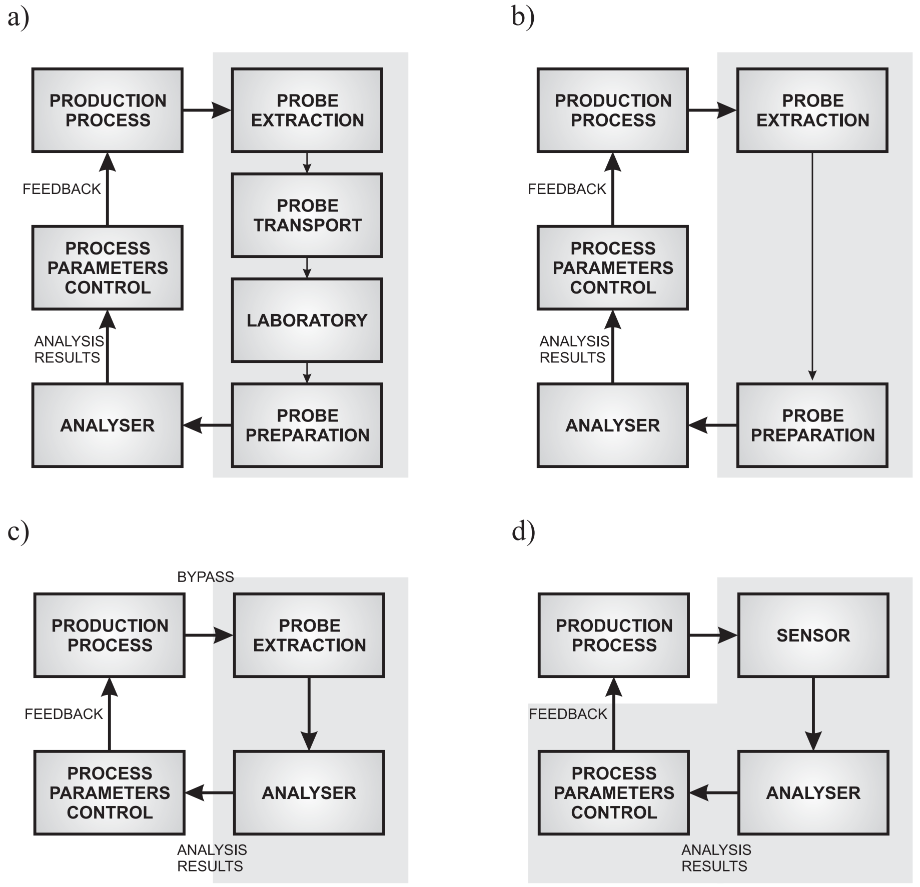

Figure 1.3: Industrial control methods: a) off-line, b) at-line, c) on-line, d) in-line.

semi-automated. In this case, transport time is significantly reduced. Still, the sampling and preparation are required which leads to a slow system response.

The third process control method - on-line - offers continuous analysis of the product as shown in Fig. 1.3 c) [11]. The analyzing instrument is installed close to the production line. The samples are fed to and from the instrument by a bypass line. The biggest advantage of this technique is that every product is examined. This method is characterized by a fast response, as long as the total time needed for measurement, evaluation and sending the feedback signal does not exceed the time in which the product parameters change. However, as reported in [11], 80% of malfunction of this method is induced by the sample drawing from the production line.

For efficient controlling of the automated production, an in-line inspection is the most desired method. In this case, a sensor is permanently installed in the production line which continuously performs the sensing of the moving or flowing product as depicted in Fig. 1.3 d) [11]. There is no sampling choice and extraction required; the tests are often performed on the entire group of products. The biggest advantage of this method is that the time for acquisition and evaluation of the part is the shortest compared with other set-ups, since the instrument is mounted directly in the production line. In-line evaluation is also more robust than the previously described methods, since no sample drawing system is required. Another benefit of this method is the direct possibility of supplying the feedback signal to the production devices. In practice should the parameter or parameters of the production be improper, a faulty part will be produced. This part will be immediately evaluated by the inspection instrument. As a inspection result, the controlling device will alter current production parameters with new-ones to overcome the problem. Since modern inspection instruments usually need a short time for evaluation and sending the adjustment signal to the production line, the number of defective parts is dramatically reduced compared to other set-ups.

1.2 The need for the automated industrial inspection

For a long time, inspection is an integral part of manufacturing activity. It is clear that testing contributes indirectly to the increase of the product quality. However, it must be taken into account that the inspection constitutes a considerable fraction of production costs. It has been shown in [12, 13] that inspection activities are performed by 10% of the entire work force. Quality testing can be either compulsory or voluntary. Special regulations demand compulsory quality assurance of pharmaceuticals [14], safety products, in aerospace automotive [8] and food industries [15]. For this group of products, evaluation contributes to 60% of the total production costs [16]. For all other products, the inspection considerations are based on economic factors.

1.2.1 Factors affected by the quality

Quality can be defined in several ways, from satisfying customers' requirements, fitness for use [17], to conformance to requirements [18]. The term quality always includes customers, since their satisfaction is the primary goal of the business. For all companies it is clear that the product quality has an influence on the income, since quality affects sales, prices and the company's reputation in the market [19].

The influence of quality on sale can be explained as follows. When a product is present in the market, it becomes a "share of the market" that is a proportion of sale of this product to the sale of the same type of product offered by all manufacturers. To obtain a high share of the market, an analysis of customer preferences is performed. Analysis has shown that features like durability, integrity and functionality play the biggest role for industrial customers. However, for home users, other factors are essential. It has been proven that a home user is more attracted by the product appearance and advertisement, than its intrinsic quality [20].

It is widely known that the quality affects the product price. For industrial customers, the marketing of capital goods is dependent on life-cycle considerations. A study presented in [20] shows that not only the quality of the original product, but also the quality of capital goods like maintenance, operation and down time have influence on the consumer preference. As a result, a product with a higher initial price can be preferred, when the quality of capital goods will be better than that of the competitor.

High quality of the manufactured products increases the company's reputation. For both types of users - industrial and consumer, the company's reputation is the key factor. Improving the product quality alters the reputation of a company, not only as a manufacturer of this specific part, but also the company prestige is raised. This may contribute to the improvement of the entire assortment sale.

1.2.2 International Organization for Standardization (ISO)

The company's reputation may be increased when it is ISO certified. The ISO standard was invented to guarantee, the customer gets a product of defined quality, as described in the standard: "If the organization is functioning today with adequate quality to satisfy its customers, then following the ISO-9000 quality management standard will assure that the organization will continue to produce adequate quality" [21]. The main goal of the ISO standard is to improve and to standardize the quality of the product. Therefore, several regulations regarding quality control have been defined. The regulations for quality management given by the International Organization for Standardization are described in document ISO-9000 (1994) and the revised document ISO-2000 (2000). In particular, the specification ISO-9001 describes the requirements of quality management systems. According to this document, quality management must be based on five layers:

1. A company must treat quality as a goal.
2. A company must have a quality manual describing all the operations and items that influence quality.
3. A company must have a set of standard operations for every process taking place in the company.
4. A company must have a defined set of work instructions for operators.
5. A company must document quality by preparing quality records on a daily basis. The records must include all significant production parameters including temperature, humidity, as well as process perturbations.

1.2.3 The inspection and the costs

Quality improvement may be achieved by effective product inspection. Evaluation can decrease production costs twofold. Firstly, careful testing contributes to material costs savings. Secondly, timely detection and removal of faulty parts from the production lines enables further savings, since no costs are spent for processing of defective items. This becomes important when the entire complex structure must be rejected because of a faulty item being a part of it. As shown, the goal of the inspection is to reduce the production cost. Furthermore, evaluation considerably decreases the detrimental costs. Assuming that a nonconforming part is not detected, it will be further processed together with conforming parts. The costs for processing of the nonconforming part apply in this case. If faulty parts need to be separated from the correct-ones, additional costs for sorting appear. If the parts go further into assembly, the costs of disassembling emerge, since the whole assembly will not meet the requirements. Additionally, the faulty parts have to be detected and exchanged. Since these procedures require time, the entire production will be delayed, which contributes to the costs of missing the deadline. If the nonconforming assembly is not tested, the warranty costs will emerge after it will be sold to the customer. The warranty costs include new assembly and service costs. If the nonconforming part caused damages to the equipment, then a cost of its repair is incurred. Finally, the company reputation may be damaged. As shown, the goal of inspection is reducing the total costs by minimizing detrimen-

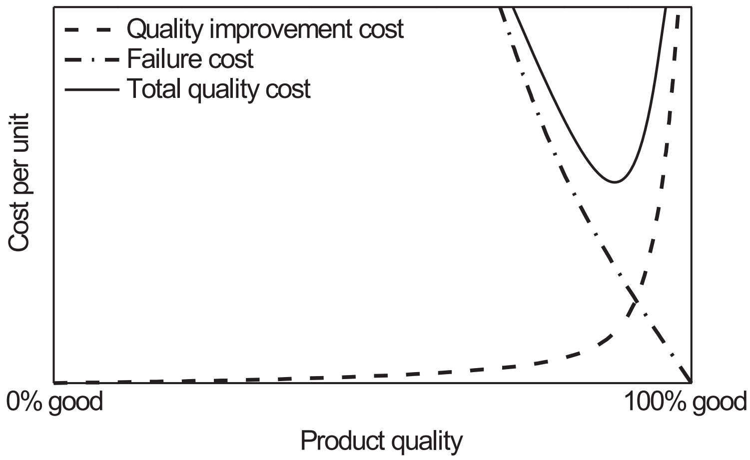

Figure 1.4: Cost per unit of the product versus its quality.

tal costs. It is easy to underestimate the detrimental costs, but they can be so large that a few nonconforming parts can change the company reputation from a winner to a loser [1].

On the other hand, it has to be considered that inspection also has its own costs. The total inspection costs include initial costs (equipment purchase, depreciation) and operating costs (maintenance, qualified personnel). Therefore, for a specific product and company, an economic balance has to be reached. The financial calculations allow finding the optimum level of quality assurance. As proposed by Feigenbaum [22], the relationship between product cost and its quality can be shown using a model for optimum quality cost. The total quality cost is the sum of failure costs and quality improvement costs. Failure costs include rework charges, downtime, material losses, whilst quality improvement costs cover inspection devices, personnel training, and data analysis. From the graph showing this model in Fig. 1.4 [22], it can be deduced that in case the company does not perform quality control (left part of the graph), the total costs per unit of product are enormous, because of high failure costs. On the other hand - excessive efforts for quality evaluation (right part of the graph) will lead to a huge cost of the product, since the quality improvement cost is high. The optimum level of product quality from the production cost point of view is defined by the minimum of the total failure and quality improvement costs.

For financial analysis it should be emphasized that the cost of inspection devices makes only about 20% of the entire quality improvement costs.

1.2.4 Industrial process and statistical process control

From the industrial point of view, a process is an entity that works continuously upon raw materials or unfinished parts till a final product is achieved. In other words a process is a systematic set of actions involving men, machines, materials and methods operating in an environment [1]. For a process, all of the listed factors are to be understood as its inputs, as schematically shown in Fig. 1.5. The outputs are: products, services, information or documents. The process works as follows: it takes one of its inputs, i.e. material, alters it to get an output having some value added to the input. The goal of a process is to obtain a desired quality of the added value. All other outputs like noise, contamination should be eliminated.

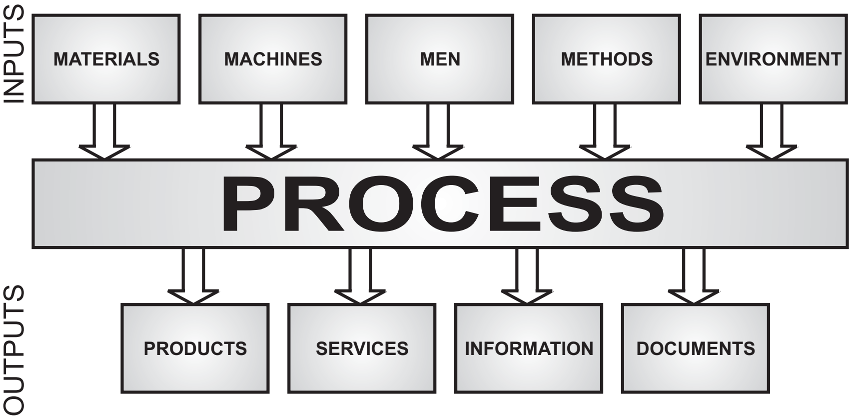

Figure 1.5: Industrial process.

Generally the process can be under control, or out of control. Although the output is monitored, and input values are modified to maintain the process under control, it may happen that the feedback control is faulty. In this case the system goes out of control. To find out if the system is under control, statistical process control (SPC) is applied. However, SPC cannot keep the process under control. The function of SPC is solely to tell with a given level of certainty if the system has gone out of control. The control chart is the oldest quality evaluation tool [23, 24]. The time is plotted on the horizontal scale, while the vertical scale shows a given parameter, which may be a result of an individual measurement, or an average as shown in Fig. 1.6. The standard level is to be understood as the range, in which the product parameter meets the requirements. This range is defined and plotted on the vertical scale in Fig. 1.6. For this particular graph, a standard level has been chosen as $\pm\ 3\sigma$. In case the average value is plotted, an additional control chart presents the range values that is the minimum value subtracted from the maximum value versus time. The average chart shows the general tendency, which can be influenced by the change of the temperature, insertion of a new material etc. The range chart shows the variation of individual parts which may be caused by a process malfunction. For both charts it is important to define the standard levels. An excessively wide range decreases the quality standard. In addition, it delays the reaction on the process malfunction. On the other hand, an extremely narrow range will cause feedback loop instability.

For the correct setting of the range, a statistical analysis is involved. The control limits are chosen based on the average value coming from a bigger amount of sample sets which are typically higher than 10 [24]. Additionally, a statistical analysis must be performed to determine the parameter frequency distribution using a histogram graph. Based on the standard deviation σ of the probability distribution, run rules for out of control conditions are defined [24]. The criteria showing the system is out of control are as follows:

1. Output parameter is situated outside the 3σ deviation.
2. Two of three successive points are outside 2σ on the same side relating to the mean value.
3. Four of five successive points are situated outside σ on the same side relating to the mean value.
4. Eight successive points on the same side relating to the mean value.

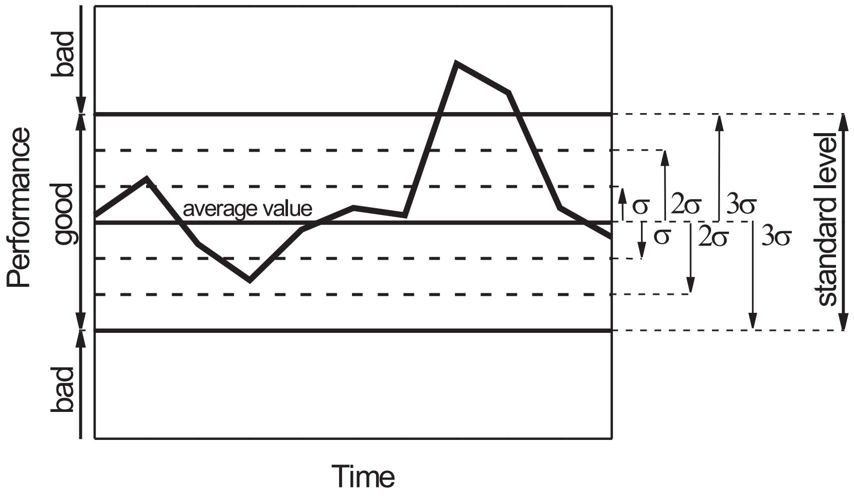

Figure 1.6: The control chart as the statistical process control method.

In case the process goes out of the control, the parts produced while the system has been out of control must be quarantined and additionally inspected. To guarantee timely delivery of the product to the customer, the factory needs to have just-in-case inventory to be shipped while the process is fixed, restarted and the parts inspected.

1.2.5 Sampling versus continuous inspection

Historically, sampling was chosen as the preferred inspection technique [19]. In this technique, the representatives from the group are extracted. The samples should be collected randomly within a lot. The mixing of parts from different lots should be avoided. There exist two sampling scenarios: single and double sampling. For single sampling a sample of n elements from a lot is chosen. Depending on the result of the evaluation of this sample, the whole lot is accepted or rejected. In double sampling scenario, a first sample of n_1 elements is extracted for testing. If the results are well above the specification, the lot is accepted. In contrast, if the results are considerably below the specification the lot is rejected. For intermediate cases, a second sample of n_2 elements is extracted, inspected and finally a decision is taken. It was proven that for identical level of conformance, the sum $(n_1 + n_2)$ of samples for double sampling technique is considerably lower than the number n of samples for single sampling. This makes a double sampling technique more cost-effective. According to Mundel [25] in the early 1980s, a 100% inspection of the entire assortment was not required. At that time, the employment of automated inline inspection was limited due to the lack of specialized devices. However, current development of electronics, robotics and computer science has lead to the automation of industrial evaluation units.

Recently, a new concept showing that inspection of the entire assortment using high-tech methods is highly recommended has been presented [1]. The main profit is the total costs reduction. It has been shown that the detrimental costs of a faulty product sold to the customer are much bigger than the cost of its testing. Therefore, using 100% inspection, a company profit may be significantly increased, whereas the costs spent for inspection are only a fraction of the total income. It must be emphasized that the methods used for 100% inspection must be non-

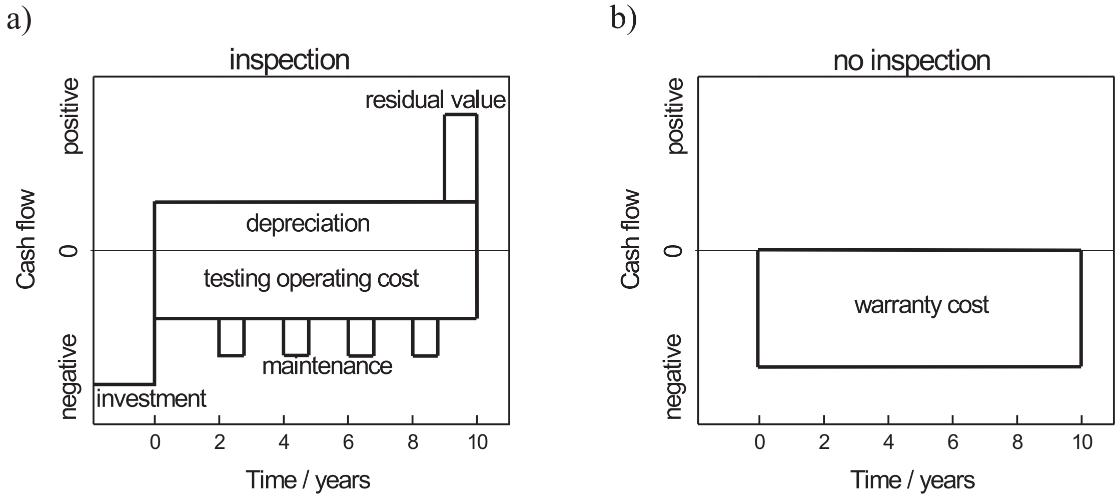

Figure 1.7: Time-adjusted rate-of-return method: a) with and b) without industrial inspection.

destructive. Otherwise, destructive methods would require sampling and could not intrinsically be performed on a whole lot.

There exist three methods for calculating the need for complete inspection of goods: the Deming inspection criterion, the time-adjusted rate-of-return and the productivity, profitability, and revenue method [1]. The common key for all methods is that the costs of testing do not exceed the detrimental costs of not testing.

For the Deming inspection criterion (DIC) method [26], three input values have to be known: cost to inspect one part k_1, the detrimental cost of one nonconforming part going further into production k_2 and the fraction of nonconforming products p. The relation between input values and the value of DIC is defined by the equation

$$DIC = \frac{k_2}{k_1} p. \tag{1.1}$$

Regarding the calculated value of DIC, a profitability of complete inspection is given. In all cases where the DIC value equals, or is bigger than unity, a 100% inspection is recommended. This criterion is used for the cases where small capital investments and large variable costs are foreseen.

For the time-adjusted rate-of-return (TARR) method, an economic situation before and after the inspection are compared to each-other. The idea given by Papadakis [27] is based on the fact that in case the current practise is continued, one stream of costs will accumulate. However, introducing new practice will produce another stream of costs. The idea is presented in Fig. 1.7 [27]. To evaluate the need for inspection, two streams are compared: a stream with and without inspection. As shown in Fig. 1.7 a), initial investment costs are exceeded by profits from the inspection, so finally, the economic balance is positive. In contrast, for the case, where no inspection is used (Fig. 1.7 b), the balance is negative, since warranty costs cause losses. This method can be successfully applied for large and long-standing investments for inspection systems.

The third method: productivity, profitability, and revenue was introduced by Papadakis in 1996 [28]. For this method, several variables must be known: number of pieces N, transfer price T, number of nonconforming parts n, detrimental cost per part V and cost to run the process C. Based on the relationship between these values, the total profit G can be calculated using the following formula:

$$G = \sum (NT - nV - C) \,. \tag{1.2}$$

For every single inspection method, the total revenue spent to improve the position of the company can be calculated.

By applying one of the three proposed methods, the need for industrial inspection for a concrete situation can be estimated on a financial basis. Clearly, the testing cannot guarantee that the item will not malfunction during the normal use. However, keeping in mind detrimental costs and the consequences of selling faulty parts, a 100% inspection using nondestructive techniques is highly recommended for every branch of industry [1], since it raises profits and decreases production costs.

1.3 Existing nondestructive inspection techniques and their applications

Nondestructive methods cover the full spectrum from elastic waves (f = 10 Hz) on one side to X-rays (f = 30 EHz) on the other. The development of physics and electronics in the twentieth century has contributed to the expansion of nondestructive techniques. Further growth of computer science and robotics has enabled the building of automated NDT systems since 1987. While NDT has the advantage of leaving the component unaltered after inspection, it finds applications in food [29, 30], nuclear [31], defence [32], aerospace [33, 34], transport [35] and offshore [36, 37] industries. The NDT applications are:

1. Structural assessment of a component.
2. The detection of unwanted separations and discontinuities in a material.
3. Metrology and dimensional purposes.
4. Determination of physical properties of a material.
5. Completeness testing.

In the following, existing NDT techniques, their applications in the industry, advantages and limitations will be presented. For every method, its feasibility for completeness testing will be evaluated.

1.3.1 Visual testing

Methods

Historically, visual methods were the first nondestructive methods applied in the industry. Visual testing can be performed manually, or automated. Before electronics developed, the human

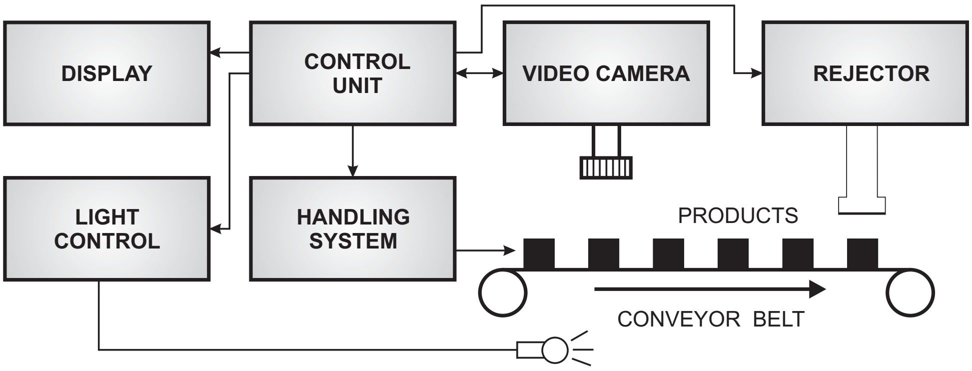

Figure 1.8: Automated visual inspection system.

eye played the role of the inspecting instrument. First tests were performed by qualified personnel evaluating the product using the naked eye [4]. To obtain qualitative information about the scanned object, different measuring gauges including scales, callipers, micrometers and depth indicators are employed. However, a naked human eye has limitations. Therefore, for inspection of small parts, hand-held lenses, microscopes and magnifiers are used. Light microscopes can be applied for structure surface evaluation. The limiting factors for direct visual aids presented above are spatial resolution, depth of focus and magnification. Furthermore, direct visual aids need a defined space to access the object.

To overcome these drawbacks, remote visual tools have been invented. The representatives of the group of remote visual tools are rigid boroscopes and cameras. The development of fiber optics enabled building of flexible boroscopes [38]. In this case, the light for product illumination is delivered through a single fiber or a bundle fibers. The other bundle leads the reflected light from the evaluated product to the inspector’s eye.

After the invention of charge coupled cameras CCD [39], a new era for visual testing has come into beeing. CCD cameras have found applications in video boroscopes [40] improving the video quality compared to standard fiber boroscopes [4]. Further miniaturisation of cameras armed with optics crowded out the boroscopes, since small cameras offer improved quality and flexibility over boroscopes.

The growth of robotics, automation and computer science has contributed to the evolution of automated visual inspection (AVI) devices [41]. In AVI system, functions like camera control, lightning and handling tasks are done autonomously by the computer, as shown in Fig. 1.8. Furthermore, the computer takes over all the steps needed to issue an action to be performed by the handling system. The AVI tasks include:

1. Image acquisition of the product to be inspected.
2. Image enhancement to improve the quality of the image for further processing.
3. Segmentation of the image to divide it into the parts of interest.
4. Feature extraction for object parameters calculation.
5. Classification of the product based on programmed rules.

The classification information based on the image recorded is used to accept, or reject a particular part, or to generate a feedback signal for the production process. Depending on the feature to be evaluated, for testing purposes binary [42], grey-level [43], colour [43] and range images [44] are acquired from the camera. As a reference, visual inspection systems employ computer-aided-design (CAD) models. CAD database includes all object parameters - its size, geometric tolerances, finish colour. In particular, CAD enables to model common defects, as presented by Hedengren [45].

Applications

Visual testing applications cover the spectrum from raw materials to end-product examination. Raw materials like ingots can be tested using magnifiers, microscopes for absence of discontinuities like voids, pipes, cracks, scabs and non-metallic inclusions. The metal joining processes like welding, soldering and brazing can be visually tested for misalignment, undercut, underfill, overlap, concavity [46, 47]. Visual methods based on magnifiers, boroscopes and cameras can be applied for service-induced discontinuities: wear, corrosion, fatigue. Since access to joints is limited, to avoid disassembly, boroscopes and miniature cameras are widely employed.

Final products having limited access for direct visual inspection methods like pressure, nuclear vessels, storage tanks, heat exchangers and boilers can be inspected by remote visual methods by means of cameras and boroscopes [48], [49]. Direct and remote visual aids have an established place for testing of buildings [50], turbines and generators and in aerospace sectors. Reported applications of CAD-based inspection range from solder joints [51] and lenses [52] to metal sheets [53] testing.

Three main AVI application areas include: mark identification, dimension checking and presence verification [8] and are applied in timber [54], textile [55] and metallurgy industry [56]. A 3D visual testing technique has been successfully applied for testing of bonding wires [57] and solder joints [58].

Summary

Visual methods belong to the group of easy to set up nondestructive inspection methods. They are relatively inexpensive, since standard cameras, or naked human eyes are used as detectors. Personnel training is not required, because contemporary systems are almost completely automated. Visual methods provide immediate results and no part preparation is required.

However, direct aids have limited access to the object. The biggest limitation of all visual methods is that it delivers exclusively surface properties information. The inner structure cannot be inspected. Generally, only large discontinuities can be detected.

Visual methods can be applied for completeness testing purposes; however, only bare items can be detected. Should the product be covered with an opaque-to-visible light material, no content information can be supplied.

1.3.2 Checkweighing

Methods

A checkweigher is a system for weighting of products passing the production line on the conveyor belt. Modern checkweighers make decision about the rejection of a nonconforming part, after the product's weight has been measured. As a standard, a checkweigher system consists of the following parts: infeed section, scale section, discharge section, line divider or rejector, and control unit (Fig. 1.9). The infeed section adjusts the product spacing to fulfill the scale requirements. The discharge section reverts the original product spacing. In contrast to static scales, the checkweighers have to deal with dynamic forces acting on the scale and package. Therefore, the accuracy of the checkweighers intrinsically cannot reach that of the static scales. The most important parameters describing the checkweigher accuracy is linearity and repeatability. Linearity shows how far the readout for the products of different weight is conforming to their real weight. Repeatability is defined by the standard deviation of the signal for the measurements of the same product. Both high linearity and repeatability have to be assured in contemporary industrial inspection applications [10].

Over a whole group of measuring techniques, two play the most important role: load cell technique and magnetic force restoration technique. In the load cell technique strain sensors are employed. Magnetic force restoration technique uses coils for weighting. The checkweighers based on this technique are less robust than those using load cells. However, the devices comprising the magnetic restoration method offer higher speed rates and better accuracy [10].

Applications

The checkweighers offer a wide range of the product quality and completeness control. The most important usage is a check for under or overweight packages. The checkweighers assure compliance with net contents laws for prepackaged products. Checkweighers also enable the classification of the product into weight groups. Knowing the product size, other parameters including volume and density can be obtained. The applications of this technique include food, chemistry, cosmetics and pharmaceutical industry. A product weighting can reveal missing

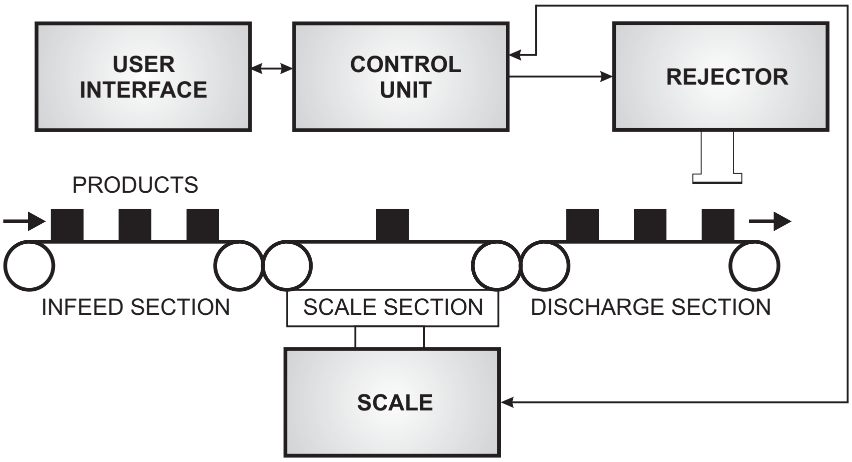

Figure 1.9: The checkweigher system.

content, for example coupons, lids, leaflets and labels in the pharmaceutical industry. Checkweighing finds applications also in completeness testing of food [15], since the number of the items in a packaging can be derived from the package weight.

The role of the checkweighers is not limited to weight measurement only. Since contemporary checkweighers incorporate automatized systems [59], additional features including statistics calculation, and sending a feedback signal to the other parts of the production line are common [60]. The most important advantage of the checkweighing is the possibility to check 100% of the products passing the production line. Based on the data acquired, statistical process control charts for manual or automatic adjustments can be provided [10].

Summary

Checkweighers are the widest applied NDT technique in many branches of the industry. Although the main goal is to check if the package is underweight, the overweight test contributes to the savings on the materials used for the production. The checkweighers offer a high reliability, accuracy, high testing speed and easy implementation into many types of the production lines. Since these systems are fully autonomic, personnel training is not needed and sample preparation is not required. The method is not invasive at all, since the measurements are done during the product movement on a standard conveyor belt.

However, besides the advantages presented above, the checkweighers have some limitations. Although they are successfully applied for completeness testing, no information about the position of the missing item can be provided. Therefore, in case when one part in a batch is faulty, the whole batch will be rejected. The location of the defect using the checkweigher is not possible. For location of the fault, additional inspection techniques, e.g. manual or automated visual inspection of the batch is required. Another limitation of weighing aroses from the fact that the checkweigher accuracy for high production throughputs is degraded because of the product vibration during the movement. There exist approaches for limiting the vibrations influence [61, 62], however this extends the system complexity and requires experienced personnel.

1.3.3 Ultrasonic testing

Methods

Ultrasound is a longitudinal wave with a frequency between 20 kHz and 200 MHz. The ultrasonic waves can propagate in gasses, fluids and solids. For generation and detection, transducers are used [63].

The most common inspection technique employing ultrasound is the pulse-echo technique. The probes are oriented perpendicular or almost perpendicular to the sample. Depending on the setup, a pair, or one transducer are employed, as presented in Fig. 1.10 a). Most common transducers are piezocomposite transducers based on lead zirconate titanate (PZT) and lead magnesium niobate (PMN). To inject ultrasounds into the material and to detect them, a direct contact between the transducer and the sample has to be assured. Once injected, the sound

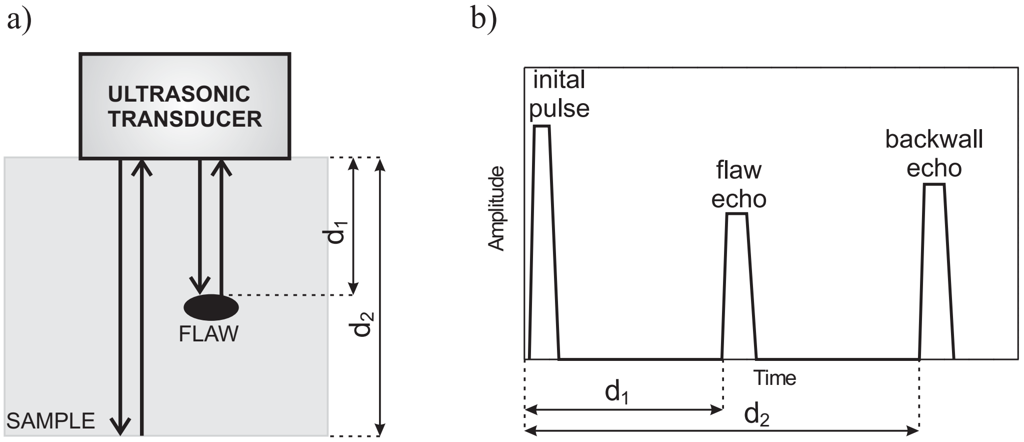

Figure 1.10: Ultrasonic inspection method: a) principle of operation , b) A-scan plot.

wave propagates through the specimen and is reflected from the back surface. After reflection the wave propagates in the material and is finally detected by the transducer. Signal intensity versus time can be displayed in a so called A-scan plot, as presented in Fig. 1.10 b). If a defect is present in the material, it will reflect the ultrasound waves which in turn arrive to the detector at a different time, than the echo from the back surface. The first peak on the A-scan plot originates from the transmitted pulse. The second rise is caused by the reflection from a discontinuity and the last pulse corresponds to back surface reflection. If the velocity of the ultrasonic wave in the material is known, the depth of the flaw can be derived from the time difference between two peaks.

In the through-transmission scanning technique, the transmitter and detector are spatially separated and positioned at the opposite side of a sample [64]. Since the sound wave travels only once through the object to be tested, this technique applies for the cases where object attenuation is too high to employ standard pulse-echo techniques.

Immersion techniques offer big flexibility, since the scanning can be performed at an arbitrary angle. In addition, the distance between the probe and the object can be easily varied without the need for coupling verification. Consistant coupling is assured by the fact that the transducer and object are immersed in the couplant.

In the time of flight diffraction (TOFD) a signal diffracted from the flaw is analysed [65]. TOFD provides more accurate flaw size data compared with the pulsed-echo technique. The synthetic aperture focusing technique (SAFT) utilizes the principles known from a radar technique [66]. Here, a transducer scans the object to reconstruct the full image. However, this approach can be applied only to flat surfaces.

To overcome the limitation of other techniques requiring the couplant, an electromagnetic acoustic transducer (EMAT) technique has been developed [67]. Using an acoustic transducer and a radio frequency coil, radio frequency eddy currents are induced in a conducting material. Interaction of eddy currents with a magnetic field yields ultrasonic waves.

Also the photoacoustic (PAUS) method does not require the couplant, since laser pulses are used for the generation of the sound waves in the material to be tested. Finally, a pressure wave created in the material is detected by the ultrasonic transducer [68].

Applications

The widest application of ultrasonic testing is thickness measurement. Since the object has to be accessible from one side only for ultrasound measurement, this is the preferred method for measuring the inside diameter of tubes, pipes and pressure vessels [69]. Ultrasound technique is extensively applied for flaws detection in several branches of industry. In particular, composite, sprayed ceramic plates delaminations [70], [71] and weld joints [72] can be successfully inspected. In the petrochemical and utility industries, ultrasonic waves determine various degrees of corrosion and erosion [73, 74]. Ultrasonic methods are effectively applied for fluid level measurements in vessels, pipes or containers [75]. Today's medicine widely uses ultrasonic techniques for fetus imaging [76], bone densitometry [77] and blood flow rates [78] measurements. TOFD methods have been used for turbine and generators inspection. Using this technique, cracks in turbine discs [79], rotor shafts [80], retaining rings [81] have been successfully detected. The same technique finds application in inspection of offshore platforms [82] and steel bridges [83].

Summary

Ultrasonic methods have a wide spectrum of advantages. Using ultrasound, not only surface, but also subsurface properties can be evaluated. Compared with other NDT methods, sound waves have the biggest depth of penetration. This enables the testing of flaws which are deeply buried in the materials. For the pulse-echo technique, only one side of the specimen has to be accessible, which is a clear advantage of this method. The ultrasound technique is flexible since it can supply the operator with a variety of material parameters. The devices are fast, relatively cheap, portable and automation-ready.

However, ultrasound is not a universal NDT method and has some limitations. Detection of discontinuities oriented parallel to the beam energy is difficult. Small discontinuities having a similar size to the material's grain structure are hard to detect. The scanning of thin sections and uneven number of surfaces is limited. Rough, irregular in shape, very small materials are difficult to inspect. The evaluation of coarse grained materials like cast iron is complicated because of increased attenuation and noise. For manual systems, personnel qualification is required.

Ultrasound methods are not applicable for completeness testing, since generally a couplant is required. Adding the couplant to the packages to be inspected, or immersing them in the couplant would damage the carton package. EMAT technique can't be applied as well, since the transducer has to be placed in close proximity of the object. Furthermore, EMAT requires that the specimen is an electrical conductor or it has certain magnetic properties. This requirement is not fulfilled by today's packaging materials. The PAUS method finds applications for the testing of soft biological tissues. However, the use of this method for the completeness testing is limited, since the evaluated material must be able to absorb the optical wave.

1.3.4 Eddy current testing

Methods

Eddy current testing is based on electromagnetic induction in the object to be inspected. Eddy current testing has been successfully employed in metal detectors, as it will be described in the subsection 1.3.5. The principle of eddy current testing can be explained as follows. A magnetic field is produced by the coil driven by an alternating current at a constant frequency in the range of 50 Hz to 10 MHz [4]. The induced magnetic field is parallel to the axis of the coil. When the coil is placed near the conducting material, the magnetic field induces eddy currents in the conductor, as depicted in Fig. 1.11. In turn, eddy currents produce a magnetic field in the sample. The magnetic field in the material is altered if a discontinuity in the sample appears. As a result, the eddy currents, the coil's magnetic field and the current will be changed. This will be manifested as a change of the complex coil impedance. Eddy currents flow only in closed concentric loops. The flow paths are circular in case no discontinuities like flaws or material boundaries are present. Discontinuities can be detected only if their orientation alters the flow paths. In case flaws are oriented parallel to the eddy currents flow path, they will be less detectable. Induced eddy currents are concentrated in the proximity of the surface of the sample because of the skin effect.

Eddy currents have limited depth of penetration, since they decay exponentially in the specimen. The penetration depth δ is dependent on the current frequency f, material permeability μ, electrical conductivity σ and can be calculated using the following formula:

$$\delta = \frac{1}{\sqrt{\pi \mu \sigma f}}. \tag{1.3}$$

Analysing the formula (1.3) it can be deduced that the penetration depth for ferromagnetic materials will be small and the eddy currents will be concentrated at the surface of the material. However, the penetration depth can be increased by lowering the signal frequency. On the other hand, increasing the frequency improves the sensitivity to surface discontinuities. Hence, small surface discontinuities can be revealed.

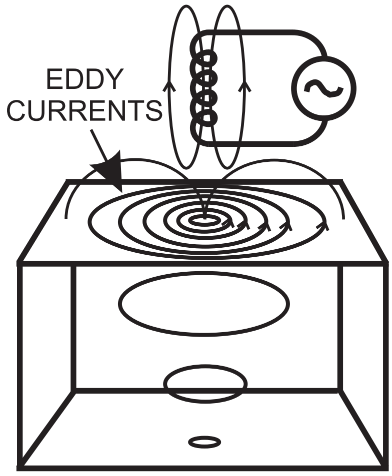

Figure 1.11: Eddy current testing principle.

Coils for eddy currents excitation can be designed as absolute or differential coil. For the absolute coil, one actual coil scans the material, whereas a second coil is used solely as load for bridge balancing. Since the eddy currents are influenced by the gap size between the probe and the sample, for satisfying testing results, a constant distance from the material must be maintained. This assumption does not need to be fulfilled for differential coils. Here, two matched coils are mounted in the probe. For this kind of probe, certain factors like probe – sample spacing cancel out. However, the interpretation of the results obtained with the differential probe is more complex.

To increase the testing speed, systems utilizing multiple probes have been developed. In order to increase the penetration depth, pulse eddy current testing is applied [84]. In this technique, pulses of high current of up to 10 A and duration of about 75 µs excite the coil. Here, a second receiving coil is applied on the other side of the object. Object parameters can be derived from the time delay and amplitude of field penetrating the sample. For testing of pipes, a remote field eddy current (RFEC) method which utilizes two probes is employed [85].

In order to overcome limitations of single frequency eddy current inspection devices, a new group of devices employing a multifrequency signal has been developed [86]. The advantages of these devices are suppression of unwanted variables, ability to test the flaws located on the surface and buried in the material and the simultaneous possibility to obtain results in absolute and differential mode.

Applications

The primary application of eddy current testing is crack detection of metal materials [87]. Fastener holes beeing areas of high stress often suffer from fatigue cracking. Metal joints like bonds can be successfully evaluated using eddy current techniques [88]. Another application is paint thickness inspection in the aviation industry. Since thick materials support quantitatively bigger magnetic field, compared to thin-ones, eddy currents can be used for material thickness determination [89]. Material loss caused by erosion and corrosion processes can be also detected. The applications include aviation (wings evaluation [90]) and petrochemical (tubes testing [91]) industry. Since eddy currents can penetrate many layers of conducting materials, the gaps or adhesives between the layers can be characterised [92]. The detected eddy current signal strength is also defined by intrinsic material properties: its electrical conductivity and magnetic permeability. Using this dependence, eddy testing can be applied for material identification purposes [93], determination of heat damage and heat treatment monitoring [94]. Pulse eddy current testing is used for wall thickness measurement and wall defects detection [84]. RFEC method finds application in the evaluation of heat exchanger tubes, pipes, wall thickness, corrosions and defects [85].

Summary

The advantage of eddy current testing is its wide applications spectrum. Inspection supplies immediate results. No couplants, powders, sample preparation is required. A contact between the test probe and the material is not necessary; however, the material must be accessible to the probe. Therefore, eddy current testing can be applied for high speed production lines without damaging the product to be inspected. The instruments are portable and lightweight.

Nevertheless, eddy current testing has some disadvantages. Inspection with eddy currents is limited to the conductors. Alternatively, isolators deposited onto a conductor can be tested. Testing of rough materials is complicated. The penetration depth is very small for ferromagnetic materials. Hence flaw testing of such materials is limited only to the surface evaluation. Method sensitivity is significantly reduced for flaws oriented parallel to the eddy currents. In all cases, signal interpretation is not unambiguous. Flaw characterisation is not straightforward since many parameters like different material composition at specific places, edge effects, temperature and spacing between the probe and the sample alter the signal. Hence, qualified and experienced personnel are required. Using multifrequency systems, specific reasons influencing the signal can be distinguished; however, a correct analysis of the results is not trivial. Remote eddy current testing and pulse eddy current methods provide signals of low signal-to-noise ratio; therefore, precise instruments for signal filtration and analysis are needed.

Standard devices using eddy currents for quality control purposes are not applicable for completeness testing. A limited feasibility of eddy currents for completeness testing of metal parts will be described in the subsection 1.3.5.

1.3.5 Metal detectors

Methods

Industrial metal detectors reveal the presence of ferrous, non-ferrous metal and stainless steel metal in nonconducting materials. The detectable materials include copper, aluminum, brass, tin, lead, and stainless steel. It is possible to sense particles down to a diameter of 1 mm [15]. Metal detectors are used for checking cleanliness or verifying the absence of tramp metal in continuous or bulk products. On the other hand, these kind of detectors is also used to verify if the desired metal material is present in a packaged product. Therefore, a completeness control of metallic parts can be performed.

There exist two types of metal detectors based a balanced coil system [95] and on a pulse detection technique [96]. For both types of detectors, the working principle is based on eddy currents induced in contaminants. In the balanced coil system, signals coming from two receiving coils are compared to each-other. The presence of a metal will disturb the initial magnetic field distribution because of eddy currents that are induced in a metal inclusion. As a result, the detector circuit unbalances and the voltage signal is produced. In the pulse detection technique, the shape of the received signal is analysed. If a metal is present, the magnetic field will be altered because of the eddy currents induced in the metallic contaminant. As a result, the detected field will have different parameters as in the initial state. The sensitivity of this technique is lower than that of the balanced coil system. However, pulse detection technique enables the detection of certain metals in aluminum containers.

Applications

Metal detectors are used in those branches of industry, where there is a possibility that metal inclusions can be present in the product. In some specific industries, e.g. in the food industry there is a requirement that 100% of the products have to be checked for metal contaminants. Also, when the product purity is crucial because of the safety consideration, the metal detectors should be employed. Further applications of metal detectors can be found in dairy, paper, cosmetics, plastic, rubber, chemical, security to textile industries [97]. Examples range from the detection of metal chips in chocolate, biscuits, peanuts [98], staples or nails in wood, metal parts in pharmaceutical products, needles in fabric sheets, metal caps in crushed glass to concealed weapons and bombs in security checkpoints.

Summary

Contemporary metal detectors are mature products for the quality testing. The advantage of this kind of quality control systems lies in a detection possibility of different metallic parts in a variety of nonconducting materials. Many devices are equipped with embedded systems and digital signal processors. Therefore not only detection, but also an indentation of certain metal inclusions is possible. Metal detectors work fast, reliable and are almost maintenance-free.

However, as the name of the method suggests, only metallic contaminants are detectable. The application in completeness testing is possible, but is intrinsically limited to the metallic parts. Additionally, the spatial resolution of metal detectors is low. This leads to high rejection rates, since the location of a single product contaminating metal part is not possible, and therefore a whole batch has to be discarded.

1.3.6 X-rays

Methods

Radiographic inspection is based on the absorption of penetrating radiation by the sample to be tested. For radiographic inspection two types of radiation can be used: X-rays and gamma rays [99]. Both have wavelengths below 10 nm and are physically indistinguishable. The difference between X and gamma rays lies in the methods used for producing of them.

X-rays are a product of the interaction between accelerated negatively charged electrons hitting a target material enclosed in a vacuum tube, as depicted in Fig. 1.12. For electron emission, a cathode filament supplied with a high voltage is used. A metallic target made of tungsten is used as an anode. Since a high voltage up to 50 kV is applied between the cathode and anode, the emitted electrons are accelerated and hit the anode. The X-radiation is produced as a result of energy exchange at the anode. Alternatively, X-rays can be produced using tubes with a resonance-type transformer, betatrons, Van de Graaff generators and linear accelerators.

Gamma rays are the product of the radioactive decay of an unstable isotope. Widely used isotopes are: iridium-192, caesium-137 and cobalt-60. Once the source is triggered, it continuously radiates gamma rays. To disable the radiation, mechanical shutters are employed.

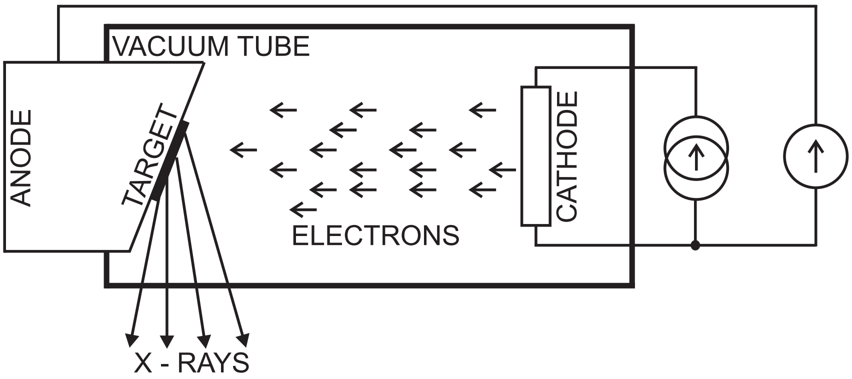

Figure 1.12: X-Rays generation method.

The photons energy $E = h\nu$ covers the range from 10^1 to 10^7 eV for X-rays and $5 \cdot 10^4$ to $5 \cdot 10^7$ eV for gamma radiation. For inspection purposes, the material to be tested is exposed to the X-rays or gamma radiation. Depending on the material properties (its thickness, structural integrity and composition) different portions of the radiation are locally absorbed. An unabsorbed part of the rays passes through the material and is projected on a photographic film. In real-time radiography (RTR), a fluorescent screen or image intensifier tube instead of the film is used. The scan result is immediately seen on a screen. Computer tomography (CT) enables the visualisation of the internal structure of a sample. For obtaining a full 3-D image, a series of 2-D images collected at different exposure angles are recorded. The reconstruction is performed by a computer. As a result, a set of images revealing the internal structure of the material is created.

Applications

X-rays are widely employed as a nondestructive quality testing method in many branches of the industry. In power generation industry, pressure vessels, piping systems, cast valve bodies are tested for the presence of cracks, corrosion, wear and discontinuities [100]. A joint quality of welds can be evaluated [101].

X-rays are extensively applied for quality assurance in the aerospace and automotive industry. Radiographic techniques enable the testing of the welds and turbine blades [102], suspension and engine components, seat belt tensioners, wheels and aluminium castings [103]. In the petrochemical industry, real time radiography is widely applied for detection of areas of degradation, erosion, corrosion and wear of metal elements. Additionally, pore cells, bonding defects and an insufficient number of welding points can be recognized [104]. X-ray technology enables the electronics to fulfil the demand for miniaturisation. Using microfocus X-ray technology, hidden interconnects in the surface mount, though-hole technology, wave soldering and semiconductor packaging can be detected [105].

However, the application of radiography is not limited to metals. Nonmetals like plastics, rubber, ceramics and explosives are successfully tested with X-rays [106]. In medicine, X-rays are the basic tool for examination of living and not living creatures. The presence of foreign bodies in tissues is possible because of the density contrast. Other medical and pharmaceutical applications include the testing of the medicine package content and syringes [107].

A further area for testing with X-rays is security applications. Using radiation, concealed weapons and explosives are easy detectable using real-time radiography [108].

In the food industry, X-radiation is employed for the detection of foreign objects and completeness testing [109, 110]. Typically, inclusions like metal, glass, stone, bone, hard plastic, teflon and polyvinyl chloride (PVC) are recognizable. Tests for additives content and for material quantity are other employed applications.

Summary

Radiographic testing offers very good sensitivity for detection of voids, cracks, thickness and material density changes. Surface and subsurface defects can be recognized. In contrast to the other techniques, radiography is not limited to a material type or its density. The evaluation can be performed on the assembled products. The objects to be inspected do not require preparation. Since X-rays and gamma radiation have a short wavelength a high spatial resolution is obtained. Real-time radiography can be automated. Therefore, this method applies well for high throughput industrial inspection. Using X-rays, the completeness testing of enclosed packages is possible. Radiographic evaluation provides a permanent record of inspection.

However, material evaluation with X- and gamma rays has several disadvantages. The most important disadvantage comes from the fact that the radiation of this wavelength range ionises the matter. Therefore, an exceptional caution has to be taken for using this radiation. Strict control and safety regulations need to be followed to guarantee the safety of the inspector, working personnel and the products tested. For safety reasons, X-ray dosses are monitored by ionisation chambers, Geiger - Mueller counters or scintillation instruments. Because of safety considerations, the use of this method requires extensive operator education. Interpretation of the results is not always straightforward; therefore, training and experience of the personnel taking the radiographs is needed. Although the scanning radiation intensities are kept at low levels, a material after the test is partially ionised. This feature is unwelcome for food and pharmaceutical industries. Another disadvantage of radiographic testing methods is limited sensitivity for flaws which are oriented perpendicular to the radiation beam. X-raying can be performed only in the case, where both sides of the material to be tested are available. The cost of the radiographic systems is still relatively high.

Completeness testing of food products with X-rays is possible, but hazardous on the other hand. Despite of wide application of radiographic devices in food industry, there as a need for a new, 100% non-ionising techniques.

1.3.7 Liquid penetrant testing

Methods

Liquid penetrant method is an extension of visual methods enabling the detection of the surface cracks with extended sensitivity. The working principle is based on a capillary effect [111]. The scanning principle is as follows. Sprayed dye is applied to the surface to be tested. Because of the capillary effect, liquid concentrates in the surface discontinuities. After the developing, surface discontinuities become clearly visible. Since the manual process is time consuming, using robotics and pattern recognition approaches, the liquid penetrant method has been automated for on-line manufacture evaluation.

Applications

Liquid penetration methods find applications in evaluating almost any material which is not extremely rough or porous. The material spectrum for liquid penetration spreads from metals, glass, ceramics and rubber to plastics. Liquid penetrant methods offer the recognition of surface breaking defects. Fatigue, quench and grinding cracks can be detected. Overload and impact fractures, seams, pin holes in welds, porosity and laps are other types of flaws recognizable with liquid penetration techniques. In the power generation industry, penetration techniques are used for the quality assurance of the nuclear power plant constructions [112]. Other industries employing penetration techniques are marine, aerospace and petrochemical. In the aerospace and marine industry, a detection of through-wall leaks is performed. Ceramics and structural weldments are tested in the aircraft industry [113].

Summary

The major advantage of the liquid penetrant method is its low cost, ease of use and portability. Being a cost-efficient method, it offers high sensitivity for flaw detection. Automated systems enable time-efficient inspection of large areas. The liquid penetrant method is also applicable for the parts with a complex geometry. It can be used in every environment, since manual evaluation technique is portable. The method does not require complicated personnel training.

However, liquid penetrant testing method has several disadvantages. The main limitation is its application area. It can be used exclusively for surface flaws detection. The materials to be tested must be nonporous. Before and after the inspection a controlled material processing has to be performed. In order to perform the evaluation, a direct access to the surface has to be assured.

The liquid penetration method is not suitable for completeness testing, since it is based on a visual inspection. In case the product is covered by the packaging, the penetrant testing method cannot be applied.

1.3.8 Magnetic particle testing

Methods

Magnetic particle inspection uses magnetisation of the object to be inspected [114]. Prior to the inspection, the object has to be cleaned and dried. A permanent magnet, electromagnet or an electric current is applied to the object surface in order to magnetise the object. If the object is homogenous, the lines of the magnetic field in the material will be distributed evenly through

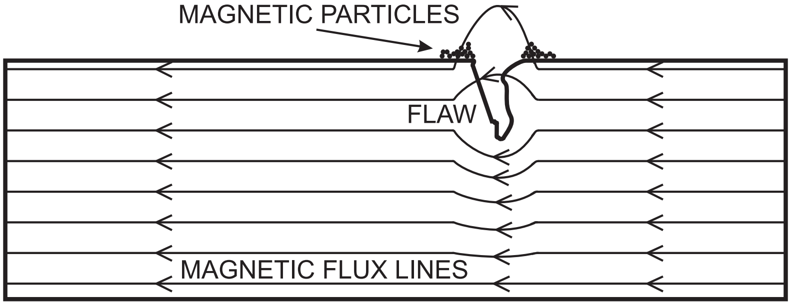

Figure 1.13: Magnetic particle inspection principle.

the material. In case a surface discontinuity appears, the field distribution is distorted. As a result, the magnetic flux approaches saturation and a local leakage appears. This is schematically presented in Fig. 1.13. For the purpose of inspection, fine ferromagnetic particles in the form of a dry powder or a liquid suspension are sprayed onto the object surface. The particles are attracted by the leakage field and therefore concentrate in the area of the discontinuity. Since high sensitivity is obtained only in the case, when the flaw is oriented perpendicular to the magnetic flux lines, the inspection is performed twice for two orthogonal magnetic lines orientation. The final inspection is performed using the naked eye, or a video camera for automated systems. After the inspection, the object has to demagnetised, since residual fields may interfere with magnetically sensitive parts of an assembly.

Applications

Magnetic particle testing is a versatile inspection method and therefore it can be employed at several production stages of ferromagnetic metals processing. Testable structures are: ingots, billets, slabs rods wires and castings. The material to be processed can be tested for the presence of non-metallic inclusions and seams. After primary processing which includes forging, casting extrusion and drawing, flaws such as bursts, laps, seams and inclusions can be recognized. In secondary processing which includes machining, grinding and plating, the following discontinuities can be detected: quench and grinding cracks and machining tears. The discontinuities are unwanted products of the welding process and they include cracks, inclusions and incomplete penetration. They can be revealed using the magnetic particle methods.

The magnetisation particle technique has applications in several branches of the industry. In the petrochemical industry inspection of pipes and vessels with the magnetic particle method has been presented [115]. The evaluation of welds is performed in the construction industry [116]. In the aerospace industry, the testing of high tensile parts for discontinuities is executed [117]. In the automotive industry vane wheel discontinuities recognition has been proposed [118]. The detection of cracking in deaerator storage vessels [119] show the usage of the magnetic particle method in the nuclear industry.

Summary

Magnetic particle inspection is a well established method and is preferred by the industry since it is portable, low cost and offers immediate inspection results providing information about the shape and the type of the flaw. Since the interpretation of the results is not a complex task, no personnel training is required. Additionally, the testing can be performed at any processing stage of the material. Magnetic particle testing can be automated for certain production lines; therefore, high throughput may be achieved.

The strongest limitation of the method is the material for which the method can be applied: exclusively ferromagnetic materials are testable. Although the type and the shape of the flaw is detectable, no quantitative information can be obtained. The method is limited to the surface and surface-breaking flaws and its sensitivity is dependent on the electromagnetic properties of the material tested. The inspection depth does not exceed 0.6 mm. Discontinuities are detectable only in case when their orientation enables interaction with the magnetic flux lines. Evaluation of large parts requires equipment with a high current output. Finally, the magnetic particle inspection technique needs processing before and after the examination.

Similar to the case of liquid penetrant method, magnetic particle inspection does not have application in the completeness testing.

1.3.9 Acoustic emission

Methods

Acoustic emission testing is based on the interpretation of elastic wave properties propagating in the material evaluated. As a result of applying the external stress to the material by change of the pressure, load or temperature, a strain is induced in the material, as schematically shown in Fig. 1.14. Alternatively, acoustic emission can be excited by phase transformation, twinning, liquefaction, solidification and the realignment or growth of magnetic domains [120]. When discontinuities are present in the material, an additional elastic stress called acoustic emission propagates though the specimen. The primary source of the acoustic emission is the plastic deformation.

The creation of the elastic waves undergoes the Kaiser effect [121]. According to this phenomenon, the acoustic emission occurs only when the stress applied to the specimen exceeds the level previously applied. Knowing the Kaiser Effect parameters for the material to be tested,

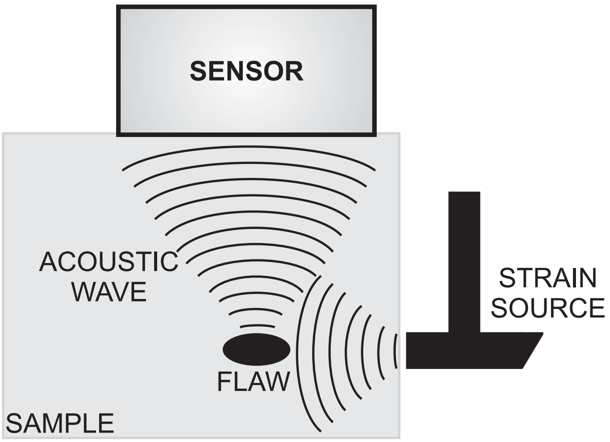

Figure 1.14: Acoustic emission technique.

the evaluation of structural defects can be performed. Generally, the amplitude and release time of the acoustic emission supplies information about the size of the flaw. The induced elastic waves cover the full spectrum from 10 Hz to 1 MHz. However, to achieve high sensitivity of the method, piezoelectric transducers working in the frequency range from 100 to 500 kHz are employed. Depending on the application, a couplant or a waveguide is employed. The analysis of the recorded waveforms enables the recognition of the discontinuity. For flaw localisation applications, systems based on multiple transducers are used. By a comparison of the signal's arrival time difference, location information is obtained.

Applications

The applications of the acoustic method include metallurgic, automotive, aerospace, marine, petrochemical industry, as well as civil engineering. The application spectrum is not only limited to metals, but the method can be successfully applied to composite materials and polymers, woods and rocks testing. The main application in metallurgy is the weld quality evaluation [122]. Lack of weld penetration, fusion, cracks, inclusions and porosity are typical features detectable. The application of acoustic emission for creeps deflection has been presented [123]. The revealing of microcracks being a result of the corrosion activity is feasible [124]. In the automotive industry, the acoustic method enables the inspection of gas trailer tubes in situ [125]. An in situ control of the wings, fuel tanks and rocket engines [126] are examples of application in aerospace. In the wood industry, wood drying processes and scratches are inspected using acoustic emission testing [127]. In the petrochemical industry, storage tanks and pipes are evaluated. The testing of engine and power plants against corrosion and discontinuities is performed in the marine sector [128]. Bridges and dams evaluation is an example of application of acoustic method in civil engineering [129]. Acoustic emission method finds applications in completeness testing [130]. The content of bottles can be tested online in production lines.

Summary

Acoustic emission is a widely used nondestructive inspection method. Its application is neither limited to a specific industry nor to a specific production process. The method is applicable both for flaw detection and completeness testing. The biggest advantage of the method is that access to the whole object under test is not needed. Hence, a global monitoring using a single sensor is possible. Moreover, inaccessible or hazardous areas can be inspected. The method gives an immediate result which is easy to interpret. Acoustic emission offers high sensitivity; therefore, relatively small discontinuities are detectable. The geometry of the object does not limit the application of the method. In general, the method is cost effective and automation is possible.

The disadvantages of the method include the need for a stimulus to excite the emission which produces unwanted noise. Since acoustic emission is stress-unique and each application of the stress is different, no repeatability and no quantitative information about the flaw size can be obtained. The sensitivity of the acoustic emission is significantly reduced in noisy environments. Therefore, for particular applications, complex signal discrimination and noise reduction is required.

Acoustic testing is successfully applied for completeness testing purposes. However, the detection of a missing item does not give any information about its position in a batch. Therefore, only a global sorting of conforming and nonconforming parts can be performed.

1.3.10 Thermal testing

Methods

Thermal testing methods measure the object's surface temperature during its heat exchange with the environment [4]. When a temperature difference exists between two objects, a heat transfer occurs. There are three energy transfer mechanisms: conduction, convection and radiation. The radiation appears as a result of the movement of the electrons into a lower energy state. The intensity and the wavelength of the emitted electromagnetic radiation are dependent on the temperature of the object's surface. The wavelength of the radiation spans from (0.1 to 500) µm and covers the infrared and terahertz region of the electromagnetic waves. The use of thermographic methods for material evaluation is based on the fact that the flow of heat from the object's surface is altered by the flaws. However, in case the flaws have the ambient temperature, no difference between the flaw and the remaining part of the surface exists. Therefore, a heat flow has to be established. This can be accomplished by using external heaters, lamps or cooling sprays.

For thermal energy detection two types of detectors are used: thermal and quantum detectors. For thermal detectors, the temperature of the device is raised as a result of thermal energy absorption. This group is represented by heat sensitive coatings, pyroelectric and thermoelectric devices including thermistors, bolometers, thermocouples and thermopiles. Quantum detectors convert the thermal radiation directly into an electrical signal. The thermal photons are absorbed by the detector and, as a result, free electron-hole pairs are created. Because of noise consideration, this group of detectors has to be cooled to 4 K or 77 K in order to achieve good sensitivity and resolution of up to 0.07 K.

To create map representing the temperature distribution of a whole object's surface, imaging systems are employed. The development of semiconductor technology has lead to the popularisation of the focal plane arrays consisting of single detectors. The infrared cameras using arrays are more robust than the scanners and offer the resolution of 0.1 K.

Applications

Most applications of thermal testing focus on flaws' detection. Typical discontinuities including disbonds, inclusions and voids affect the heat flow on the surface of the object tested [131]. Another application in metallurgy is welds quality inspection [132]. Flaws like clogged tubes and disbonded films appearing in automotive radiators are successfully detectable using infrared radiation techniques [133]. The thermal methods can be employed for the testing of electrical and mechanical systems in architecture, transportation and electric power transmission. Typical abnormalities including loose electrical connections, failing transformers, improper bearing lubrication in motors, coupling misalignment are manifested by the local rise of the temperature [134]. By measuring the heat distribution, the optimization of integrated circuits' and printed circuit boards' form can be performed [135]. Material thinning detection of an aircraft wings protective layer is another application for the infrared instrumentation [136].

Summary

Thermal testing is a versatile method for industrial inspection. The method is fast, reliable and creates a complete image of the device under test. Using infrared cameras, remote testing of inaccessible samples is feasible.

The most important disadvantage of thermal testing is that it is limitated to surface scanning only. Since the analysis of the thermographs is not straight-forward (many parameters have to be considered simultaneously), the inspection personnel have to be qualified and experienced. For outdoor applications, the weather dependence of the results has to be taken into account.

Thermal techniques are not applied for the package completeness testing, since the scanning feasibility is limited to the surfaces, only.

1.3.11 Terahertz

Methods

The technical use of terahertz waves is a relatively new branch of science and technology. This frequency region has been previously unexploited because of a lack of efficient devices working in this range. Terahertz radiation covers the frequency range from 100 GHz up to 20 THz, which spans the spectral interval between the microwave and the infrared regions of the electromagnetic spectrum. The wavelength of THz waves is spread between 15 µm and 3 mm.

Starting from the 1980's, significant progress in the development of the terahertz sources has been observed. Sources based on Gunn and Impatt diodes have their applications in the THz range [137], but the generation of a few hundred GHz with high output power is extremely costly. On the other hand, quantum cascade lasers are able to generate waves with frequencies around 20 THz [138], however, cryogenic cooling is required. Another approach to terahertz generation is the use of free electron laser (FEL), but because of the size and complexity, its practical usage is limited. Gyrotrons use strong magnetic fields to generate the terahertz radiation. Backward wave oscillators generate radiation with frequencies up to 1.5 THz. Similar to FEL, the application of gyrotrons and backward wave oscillators in industry for quality control is limited because of their volume and extensive power requirements. Therefore, the most applied method for the generation of the terahertz radiation involves the internal photoeffect in a semiconductor [139]. The achieved terahertz waves' frequency can be as high as 70 THz in GaAs, and InP, as proven by Leitenstorfer et al. [140]. Another way to generate THz radiation is to use an opto-electronic method. THz radiation may be achieved in an electro-optic medium, e.g. non-linear crystal, via difference - frequency mixing [141]. Using this method electric fields ranging from DC to the mid-infrared can be produced [142]. To generate terahertz radiation, Auston switches can be employed [143]. Historically, the oldest continuous wave (CW) source is the molecular far infrared laser [144]. However, this source is tunable only in a narrow range unless the active gas is exchanged. One approach to develop a tunable continuous-wave (CW) THz source is achieved by the mixing of two laser frequencies in a photoconducting antenna [145]. The disadvantages of this method are the lasers' price, and the quite complex laboratory setup. Instead of two lasers, a two-colour electronically tunable external-cavity laser diode can be employed [146].

There exist several devices and techniques for the detection of the terahertz radiation. Since the terahertz photons energy is too small to be detected by detector diodes or photodiodes, thermal detectors are used. The bolometer invented in the nineteenth century belongs to the group of the thermal detectors. Employing a Wheatstone bridge, the absorber's temperature is measured with the accuracy of 10 μK, therefore high sensitivity for the measurement of the terahertz waves' intensity is assured. However, since the bolometer requires cryogenic cooling, its practical usage is limited. Hence, another type of thermal detector, the Golay cell is applied for the detection of the terahertz radiation. The Golay cell voltage response is linear over a wide range of input intensities; moreover it is more compact than a bolometer and does not require cooling. However, its sensitivity is lower than that of the bolometer for the terahertz range. If high sensitivity of the detector is not required, and simultaneously the detector's size and cost has to be reduced, a pyroelectric detector is an alternative. Today's pyrodetectors offer almost the same sensitivity as Golay cells, while they have a broader spectral range. However, all detectors presented above suffer from a slow response time because of the thermal capacitance of the sensors. Moreover none of the detectors provides phase information. Using coherent detection employing photoconductive antennas based on silicon-on-sapphire or LT-GaAs, phase information can be obtained.

Beside terahertz sources and detectors, passive devices like modulators, reflectors and filters are needed. So far, several practical realizations of the modulators have been presented. The first THz modulator was built by Libon et al. [147]. Unfortunately, this device does not work well at temperatures over 150 K. Another realization of the room-temperature modulator employs two-dimensional electron gas confined at a semiconductor AlGaAs/GaAs heterointerface [148]. The use of liquid crystals opened new possibilities for terahertz wave modulation, as presented for the sub-terahertz [149, 150] and the terahertz regions [151]. Since the working principle is based on the reorientation of the liquid crystals, these devices suffer from relatively slow response time. Using hybrid metamaterials based on split ring resonators, the modulation frequency has been extended well beyond 2 MHz [152].

Applications

In the following section the possible applications of terahertz technology will be discussed. However, in contrast to the techniques presented so far, terahertz technology is rather young and therefore, its position in the industry is still not well established.

The main application of the early terahertz systems was spectroscopy. This application arose from the presence of the "optical" transitions (rotational and vibrational levels of molecules, crystal-field-split levels of magnetic ions, phonons, magnons and plasmons) between different energy states in the terahertz region. Since many materials have characteristic fingerprints, e.g.

absorption maxima at particular frequencies, their identification can be performed based on the previously obtained spectroscopic data. As a result of basic laboratory research on different materials, several promising applications in quality control, medicine, security and wireless communications have emerged.

Preliminary results revealing the content of a cereal box and chocolate for quality control applications has been presented by Mittleman et al. [153]. The biggest advantage of terahertz technology for quality control arises from the fact that most of the packaging materials used by the contemporary industry are transparent for the terahertz waves. The pharmaceutical tablets can be inspected for the completeness purposes in the production line by utilizing terahertz waves [154]. A wide application spectrum for the testing of polymeric materials has been shown. Using terahertz radiation, quality control of a glass-fiber reinforced epoxy sample can be performed [155]. The measurement of the polymeric compound refractive index enables the calculation of the additive content [156]. The real life application of this idea was presented by Krumbholz et al. [157] showing the online control of the compounding process. Terahertz waves can be applied for the quality assurance of plastic weld joints, as presented in [158]. Applications for quality control in the food industry have been proposed [159]. Here, different types of contaminations in chocolate have been successfully recognized.

The non-ionising nature of terahertz radiation allows the safe imaging of biological tissues. The most promising field for terahertz technology in medicine is cancer detection [160]. Other sources show that tooth diseases including decay can be recognized [161]. In biology, the use of terahertz for density mapping [162], RNA identification [163] and estimation of water content in plants has been proposed [164].

Since terahertz radiation does not ionise the scanned matter, it is a preferred technique for the imaging of the people at airports. Preliminary results showing the possibility of the detection of concealed weapons, explosives and drugs has been published [165]. The application of terahertz for mail inspection against harmful material content is promising [32].

In the future, it is highly possible that terahertz waves will be the solution for increasing demand for bandwidth in telecommunications. Recently, highly directive antennas [166] and efficient reflectors [167] have been proposed. The practical realization of the transmission systems at 120 GHz [168] and 300 GHz [169] working at distances of 2 km and 22 m, respectively, have been shown. It is believed the terahertz transmission will replace the current solutions in WLANs and in short-range communication systems in 10 - 20 year's time.

Summary

The biggest advantage of terahertz technology is the fact that it offers nondestructive imaging and spectroscopic measurements of many different materials. Since many packaging materials in the industry are made of terahertz-transparent materials, terahertz technology offers the scanning of the package content. The package completeness and filling height can be checked without the need to open the package. In contrast to X-rays, terahertz radiation does not ionise the specimen; therefore, it is preferred for inspection in the food and pharmaceutical industry. Measurements using terahertz technology can also be performed in a reflection setup. In this case, only one side of the product has to be accessible. A further advantage is the fact that no sample preparation is required. The testing is contactless and nondestructive. This is advantageous over the ultrasound technique, where the couplant is needed. Still, the terahertz system's spatial resolution is comparable to that of the ultrasound.

The most important disadvantage of the terahertz technology limiting the applications for the industrial control is system complexity. Today's systems require advanced instrumentation including fragile lasers, fibers and antennas. In order to achieve a reasonable signal-to-noise ratio, a lock-in technique has to be employed. As a result, the time required for signal detection limits the scanning speed. Because of the system's sensitivity to temperature changes and heavy industrial conditions, no instruments have been applied for the permanent process control so far. Additionally, the use of terahertz systems requires extensive personnel training. Today's terahertz instruments are still bulky, therefore they are not portable. The implementation of the system is not easy and has to be performed by qualified personnel. Initial and maintenance expenses still remain well above the costs of the other techniques.

The application of terahertz waves for completeness testing is promising, particularly in the food industry, where packaging materials such a polyethylene or polyester are transparent to the THz radiation while the package content is opaque. However, as discussed above, the current costs and the complexity of these systems are by far too high. Therefore the application of terahertz waves for completeness testing is still limited.

2 Microwaves

The microwave spectrum spans from 300 MHz to 300 GHz and is placed between radio waves and terahertz radiation in the electromagnetic wave chart. The upper part of this frequency region is called millimeter waves because of the wavelength ranging from 10 mm (30 GHz) to 1 mm (300 GHz) in free air. Since terahertz technology is well established these days, the millimeter waves are alternatively called sub-terahertz waves.

Historically, the German scientist Heinrich Hertz validated the electromagnetic theory developed by James Clerk Maxwell for the microwave regime. The development of the microwave technology was limited till the 1940s because of the lack of generators and detectors. The Radiation Laboratory established at Masachussets Insitute of Technology contributed to the significant development of the microwave theory. The achievements in radar technology activated the research activities of microwaves, especially for communications systems [170].

Today's applications of microwaves concentrate mainly on remote sensing and communication. Using radars, the object's speed, distance, angular direction, size and form can be determined [171]. Moreover, radars are widely used for missle-tracking, weather detection, airport traffic control [172]. Chemical substances in the earth atmosphere have characteristic absorption spectra in the microwave range and therefore can be detected using passive remote sensing. The application of radio telescopes in radio astronomy enables to detect cosmic objects, e.g. pulsars and radio stars. Microwave imaging belongs to the group of remote sensing applications. Recent development of the imaging systems has enabled scanning anomalies in the space shuttle external fuel tank insulating foam using a 100 GHz scanner [173]. Another field of microwaves application is the communication links. Terrestrial and satellite links are widely used by television networks. A frequency range from 50 MHz to 22 GHz is used to carry the television signals [174]. Additional uses of satellite communication links include collecting data on atmospheric and weather conditions [172]. Contemporary demand for a high speed communication links can be fulfilled by the use of microwaves frequencies. In practice, all existing and new communication protocols are located in the microwave range of the electromagnetic spectrum. The examples include WLAN, Bluetooth [175], CB, GSM and UMTS [176] protocols. All currently exploited and developed navigation systems: GPS, Galileo, Glonass and Beidou are based on microwave signals [177]. Since microwaves cause the vibration of water molecules, there exist several applications besides microwaves ovens. In the industry, microwaves at frequency of 2.45 GHz are used for curing, drying and plasma etching in the semiconductor sector [178].

In this chapter, the fundamentals of the microwave technology are presented. This includes a description of the sources, detectors, antennas and planar transmission lines.

2.1 Sources

Microwave sources can be divided into 2 groups: solid state and tube sources. Typically, the power generated by solid state sources does not exceed several watts at frequencies below several hundred gigahertz [179]. However, this kind of sources has several advantages over tube generators. Solid state oscillators are compact and therefore, can be easily integrated with other devices. Because of the dense design, a high robustness and reliability can be offered.

Solid state sources

Microwave solid state sources fall in three categories: Gunn diodes, impact ionization avalanche transit-time (IMPATT) diodes and field effect transistors (FET). The sources based on diodes require resonant structures for operation. Therefore, their integration capabilities with monolithic microwave integrated circuits (MMICs) are somewhat limited. This is in contrast to transistor sources, where bulky resonators are not needed. As a result, transistor sources can be integrated with other devices on the same substrate. In the following, solid state sources will be discussed.

The most common oscillators employ the Gunn diode. Physically the Gunn diode is based on a bulk intrinsic semiconductor, e.g. GaAs, InP or CdTe [172]. All mentioned semiconductors have a specific structure of the conduction band which is schematically shown in Fig. 2.1 a). As can be seen, beside the central valley there exist satellite valleys in the conduction band. When a low bias voltage is applied to the semiconductor, the electrons occupy the central valley. In contrast, after applying higher voltage, the electrons are distributed in the satellite valley. Here, effective electron mass is higher; and therefore, electron mobility is lower compared to that in the central valley. Since the semiconductor's conductivity is proportional to the carriers' mobility, increasing the bias voltage leads to the decrease of the conductivity [172]. Hence, the semiconductor has a negative resistance for a defined voltage range, as presented in Fig 2.1 b). The typical Gunn oscillator involves an additional resonant structure for effective employment of the Gunn diode oscillations. As a result, a power up to several watts can be achieved. The resonator's cavity uses a transformer for matching of the diode and the waveguide impedances. The Gunn diode based oscillators can be tuned within the range from -20% to 20% of the nominal frequency. Depending on the design, a mechanical or an electrical tuning can be obtained.

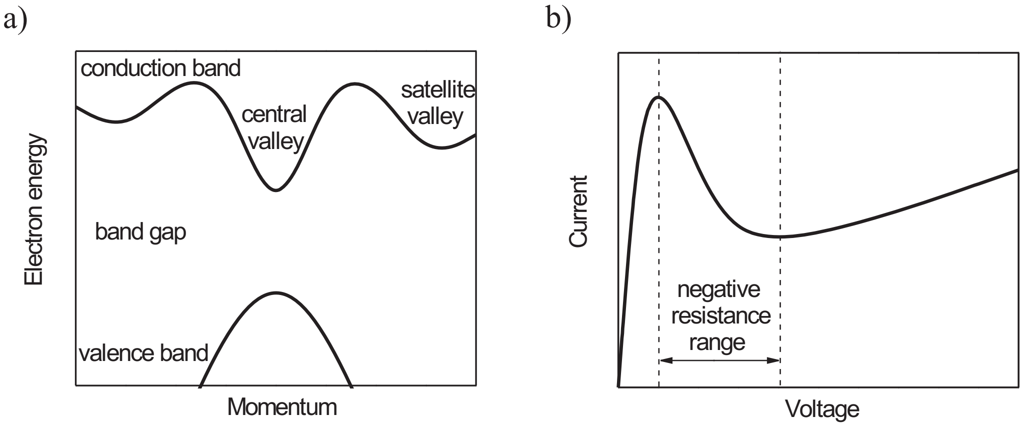

Figure 2.1: The Gunn diode: a) simplified band structure, b) current-voltage characteristics.

Mechanically tuned oscillators involve a tuning screw placed in the cavity. In electronically tuned devices an additional diode, a varactor, changes the properties of the cavity by means of its variable capacitance.

The IMPATT diode employs a reversed-biased Si or GaAs pn junction and high-Q resonator for the microwaves generation. If a phase delay between an applied radio frequency voltage and the avalanching current exceeds $\pi/2$, the diode exhibits a negative resistance. Therefore, it can be used as a source for microwaves. While this kind of source is noisier than a Gunn diode-based oscillator, a higher efficiency reaching up to 30% and a higher power can be achieved [172].

Transistor sources offer lower power levels and frequencies of the generated microwaves; however, they can easily be integrated with other passive or active components. Depending on the design frequency, bipolar junction transistors (BJTs), metal semiconductor field effect transistors (MESFETs) and high-electron-mobility transistors (HEMTs) are employed. For generation, transistors are arranged in Hartley, Colpitts, or Clapp oscillator circuits. For oscillations, a positive feedback between the output and input of the transistor has to be assured. This is realized by means of a series reactance placed in the emitter, source, base or gate sub-circuit. As a frequency-selective component, a high-Q dielectric resonator leading to low phase noise is employed [180]. Transistor oscillators are tunable over a wider range compared with the diodes. For tuning, a reverse biased varactor is utilized. Since the voltage bias determines the varactor capacitance, the resonant load parameters are adjusted, which leads to microwave generation at a particular frequency. The typical tuning range is one-fifth of a decade. As an alternative, an yttrium iron garnet (YIG) sphere alters the inductance of the load circuitry. The YIG sphere is controlled by the magnetic field strength determined by the applied bias voltage. The tuning range is well above one decade; however the physical factors limit the tuning speed, which is lower than for a varactor-type oscillator [172]. For further integration of transistor oscillator circuits, MMICs are used (see section 2.4).

Microwave tubes

The working principle of every microwave tube is based on the interaction of an electron beam with an electromagnetic field. Generally, the source of the electron beam is a biased thermocathode. To focus the beam onto an anode, a high voltage between the cathode and the anode is applied. Alternatively biasing magnets can be employed for the electron beam focusing. Since vacuum is required for the generation of electron beams, the cathode and the anode are encapsulated in a vacuum tube. The efficiency of the microwave tubes is about 40%; therefore, for high output power sufficient cooling of the tube has to be assured. As a result, these devices require high volumes for effective heat dissipation. Hence, all microwave tubes are significantly larger than solid state sources.

Two types of tubes exist: linear beam and crossed-field tubes. In linear beam tubes the electron beam is parallel to the electric field. In contrast, in crossed-field tubes the electron beam is oriented perpendicular to the electric field [170]. In the following, the most common microwaves tubes will be presented.

The magnetron is the oldest microwave tube and it belongs to the crossed-field tubes group. For this source the resonators arranged in a cylindrical pattern comprising the anode with the cathode placed in the rotation axis of the anode play the key role. The electrons generated by the hot cathode are accelerated by the magnetic field induced by the permanent magnets. The resonant nature of the anode forms the electrons into groups, what leads to the microwave radiation. The magnetron's frequency reaches 40 GHz with power levels not exceeding several megawatts with a nominal efficiency of 80% [181].

The klystron belongs to the group of linear beam tubes. Typically two cavities are employed. The goal of the first cavity is to modulate the velocity of the electron beam. The second cavity is used for the signal decoupling. A part of the developed signal is fed to the first cavity to maintain self-oscillations [172]. Additionally, this type of klystron can be employed as an amplifier. For oscillator applications, a reflex klystron containing one resonator can be used. The klystron can deliver up to 45 MW of microwave power with the efficiency of 42% [182]. Klystrons have low noise; however, they can be operated only at a single design frequency.

To overcome the narrow-band nature of the klystron, a group of travelling wave tubes (TWT) is applied. Here, a wire helix, magnets between cathode and anode, and couplers are employed. The signal introduced by the input coupler to the helix interacts with the electron beam, what leads to the velocity modulation of the electrons. The signal is decoupled by the second coupler located close to the anode [170]. Similar as in the klystron tube, a positive feedback between two couplers is assured for self-oscillations. Since the couplers are wide-band devices, the travelling wave tube is a tunable generator. In the backward wave oscillator (BWO), the signal is coupled close to the anode and it propagates in the cathode direction [170]. A power up to 2 GW in pulse mode is achievable [183].

The gyrotron is a representative of the crossed-field tubes. Here the interaction of the electromagnetic field with the cyclotron motion of the electrons is the operating principle. In gyrotrons, high magnetic fields cause that the rotation frequencies of the electrons directly correspond to the millimeter wave range. Gyrotrons are capable of generattion high frequency radiation reaching 1 THz at high output power [184].

2.2 Detectors

For the detection of microwaves, diode detectors and transistors are employed [170]. The diodes used for the detection purposes are Schottky or Esaki tunnel diodes. Schottky diodes use the rectifying properties of a metal to semiconductor junction. For this kind of junctions, the metal's work function is higher than the semiconductor's one. As a result, an energy barrier between the semiconductor and the metal is created. Because of the work function relationship, electrons move from the semiconductor to the metal surface. The carriers' movement produces a negative charge in the metal and a positive charge in the semiconductor. In equilibrium state further charge movement is cancelled by the electric field created by this charge. If the diode is forward biased by the incident microwave radiation, the barrier between the semiconductor and the metal lowers allowing additional electrons to move from the semiconductor to the metal. This results in a current. In case the diode is biased reversely, the barrier gets higher, and no current is observed. Detector diodes use the p-type semiconductors, since their $1/f$ noise is smaller compared to the n-type semiconductors. Theoretically, GaAs and Si can be used. However, since the forward voltage of a GaAs diode is high, only Si finds applications in detector diodes. Typically the diode detectors follow the square-law rule at low input levels. It means the detector produces the output voltage which is proportional to the second power of the input voltage and eventually to the power of the input signal. The voltage V - current I dependence is defined by the Shockley's diode equation:

$$I = I_S e^{\frac{V}{nV_T} - 1}, \tag{2.1}$$

where I_S corresponds to the saturation current, n is the ideality factor and V_T is the thermal voltage which is 26 mV at the temperature of 300 K.

For the biased diode, the relation between the current and voltage can be also presented using the following equation:

$$V = \frac{dI}{dV}\bigg|_{V=V_B} V + \frac{1}{2}\frac{d^2I}{dV^2}\bigg|_{V=V_B} V^2 + \frac{1}{6}\frac{d^3I}{dV^3}\bigg|_{V=V_B} V^3 + \frac{1}{24}\frac{d^4I}{dV^4}\bigg|_{V=V_B} V^4 + \dots, \tag{2.2}$$

where V_B stands for the bias voltage. The direct current component originates mainly from even-degree terms [185]. If higher order terms presented in equation (2.2) are small compared to the first even term, the diode operates as a square-law detector. Merging the Shockley equation and the equation (2.2), the following relationship can be obtained:

$$I = I_S e^{\frac{V}{nV_T}} \left(\frac{V}{nV_T} + \frac{1}{2}\left(\frac{V}{nV_T}\right)^2 + \frac{1}{6}\left(\frac{V}{nV_T}\right)^3 + \frac{1}{24}\left(\frac{V}{nV_T}\right)^4 + \dots \right). \tag{2.3}$$

The term $\frac{1}{24}\left(\frac{V}{nV_T}\right)^4$ can omitted only in the case when

$$\frac{1}{24}\left(\frac{V}{nV_T}\right)^4 \ll \frac{1}{2}\left(\frac{V}{nV_T}\right)^2. \tag{2.4}$$

Since the left term of the equation (2.4) has to be much smaller than the right term, after the introducing of a factor $W = 250$, the equation can be rewritten in the following form:

$$\frac{W}{24}\left(\frac{V}{nV_T}\right)^4 < \frac{1}{2}\left(\frac{V}{nV_T}\right)^2, \tag{2.5}$$

In view of the approximation (2.5) the applied voltage has to fulfill the following equation:

$$V < \frac{\sqrt{12W}nV_T}{W} \tag{2.6}$$

Therefore, assuming the ideality factor $n = 1.25$ and the source impedance $Z = 50\,\Omega$, the maxium power P_M for which the square-law is applicable equals:

$$P_M < \frac{12n^2V_T^2}{WZ} = 1\ \mu\text{W},$$

$$P_M < -30\ \text{dBm}.$$

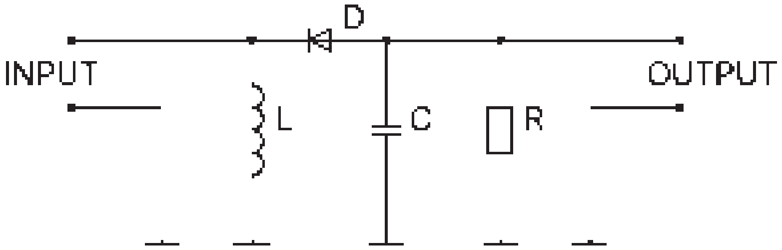

Figure 2.2: The diode detector circuit.

For power levels exceeding P_M, the diode output voltage is proportional to the square root of the incoming RF power. For increasing the diode sensitivity, a dc bias applied in the forward direction may be used.

A detector circuit employing a diode in a half-wave rectifier configuration is shown in Fig. 2.2. For RF frequencies the reactance of the inductor L is high and the reactance of the capacitor C is low; therefore, the diode is connected parallel with the input port. For the rectified signal, the reactance of the inductor is low, and the reactance of the capacitor is high; therefore the diode is connected parallel to the output port. The resistor R together with the capacitor C builds a low pass filter. For detecting low frequencies, the passive parts presented in Fig. 2.2 may be lumped elements. For high frequencies, transmission-line stubs are employed [185]. In order to improve the detector sensitivity a forward diode bias is applied.

2.3 Antennas

The goal of antennas is to interface the transmitters and receivers to the propagation channel. The transmitting antenna acts as transducer and it converts the input currents into an electromagnetic wave, whereas the receiving antenna transforms the propagated electromagnetic wave into an electric current.

Field regions of the antenna

Depending on the antenna dimensions, operating frequency and observation distance, two field regions of the antenna: the near-field and the far-field can be defined. The near field region can be further divided into the reactive and radiating region. The reactive region extends from direct proximity with the antenna to the distance r_1 defined as

$$r_1 = 0.62\sqrt{\frac{D^3}{\lambda}}, \tag{2.7}$$

where D is the largest dimension of the antenna and λ is the wavelength. The antenna's charges are the origin of reactive fields. The reactive components decay with the cube of the distance from the antenna decreases. Starting from the distance λ from the antenna, the reactive fields are considered negligible compared to the radiating fields [186]. The radiating region extends from the distance defined by the equation (2.7) to the distance r_2 calculated from:

$$r_2 = \frac{2D^2}{\lambda}. \tag{2.8}$$

In this region, radiating fields are dominant; however, the radiation pattern is dependent on the observation angle and the observation distance. The reason of this dependence can be explained by the fact that the observation distance is comparable with the antenna's dimensions. For larger distances, the observation distance is much bigger than the size of the antenna; therefore, the radiation pattern is independent from the distance from the antenna. This region is called the far-field and it starts from the distance given by the equation (2.8) and extends to infinity. For the far-field region, the power intensity is inversely proportional to the square of the distance.

Antenna parameters

Every antenna can be characterized by several parameters. The radiation pattern shows the relative power distribution in space. Typically, the radiation pattern is presented in a polar or Cartesian plot. A half-power beamwidth (HPBW) is a parameter describing the radiation pattern and is defined as an angular width of the main lobe for which the power decreases to the half of the maximum beam power. The directivity D_R is a ratio of the maximum radiation intensity I_M to the radiation intensity averaged over all directions of the isotropic radiator P_R [187]:

$$D_R = \frac{4\pi I_M}{P_R}. \tag{2.9}$$

The antenna efficiency η is the factor of the radiated power to the power fed to the antenna. Since the antenna material has losses, the efficiency is intrinsically lower than unity. The overall antenna efficiency is influenced by the reflection mismatch efficiency η_R, conduction efficiency η_C and the dielectric efficiency η_D as presented in the following equation:

$$\eta = \eta_R \eta_C \eta_D \tag{2.10}$$

The antenna gain G is the ratio between the maximum radiation intensity and the radiation intensity produced in the same direction from an isotropic radiator P_I [187]:

$$G = \frac{4\pi I_M}{P_I}. \tag{2.11}$$

Therefore, the antenna's gain can be presented in the terms of the directivity, as follows:

$$G = \eta D_R. \tag{2.12}$$

The polarization of the antenna is to be understood as the polarization of the wave radiated by the antenna. The wave polarization describes the time varying direction and relative magnitude of the electric field vector [188]. There exist three types of polarization: linear, circular and elliptical. However, most antennas transmit linear polarized waves.

Antennas overview

Several types of antennas are employed for the microwave range.

Wire antennas may take the form of a dipole, monopole, loop or helix. These antennas are characterized by relatively low gain not exceeding 6 dB. The bandwidth of this antenna type is narrow; it is limited to about 10% of the design frequency. Wire antennas are radiating the power equally in the azimuth plane; therefore, their HPBW parameter equals to 2π. The operation frequency does not go beyond several gigahertzes.

Aperture antennas can have the form of a pyramidal, conical, E-plane and H-plane sectoral horn. For demanding applications, ridged and flared horn antennas are designed to increase the aperture efficiency. Horn antennas cover the frequency range from 50 Hz to 2 THz [189] at gains ranging from 5 to 22 dB and they provide a broadband operation. The HPBW parameter spans from $\pi/20$ to $\pi/3$.

Microstrip antennas utilize a conductor patch on a grounded dielectric substrate. These antennas are very small in size, light and low-profile and easy to fabricate. Since they can be etched directly into the microwave substrates, the integration with passive elements and MMICs is possible. The limitations of the microstrip antennas include low efficiency, poor polarization purity and narrow band below 5% of the design frequency. The gain offered by the antenna is between 5 and 9 dB. The design frequency covers almost the entire microwave and millimeter wave range. The HPBW varies from $\pi/12$ to $\pi/2$.

Reflector antennas are used for the signal transmission over great distances. The widest applied reflector is a parabolic and a corner reflector. As feed elements, horn and dipole antennas are used. Because of high aperture sizes, reflector antennas have gain between 20 and 70 dB. The design frequencies are located in the range from 400 MHz to 30 GHz. These antennas are wide-band enabling for the operation at the frequencies $\pm30\%$ of the design frequency. HPBW is very low, typically between $\pi/360$ to $\pi/18$.

Array antennas consist of several single antennas with the goal to increase the total gain of the antenna. Alternatively, arrays enable for the beam steering. The single elements of the array are arranged in that way, that a constructive interference takes place. Typically, the arrays of wire antennas (Yagi antenna), microstrip and aperture antennas are built.

Free-space propagation

When the transmitting and the receiving antenna are separated spatially by the distance d, a free space loss occurs. The free-space loss FSL is defined by the equation:

$$FSL_{dB} = 20\lg\frac{4\pi df}{c}, \tag{2.13}$$

where the constant c denotes the speed of light and f is the frequency.
For the calculation of the factor of the received power P_R by the receiving antenna with gain G_R to the power sent P_T by the transmitting antenna having gain G_T the Friis equation is employed [190]:

$$\frac{P_R}{P_T} = G_R G_T \left(\frac{c}{4\pi df}\right)^2. \tag{2.14}$$

Merging the equation (2.13) and (2.14) the power received can be calculated as follows:

$$P_{RdBm} = P_{TdBm} + G_{RdB} + G_{TdB} - FSL_{dB}, \tag{2.15}$$

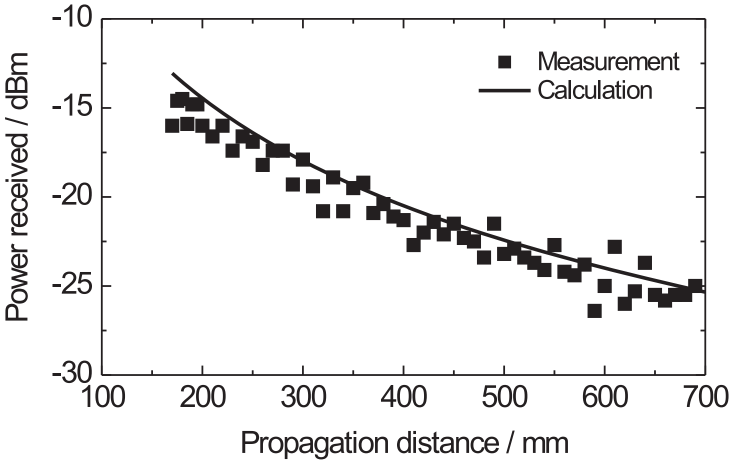

Figure 2.3: Power received as the function of the distance between the 21 dB gain horn conical antennas.

where the units with dB index are expressed in decibels.
As it can be deduced from the Friis equation, doubling of the distance increases the free space loss by 6 dB. However, it must be emphasized, the Friis formula is valid for the far field of the antenna. In case for the 21 dB gain horns having the aperture diameter 16 mm, the far field for the frequency 100 GHz can be obtained using the equation (2.8) and equals to 170 mm. The graph 2.3 presents the measured and the calculated power received. As it can be seen, the measurement data are 0.5 dB below the calculated power. This fact is attributed to a not perfect setup alignment and additional antennas losses. The reason for the data scattering is the multipath reflections from the ground.

Including the transmitter and receiver connector losses, L_{TdB} and L_{RdB}, respectively, the link budget equation can be presented as follows:

$$P_{RdBm} = P_{TdBm} + G_{RdB} + G_{TdB} - L_{RdB} - L_{TdB} - FSL. \tag{2.16}$$

Generally, for transmission links the atmospheric attenuation has to be considered. As presented in [170], the atmospheric attenuation does not exceed 1 dB/km and 0.15 dB/km for the W-band and Ka-band, respectively. Therefore, for further described microwave imaging purposes where the free air propagation distances are below 700 mm, the atmospheric attenuation is negligible.

2.4 Planar technology

Conventional microwave systems are based on the waveguide technology. The components being part of this technology are bulky, heavy and expensive. Therefore, the planar technology has been invented to overcome these drawbacks. The planar technology enables for miniaturization and integration of the microwave and millimeter wave devices using well developed microelectronics technology. As a result, the weight, size and production cost can be minimized, a low profile and an easy integration with semiconductor devices can be obtained.

Substrates

In the planar technology, different types of substrates including crystalline, ceramic and composite materials are used as carriers for the active and passive components. Existing substrates can be divided into the two groups: hard and soft substrates. Fused quartz, aluminium oxide and sapphire belong to the group of hard substrates. Fused quartz has very good properties in the microwave range, since the dielectric constant and losses are low. However, its practical use is limited, since the material is fragile and hence the machining is complicated. Additionally, the metal adhesion to fused quartz is low and the thermal expansion coefficient is matched only to a few materials. Another substrate material - aluminium oxide - can be easier machined in comparison to the fused quartz. It is temperature stable and offers a good thermal conductivity. However, because of the high dielectric constant, its practical application is limited to the systems working at frequencies below 20 GHz [185]. As the conductor layer, gold is employed. Sapphire has similar properties to the aluminium oxide; however, it has significantly higher smoothness. Therefore, the conductor and dielectrics losses are minimized. Nevertheless, a high dielectric constant is impractical for high frequency devices. Finally, the last representatives of the hard substrates are gallium arsenide and indium phosphide. The advantages of these materials are low bulk conductivity and low losses. Therefore, both materials are used as a substrate for monolithic circuits despite of a relatively high price.

Composite materials are the most common used soft substrates in microwave technology. They are based on the polytetrafluoroethylene (PTFE) loaded with glass fibers or ceramic powder. These materials are characterized by a relatively low losses and low dielectric constant. Although the losses and the dielectric constant of many substrates are specified by the manufacturer for the lower frequency band, it has been shown that the composite materials hold low losses and dielectric constant in the upper part of the millimeter wave range, as well. As an example, the substrates belonging to the RO4000 group specified for 10 GHz still offer relatively low losses at the frequency of 94 GHz [191]. Besides good electrical properties in the high frequency range, the composite materials are easy to process. Typical processing steps including cutting, etching and drilling which have been developed for the circuits working at lower frequencies based on the FR4 substrates can be applied directly to the composite substrates, since the mechanical properties of both types of the substrates are similar. Composite materials are temperature stable, since the thermal expansion coefficient is matched to that of the copper which is typically used as a conductive layer. As the alternative to the materials based on PTFE, liquid crystal polymers (LCPs) are employed. Besides good electrical properties, these materials have advantages over previously described substrates. As an example, the thermal expansion coefficient can be matched in the fabrication process to that of the conductor, or the semiconductor.

Transmission lines

Generally, there exist four main types of planar transmission lines to be used in the microwave technology: microstrip, coplanar waveguide (CPW), stripline and suspended substrate stripline (SSSL) as presented in Fig. 2.4. The microstrip is the most common type of the transmission line. It finds applications in hybrid and monolithic circuits. As shown in Fig. 2.4, the struc-

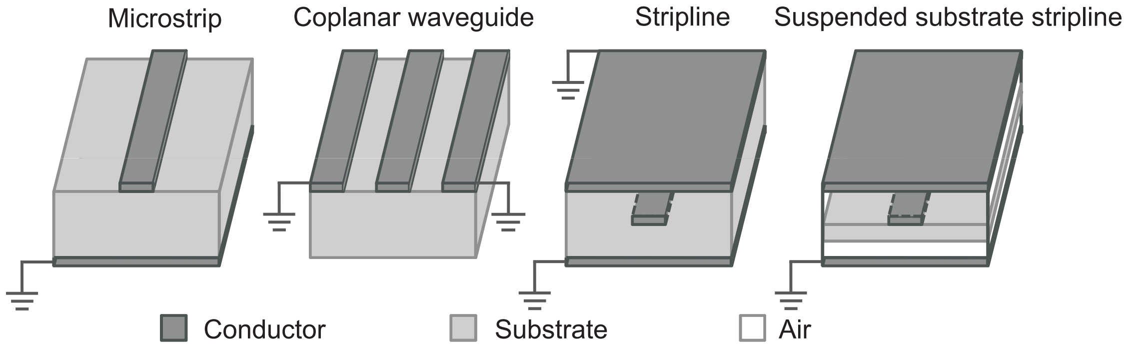

Figure 2.4: Planar transmission lines.

ture consists of a conducting strip on one side of the dielectric substrate and from the ground plane on the other. For the CPW the ground is located on the same layer, as the conducting strip. Therefore, CPW transmission lines do not require the use of the vertical interconnect access technology. Grounds which are made on the same layer have lower inductance and resistance. Using CPW, a large scale of integration can be achieved, since it is possible to obtain low impedance lines which have small widths. This is in contrast to microstrip lines, where the strip width is determined by the thickness of the substrate. However, CPW lines have some disadvantages. Since the field is not completely localized in the substrate material, the radiation and dispersion are worse than in the microstrip lines [185]. In CPW lines the currents concentrate at the edges of the conductors. Since the edges have higher roughness, surface losses appear. The stripline uses a conductor which is sandwiched between two parallel ground planes. The substrate is used as a carrier for the conductor. The stripline is nondispersive and enables to build low loss devices. However, since two parallel ground planes are employed, parallel-plate modes can be excited. While advanced manufacturing technology has to be employed, generally the striplines' applications are limited to directional couplers in which the highest coupling over other transmission lines can be achieved [185]. Technologically only soft substrates can be used for the striplines. To overcome this limitation, a suspended-substrate stripline can be applied. Since in this type of the transmission line the conductor is surrounded from one side by the air, the effective dielectric constant is very low. As a result the losses are lower compared to the stripline. To the disadvantages of the SSSL belong high dispersion and the waveguide-like modes [185]. Besides the four types of the transmission lines described here, several modifications of them exist. A conductor-backed coplanar waveguide (CBCPW) is a CPW with added ground plane. Using another ground plane on the top of the structure leads to a double shielded coplanar waveguide.

Active components

The mostly used active devices in the microwave technology are monolithic microwave integrated circuits (MMICs). The MMICs are fabricated from a single semiconductor substrate and consist of active and passive elements building a complete device. The devices operating above 30 GHz are called monolithic millimeter wave integrated circuits (MMWIC) and nowadays they cover almost the full millimeter wave range [192]. MMICs have replaced discrete circuits consisting of individual transistors, resistors, inductors and capacitors. Since these elements are integrated on a single substrate, MMICs are more compact, more cost-effective and more reliable than their discrete-elements equivalents. Typically a carrier for MMICs is GaAs substrate. The transistor types employed in the MMIC devices range from metal semiconductor field effect transistors (MESFETs), high electron mobility transistors (HEMTs), pseudomorphic-HEMTs (pHEMTs) to heterojunction bipolar transistors (HBTs). For the fabrication, standard microelectronics techniques including ion implantation, epitaxy and molecular beam epitaxy (MBE) are applied. Current devices realized in the MMIC technology are low noise amplifiers, mixers, detectors, frequency multipliers and oscillators. Practically no limitation exists for MMIC applications excluding high power amplifiers for which the proper heat dissipation is still challenging.

Passive components

On the basis of the planar technology distributed elements for the microwave range can be built. They have several advantages over the lumped elements. Firstly, distributed elements have superior electrical properties at high frequencies. Often no alternatives for them exist at millimeter wave frequencies. Secondly, the distributed elements can be easily manufactured in a single etching process. Passive components including resistors, capacitors and inductors can be produced in planar technology. The resistors are realized by material deposition on the substrate. Low-value capacitors are manufactured as interdigital structures. Inductors can be realized as spiral inductors in the planar technology. Short or open circuits can be obtained by employing the stubs which are easily fabricated by etching of the conductive layer. Other components which can be easily realized in the planar technology are power dividers and combiners, directional couplers and band filters.

3 Millimeter wave optics

For the complete mathematical description of wave propagation through optical systems a complex formalism is required. Therefore, to reduce the complexity and the computation time, several simplifications are usually made. Assuming the existence of point objects, point images and uniform spherical waves the beam propagation can be described by the geometrical optics. This approach works well for the optical range in which the lateral component size is significantly larger than the wavelength. However, for the millimeter range of the electromagnetic spectrum these assumptions cannot be made. The explanation is that at these frequencies the wavelength is comparable with the components' geometrical dimensions. In this case, the diffraction effects play a significant role in the beam propagation and therefore need to be considered. To overcome this limitation, Gaussian optics have to be employed to describe wave propagation at microwave frequencies.

Lenses are the most commonly used elements to shape electromagnetic beams. The principle of operation is based on the wave front alteration using a material with different refractive index, than the one in which the wave propagates. This principle has initially found applications in the visible range; however, it can be successfully transferred to other regions of the electromagnetic spectrum. The lens material for a particular wavelength needs to have a low absorption coefficient and an appropriate refractive index in the desired part of the spectrum. Therefore, in the visible range a variety of glasses is employed as the lens material. The glass manufacturing technology is mature; hence, following types of lenses can be produced: spherical, aspherical, Fresnel and gradient-index lens (GRIN). In spherical lenses, the lens surface curvature is a segment of a sphere. The aspherical lenses use a polynomial asphere for the surfaces definition. The Fresnel lens uses concentric annular sections called the Fresnel zones. In GRINs the refractive index varies with the distance from the optical axis. In contrast to the materials used in the visible part of the electromagnetic spectrum, for the terahertz and microwave range dielectrics offer low losses. Commonly used lens types are spherical, aspherical and Fresnel lenses. Depending on the application, three types of surfaces a convex, a concave and a planar can be employed. These kind of surfaces enable to build following lens types: biconvex, plano-convex, plano-concave and biconcave.

Since lenses have limitations, no perfect image of the object can be obtained. The lens imperfections are called aberrations and they manifest as distrortions of the image. Two types of aberrations exist - monochromatic and chromatic aberrations, whereby the former can be divided into spherical aberration, coma, astigmatism and distortion.

Spherical aberration is defined as the variation of the focus with aperture [193]. This results in the fact that the rays propagating close to the optical axis (paraxial rays) focus at a greater distance than the rays meeting the lens at greater heights. The longitudinal spherical aberration is given by the distance range of the focus for rays at different heights. In contrast, the aberration measured along the parallel axis to the lens surface is defined as the lateral spherical aberration.

For a given focal and aperture length the spherical aberrations are solely conditioned by the object position and its shape.
Coma is that kind of aberration, where the magnification varies with the aperture [193]. As a result, the image height for the rays passing the edge portions of the lens is different than for those intersecting the optical axis. The most important parameters influencing the coma is the lens' shape, the beam incidence angle and the image distance. However, coma exists only for systems in which the input beam is not parallel to the optical axis.
Astigmatism describes an image aberration where the foci positions for tangential and sagittal planes differ from each-other. As a result, an elliptical or circular blur appears in the image position [193]. The astigmatism increases with the increase of the object - lens distance. Additionally the astigmatism amount is defined by the lens shape and the focal length. However, axially symmetrical lenses exhibit no astigmatism in axially symmetric systems.
Distortion appears when the image height proportion between off-axis and paraxial position differs from the height proportion of the object situated in off-axis and paraxial position [193]. The distortion is proportional to the cube of the object height.

The origin of chromatic aberrations is the dispersion; that is spectral dependence of the refractive index of the lens' material. For the optical range, the refractive index is inversely proportional to the wavelength. Hence, the focal length for the short wavelengths is smaller than for the longer - ones. The longitudinal chromatic aberration is defined as the distance along the axis between the focal points created by the different wavelengths [193]. The transverse chromatic aberration is the distance between image heights created by diverse wavelengths. The chromatic aberrations can be minimized by using low dispersion materials for lens fabrication. If a monochromatic source is utilized, no chromatic distortion appears.

In the following chapter, principles and consequences of the geometric and Gaussian optics will be discussed and compared to each-other. In particular, a convenient method for the calculation of the image position for lens systems in the millimeter range will be presented.

3.1 Geometrical optics

Geometrical optics uses rays of light for the description of the wave propagation. The ray of light can be defined as the path of a hypothetical point on the surface as a wave front is moving through space [193]. Rays are defined in corpuscular and wave theory, but are always perpendicular to the wave fronts. In corpuscular theory the ray is called the path of the corpuscle and the path of a photon. Wave theory defines the rays as wavefronts normals or the Poynting vectors. As it was stated, the ray is an imaginary product but it enables the understanding of optical systems. For geometrical optics, the source is assumed to be infinitively small. It radiates spherical waves whose radii curvatures R equal the distance z from the source, that is:

$$R(z) = z. \tag{3.1}$$

At a sufficient distance from the point source, the radius of the wave front may be regarded as infinite. Such a wave front is called a plane wave. As a consequence, the rays propagate along straight parallel lines in defined directions. However, for this model, the wave properties like diffraction, interference and polarization are totally neglected. It has been proven that for the optical system design all previously mentioned wave properties can be omitted if the geometrical dimensions of the elements are much larger than the wavelength. In general, geometrical optics is based on the five following assumptions:

1. The wavelength is infinitively small compared to the size of the optical component.
2. Only paraxial rays that is rays propagating in an infinitesimal small region around the optical axis are considered.
3. The waves propagate along straight lines in isotropic materials.
4. The waves propagate independently from each-other.
5. The diffraction and reflection of the waves follow the refraction and reflection law [194].

3.1.1 Lens transformations in geometrical optics

In the following section, the beam transformations by a lens according to geometrical optics will be considered. In particular, image position and its size will be determined. Figure 3.1 presents the ray tracing of rays coming from an object of height H. The rays propagate through the lens having the focal length F and build the image of height H'. The object and image distances from a lens are S and S', respectively. Using the similar triangles law two equations can be written:

$$\frac{H}{X} = \frac{H'}{F}, \tag{3.2}$$

$$\frac{H}{F} = \frac{H'}{X'}. \tag{3.3}$$

Merging these two equations leads to:

$$F = \frac{XH'}{H} = \frac{XX'}{F}. \tag{3.4}$$

Since $S = X + F$ and $S' = X' + F$,

$$F^2 = (F - S)\,(S' - F)\,, \tag{3.5}$$

and eventually

$$\frac{1}{F} = \frac{1}{S} + \frac{1}{S'}. \tag{3.6}$$

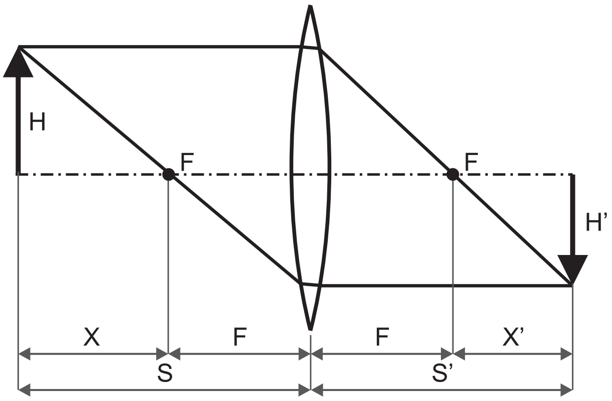

Figure 3.1: The imaging in geometrical optics theory.

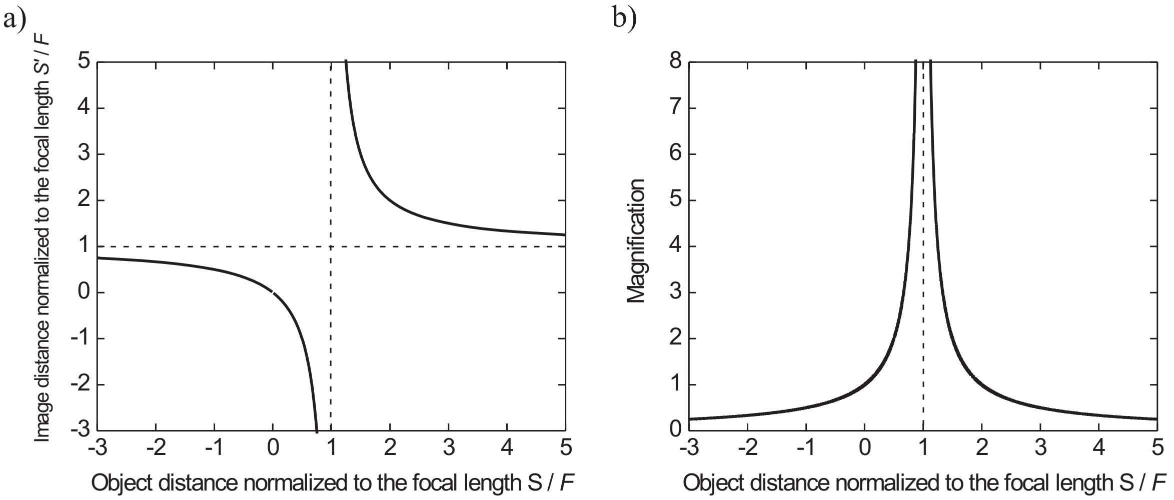

Figure 3.2: Lensing properties described by geometrical theory: a) normalized image position as a function of normalized object position, b) lens magnification as a function of normalized object position.

The practical meaning of the equation (3.6) is that knowing the object position and the focal length of the lens, the image position can be calculated. For visualization, the expressions present in the equation (3.6) have been plotted in Fig. 3.2 a). There exist two special cases that will be briefly discussed. Firstly, if the object is located in the focal plane ($S = F$) the image appears at infinity ($S' \to \infty$) according to the geometrical optics. Secondly, if the object is localized in a distance smaller than the focal length from the lens ($0 < \frac{S}{F} < 1$) then the image is always virtual, since $\frac{S'}{F} < 0$. These two cases will be discussed again in chapter 3.2.2 for the Gaussian optics. The transversal system magnification is defined by the proportion of the image size to object size. Combining the equation (3.2) with the relationship $X = S - F$ the magnification m can be calculated using following formula:

$$m = \left|\frac{H'}{H}\right| = \frac{1}{|1 - \frac{S}{F}|}. \tag{3.7}$$

The graphical presentation of the equation (3.7) is presented in Fig. 3.2 b). It can be easily noted that in consequence of the geometrical approach the magnification factor approaches infinity when the object is placed in the focal plane.

3.1.2 Geometrical optics software

For the design of complex optical systems a dedicated computer aided design software is employed. The main function of the optical design software is to supply the user with a mathematical description of an optical system that satisfies the given specification [195]. Generally the design program consists of three layers: the data entry, the evaluation and the optimization. The main function of the software from the user point of view is the optimization procedure leading to the best possible design. In this step, iterative optimization and evaluation of the design are performed. These processes are repeated until the final design is obtained. If the current design does not meet the requirements, the user applies a modified lens data or new optimization data. Practically, modifying the lens data can be achieved by the change of the lens curvature or its position. Finally, after the requirements are fulfilled, the final design is obtained.

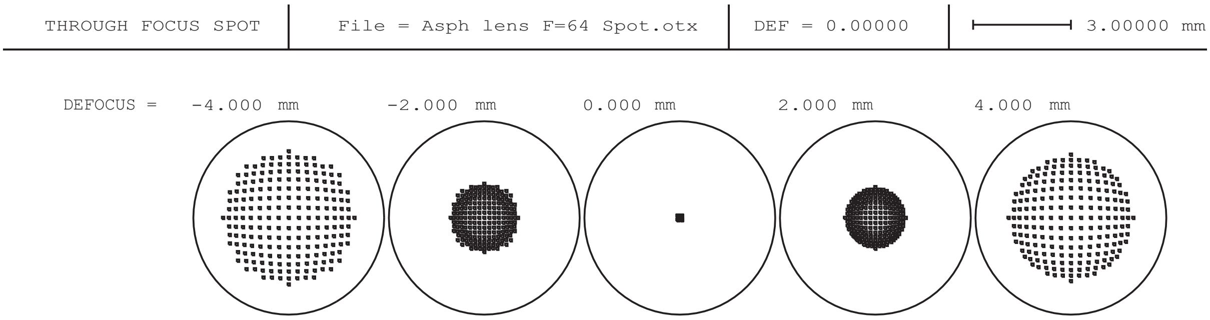

Figure 3.3: Spot diagrams for the aspherical lens $F = 64$ mm.

As a standard, all programs use ray tracing for the purpose of evaluation and optimization. Since rays are hypothetical in nature, typically the programs start the ray tracing from a specified object. Consequently rays are traced until the image defined as the rays intersection place emerges. If rays meet the optical component, the reflection and refraction laws are applied for the calculation of the ray direction leaving the component. All programs are capable to compute path lengths, refraction and reflection angles. As a result the rays propagating through, or reflecting from optical components can be traced. Since the mathematical model describing the rays propagation is relatively simple, the optical system can be completely characterized by tracing a few rays. Additionally, ray tracing programs calculate the spot diagrams which present the transverse aberrations in the image plane. Fig. 3.3 presents typical spot diagrams for the lens shown in Fig. 4.6 a) (see chapter 4.2). The optical system has been simulated using the OpTaliX software. Five spot diagrams are presented in the graph. Each spot diagram was plotted for a different defocus parameter. This parameter defines the position on the optical axis at which the spot diagram is calculated. The value 0 mm corresponds to the image position denoted in Fig. 4.6 a). Defocus values below 0 mm apply to a position shift in the lens direction. Obviously, the beam diameter increases significantly for non-zero defocus values. As it can be seen, the beam diameter at the focus of the considered lens is below 0.1 mm. It has to be emphasized that these results have been obtained applying the geometrical approximation. The beam diameter of the same lens will again be calculated in chapter 4.2 taking the diffraction into account.

The most popular optical design programms based on the geometrical analysis are Code V, OpTaliX, Oslo, Synopsys and Zemax (sorted in alphabetical order). Using Code V optical design, comprehensive analysis and optimization can be performed. OpTaliX includes comparable functionality, additionally non-sequential surfaces can be ray traced and thin film analysis can be executed. Oslo offers system design and optimization based on geometrical and Gaussian optics. Its application range is not limited to lenses, but includes the calculation of reflectors, laser collimators, and illumination systems. The Synopsys is a powerful tool and enables to design a variety of optical systems. It offers performance analysis, tolerance budget and an exhaustive lens library. Zemax can be used for sequential and non-sequential analysis, tolerancing and optimizing of the optical systems. The purchase price level of the programs OpTaliX, Oslo, Synopsys and Zemax is comparable to each other and spans from 1500 to 2100 € (June 2009) per a single licence. The price for Code V goes beyond 10000 €, yearly.

3.2 Gaussian optics

For typical optical systems dealing with the wavelengths from 380 nm to 780 nm the diffraction effects are small and localized of the edge of the beam. Therefore, for the description of such systems geometrical optics, where the wave properties of light like diffraction, polarisation, absorption and scattering are neglected, can be applied. If the wavelength is comparable with the geometrical system dimensions the propagation of radiation is dominated by the diffraction effects. In this case a complex formalism has to be applied to the beam analysis, since direct application of the geometrical optics leads to major errors. If the wavelength is smaller, but still in the order of the components' dimensions the Gaussian beam propagation can be employed, since this approach supports the diffraction effects [196].

In geometrical optics, point sources emitting plane waves were considered. In contrast, Gaussian optics assumes sources of finite size. The transverse electrical field excited by the finite size source can be described by the Gaussian-shape curve as shown in Fig. 3.4 a). Assuming the Gaussian beam propagates along the z axis as presented in Fig. 3.4 a) and the source is localized at $z = 0$, the electrical field distribution can be described using the following formula [196]:

$$E\left(r,z\right) = \frac{j2\pi\omega_0^2}{\lambda\left(2z + jk\omega_0^2\right)} A \exp\left(-jkz\right) \exp\left(-j\frac{2kzh^2}{4z^2 + k^2\omega_0^4}\right) \exp\left(-\frac{k^2\omega_0^2h^2}{4z^2 + k^2\omega_0^4}\right), \quad (3.8)$$

where $h = \sqrt{x^2 + y^2}$ represents the lateral distance from the z axis, ω_0 is the beam waist radius at $z = 0$ defined as transversal distance from the z axis for which the electrical field drops to the value e^{-1} and $k = \frac{2\pi}{\lambda}$ is the wave number. The equation (3.8) consists of three exponential terms which have the following physical meaning. The first term defines the phase of the plane wave. The second term describes the curvature of the phase front. The third term represents the intensity distribution in the plane normal to the direction of propagation.

To obtain the relationship between the beam radius ω and the longitudinal distance z, the case in which the field amplitude drops by the factor e^{-1} for $z \neq 0$ is considered. Thus, the third term of the formula (3.8) is equalled to e^{-1} and as a result the equation can be written:

$$-\frac{k^2\omega_0^2h^2}{4z^2 + k^2\omega_0^4} = -1. \quad (3.9)$$

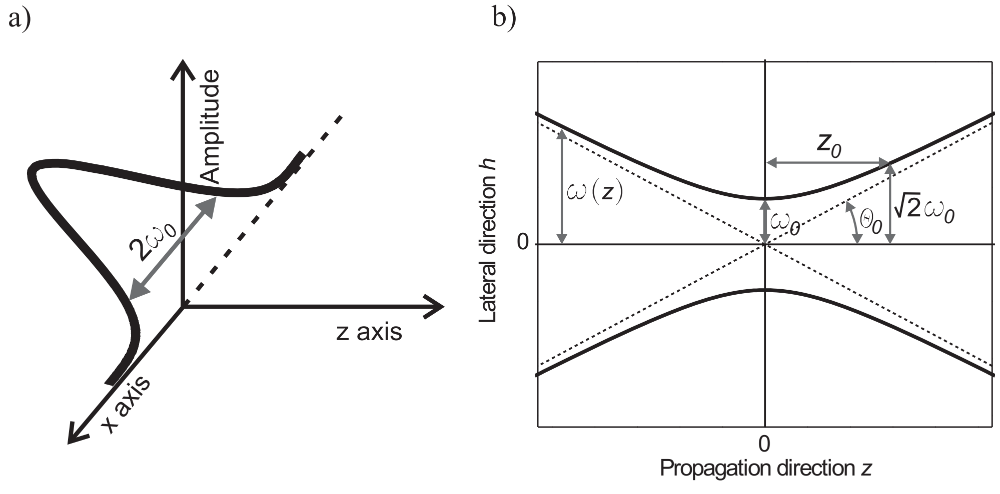

Figure 3.4: Gaussian wave propagation.

After basic algebra transformation, the beam radius can be written as:

$$\omega\left(z\right)=\omega_0\sqrt{1+\left(\frac{2z}{k\omega_0^2}\right)^2}. \tag{3.10}$$

Inserting the relation between the wave number and the wavelength yields:

$$\omega\left(z\right)=\omega_0\sqrt{1+\left(\frac{z\lambda}{\pi\omega_0^2}\right)^2}. \tag{3.11}$$

Since ω is inversely proportional to ω_0 it is noticeable that for a given wavelength the beam radius will be the larger the smaller is the beam waist. The practical meaning is that the beams which are tightly focused are more divergent in the direction of propagation than the beams having a larger waist.

By introducing the confocal parameter z_0, which is also called the Rayleigh range:

$$z_0=\frac{\pi\omega_0^2}{\lambda}, \tag{3.12}$$

the beam radius equation reduces to:

$$\omega\left(z\right)=\omega_0\sqrt{1+\left(\frac{z}{z_0}\right)^2}. \tag{3.13}$$

As it can be seen, the beam radius has its minimum for $z=0$ and equals ω_0. Within the Rayleigh range, that is for the values $|z|<z_0$ the beam radius increases insignificantly and reaches $\omega=\sqrt{2}\omega_0$ at $z=z_0$ (see Fig. 3.4 b)). Since in this range the beam is not considerably divergent it is assumed that the beam is collimated on the distance from $-z_0$ to z_0. This region is called the near field [196]. At the distance $z=|z_0|$ a transition from the near field to the far field occurs. Starting from the distance $z>z_0$ (and analogically $-z<-z_0$), the beam gets divergent and its divergence is described by the asymptotic beam growth angle θ_0. Using the trigonometry (Fig. 3.4 b)) the beam growth angle is defined by the beam radius and the distance:

$$\tan\theta_0=\frac{\omega}{z}. \tag{3.14}$$

For large values of z, the equation (3.13) can be rewritten as follows:

$$\omega\left(z\right)=\frac{\omega_0 z}{z_0}. \tag{3.15}$$

Inserting formula (3.15) and (3.12) into (3.14) leads to:

$$\theta_0=\arctan\frac{\omega_0}{z_0}=\arctan\frac{\lambda}{\pi\omega_0}. \tag{3.16}$$

For small angles the paraxial approximation can be applied:

$$\theta_0\cong\frac{\lambda}{\pi\omega_0}. \tag{3.17}$$

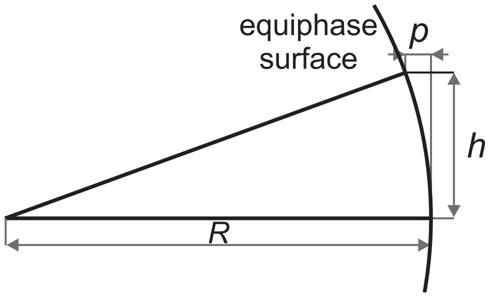

Figure 3.5: Phase shift between the spherical and plane wave.

Again, the equation (3.17) has illustrated that the beam growth angle is proportional to the wavelength and inversely proportional to the beam waist. Therefore, beams that have small waist and large wavelengths are considerably divergent.

To investigate the curvature radius of the phase front change along the propagation direction $R\left(z\right)$ the second exponential term of the formula (3.8) will be used. The graph 3.5 presents the geometrical phase shift p between the spherical and plane wave. Using the trigonometry, the phase shift at the distance h from the axis of propagation can be expressed as:

$$\left(R-p\right)^2+h^2=R^2. \tag{3.18}$$

Basic algebra leads to:

$$R=\frac{h^2+p^2}{2p}. \tag{3.19}$$

However, since the $p \ll h$ the term p^2 can be omitted:

$$R=\frac{h^2}{2p}. \tag{3.20}$$

On the other hand, the phase shift expressed in the wavelength terms is kp and therefore can be equalled to the second term of formula (3.8):

$$kp=\frac{2kzh^2}{4z^2+k^2\omega_0^4}. \tag{3.21}$$

Merging the equations (3.20) and (3.21) together, the formula describing the phase front curvature is:

$$R\left(z\right)=z\left(1+\left(\frac{\pi\omega_0^2}{\lambda z}\right)^2\right). \tag{3.22}$$

Using formula (3.12), the curvature of the phase front can by expressed by the equation:

$$R\left(z\right)=z+\frac{z_0^2}{z}. \tag{3.23}$$

For small distances from the source ($z \to 0$) the term $\frac{z_0^2}{z}$ plays an important role and therefore, the radius reaches infinity for the $z=0$. As the distance z increases, the radius of curvature reaches its minimum at $z=z_0$. For large values of z, the term $\frac{z_0^2}{z}$ reaches zero and the equation (3.23) reduces to the geometrical case, that is $R\left(z\right)=z$ as shown in Fig. 3.6. As a consequence, for sufficient distances from the source, the Gaussian beam can be considered as a

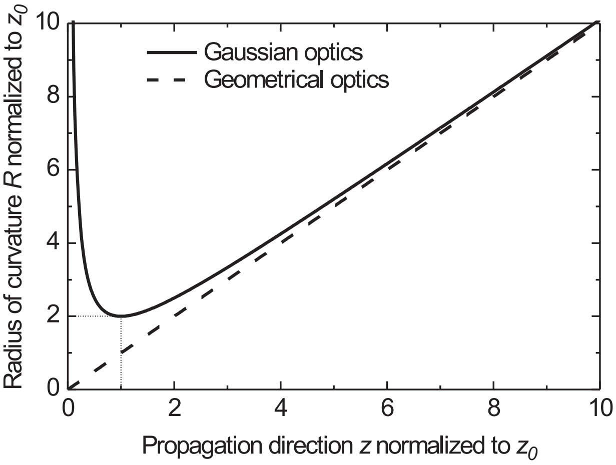

Figure 3.6: Radius of curvature in geometrical and Gaussian optics.

spherical wave. Similar, if the wavelength and the beam waist are decreased, then the Rayleigh range decreases as well; and therefore the relationship between the distance and the Raylength range meets the condition $z_0 \ll z$. Again the radius of curvature at the distance z equals the distance z. In reality this situation approaches geometrical optics, since the wavelength is small compared to the components dimensions.

3.2.1 Beam properties of the radiation generated by concial horn antennas

Millimeter wave systems described in this thesis employ circular horn antennas for the wave propagation in the free space. Excited by circular waveguide conical antennas generate mainly the fundamental TE_{11} waveguide mode, however higher-order modes are also present. The table 3.1 shows the normalized powers of the fundamental (M_0) and higher order axisymmetric Laguerre-Gaussian modes ($M_1, M_2,\ \ldots\ ,M_5$) [197].

Mode	M_0	M_1	M_2	M_3	M_4	M_5
Power	0.9436	0	0.0266	0.0067	0.0002	0.0037

Table 3.1: The normalized power for the six modes excited by the conical horn antenna.

Analysing the data presented in the table 3.1 it can be summarized that 95% of the power is carried by the fundamental mode. It has been shown [196] that each of the modes has the same beam radius and radius of curvature. In contrast, the dominant mode in the rectangular waveguide is the TE_{10} mode. Higher modes may also be present. Since every mode has a cutoff wavelength $\lambda_{c,nm}$ given by

$$\lambda_{c,nm} = \frac{2ab}{\sqrt{n^2b^2 + m^2a^2}}, \tag{3.24}$$

where nm is the mode number, a, b describe the dimensions of the waveguide, it can be proven that higher modes have significantly smaller cutoff wavelengths than the dominant mode [172]. Consequently, the frequency of the wave carried by the waveguide is chosen in that way that only the dominant mode exists. For these reasons, in further considerations only the fundamental mode will be taken into account.

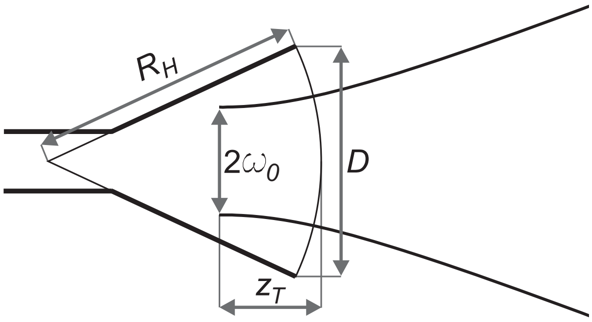

Figure 3.7: Beam waist and its position in a conical horn.

To calculate the beam waist size ω_0 and its position z_T of the radiation generated by the conical horn as shown in Fig. 3.7, the equations (3.11) and (3.22) are merged and transformed into the following equations:

$$\omega_0 = \frac{\omega}{\sqrt{1+\left(\frac{\pi\omega^2}{\lambda R}\right)^2}}, \tag{3.25}$$

$$z_T = \frac{R}{1+\left(\frac{\lambda R}{\pi\omega^2}\right)^2}. \tag{3.26}$$

For highest coupling between the component of the fundamental mode and a Gaussian beam having the radius ω, the relationship between the aperture dimension of the horn and the beam waist has to be evaluated. The table 3.2 presents the coupling efficiencies of the fundamental mode to a Gaussiam beam with beam waist radius ω_0 [197].

$\boldsymbol{\omega/D}$	0.3	0.35	0.384	0.4	0.45
Power	0.7973	0.8561	0.8662	0.8643	0.8383

Table 3.2: The normalized power as a function of the parameter ω/D.

As it has been shown, the maximum coupling efficiency can be obtained for $\omega = 0.384D$. Assuming that the radius of curvature equals the horn slant radius R_H, after insertion of the formulas for beam and curvature radius into equations (3.25) and (3.26), the following equations are obtained:

$$\omega_0 = \frac{0.384D}{\sqrt{1+\left(\frac{\pi(0.384D)^2}{\lambda R_H}\right)^2}}, \tag{3.27}$$

$$z_T = \frac{R_H}{1+\left(\frac{\lambda R_H}{\pi(0.384D)^2}\right)^2}. \tag{3.28}$$

To validate the equation describing the beam radius as a function of the distance from the antenna (equation (3.11)), the spatial distribution of the horn antennas field has been investigated. For the measurements two commercially available horn antennas covering the W-Band are chosen. The geometrical dimensions are D = 16 mm and R_H = 35 mm. Using equations (3.27) and (3.28) the beam waist and its position for the frequency 100 GHz have been determined to be ω_0 = 4.07 mm and z_T = -19.6 mm. Based on formula (3.11) the beam radius distribution as a function of the propagation distance has been plotted in Fig. 3.9 (solid line). The distance

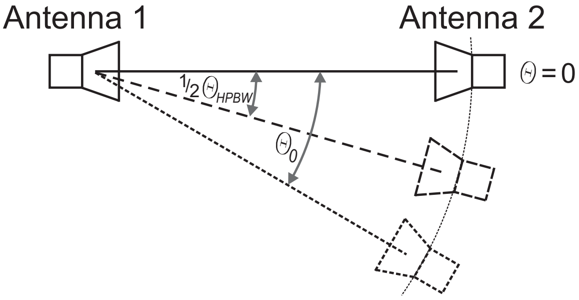

Figure 3.8: Beam growth and half-power beam width angle measurement setup.

$z = 0$ is referred to the edge of the horn. Therefore, the values $z < 0$ present the beam size inside the horn antenna. For a comparison, the beam radius has been measured in the setup depicted in Fig. 3.8. Here, one of the antennas is fixed, and the second scans the propagating beam. The distance z is discretized and for every value of z the lateral position of the antenna is found, for which the scattering parameter S_{21} decreases by 8.69 dB from the initial position $\theta = 0$. The value 8.69 dB corresponds to the power drop to e^{-2} of its initial value. The measurement results are plotted in Fig. 3.9. As it can be noticed, the measured data correspond well with the calculations, however, some discrepancies are present. They are attributed to alignment errors and multiple reflections.

The radiation properties of the antennas are described by radiation patterns. Radiation patterns present the field distribution which is measured or calculated in the far field in angular coordinates. From the antenna pattern, the half-power beam width θ_{HPBW} can be derived. The θ_{HPBW} is defined as the angular separation between the points in the antenna power pattern for which the radiation intensity is 50% of the maximum intensity. Using the setup depicted in Fig. 3.8, θ_{HPBW} of the conical horn antennas employed in this thesis has been measured and equals $\theta_{HPBWmeas} = 15.2°$.
In the following section the relation between θ_{HPBW} and θ_0 desribed by the equation (3.16) will be derived. The angular distribution of the electric field in the far field can be expressed

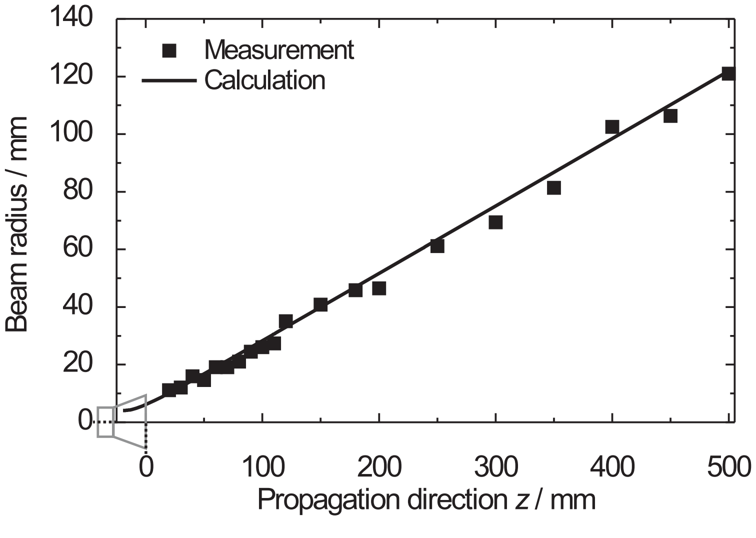

Figure 3.9: Radius of the beam as a function of the distance.

as [196]:

$$\frac{E(\theta)}{E(\theta=0)} = e^{-\left(\frac{\theta}{\theta_0}\right)^2}, \tag{3.29}$$

where $E(\theta)$ is the electric field at an arbitrary angle θ. To obtain the relation between θ_{HPBW} and θ_0, a definition of the θ_{HPBW} is employed:

$$\frac{E\left(\theta_{HPBW/2}\right)}{E(\theta=0)} = \frac{\sqrt{2}}{2}, \text{ where } \theta_{HPBW/2} = \frac{1}{2}\theta_{HPBW}. \tag{3.30}$$

After basic algebraic manipulation θ_{HPBW} can be expressed in terms of θ_0 as:

$$\theta_{HPBW} = \sqrt{-\ln\frac{\sqrt{2}}{2}}\,\theta_0 \cong 1.177\,\theta_0 \tag{3.31}$$

Since equation (3.17) yields $\theta_0 = 13.2°$ for the examined horn antennas, the calculated value using the equation (3.31) is $\theta_{HPBW} = 15.4°$. This value agrees well with the measured-one which is $\theta_{HPBWmeas} = 15.2°$.

3.2.2 Lens transformations in Gaussian optics

For the transformation of the beams, lenses or mirrors are employed. In the following chapter, the equations describing the Gaussian beam transformations by lenses will be presented.

Position of the image waist

As a result of the beam propagation through a single lens, the beam radius remains unchanged, while the radius of the curvature is transformed by the factor $\frac{1}{F}$ [198]. Using the nomenclature presented in Fig. 3.10 the equations become:

$$\omega(z=S) = \omega'(z=S'), \tag{3.32}$$

$$R(z=S) = \frac{R'(z=S')}{F}, \tag{3.33}$$

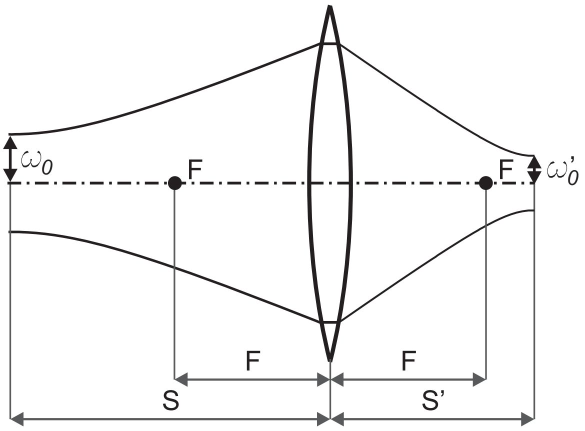

Figure 3.10: Beam transformations in the Gaussian optics.

while ω and ω' are object and image beam radii, respectively and R and R' define the radii of curvature for the object and image beam. Inserting equations (3.13) and (3.23) into (3.32) and (3.33) leads to:

$$\frac{1}{F} = \frac{1}{S + \frac{z_0^2}{S-F}} + \frac{1}{S'}, \tag{3.34}$$

where S and S' are distances of the object and image waists from the lens, respectively. The parameter z_0 is the Rayleigh range of the object beam. Graph 3.11 a) presents the object and image waist distances from a lens which are normalized to the focal length. As a parameter, the normalized Rayleigh range is chosen. The equation (3.34) reduces to the geometrical case (equation (3.6)) if the confocal parameter z_0 approaches zero. As shown in Fig. 3.11 a) the image position differs significantly from the position calculated in the geometrical approach (equation (3.6)). This is extremely pronounced when the object is localized close to, or at the focal length of the lens, that is $S \cong F$. In Gaussian optics the term $\frac{z_0^2}{S-F}$ removes the pole at $S = F$; therefore, for non-zero values of the Rayleigh length, the image appears at a finite distance from the lens. In particular, when the object beam waist is localized at the focus of the lens, the image waist appears at the back focus. This is in a contrast to geometrical optics, where in that case the image emerges at the infinity. Unlike the case of geometrical optics, the real object located at the position $0 < \frac{S}{F} < 1$ can produce also a real image, depending on the confocal parameter as presented in Fig. 3.11 a).

Lens magnification

Defining the magnification as a ratio of image to object beam waist and employing the equations (3.13), (3.23), (3.32), (3.33) the magnification formula can be written:

$$m = \frac{\omega_0'}{\omega_0} = \frac{1}{\sqrt{\left(1 - \frac{S}{F}\right)^2 + \left(\frac{z_0}{F}\right)^2}}. \tag{3.35}$$

It can be noticed that this equation is similar to the one obtained in geometrical optics (3.7); however, additionally a term $\frac{z_0}{F}$ is present. If the Rayleigh range reaches zero, or $z_0^2 \ll (F - S)$, equation (3.35) reduces to equation (3.7). In Gaussian optics, the term $\frac{z_0}{F}$ removes the pole at $S = F$; therefore, the magnification is limited to the factor $\frac{F}{z_0}$. Figure 3.11 b) depicts the magnification as the function of the normalized object waist distance from the lens. The parameter for the curves is the Rayleigh range normalized to the focal length.

Other beam parameters like the Rayleigh range and the beam growth angle are also transformed by the lens. Based on the equation (3.35) the image beam's properties denoted as z_0' and θ_0' are expressed as [198]:

$$z_0' = m^2 z_0, \tag{3.36}$$

$$\theta_0' = \frac{\theta_0}{m}. \tag{3.37}$$

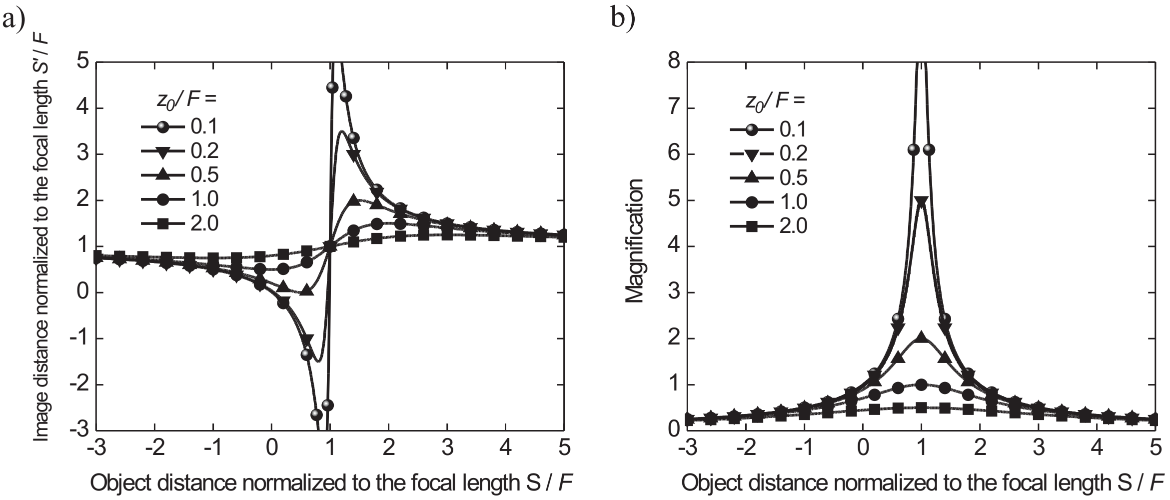

Figure 3.11: Lensing properties described by Gaussian theory: a) normalized image waist position as a function of normalized object waist position, b) lens magnification as a function of normalized object position. For both graphs the parameter is normalized Rayleigh range.

Position of the object and image waist by defined object and image waist size

For the lens design, the equations (3.34) and (3.35) enable to calculate the image position and the image beam radius. However, for practical design, transformations of these equations are of particular interest. Merging equation (3.34) and (3.35) it can be written:

$$\frac{S'}{F} - 1 = \pm \frac{\omega_0'^2}{\omega_0^2} \sqrt{\frac{\omega_0^2}{\omega_0'^2} - \frac{z_0^2}{F^2}}. \tag{3.38}$$

For the given object and image waist, the smallest value of the focal length which enables a given transformation is [196]:

$$F_0 = \frac{\pi \omega_0 \omega_0'}{\lambda}. \tag{3.39}$$

For a given size of the object and image beam waist, an arbitrary value of the focal length $F \geq F_0$ can be used. The object and image positions are defined by:

$$S = F \pm \frac{\omega_0}{\omega_0'} \sqrt{F^2 - \frac{\pi^2 \omega_0^2 \omega_0'^2}{\lambda^2}}, \tag{3.40}$$

$$S' = F \pm \frac{\omega_0'}{\omega_0} \sqrt{F^2 - \frac{\pi^2 \omega_0^2 \omega_0'^2}{\lambda^2}}, \tag{3.41}$$

To summarize, the choice of the focal length is arbitrary, however, the particular focal length determines the distance between the image and the object waist.

Position of the object and image waist by defined object and image waist size and waist separation

Since equations (3.40) and (3.41) do not enable the design of a lens for which the waist separation S'' is given, the relation $S'' = S + S'$ is inserted into formulas (3.40) and (3.41). After solving for F, the focal length is given by:

$$F = \frac{\pm\sqrt{\left(\frac{\omega_0'}{\omega_0} - \frac{\omega_0}{\omega_0'}\right)^2 \frac{\pi^2\omega_0^2\omega_0'^2}{\lambda^2} + S''^2}\left(\frac{\omega_0'}{\omega_0} + \frac{\omega_0}{\omega_0'}\right) - 2S''}{\left(\frac{\omega_0'}{\omega_0} - \frac{\omega_0}{\omega_0'}\right)^2}. \tag{3.42}$$

Equation (3.42) provides two values of the focal lengths for $F > F_0$. For the chosen focal length values, the waist locations can be calculated from:

$$S = \frac{S'' - F\left(1 - \frac{\omega_0'^2}{\omega_0^2}\right)}{1 + \frac{\omega_0'^2}{\omega_0^2}}, \tag{3.43}$$

$$S' = \frac{S''\frac{\omega_0'^2}{\omega_0^2} + F\left(1 - \frac{\omega_0'^2}{\omega_0^2}\right)}{1 + \frac{\omega_0'^2}{\omega_0^2}}. \tag{3.44}$$

Position of the image waist by defined object and image waist size and object waist position

If the object waist position and the object and image waist are given, the required focal length can be obtained from [196]:

$$F = \frac{S\left(1 \pm \sqrt{1 - \left(1 - \frac{\omega_0^2}{\omega_0'^2}\right)\left(1 + \frac{z_0^2}{S^2}\right)}\right)}{1 - \frac{\omega_0^2}{\omega_0'^2}}. \tag{3.45}$$

To calculate the image position, the equation (3.34) is solved for S':

$$S' = F + \frac{S - F}{\left(\frac{S}{F} - 1\right)^2 + \frac{z_0^2}{F^2}}. \tag{3.46}$$

Image waist size

In the design of optical systems there is often a need to calculate the image waist size. Generally the size of the beam which propagates through the lens can be obtained from the equation (3.13) and (3.36). However, under the assumption that the object beam is collimated, the calculations can be simplified. Solving equation (3.35) for ω_0' it can be written:

$$\omega_0' = \frac{F\omega_0}{\sqrt{\left(S - F\right)^2 + z_0^2}}. \tag{3.47}$$

Under the assumption $z_0^2 \gg (S - F)^2$, the term $(S - F)$ can be neglected. As a result, equation (3.47) reduces to:

$$\omega_0' = \frac{F\omega_0}{z_0}. \tag{3.48}$$

Inserting equation (3.12) into (3.48) yields:

$$\omega_0' = \frac{\lambda F}{\pi \omega_0}. \tag{3.49}$$

As it has been shown, equation (3.49) allows us to calculate the image waist size, if the object waist radius, the focal length and the wavelength are known. It is remarkable, that the image radius size is proportional to the focal length and the wavelength, and inversely proportional to the object beam size. Therefore, in order to achieve tight focusing the focal length and the wavelength should be minimized, whereas the object beam should cover the entire surface of the lens.

The equation (3.49) is valid only for ideal Gaussian beams. In practical systems, the beam intensity distribution indicates a discrepancy from Gaussian shape. The discrepancy is a result of the fact that not only the fundamental mode, but also higher modes propagate. Additionally the diffraction and aperture effects caused by the lens lead to deviations from the pure Gaussian beam profile. Therefore, a beam propagation factor M^2 which describes the beam quality has been introduced [199]. The beam propagation factor is a ratio between actual and ideal Gaussian beam shape. For ideal Gaussian beam $M^2 = 1$, but in practical systems $M^2 > 1$. The beam growth angle for the fundamental mode is defined by the equation (3.17). Considering higher order modes and the aperture effect, the beam growth angle for the multimode beam can be written as:

$$\theta_{0M} = \frac{M^2 \lambda}{\pi \omega_0}. \tag{3.50}$$

Therefore, the beam waist size for practical beam is given by the equation:

$$\omega_{0M}' = \frac{M^2 \lambda F}{\pi \omega_0}. \tag{3.51}$$

Gaussian beam telescope

To simplify the lens design, a Gaussian beam telescope can be employed. The Gaussian beam telescope consists of two lenses separated by the distance which is the sum of the focal lengths of the lenses. Assuming the focal length of the first lens is F_1 and F_2 is the focal length of the second lens, the system magnification is [196]:

$$m = \frac{F_2}{F_1}. \tag{3.52}$$

For this system it is characteristic that the magnification is independent from the object beam radius and its location. The image is created at a distance

$$S' = \frac{F_2}{F_1}\left(F_1 + F_2 - \frac{F_2 S}{F_1}\right) \tag{3.53}$$

from the lens. As it can be seen, the image position is also independent from the wavelength. Therefore, the Gaussian beam telescope is widely used in broadband systems.

Millimeter wave system design in geometrical and Gaussian optics

To present the differences between Gaussian and geometrical optics, the optical system shown in Fig. 3.12 will be discussed at a frequency of 100 GHz. The beam propagation defined by the geometrical optics is schematically presented as a dashed line. In contrast, a solid line presents schematically the beam propagation according to the Gaussian theory.
The distances between the components have been calculated using geometrical optics. Since the microwave beam's waist is localized at the distance $z_T = d_0 = 19.6$ mm from the horn antenna H_1 edge, the lens $F_1 = 60$ mm is situated at the distance $d_1 = 40.4$ mm from the horn edge. It is assumed that the beam is collimated after passing through the lens $F_1 = 60$ mm at the distance $d_2 = 20$ mm. The lens $F_2 = 80$ mm focuses the beam. The expected focusing produced by the lens F_2 occurs at the distance $d_R = F_2 = 80$ mm according to the geometrical optics (equation (3.6)). The lens $F_3 = 60$ mm collimates the beam at the distance $d_4 = 20$ mm. Eventually the lens $F_4 = 60$ mm focuses the beam which in turn is coupled to the horn antenna H_2 localized at $d_5 = 40.4$ mm from the lens F_4.
In the first step the beam diameter at the geometrical focus has been measured. To obtain the beam distribution at the focus the measurement employing the blade edge has been performed. The measurement details will be described in the section 4.1. The resulting curve (dashed line) is presented in Fig. 3.13 a) and obtained beam profile is depicted in Fig. 3.13 b). The beam diameter at the position of the geometrical focus has been extracted from the Fig. 3.13 b) and equals $2\omega_{RM} = 11.1$ mm.
In the second step, the position of the Gaussian waist is calculated using the equation (3.34). For the lens F_1 the following quantities are known: $S = 60$ mm, $F = 60$ mm, $z_0 = 17.4$ mm (equation (3.12)). Employing the equation (3.34) the image position is calculated $S' = 60$ mm. The magnification obtained from the equation (3.35) is $m = 3.45$. Therefore, the Rayleigh range of the beam leaving the lens F_1 is $z_0' = 207.2$ mm (equation (3.36)). For the lens F_2, the input parameters are: $S = -40$ mm, $F = 80$ mm, $z_0 = 207.2$ mm. The image position calculated from (3.34) is $S' = 66.6$ mm. Therefore, the position of the beam waist according to the Gaussian optics is denoted as $d_G = 66.6$ mm.
In the third step the beam diameter at the distance d_G is measured employing the blade edge method. The resulting curve (solid line) is presented in Fig. 3.13 a), whereas the obtained beam

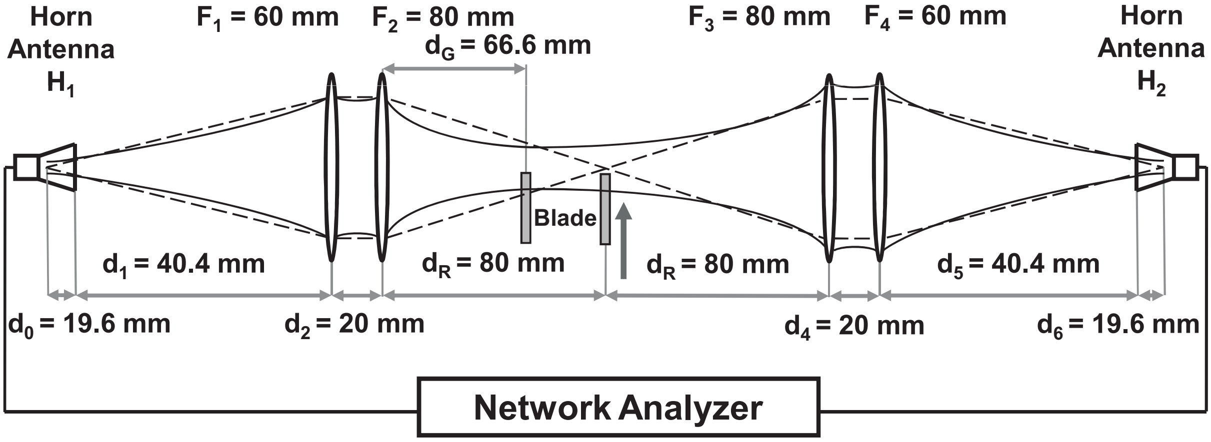

Figure 3.12: Beam propagation in geometrical (dashed line) and Gaussian (solid line) optics.

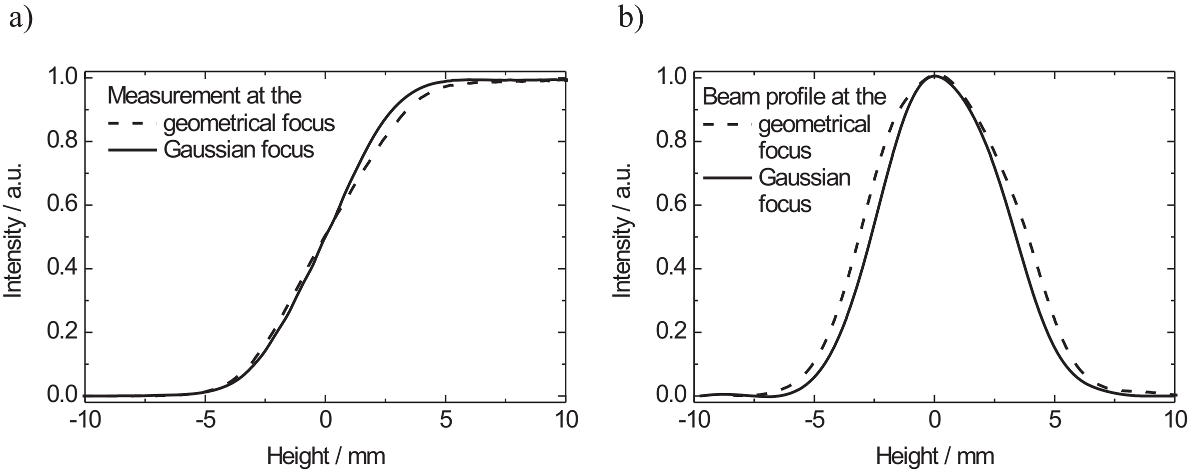

Figure 3.13: Beam profiles at the distances corresponding to the geometrical (dashed line) and Gaussian focus positions (solid line): a) blade edge measurement curve, b) beam profile.

profile is plotted in Fig. 3.13 b). Based on the latter graph the beam diameter at the position d_G is $2\omega_{GM} = 9.4$ mm and it is smaller than the beam diameter $2\omega_{RM}$.

To validate the measurements, in the fourth step the beam diameters at the geometrical and Gaussian foci have been calculated. In order to obtain the beam radius at the Gaussian focus, the magnification of the lens F_2 is calculated using the equation (3.35). Since $m = 0.33$, the Rayleigh range is $z_0' = 23.1$ mm (equation (3.37)). Finally, employing the equation (3.12) the calculated beam diameter is $2\omega_{GC} = 9.4$ mm. To obtain the beam diameter at the geometrical focus, the equation (3.13) is used, where $z = d_R - d_G = 13.4$ mm. After inserting $z_0 = 23.1$ mm and $\omega_0 = 4.7$ mm the calculated beam diameter at the geometrical focus is $2\omega_{RC} = 10.9$ mm. To summarize, obtained results are presented again in the table 3.3.

Analyzing the data enclosed in the table it is clearly seen that the positions of the beam foci calculated according to the geometrical and Gaussian optics theories are different from eachother. As a result, the calculated and measured beam diameters for the focus position obtained from the geometrical optics are greater than those for which the focus position was determined by the means of the Gaussian optics theory. The discrepancy between the geometrical and the Gaussian method of the focus position calculation is the bigger, the smaller is the focal length compared to the confocal parameter. To sum up, it has to be emphasized that the geometrical approach cannot be used for the design of the systems for which the wavelength is comparable with the components' dimensions. As it has been proven for the millimeter wave systems the geometrical theory leads to errors. Therefore, for these type of systems, Gaussian beam theory

Approach	**Beam focus position**	**Calculated beam diameter at the focus**	**Measured beam diameter at the focus**
Geometrical optics	80.0 mm	10.9 mm	11.1 mm
Gaussian optics	66.6 mm	9.4 mm	9.4 mm

Table 3.3: Results summary.

has to be applied. In particular, the equations (3.11 – 3.13, 3.25, 3.26 and 3.34 – 3.36) have to be employed.

3.2.3 Gaussian optics software

Many programs described in chapter 3.1.2 apply additionally the diffraction theory for the calculation of the modulation transfer function (MTF) and point spread function (PSF). As a mathematical apparatus, geometrical ray tracing and far-field calculations based on the Fraunhofer diffraction pattern analysis is employed. MTF describes the optical system performance since it is influenced by the diffraction, aberration and alignment errors. By the definition, MTF is the ratio of the image modulation to the object modulation and it is a function of spatial frequency. Since optical systems have a defined transfer function, the resulting image is the convolution of the object and the PSF. Therefore, the PSF is the image of a point object transformed by the system. However, the practical use of these tools is limited to the strictly optical cases, where the wavelength is small compared to the dimensions of the optical elements.

Another group of programs represented by Advanced System Analysis Program (ASAP) and OptaliX offers additionally the tracing of the Gaussian beams. Therefore, the effects including diffraction, refraction, reflection, absorption and polarization can be calculated. As an example, OpTaliX employs diffraction based beam propagation routines for the calculation of the beam size at the focus. Here, the coherent beam is modeled by a complex valued function which describes the transverse beam distribution. The input beam is split into individual Gaussian beams which are propagated through the optical system. The field can be reconstructed at any point on the optical axis as a coherent overlap of the single Gaussian beams. For the calculation of the fields the Fresnel approximation is used. The input field can be arbitrary; however the individual Gaussian beams have to follow the paraxial approximation that is they have to propagate at small angles in respect to the optical axis. This tool will be used in chapter 4.2 to evaluate the focusing properties of the designed lenses. As it will be shown in Fig. 4.6 b), the beam diameter at the focus of $F = 60$ mm lens calculated using the diffraction based beam propagation is 4.0 mm. A direct comparison of this value with the value obtained employing ray tracing (<0.1 mm) shows that the spot diagram is not a reliable method for the calculations in the millimeter wave range. Therefore, the diffraction effects present in this range require the methods based on Gaussian beam propagation.

However, the diffraction based beam propagation implemented in the OpTalix software has some limitations. The practical use of this tool is limited to the cases, where the beam propagation is parallel to the optical axis. As a result, this approach is useless for the design of mirrors. Moreover the OpTaliX software does not employ the Gaussian beam propagation apparatus for the optimization process of the lens' surface. Finally, the position of the image cannot be calculated precisely, since the input beam is defined by the geometrical optics rules and the image position is calculated using ray tracing.

To overcome previously described limitations full-wave simulators can be employed. The full-wave simulators are based on finite-difference time-domain (FDTD), finite-difference beam propagation method (FDTD-BPM) or modal methods.

Theoretically, the FDTD method can be used to calculate any optical system, since the grid size can approach zero and therefore, no approximation has to be made. However, since up to 20 grid points per wavelength are required, a number of grid points needed to solve a 3D optical system increases dramatically. Therefore, practical applications of this method are intrinsically limited by the computational power to about 10 wavelengths in each direction [200]. A modification of this method - FDTD-BPM finds applications for systems, where the paraxial approximation applies. Here, the grid for normal directions to the optical axis remains identical as in the FDTD, but only slow changes are assumed in the propagation direction. As a result, the calculation time is reduced.

In contrast to FDTD methods, modal techniques assume a limited number of modes. The most significant methods are eigenmode expansion and coupled-mode theory. On the one hand the eigenmode expansion method allows reducing a number of grid points per wavelength to 0.2, on the other hand coupled-mode methods are more time-efficient for the simulation of regular structures.

To sum up, all full wave methods require considerable computation time, or they are based on approximations. For many systems the user has to judge if the approximations are still valid for the structure to be simulated.

In order to reduce the calculation time and to avoid the need for the method evaluation for a specific case, hybrid solutions for the analysis of optical and quasi-optical systems can be applied. This solution is based on the synergy of standard ray tracing software and FDTD algorithms. As a result, the speed of standard ray tracing software with the versatility of the FDTD method can be combined together. For the calculations to be performed on a macroscopic scale, the ray tracing software ASAP is employed. In the next step, the field distribution is exported to the FDTD Solutions software which carries out the calculations in the microscopic scale. Depending on the system configuration, the results given by the FDTD method are the final results, or they can be translated back and handled by the ray tracing software. Currently, the FDTD Code has been implemented in the ASAP PRO software. Therefore, the program ASAP PRO is a comprehensive tool for the calculations in the macro and microscopic scale. However, since the feature spectrum is beyond that of standard ray tracers, the licence price is also much higher.

Another entry-level group of programs is based solely on the Gaussian optics propagation theory described in the section 3.2. To investigate systems consisting of lenses, scripts employing the equations (3.11 – 3.13, 3.25, 3.26 and 3.34 – 3.36) may be used.

For the verification of the millimeter wave designs being part of this thesis, a Gaussian Beam Calculator (GBC) has been employed. The GBC is a simple script which calculates the radius of the beam which propagates through the lenses. Additionally, for every lens used in the system, the object and image positions are calculated. After defining the object beam waist and the wavelength, the parameters including object and image Rayleigh range, as well as the lens magnification are evaluated for each lens. Moreover, the beam radius at every position of the system can be determined.

As an example, Fig. 3.14 presents the system depicted in Fig. 3.12. In the upper part of the window, the beam parameters are calculated. Every row corresponds to one lens depicted in the graph below. The lower part of the program's main window shows the beam propagation graphically. Using the diagram, the beam radius at an arbitrary location can be obtained.

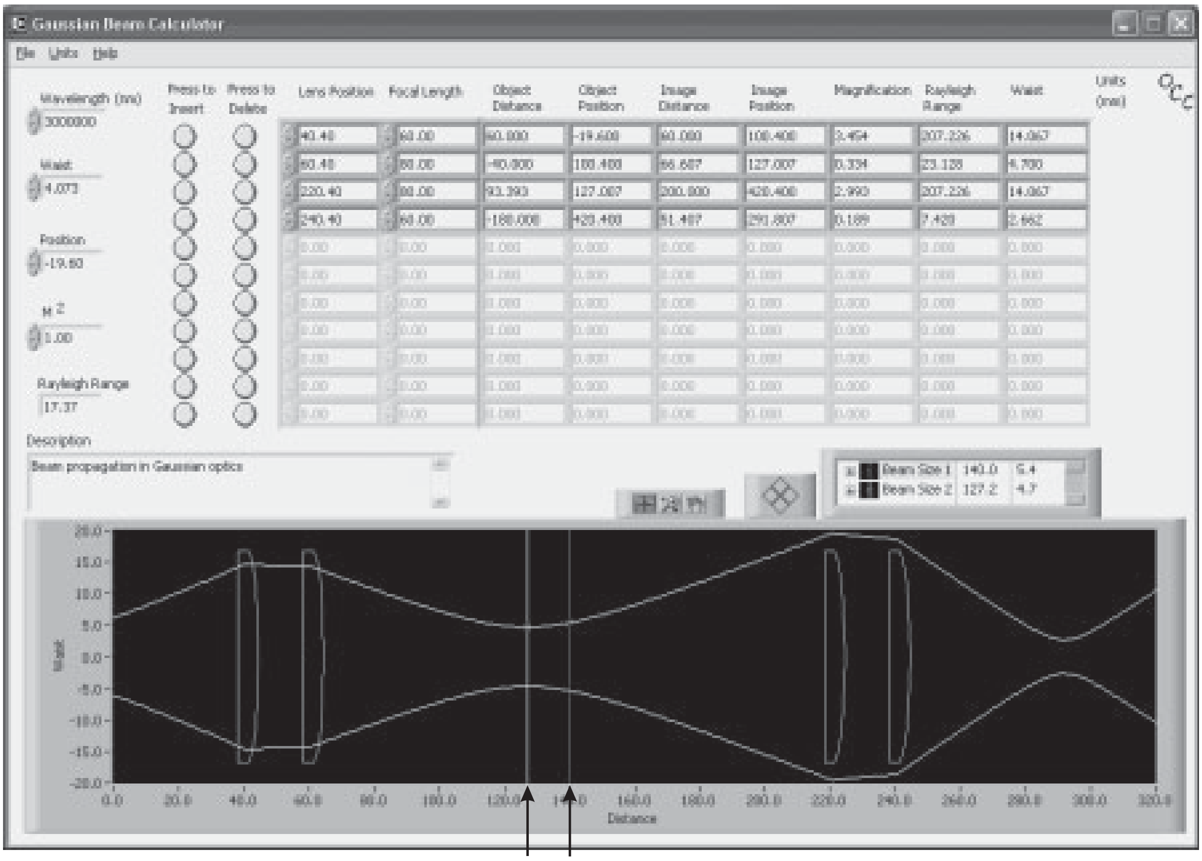

Wavelength (nm): 3000000

Waist: 4.073

Position: -19.60

M 2: 1.00

Rayleigh Range: 17.37

Lens Position	Focal Length	Object Distance	Object Position	Image Distance	Image Position	Magnification	Rayleigh Range	Waist
40.40	60.00	60.000	-19.600	60.000	100.400	3.454	207.226	14.067
60.40	80.00	-40.000	100.400	66.607	127.007	0.334	23.128	4.700
220.40	80.00	93.393	127.007	200.000	420.400	2.990	207.226	14.067
240.40	60.00	-180.000	420.400	51.407	291.807	0.189	7.420	2.662
0.00	0.00	0.000	0.000	0.000	0.000	0.000	0.000	0.000
0.00	0.00	0.000	0.000	0.000	0.000	0.000	0.000	0.000
0.00	0.00	0.000	0.000	0.000	0.000	0.000	0.000	0.000
0.00	0.00	0.000	0.000	0.000	0.000	0.000	0.000	0.000
0.00	0.00	0.000	0.000	0.000	0.000	0.000	0.000	0.000
0.00	0.00	0.000	0.000	0.000	0.000	0.000	0.000	0.000
0.00	0.00	0.000	0.000	0.000	0.000	0.000	0.000	0.000

Description: Beam propagation in Gaussian optics

Beam Size 1	140.0	5.4
Beam Size 2	127.2	4.7

Gaussian focus position Geometrical focus position

Figure 3.14: Gaussian Beam Calculator.

Therefore, the beam diameters at the geometrical and Gaussian foci positions can be directly computed. The values obtained from the GBC are identical to the ones which were calculated in chapter 3.2.2.

4 Lens design

For the systems described in this thesis it is crucial that the beam size in the imaging plane is minimized. In order to achieve a small antenna footprint in the imaging position, lenses can be used. Spherical lenses are relatively easy to design; however, this type of lens has spherical aberration. Therefore, to increase the image quality, aspherical lenses are preferable. The following chapter presents the design, measurements and the comparison of spherical and aspherical lenses that are developed for the sub-terahertz systems presented in chapters 5, 6 and 7 of this thesis.

4.1 Spherical lenses

As it was mentioned in chapter 3, the lens material should have low absorption and its refractive index must differ from that of the air. For manufacturing purposes it is advantageous that the material is well processible. All three requirements are fulfilled by high density polyethylene (HDPE). Its physical features enable to employ a standard machining process for the material processing. The parameters of the HDPE have been measured using the VNA in the W-band (75 - 110 GHz). Based on the scattering parameter S_{21}, the absorption coefficient α and the real part of refractive index n can be obtained applying the derived equations:

$$n = \frac{\phi\left(S_{21}\right)c}{2\pi f t} + 1, \tag{4.1}$$

$$\alpha = -\frac{\ln \frac{|S_{21}|^2}{c_T}}{t}, \tag{4.2}$$

$$c_T = \left(1 - \left(\frac{n-1}{n+1}\right)^2\right)^2, \tag{4.3}$$

where t denotes the sample thickness, c_T stands for transmission losses on the air - sample and sample - air boundaries, and $\phi\left(S_{21}\right)$ denotes the phase of the parameter S_{21}.

Figure 4.1 a) and b) show the absolute value of S_{21} for a 12 mm thick HDPE sample and the phase of S_{21} a for 37 mm thick HDPE sample, whereas the extracted refractive index and absorption coefficient are presented in Fig. 4.1 c) and d), respectively.

The curvature radii R_1 and R_2 (shown in Fig. 4.2) defining the lens surfaces for a given focal length F can be calculated using the lensmaker's equation [201]:

$$F = \left((n-1)\left(\frac{1}{R_1} - \frac{1}{R_2}\right) + \frac{t\left(n-1\right)^2}{nR_1R_2}\right)^{-1}. \tag{4.4}$$

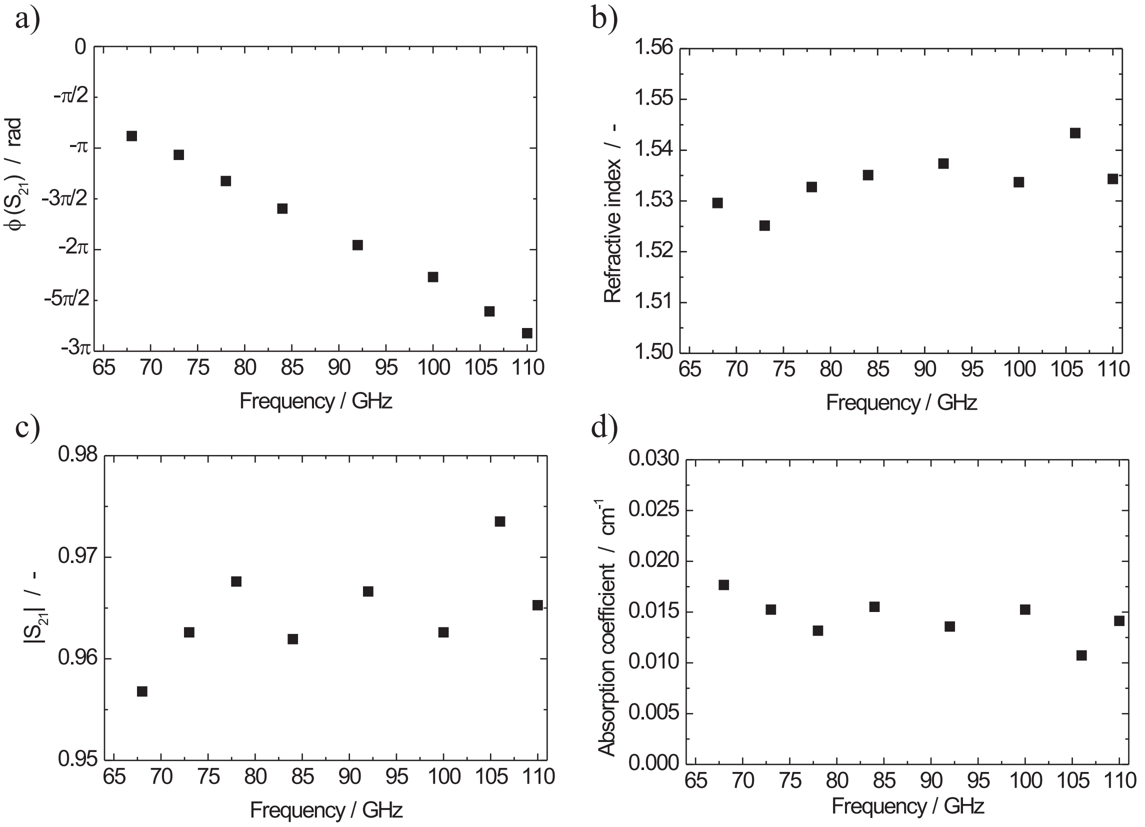

Figure 4.1: The absorption coefficient and refractive index of HDPE.

However, this equation is valid only for paraxial rays, that is for rays propagating at small angles to the optical axis. For that kind of rays the condition $\theta = \sin\theta = \tan\theta$ is fulfilled with the maximal error below 3% for incidence angles smaller than $\pi/12$. As it can be seen, there exist an infinite number of solutions R_1 and R_2 leading to the target focal length. However, for the ease of fabrication it is profitable, when one of the surfaces is plane that is $R_2 \to \infty$. In this case, the equation (4.4) transforms into:

$$F = \frac{R_1}{n-1}. \tag{4.5}$$

Since the beam diameter at the focus is inversely proportional to the illuminated aperture size (see equation (3.49)) and the lens aperture should not truncate the lower energy components, the lens diameter size has been set to 80 mm. For further minimization of the focus diameter, the focal length of the lens has been chosen to be 64 mm. Based on the equation (4.5), the curvature radius for the spherical lens having the focal length F = 64 mm has been calculated. The calculations were verified in OpTaliX software. The ray tracing graph and the beam profile

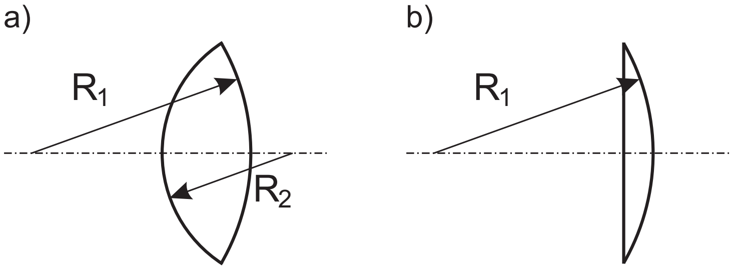

Figure 4.2: The design of a) biconvex and b) plano-convex lenses.

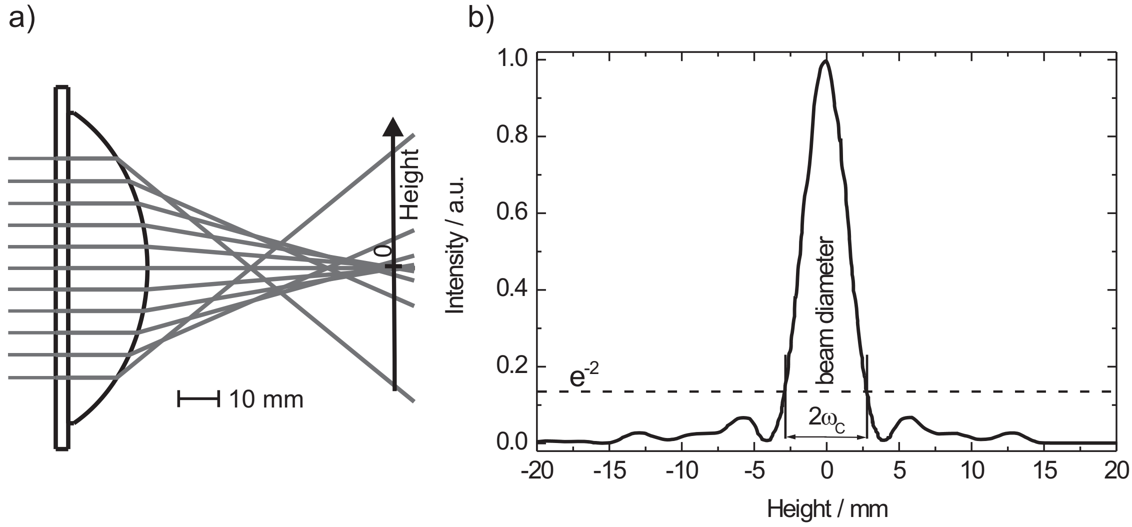

Figure 4.3: The simulation of the spherical lens, focal length 64 mm: a) ray tracing, b) beam profile.

at the focus are presented in Fig. 4.3. As it can be seen from Fig. 4.3 a), strong spherical aberrations emerge. Only the paraxial rays are focused in the distance of the focal length. The rays which meet the lens at a greater height focus at a smaller distance. Fig. 4.3 b) presents the intensity distribution over the plane parallel to the lens surface (height). The graph is normalized to unity. The beam diameter defined as the intensity decrease to the e^{-2} of the initial value is 5.75 mm. As shown in graph 4.3 b) the field intensities have non-zero values for heights below -5 mm and above 5 mm. This is attributed to spherical aberrations.

Using a standard machining process, the lenses have been manufactured. They are characterised using the setup presented in Fig. 4.4. All the distances between the lens, horn antennas and blade have been calculated using equations (3.12), (3.34) and (3.35). The calculations have been verified using the GBC script. In order do determine the beam diameter, an intensity measurement for a variable blade position is performed. The blade movement plane is normal to the optical axis. Fig. 4.5 a) presents the radiation intensity, that is $|S_{21}|^2$ versus the blade position. For this measurement the resulting curve E presented in the graph is the convolution of the real beam profile G and the unit step function H, as follows:

$$E = G * H. \tag{4.6}$$

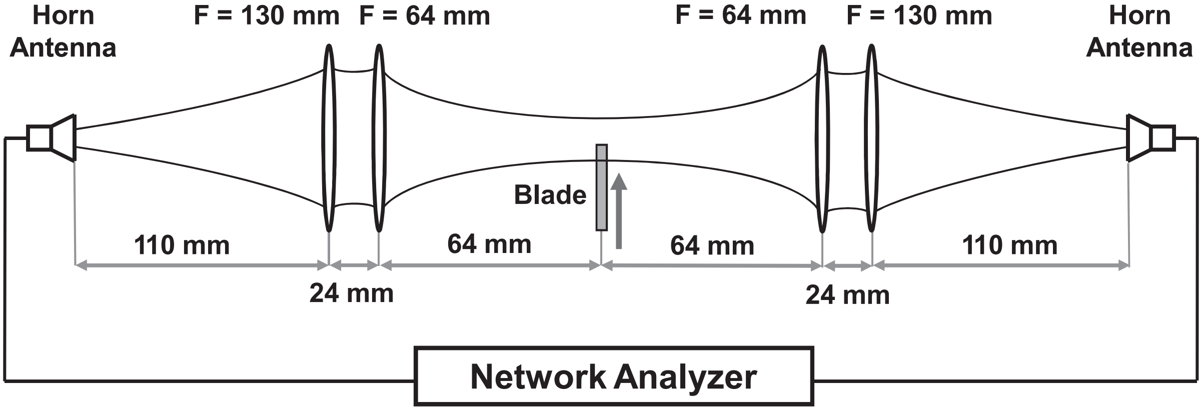

Figure 4.4: The beam diameter measurement setup.

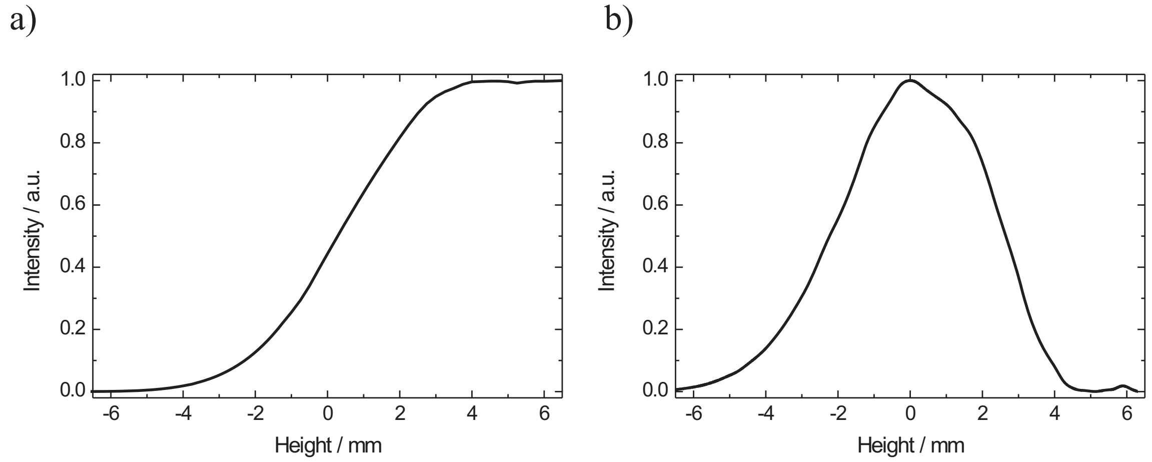

Figure 4.5: Spherical lens $F = 64$ mm focus diameter measurement: a) blade measurement, b) deconvoluted beam profile at the focus.

To obtain the beam profile, a deconvolution operation has to be performed:

$$G = E \diamond H, \tag{4.7}$$

where the symbol $\diamond$ stands for the deconvolution process.

For the deconvolution operation, a Matlab script based on the equation (4.7) [202] has been applied. The obtained intensity of the beam profile is presented in Fig. 4.5 b). For the lens $F = 64$ mm, the measured beam diameter equals 7.75 mm and is greater than the simulated value. Therefore, the beam propagation ratio obtained from the equation (3.51) is $M^2 = 1.35$. The discrepancy between the simulated and the measured value of the beam diameter can be explained as follows. Since the beam reaching the lens has a considerable width, the aperturing effect caused by the lens with a relative small aperture size takes place. As a result, the profile of the focused beam width does not have a perfect Gaussian shape. Therefore, the beam propagation factor M^2 is higher than unity.

4.2 Aspherical lenses

As it was mentioned in chapter 4, spherical lenses have monochromatic aberrations. In order to minimize spherical aberrations, aspherical lenses are employed. Physically, the aspherical lens' surface can be given by the parabolic, hyperbolic or elliptical shape. Mathematically, the surface can be described by the polynomial expression:

$$\begin{aligned} z(h) = {} & \frac{h}{R(F)\left(1+\sqrt{1-\frac{h^2}{R^2(F)}(K+1)}\right)} + \\ & + Ah^4 + Bh^6 + Ch^8 + Dh^{10} + Eh^{12} + Fh^{14} + Gh^{16} + Hh^{18}, \end{aligned} \tag{4.8}$$

where $z(h)$ depicts the surface curvature, h is the lateral distance measured from the optical axis, $R(F)$ describes the curvature radius and K is the conic constant. The parameters A, B, $\ldots H$ are the asphere coefficients. The simulation software calculates the asphere coefficients for a given focal length using the Kuhn-Tucker and Levenberg-Marquardt optimization algorithms.

As a result, the lens curvature profile $z = \text{f}(h, F)$ is obtained. Using OpTaliX, three types of aspherical lenses $F = 64$ mm, 104 mm and 165 mm have been designed. Fig. 4.6 a) presents the ray tracing for the lens $F = 64$ mm. The simulated field intensity distributions for the lenses with $F = 64$ mm, 104 mm and 165 mm are shown in Fig. 4.6 b), c) and d), respectively. Based on the simulated profiles the beam diameters have been extracted and presented in the table 4.1.

Additionally, the beam diameters have been calculated using the equation (3.49). The results are also included in the table 4.1. As it can be seen, the data obtained by the calculation and the simulation are consistent.

For a comparison, the simulated intensity distributions for the spherical and aspherical lens $F = 64$ mm have been plotted in Fig. 4.7. In this graph, the intensity profile of the spherical lens has been normalized to that of the aspherical lens. As it can be noticed, the aspherical lens has much less field components than spherical-one outside the bell-curve that is for heights below -3 mm and above 3 mm. As a result, using the aspherical lens leads to higher power densities at the focus. Additionally, the calculated focus diameter for the aspherical $F = 64$ mm lens is 4.0 mm and therefore is smaller than for the spherical lens with identical focal length, which is 5.75 mm.

As it can be seen in Fig. 4.6, the aspherical lenses also have non-zero field components for heights greater than 5 mm. This is attributed to the significant phase shift of the fields for these heights. As a result, the constructive interference emerges.

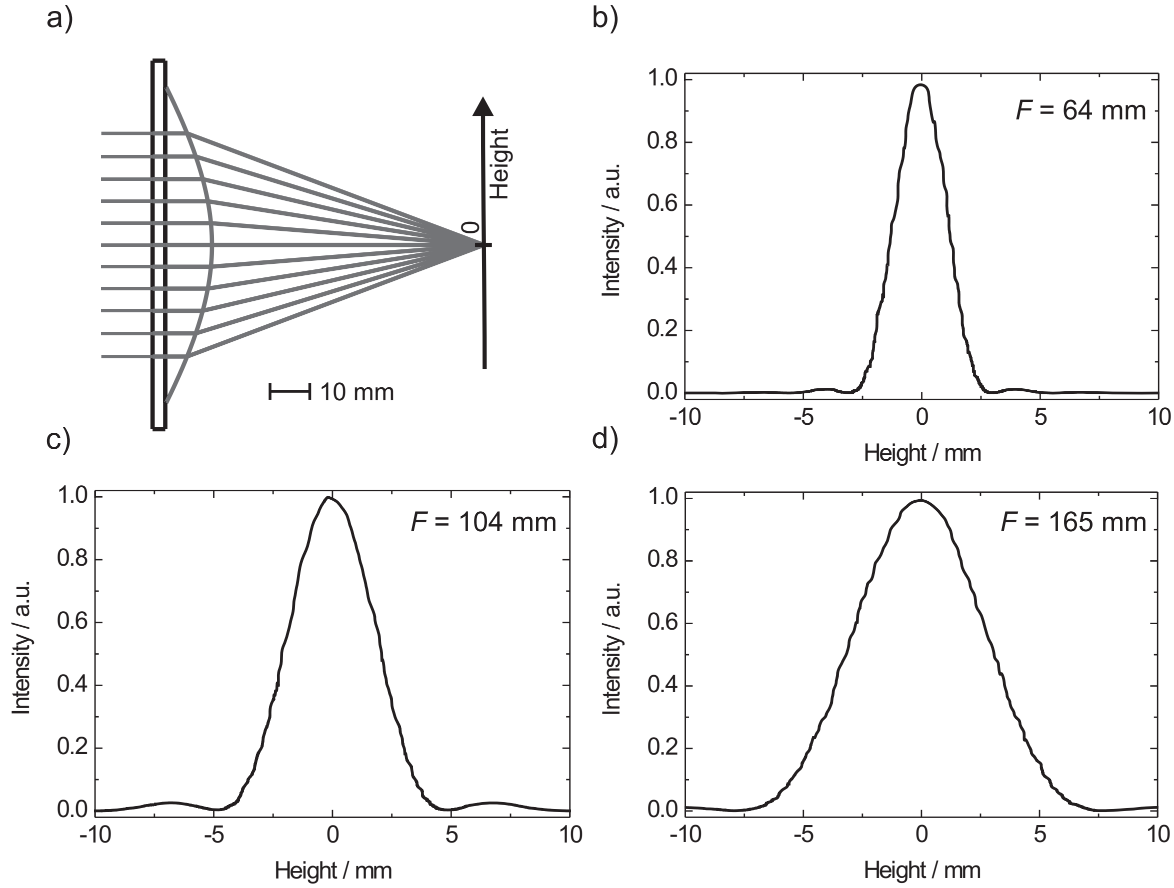

Figure 4.6: The simulation of the aspherical lens, focal length 64, 104 and 165 mm.

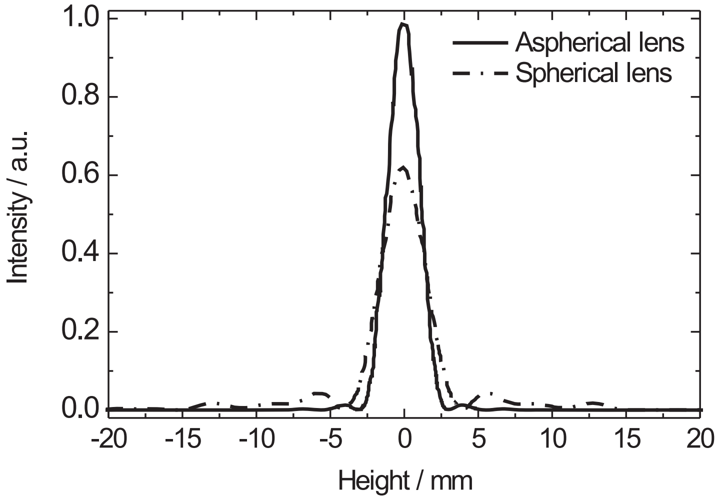

Figure 4.7: The intensity profiles for the aspherical and the spherical $F = 64$ mm lens.

The three HDPE lenses designed above have been manufactured and measured using the setup presented in Fig. 4.4. For every lens, the distance blade-lens is adjusted in this way, that the blade is located at the focus position obtained by the Gaussian theory. In the discussed setup, the first lens is located at a position, for which the leaving beam produces almost a perfectly collimated beam. As a result, in this case the focus position obtained by the Gaussian theory overlaps with this which is obtained from the geometrical optics. Analogically as in the case of the spherical lenses, the curves similar to those presented in Fig 4.5 a) have been obtained. To derive intensity profiles, deconvolution of the measured data with unit step function has been performed. Resulting profiles normalized to unity are presented in Fig. 4.8. For each lens, the beam diameter at the focus has been extracted. The results are shown in the table 4.1. Based on the equation (3.51), the beam propagation factor M^2 has been calculated and included in the table.

Analyzing the results presented in the table, it is clear that the measured values of the beam diameter are greater than the simulated ones for the lenses $F = 64$ mm and $F = 104$ mm. The discrepancy between the simulation and the measurement can be explained as follows. The design and simulation software OpTaliX optimizes the lens surfaces geometry according to the geometrical optics. As a result, all rays are assumed to focus in the focal point at an infinitively small height. However, for millimeter waves the beam diameter at the focus is comparable with the lens aperture. Therefore, a significant phase shift for different components with different heights within the focal plane occurs. Eventually, the interference leading to

Method	***F* = 64 mm**	***F* = 104 mm**	***F* = 165 mm**
Simulation (OpTaliX)	4.0	6.6	10.1
Calculation (equation (3.49) and GBC)	4.0	6.4	10.0
Measurement	5.5	6.9	10.0
M^2	1.38	1.08	1.00

Table 4.1: The comparison of the calculated and measured beam diameters for aspherical lenses (all units are millimeters).

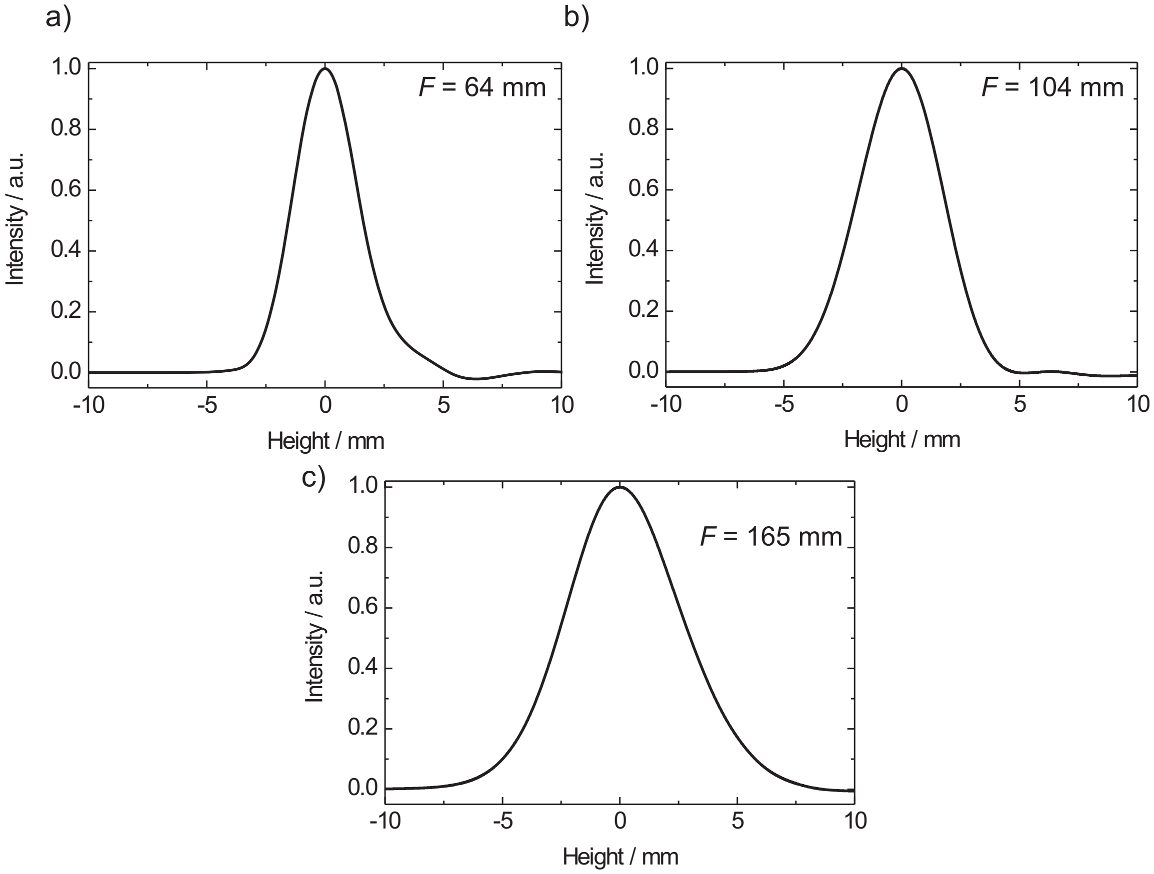

Figure 4.8: Measured beam profiles for three aspherical lenses: a) $F = 64$ mm, b) $F = 104$ mm, c) $F = 165$ mm.

increased beamwidth appears. This phenomenon is the more pronounced, the smaller the focal length compared to the aperture size. For the lens $F = 165$ mm the focal length is greater than the aperture size. Therefore, the phase shift between the field components is negligible and the parameter M^2 which describes the beam quality approaches unity. This is clearly seen in Fig. 4.8, since the profiles for the lenses with higher focal lengths come close to the Gaussian profile.

For imaging purposes described in chapter 5, the aspherical lenses with $F = 64$ mm have been chosen, because they assure the smallest beam diameter at the focus. The lenses $F = 104$ mm and $F = 165$ mm will find application in the systems presented in chapter 6 and 7.

5 W-band VNA imager

Microwave imaging is a mature material characterisation technique that has existed since the 1950s. The first imaging system based on cathode-ray tube sources operating at 35 GHz was built in 1955 [203]. The development of solid state devices in the microwave region, which was mainly driven by radar and communications applications, has lead to the growth of compact, low-noise and cost-effective solid state sources and detectors.

In general, imaging systems can be passive or active. Passive systems use the cold sky as a source of image contrast. The main applications for these systems is navigation in poor weather. In such conditions, microwave imagers offer better quality compared to the imagers working in the visible range. The second important application of passive imagers is security scanning. Several publications have presented systems for detecting weapons that are concealed under clothes. However, the practical usage of passive systems is limited to outdoor applications. For indoor applications, active systems employing microwave sources are required. These systems can be divided into two groups: free space systems and waveguide systems.

Generally, free space imaging systems use horn antennas to emit and receive the microwave signals. The distance between the antenna and the device under test (DUT) is significantly greater than the wavelength. The resolution is mainly determined by the wavelength and the aperture type and size of the antennas. Depending on the final application, free space systems are realized in the transmission or reflection mode. The reflection mode is widely applied for the detection of objects of high reflectivity surrounded by other materials which are not transparent to microwaves. Several systems for the concealed weapon detection have been practically realized in the reflection geometry so far [204, 205]. However, if the surrounding material neither absorbs nor scatters the microwaves completely, the transmission mode is advantageous since a higher signal-to-noise ratio can be obtained. The applications of imaging systems based on the transmission geometry for the detection of a weapon (a firearm) hidden in a leather briefcase have been shown [206].

In general, by performing a raster scan in two orthogonal directions x and y of the specimen, the received signal $E = f\left(x,y,\omega\right)$ is the convolution of the transmission function $G = f\left(x,y,z\right)$, which describes the specimen properties and the PSF $H = f\left(x,y,z,\omega\right)$, hence [207]:

$$E\left(x,y,\omega\right) = G\left(x,y,z\right) * H\left(x,y,z,\omega\right). \tag{5.1}$$

The PSF is a system-unique function and it is defined by the antennas and other components which guide the beam. In order to improve the image resolution, several numerical techniques can be applied. Using the Synthetic Aperture Radar (SAR) algorithm [208], which includes the coordinate transformation - Stolt interpolation, object reconstruction can be performed [207]. Hence, the lateral resolution is increased. Another reconstruction technique is the Constrained Least Squares (CLS) method [209]. In this technique a deconvolution operation is used. However, to achieve reliable reconstruction results, a proper choice of the regularisation parameter

is required [207]. Algorithms based on the Matrix Pencil Method [210] enable an increase in the range resolution as shown in [207]. Other algorithms leading to increased resolution are Estimation of Signal Parameters via Rotational Invariance Techniques (ESPRIT) [211] and Generalized Pencil-of-Function Method (GPOF) [212]. All techniques mentioned here require additional hardware or software. Moreover, in order to achieve satisfactory results, proper parameters for the reconstruction for every individual case have to be chosen.
Waveguide systems focus on the imaging in the near-field. Here, the probe is located at a small distance from the DUT. Typically, the separation is well below the wavelength. The spatial resolution of the near field imagers is mostly the function of the probe size. Recently, several applications of the near-field methods for cancer detection and glass thickness evaluation have been presented [213].

However, for real life industrial applications the distance between the probe and the DUT cannot be arbitrarily small. Often, the DUT is packaged and therefore, the probe cannot physically approach the DUT. Hence, for industrial inspection purposes free space systems have to be used. The implementation of the reconstruction algorithms in industrial imagers is difficult, since the time available for supplying the evaluation result is relatively small. Generally, the time needed for the evaluation has to be lower than the time in which two subsequent DUTs driven by the conveyor cross the reference point. Nowadays the conveyor belts' speed reach 180 items per minute; therefore, manual analysis of the raw data and the proper choice of the parameters for the signal reconstruction make these methods infeasible for industrial inspection. Hence, systems employing hardware components (lenses) for the enhancement of the spatial resolution are the scope of this thesis. These systems are compact, flexible, fast and they offer good resolution for industrial inspection applications.

In the following chapter new applications for microwave imagers working in the W-band will be shown.

5.1 System design

The W-band transmission mode imager is based on the VNA Agilent Technologies E8361A with extension module N5260A. For the wave excitation and detection two external mixers with waveguide ports WR-10 are employed. For efficient coupling of the microwaves to the air two conical horn antennas with the gain $G = 21$ dB and the aperture $D = 16$ mm are used. To achieve small antenna footprint in the imaging plane, a set of aspherical HDPE lenses $F = 130$ mm and $F = 64$ mm described in chapter 4.2 is employed as presented in Fig. 4.4. The setup has been designed according to Gaussian theory described in chapter 3.2.2. Additionally, the optical part of the system has been simulated in the GBC, as presented in Fig. 5.1 a). As it has been shown in chapter 4.2 the measured beam at the focus plane is 5.5 mm. The optical elements have been designed for the centre frequency 100 GHz. However, for most of the imaging results presented in this chapter the spectrum ranging from 90 GHz to 110 GHz is acquired and the average value is recorded. By acquisition of the spectrum of the scattering parameter S_{21} the influence of standing waves between the lenses and antennas is minimized. The lenses and the mixers are fixed on the optical rail, as depicted in Fig. 5.1 b). The DUT is

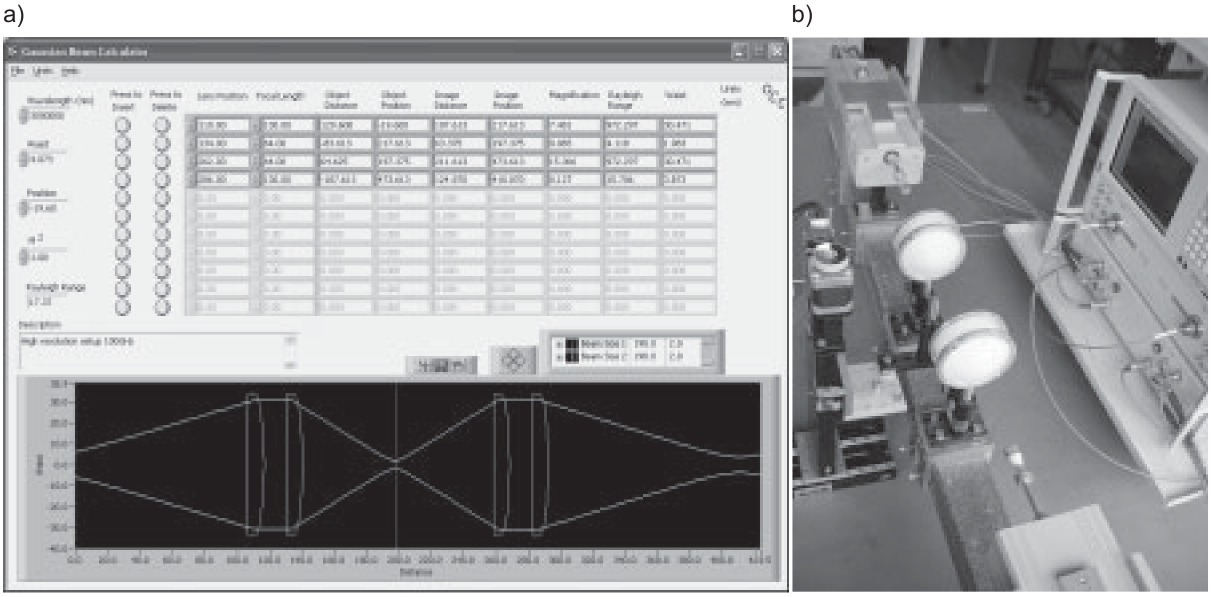

Figure 5.1: The W-band imager: a) optical design, b) photograph of the system.

driven by the 2-axis motorized translation stage and it is placed in the focus plane, normal to the optical axis. For the control of the translation stage, data acquisition and storage, a dedicated routine in LabView has been written. As a result, for each raster scan a data matrix is created. Finally, the data matrix is imported and visualized in the Origin software.
The following subchapters include the measurement results employing the VNA imager.

5.2 Test structures

In order to characterize the system properties a test structure made from HDPE shown in Fig. 5.2 is imaged. The structure consists of five 5 mm steps separated by a distance of 40 mm; hence, the structure thickness varies from 5 mm to 25 mm. Additionally, through holes with diameters ranging from 2 mm to 20 mm are drilled in the structure. For this sample, two raster scans of area A and B are performed. Moreover, for every scan area, cross-sections along the marked lines are shown in Fig. 5.3. The raster scan step is 1 mm in both orthogonal directions. The graph includes the value of the S_{21} parameter which is averaged over the band from 90 GHz to 110 GHz. Fig. 5.3 a) presents the measurement results of the area A. As can be seen, all steps are clearly resolved. The attenuation of the HDPE increases by 0.6 dB per every step. Graph 5.3 b) depicting the image of the area B shows the holes scanning results. All holes, including the smallest one, are present in the microwave image. It is apparent that the transmission is significantly lowered at the positions $X = 40, 80 \ldots 160$ mm, that is at the positions where the steps emerge. The attenuation of the signal does not originate from the properties of the test structure, but is caused by diffraction. To investigate diffraction effects, an additional raster scan at the frequency 110 GHz has been performed. As can be seen in Fig. 5.4 a), the transmission in the transition region is -3.2 dB. The transmission in the transition region has been calculated numerically. If the beam is focused on the transition region between step 4 and

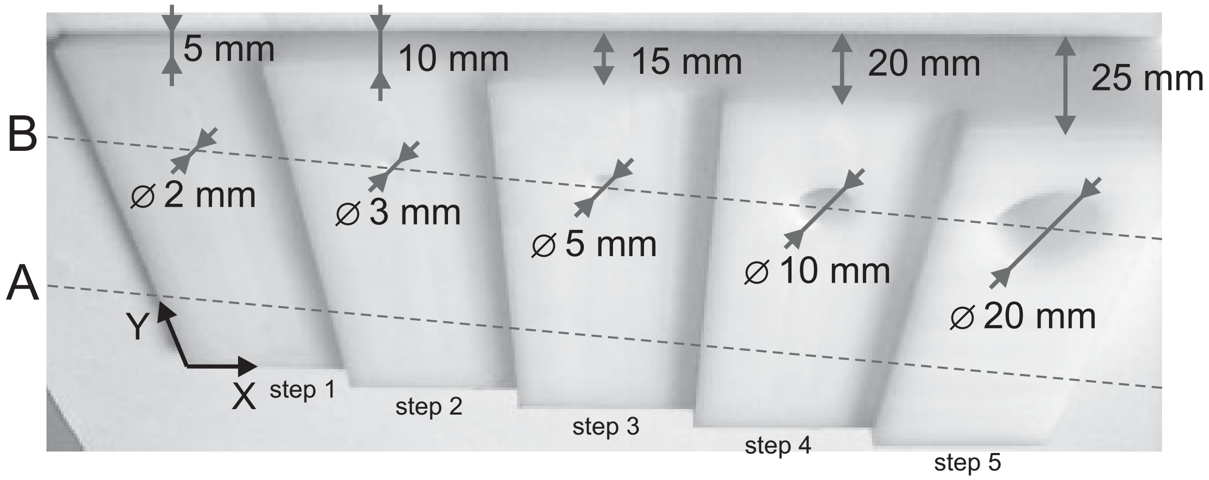

Figure 5.2: The HDPE test structure.

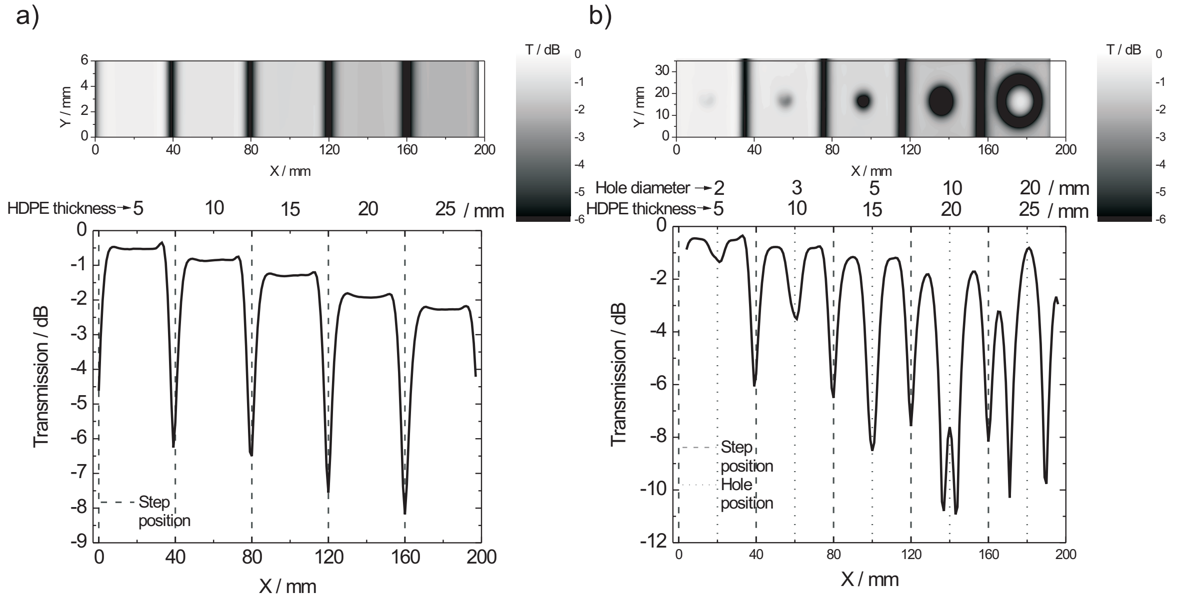

Figure 5.3: HDPE imaging results: a) steps, b) holes.

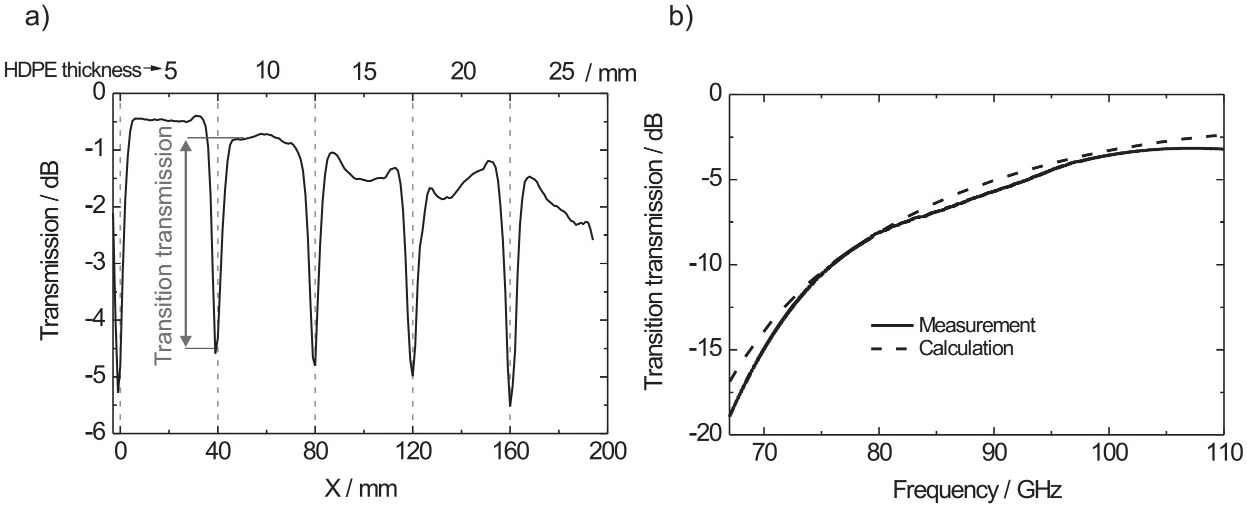

Figure 5.4: Transmission in the transition region: a) imaging at 110 GHz, b) the calculation and the measurement.

step 5 (Fig. 5.2), the equations for the wave amplitudes travelling through the steps are:

$$S_4 = T_4 \sin(\omega t + \phi_4), \tag{5.2}$$

$$S_5 = T_5 \sin(\omega t + \phi_5), \tag{5.3}$$

where T_4 and T_5 are the transmission coefficients, and ϕ_4 and ϕ_5 are the phase shifts of the waves propagating through the steps 4 and 5, respectively. Basic algebra shows that the phase shifts can be expressed as:

$$\phi_4 = \frac{2\pi d_4 c}{nf}, \tag{5.4}$$

$$\phi_5 = \frac{2\pi d_5 c}{nf}, \tag{5.5}$$

where d_4 and d_5 denote the thickness of steps 4 and 5, respectively. The wave parts exiting the structure interfere with each other and depending on their phases the transmission in the transition region T_T is:

$$T_T = \min\left(\frac{S_4 + S_5}{2}\right) = \min\left(\frac{T_4}{2}\sin\frac{2\pi\left(nf^2 + d_4 c\right)}{nf} + \frac{T_5}{2}\sin\frac{2\pi\left(nf^2 + d_5 c\right)}{nf}\right). \tag{5.6}$$

Assuming the following values, T_4 = -1.93 dB, T_5 = -2.27 dB (see Fig. 5.3 a), d_4 = 20 mm, d_5 = 24.7 mm, n - data adopted from Fig. 4.1 b), the values of the transmission of the transition region calculated by the equation (5.6) are plotted in the Fig. 5.4 b), dashed line. For comparison, the microwave beam has been focused directly on the transition region, and the transmission in the range from 67 GHz to 110 GHz has been measured (Fig. 5.4 b), solid line). The calculation and the measurement results in Fig. 5.4 b) are in a good agreement. Additionally these values correspond with the transition transmission obtained from the graph 5.4 a) and equal T_T = -3.5 dB. Similarly, the spikes seen at the positions X = 20, 60 … 180 mm in Fig. 5.3 b) originate from wave diffraction and interference of the wave parts propagating through the material and the air.

As a second test structure, an object made of PVC presented in Fig. 5.5 a) has been chosen. Here, the depth of the holes ranges from 1 mm to 5 mm and the diameter varies from 1 mm to 20 mm. The thickness difference between two subsequent steps is 1 mm. The imaging results are presented in Fig. 5.5 b). The steps are clearly pronounced as the areas of lower transmission

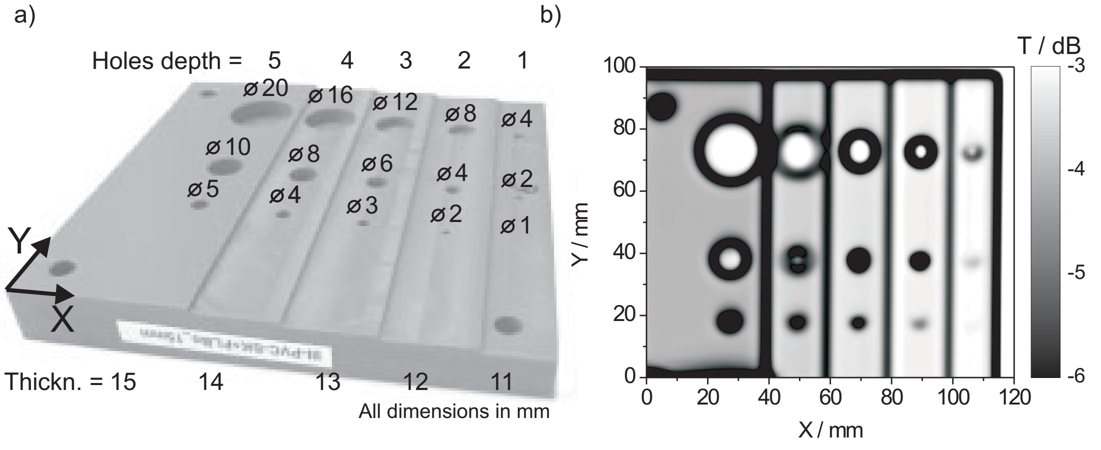

Figure 5.5: PVC test structure: a) photograph, b) imaging results.

for $X = 38$, 58, 78, 98 mm. Similar to the HDPE structure, it is explained by the destructive interference of the wave parts travelling through a material of varying thickness. It is clearly seen that the transmission increases when the step thickness is reduced. The estimated signal attenuation is 0.25 dB/mm for PVC.

The depth (1 mm) of a 1 mm diameter hole is too small to be resolved in the image. However, all other holes, including the 2 mm diameter, 1 mm deep hole are seen in Fig. 5.5 b). It is apparent that within the holes of the same diameter (e.g. 2 mm) the holes that have greater thickness provide a better contrast. This can be easily explained by reduced attenuation of the signal for the holes of greater depth.

As it has been shown, using a W-band imaging system, the sub-wavelength longitudinal and lateral resolution reaching $\lambda/3$ can be obtained. It has to be emphasized that this conclusion is based on the imaging results of relatively low loss structures (HDPE and PVC). It is believed that the structures which have greater absorption will provide a better contrast. This in turn enables us to resolve even smaller structures in the image. However, diffraction and interference effects have to be considered for the correct interpretation of the results.

5.3 Imaging of food products

This chapter presents the imaging results of packaged food products. In general, in the food industry several parameters including product moisture, pH value, flavour and texture have to be controlled. Besides, control for unwanted inclusions in the product plays an important role. Nowadays, X-ray scanners, visual methods and metal detectors are typically used. This subsection presents the results on the foreign bodies' detection and quality assessment of food products using the millimeter wave W-band imager.

In order to check the method's feasibility, typical packaging materials like glass, cardboard, polyethylene (PE), polypropylene (PP), polyethylene - terephthalate (PET) and drink carton (tetrapack) have been measured. All samples are from 0.1 mm to 2.0 mm thick. These values are standard values for the packages used for food products. The results showing the attenuation of the evaluated materials have been presented in Fig. 5.6 a). As can be seen, carton and plastic packages including PE, PP and PET have very low attenuation, well below 2 dB. The absorption of millimeter waves by glass is higher but it does not exceed 5 dB. Since tetrapack includes metal foil, its attenuation is very high, typically above 50 dB. For imaging purposes it is essential that the attenuation of the packaging material is low. Therefore, for all packaging materials presented here that do not contain metal foil, the information about the content can be obtained.

In the second step the properties of food products sold in the packages mentioned above have been investigated. For tests, the following goods have been chosen: ham slice, chocolate bar, milk, ice-cream and ketchup. The results depicted in Fig. 5.6 b) show that most products have an absorption between 5 and 25 dB. Only milk is a strong absorbing fluid and therefore, for these kind of materials the W-band imager cannot be used for inspection purposes.

In the third step, three chosen products were contaminated with different materials. Additionally, every product was packaged in the original container. The ham was contaminated with a

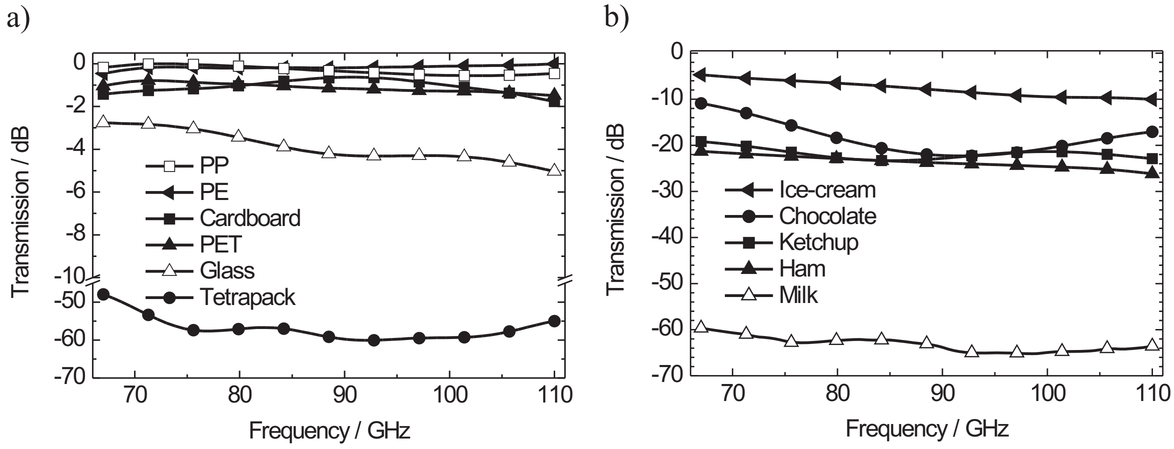

Figure 5.6: Transmission spectra of the: a) food packaging material, b) food products.

bone and packaged in a PE foil. Inclusions like stone, glass splinter and screw were placed in the chocolate bar. After the preparation, the chocolate bar was packaged in the original PE foil. Finally, a stone contaminated the ice-cream. For the evaluation, a part of the ice-cream in PE packaging was measured. The photographs of the test products and the measurement results are shown in Fig. 5.7. The inclusions placement and scan areas are marked on the photographs. Fig. 5.7 a) presents the slice of ham contaminated with the bone. The bone has a higher absorption coefficient than the ham. Hence, the overall transmission through the bone and the ham is decreased to -70 dB. Therefore, the bone can be easily distinguished from the ham. Three materials contaminating the chocolate are present in the imaging results in Fig. 5.7 b).

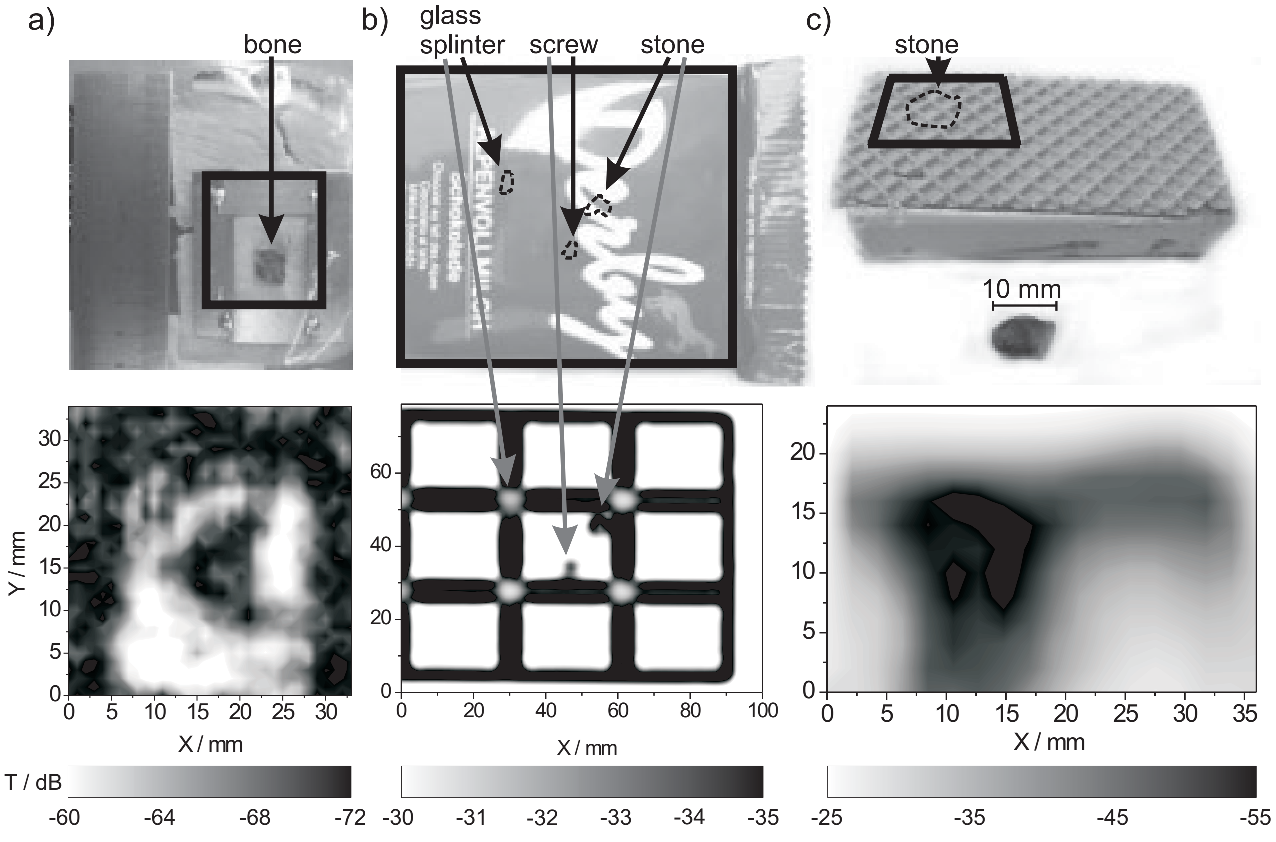

Figure 5.7: Imaging of the food products: a) ham slice, b) chocolate, c) ice-cream.

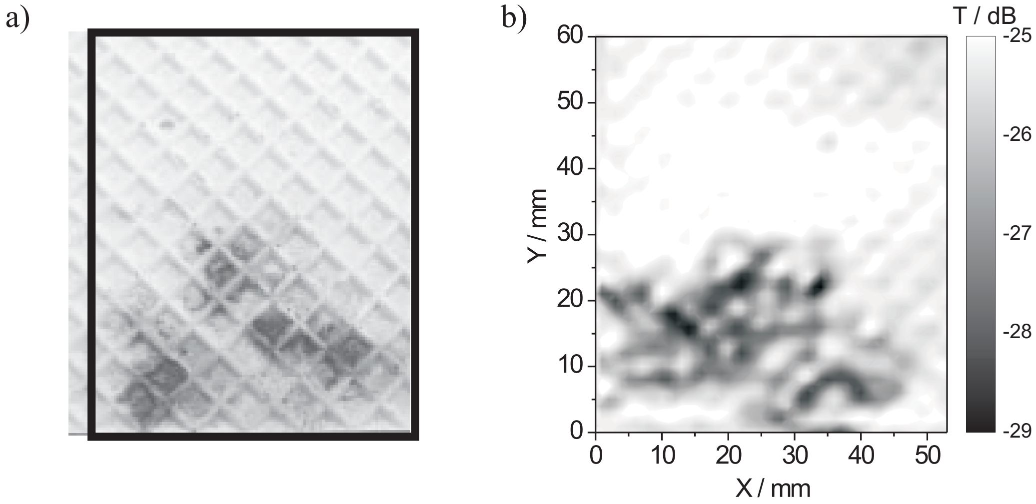

Figure 5.8: Evaluation of the burned wafer: a) photograph, b) imaging results.

Since the absorption coefficient of the screw and the stone is significantly higher than that of the chocolate, these objects are clearly resolved in the millimeter wave image. The glass splinter has lower absorption; however it is still detectable in the image as a darker area. Black lines separating the single piece originate from the interference. Figure 5.7 c) presents the ice-cream contaminated with the stone. Here, the contrast seen in the lower part of figure is provided by different absorption coefficients of the stone and the frozen ice-cream.

A second important application of the W-band system for the food industry is quality assesment. To test the feasibility of the system for quality assurance a wafer pictured in Fig. 5.8 a) was inspected. As can be seen, the heat exposure was too long in the lower part of the wafer, which resulted in a partial burn. The wafer was imaged in the original package. The imaging results are depicted in Fig. 5.8 b). Since the burned part has different properties, the transmission through this part is decreased to -28 dB, as depicted by the dark areas in the image.

Another area for millimeter wave systems in the food industry is the fluid fill level control. Using the W-band imager, the fill level of a 0.33 l beer bottle is investigated. Based on the fill level measurements of the bottles the standard level is 193 mm from the top of the bottle. For the measurements, the setup shown in Fig. 4.4 is used; however, the bottle is placed 9 mm out of the focus, that is, at the place where the beam diameter is increased to 10 mm. As is presented in Fig. 5.9, a strong dependence between the fill level and the transmission emerges. Using this particular setup, the fill levels between 186 mm and 197 mm can be clearly detected. In case another measurement range is required, the optical system has to be adjusted. Generally, the diameter of the screening beam should correspond with the fill level range that needs to be evaluated.

As has been shown, millimeter wave imagers have potential in the quality assurance of food products. In particular, foreign objects can be detected. The W-band imager can find applications for the testing of products which are dry, frozen or which contain fat. Moreover, it has several advantages over existing systems. In contrast to X-ray scanners, the W-band imager does not ionize the matter. The millimeter wave imager offers higher spatial resolution than standard metal detectors. Therefore, a lower rejection ratio can be obtained. Finally, the

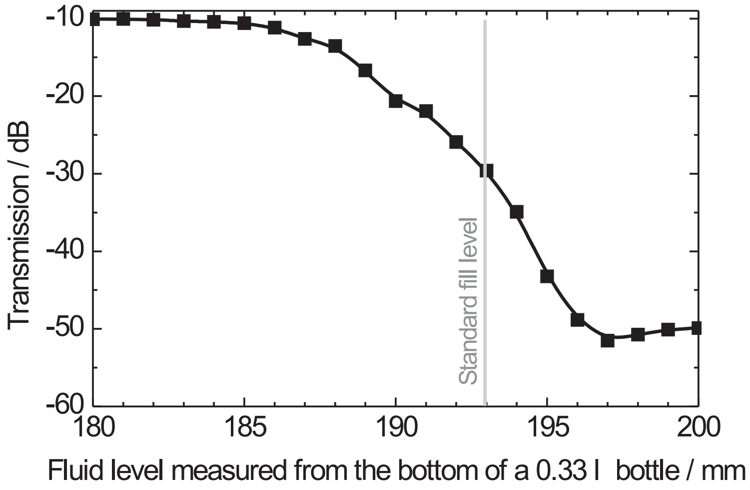

Figure 5.9: Evaluation of the liquid fill level in a 0.33 l bottle.

W-band imager is a nondestructive, contactless and real-time evaluation method which can be applied to 100% of the products. However, strict method limitations emerge if the packaging materials contain metal, or if the tested product contains water.

5.4 Imaging of plastics

Recently, plastics materials have experienced a considerable growth. This is attributed to their unique properties which include resistance to corrosion, high stiffness referred to their low gravity and fabrication simplicity. By including additives in the plastic structure, the mechanical properties can be altered. This contributes to a high design flexibility. To improve the stability and the stiffness, spatially arranged fibrills can be added. As an example, liquid crystal polymers (LCPs) find applications in avionics for the production of helicopter stators [214]. As an alternative, two or more plastic sheets can be joined together to improve the mechanical properties. This method is widely used for the fabrication of window frames or pipes.
For the plastics industry it is crucial that a high quality of joints is assured. The plastics incorporating additives demand that a uniform distribution of the additive is assured. Since the mechanical properties of LCPs depend on the crystal's orientation, a proper alignment of the crystals in the polymer is required. Eventually, the thickness of the plastic material has to be inspected. The remainder of this subchapter concentrates on the nondestructive inspection of plastics.

Welding is a standard process that is applied for the joining of plastics. For this process it is essential that no contaminations including gases, fluids or solids are present in the weld area. Otherwise the quality will deteriorate. The goal of the following investigations is to prove the feasibility of the W-band system for the quality inspection of plastics. In the first step, the HDPE weld was contaminated with metal staples as shown in Fig. 5.10 a). The lower part presents an image which is obtained using the W-band imager. Since metal inclusions have a

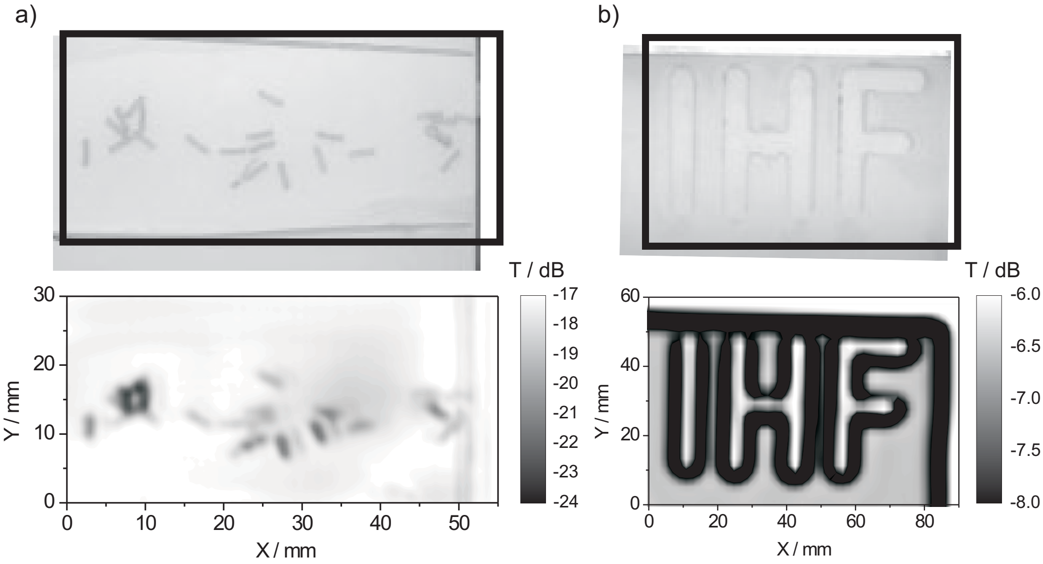

Figure 5.10: Evaluation of plastics: a) staples inclusions, b) air inclusions.

very high reflection coefficient, a good contrast with low absorbing plastic is achieved. Therefore the staples having the thickness of $\lambda/3$ are clearly seen in the image. In the second step, the effect of plastics delaminations has been investigated. For this purpose, a transparent sample consisting of two welded plastics has been chosen. The inner side of one of the parts contains the IHF logo which has been placed by locally removing the material (refer to Fig. 5.10 b). As presented in the millimeter wave image, the air filling the logo areas is clearly resolved. The edges of the logo letters are pronounced because of diffraction. On the other hand, in the middle of the letters the overall transmission is increased, since the effective HDPE thickness is lower. To investigate the W-band imager feasibility for the measurements of the alignment of the LCP fibrils, the injection molded LCP presented in Fig. 5.11 has been imaged. The black lines on the photographs show the presumed orientation of the molecules. For the measurement, the receiving antenna has been rotated by 90° around the transmitting module. Since in this case the polarisation of the transmitter and the receiver differ by 90°, only a weak signal is detected. However after the insertion of the LCP sample at the focus, the molecules present in the inner area of the sample rotate the polarisation of the microwave beam. As a result, the detected signal is enhanced by 20 dB. To exclude the possibility that the transmission increase comes from the intrinsic parameters of the sample, the experiment has been repeated for a different orientation of the LCP. As can be seen in Fig. 5.11 b), the sample is rotated by 45° from its initial position (Fig. 5.11 a). Again, the molecules aligned at the angle of 45° according to the transmitter and receiver positions rotate the polarisation of the wave. As a result, increased transmission is observed at the outer parts of the structure. Since the molecules placed in the inner part of the LCP are oriented parallel to the field polarisation, no polarisation rotation emerges, and therefore the transmission is low.

Wood Plastic Components (WPCs) consist of wood particles which are dissolved in plastics. The application area of WPCs includes the building industry, the packaging industry and the automotive industry. The addition of wood particles improves the mechanical properties of the material. In particular, the thermal expansion and the costs are reduced, whereas the component's stiffness is increased. However, the improvement of the component's properties can be

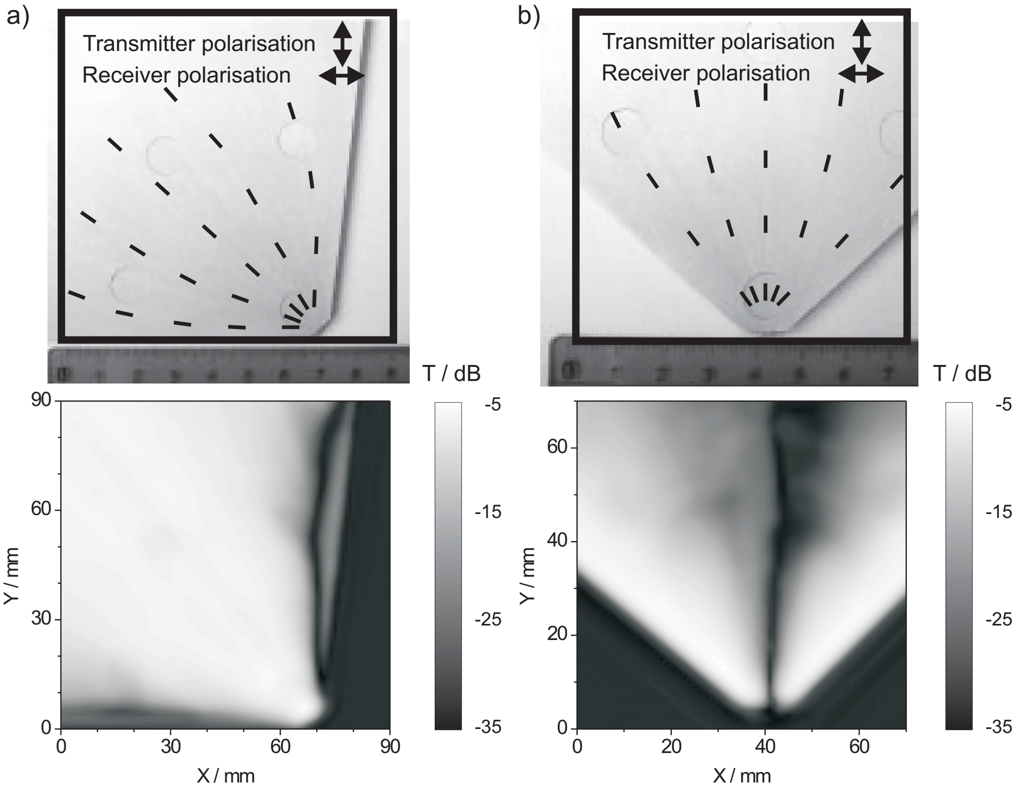

Figure 5.11: Testing of LCPs: a) orientation A, b) orientation B.

achieved only in the case if the additives are distributed uniformly in the plastic. Therefore, there is a need for the evaluation of the wood distribution. One possible approach is microwave imaging. As an example, a WPC sample shown in Fig. 5.12 a) has been imaged. The sample is made of PP, whereas the timber serves as the additive. In the millimeter wave image (Fig. 5.12 b) five round-shaped areas are clearly visible. They originate from the injection die casting. Analysing the image it is clear that the right-hand areas show decreased signal transmission. This effect is attributed to an increased concentration of the additive. Therefore it is concluded that the additive agglomerates are located mainly in the right-hand part of the sample.

Millimeter wave systems can be also employed for the thickness evaluation of plastics. As an example an air bag cover presented in Fig. 5.13 a) is presented. For the proper functioning of the cover it is crucial that the cavity has a defined thickness. In case the thickness is too high, the cover of the airbag will not open. On the other hand, if the cavity thickness is not

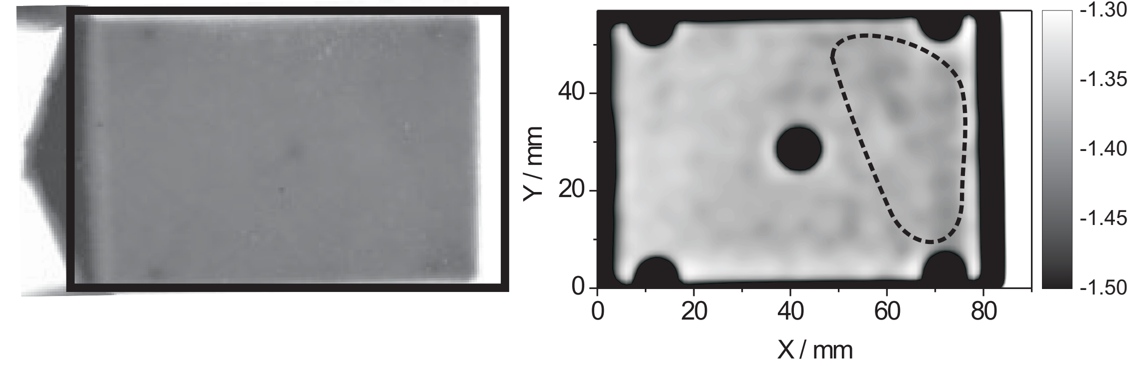

Figure 5.12: Additives distribution measurement: a) evaluated sample, b) imaging results.

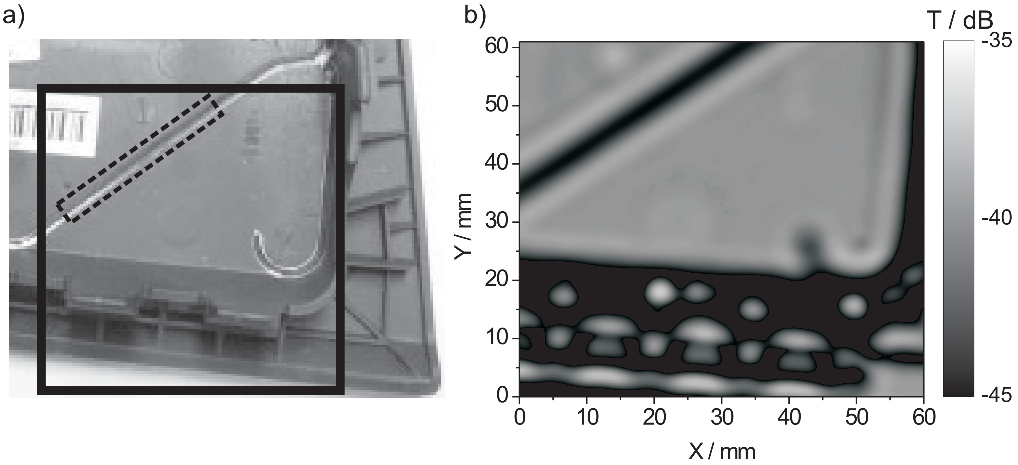

Figure 5.13: Airbag imaging: a) evaluated sample, b) imaging results.

high enough, the cover can open itself by chance. Since the cavity is clearly resolved in the microwave image (Fig. 5.13 b), the qualitative information about its thickness can be obtained using the modelling.

In this chapter several applications of the W-band imager for the plastics industry have been presented. As it has been shown, the scanner based on millimeter waves is capable of evaluating the product quality. In particular the quality of the weld joints, the orientation of the molecules in the polymers, the additive distribution and the plastics' thickness can be successfully tested. It has to be emphasized, that this technique is fast, powerful, nondestructive and affordable; therefore it can be applied for tests on complete assortments.

5.5 Imaging of plants

For biologists, the monitoring of the water status in plants is of great importance. On one hand information about the water content enables the optimization of the watering process. On the other hand, the determination of the water status leads to a better understanding of the drought stress. To obtain the water content of a plant the thermogravimetric method is employed [215]. Here, the weight of the original and the dried leaf is measured. The weight difference provides information about the water content. This method offers very good accuracy, however it is destructive. Therefore, only a part of the population, a sample can be chosen for the measurement. Moreover, the measurement results relate to the particular sample and there is no guarantee that the other samples have identical properties. Therefore, there is a need for a cost-effective, nondestructive and fast method for the evaluation of the irrigation status. As has been proven in [216], the water content can be obtained by the measurement of the transmission in the microwave range. The idea is based on the attenuation of the signal by the water which is concentrated in the plant.

In this work the imaging of two leaves cut from the plant has been performed. Fig. 5.14 a) presents a photograph of the 900 µm thick violet leaf. The measurement results are shown in the graph below. As can be seen, almost all veins are clearly visible in the millimeter wave image. It is straight-forward to distinguish between well-watered (A) and poorly-watered (B) veins because of the different transmission values. It is also remarkable that the main vein has

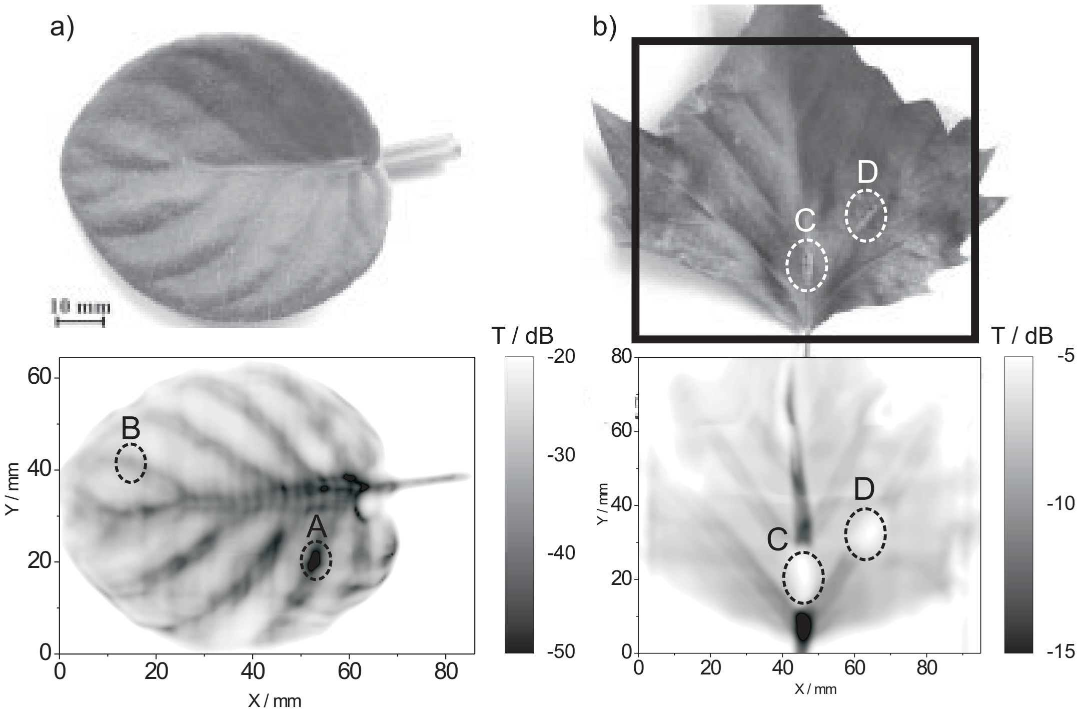

Figure 5.14: Imaging of the a) violet leaf and b) plane tree leaf.

the greatest water content. Using equations (4.1 – 4.3) the absorption coefficient $\alpha = 35$ cm^{-1} and the real part of the refractive index $n' = 2.61$ have been obtained. As a second example, a 200 µm thick plane tree leaf depicted in Fig. 5.14 b) has been measured. The leaf of the plane tree has a lower absorption coefficient, that is $\alpha = 25$ cm^{-1} and the refractive index is $n' = 1.79$. The results shown in the graph clearly reveal the leaf structure. Firstly, the veins - in particular the main-one - are seen as darker areas. Secondly, the dried, dead tissues marked in the picture as (C) and (D) are pronounced as areas of significant higher transmission. This is obvious, since the dead tissues do not contain water; therefore, local absorption is decreased. Finally, to obtain the relation between the transmission and the water content, a series of reference measurements or a modelling [217] of every leaf sort has to be performed.
To investigate the rehydration dynamics of the leaves, a series of single point scans of a cacao leaf was recorded in a time period of 57 hours. Prior to the measurement the plant was not watered for 60 hours. As it can be seen in Fig. 5.15, the transmission through the blade is higher than that through the vein. This is explained by lower water content in the leaf blades. The transmission profile plotted in the time domain is periodic, since it is remarkable that the transmission has its maxima at the end of nights and the minima at the end of the days. This observation is consistant with the measurements presented in [216]. However, the watering of the plant which occurred in the 41^{st} hour has increased the transmission minimum by 0.15 dB. This is caused by the improved water content in the veins as well as in the blades. It is also noticeable that the transmission slightly decreases directly after watering. This is attributed to biological processes in the leaf which follow the watering.

To summarize, millimeter wave systems offer the control of the irrigation process by measuring the water content in plants. The systems employing microwaves are cost-effective, while the resolution is still high enough for the imaging of the leaf structure. However, for every leaf type the calibration is required. In order to obtain consistent data, the water salinity should be kept constant, since it can influence the results as presented in [217].

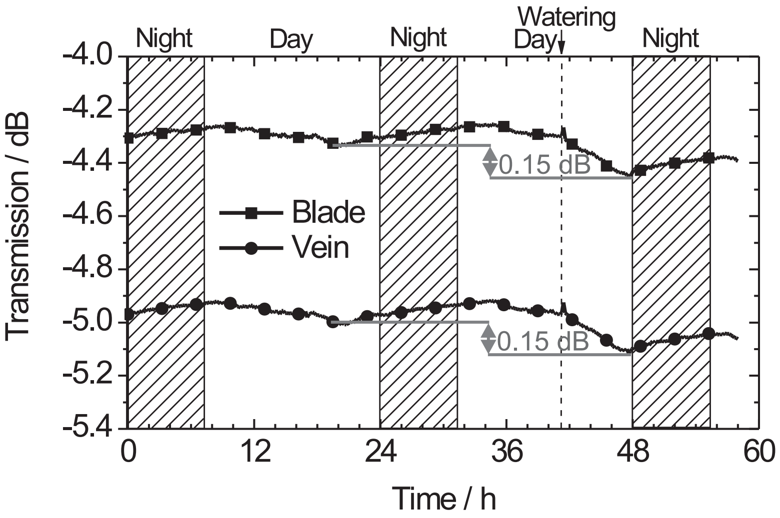

Figure 5.15: Rehydration dynamics in cacao leaf.

5.6 Millimeter wave systems for security applications

In general, security is of great importance for luggage, freight and mail shipment. In particular, the detection of concealed weapons and explosives is crucial. Contemporary screening systems are based on X-ray imagers. However, these devices have limitations. Firstly, radiographic scanners are not compact. Secondly, caution has to be taken while operating the system because of the ionisation danger. This relates to the operator, as well as to the screened persons or items. Therefore, there is a need for compact and non-ionising screening systems. One of the possible approaches is to employ millimeter waves.

In order to check the feasibility of the W-band imager for security applications, a handbag is raster-scanned. Fig. 5.16 a) presents the microwave image of the 200 mm thick handbag which includes typical personal-usage objects. In the second step a metal knife shown in Fig. 5.16 b) was inserted in the handbag. Since the metal is opaque to millimeter waves, the transmission is significantly decreased, as is seen in the image. Admittedly, the scanning resolution of the thick

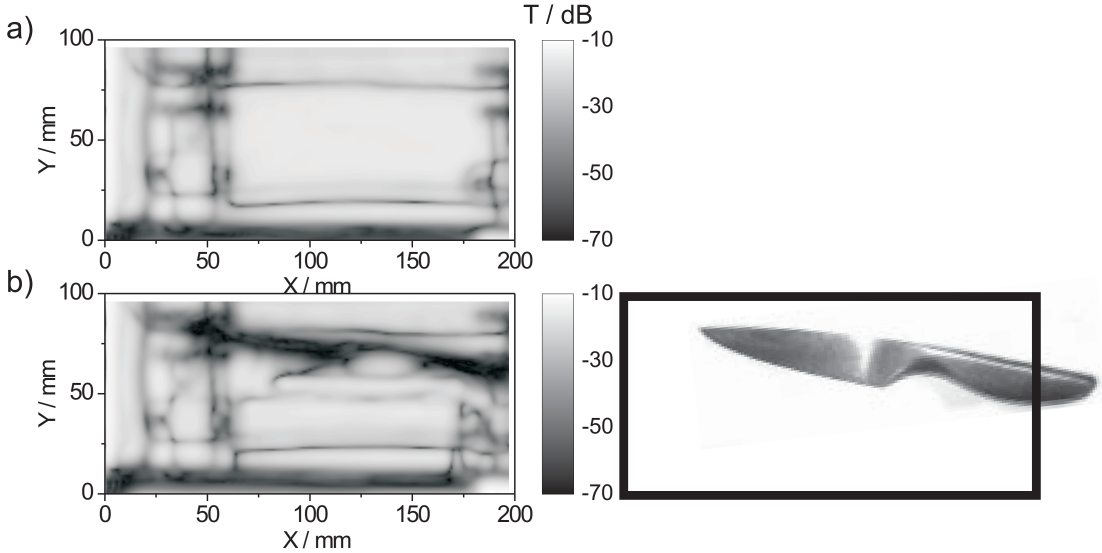

Figure 5.16: Detection of a knife in a handbag: a) handbag without the knife, b) handbag including the knife.

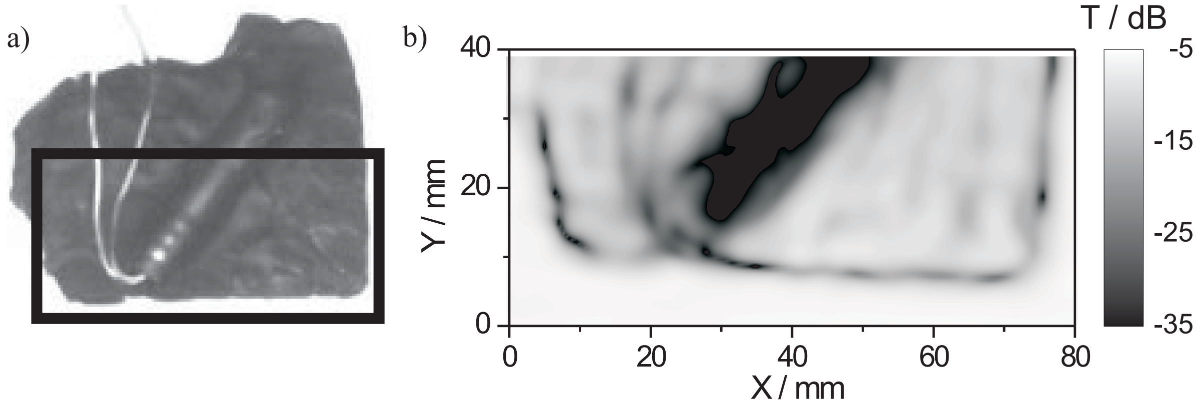

Figure 5.17: Explosive detection for the security applications: a) photograph, b) imaging results.

items like the handbag is somehow limited. This is attributed to the relatively small Rayleigh range. As a result, only the items which are placed within the Rayleigh range can be clearly resolved. Since the beam is divergent outside the Rayleigh range, the objects need to have sufficient geometrical dimensions in order to be seen in the image.
To evaluate the possibility to scan the mail contents, an explosive model presented in Fig. 5.17 a) was enclosed in an envelope. The model consists of plasticine which imitates C4 explosive, and authentic wired detonator. The measurement results are depicted in Fig. 5.17 b). As can be seen, the plasticine is detectable, since the transmission decreases by 5 dB due to absorption. Moreover, the local thickness can be evaluated. Additionally, the presence of the metal detonator is clearly pronounced. The wires which have thickness below 1 mm are also noticeable.

The W-band imager is a suitable system for security applications. The most promising area is mail inspection, since the presence of items different from the paper sheets can be easily detected. The millimeter wave systems can also be employed for the screening of luggage or freight. Here, metallic weapons can be identified. However, it has to be emphasized that the objects to be detected must not be covered by other metallic items. This also relates to the materials out of which the luggage carrier is fabricated. Therefore, the screening of the metal suitcases is not possible.

5.7 Conclusions

In this section several new application fields for millimeter wave systems working in the transmission mode have been presented. Employing the microwave W-band, the longitudinal and transversal resolution of the system equipped with lenses reaches 1 mm. This is sufficient for most industrial applications. Simultaneously, the penetration depth of the W-band radiation enables us to perform the scan through many different materials.

The systems based on the microwaves can be compact, cost-effective, fast and safe. The applications spectrum ranges from foreign-object detection, thickness measurements, welds quality control, irrigation process control to security applications. Therefore, millimeter wave systems can be successfully employed in the food, building, automotive and security industry.

6 Ka-band industrial inspector

In food industry production plants, it is important that the package content is consistent with the label. In case the product does not conform its specification, significant costs of the product withdrawal or replacement can arise. As an example, a drink box containing bottles has to be complete, that is, it must contain the correct number of bottles. Additionally, all bottles have to be filled with the drink specified on the label. Since contemporary industrial plants operate at very high throughput rates, the overall fabricating reliability can be decreased. As a result, boxes with missing or incomplete items may be manufactured. The main motivation for this work is to design a new system for completeness testing of drink boxes. Moreover, it is crucial to overcome the limitations of the existing completeness testing methods. As presented in chapter 1, there exist several different systems for quality control in the food industry. The most important are: visible methods, checkweighers, radiographic methods, metal detectors and ultrasounds. However, every method has some disadvantages for application in the food sector. Visible methods are applicable solely to packages that are transparent to visible light. Scales do not provide information about the position of the nonconforming element. Additionally, high product throughputs limit the measurement accuracy because of the scale vibrations. Radiographic methods are not completely safe because of concerns about the ionisation of food material. Metal detectors offer very low spatial resolution. In the food industry, they can be used only for the detection of metallic contaminants. Ultrasound methods are not contact free, which limits their application for packaged products. Hence there is a need for a system that not only offers good spatial resolution but is also safe. Simultaneously, the device has to check the contents of the bottles packaged in an opaque six-pack in a nondestructive way and it has to do it fast enough to provide screening at the typically used conveyor belt speeds. Additionally, the system has to be easily integrable with existing industrial conveyors.

This chapter presents the complete design of a 35 GHz stand-alone industrial inspector for completeness testing of the drink containers.

6.1 Preliminary results

To check the feasibility of millimeter waves to screen the bottles, a measurement on a single bottle is conducted. In the first step, a simple system working at the centre frequency of 60 GHz consisting of an oscillator, a diode detector, two conical horn antennas and four spherical lenses depicted in Fig. 6.1 a) is employed. The bottle is mounted on a single axis translation stage. Using LabView software, an one-dimensional scan of the bottle in the plane perpendicular to the optical axis is performed. The measurement results are presented in Fig. 6.1 b). Analysing the graph it is easy to distinguish between a full and an empty bottle. Since the full bottle is filled with water which has the absorption coefficient 50 cm^{-1} for the considered frequency [218], the microwave signal is significantly attenuated. As can be seen, the transmission reaches -30 dB.

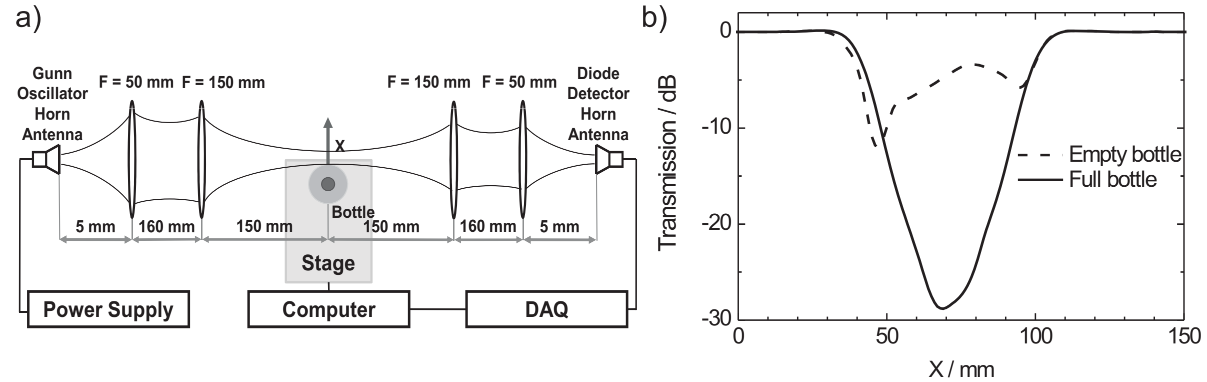

Figure 6.1: Single bottle scan: a) measurement setup, b) results.

This value approaches the noise level of the system. In contrast, the empty bottle does not contain water; therefore, the received signal is solely determined by the attenuation of the two glass layers. In this case the transmission falls to -7 dB. The spikes which are observed in the curve originate from diffraction and interference. To sum up, the preliminary results prove that the application of millimeter waves for the detection of empty bottles is possible.

For the choice of the target frequency, several aspects including spatial resolution, economic factors and the availability of components have to be considered. Preliminary results were obtained at the frequency of 60 GHz. By increasing the frequency, higher spatial resolution can be obtained because of the decreasing wavelength. However, the price of the components grows approximately proportional to the second power of the frequency. This, in turn, dramatically raises the price of the whole system. As a result the microwave system could be economically unattractive compared to other competitors, e.g. checkweighers. Since the geometrical dimensions of the bottles are in the centimetre range, it was estimated that the spatial resolution in the range from 1 cm to 3 cm will be sufficient for the quality control of the six-pack. Based on the target resolution, availability of components and their price, the microwave Ka-band covering the frequency range from 26.5 GHz to 40 GHz is chosen. Since the wavelength for the chosen microwave band is in the centimetre range, the expected spatial resolution is assumed to be sufficient for the completeness control of the six-packs, as will be proven in section 6.3.

6.2 Optical design

The beam parameters of the testing system to be designed have to be optimized for the specific application. In the case of a beer six-pack, the bottles are arranged in 3 columns and 2 rows (Fig. 6.2 a). As shown in section 6.1, one full bottle completely attenuates the microwave signal. Therefore, it is easy to obtain the information about the fill status if the bottles are arranged in one row, which is perpendicular to the microwave path. If there are additional rows of bottles organized perpendicular to the path (Fig. 6.2 a) no information about bottle status is achievable. This is due to the fact that one full bottle totally attenuates the microwave signal and therefore, the status of another bottle in the same column does not influence the millimeter wave signal. Hence, the optimum tilt angle α between the six-pack and the scanning path (Fig. 6.2 b) needs to be calculated.

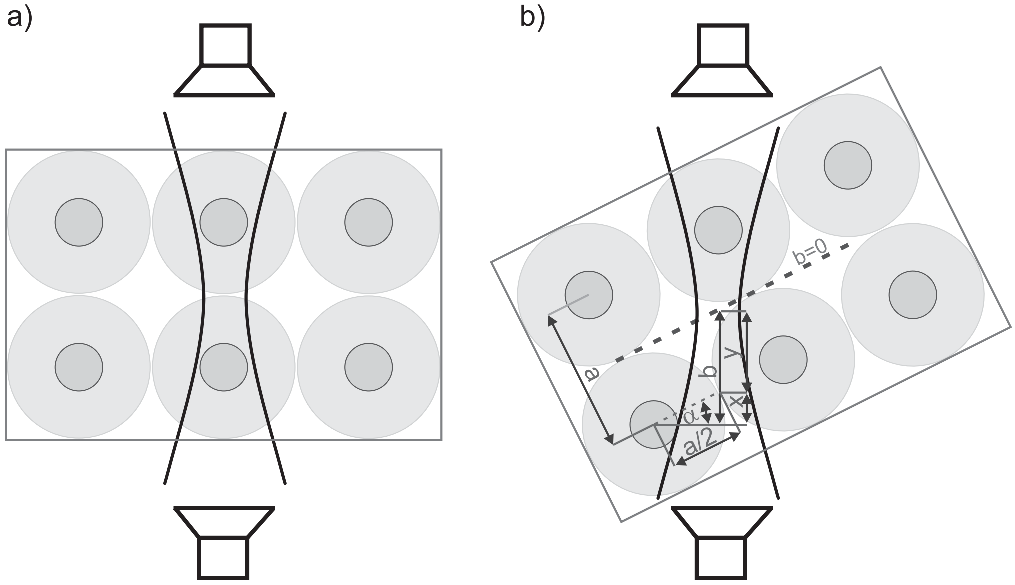

Figure 6.2: Bottle arrangement: a) perpendicular to the path, b) tilted to the path.

For the six-pack considered here, the distance between two bottles is $a = 62$ mm. Using simple trigonometric equations the optimal tilt angle α is calculated to $\alpha = 26.6°$. For the optimization of the beam profile it is assumed that the beam diameter scanning the outer bottles has to be minimized. The distance between the position of the outer bottles and the focus position is denoted as b. According to the nomenclature used in Fig. 6.2 b), the following equations can be written:

$$x = \frac{a \sin\alpha}{2}, \tag{6.1}$$

$$y = \frac{a}{2\cos\alpha}. \tag{6.2}$$

Since $\alpha = 26.6°$ and $b = x + y$, eventually

$$b = 0.783a \tag{6.3}$$

Based on the equation (3.11) the beam radius ω can be expressed as the function of the distance b as follows:

$$\omega\left(b,\omega_0\right) = \omega_0\sqrt{1 + \frac{b^2\lambda^2}{\pi^2\omega_0^4}}. \tag{6.4}$$

To simplify the calculations, a constant N is introduced:

$$N = \frac{b^2\lambda^2}{\pi^2}. \tag{6.5}$$

Therefore, the equation (6.4) can be rewritten as:

$$\omega = \omega_0\sqrt{1 + \frac{N}{\omega_0^4}}. \tag{6.6}$$

Since it is necessary to calculate the minimum of the function $\omega = f\left(\omega_0\right)$, the derivative of the equation (6.6) is:

$$\frac{d\omega}{d\omega_0} = \frac{2\omega_0^4}{\sqrt{\omega_0^4 + N}} - \sqrt{\omega_0^4 + N} \tag{6.7}$$

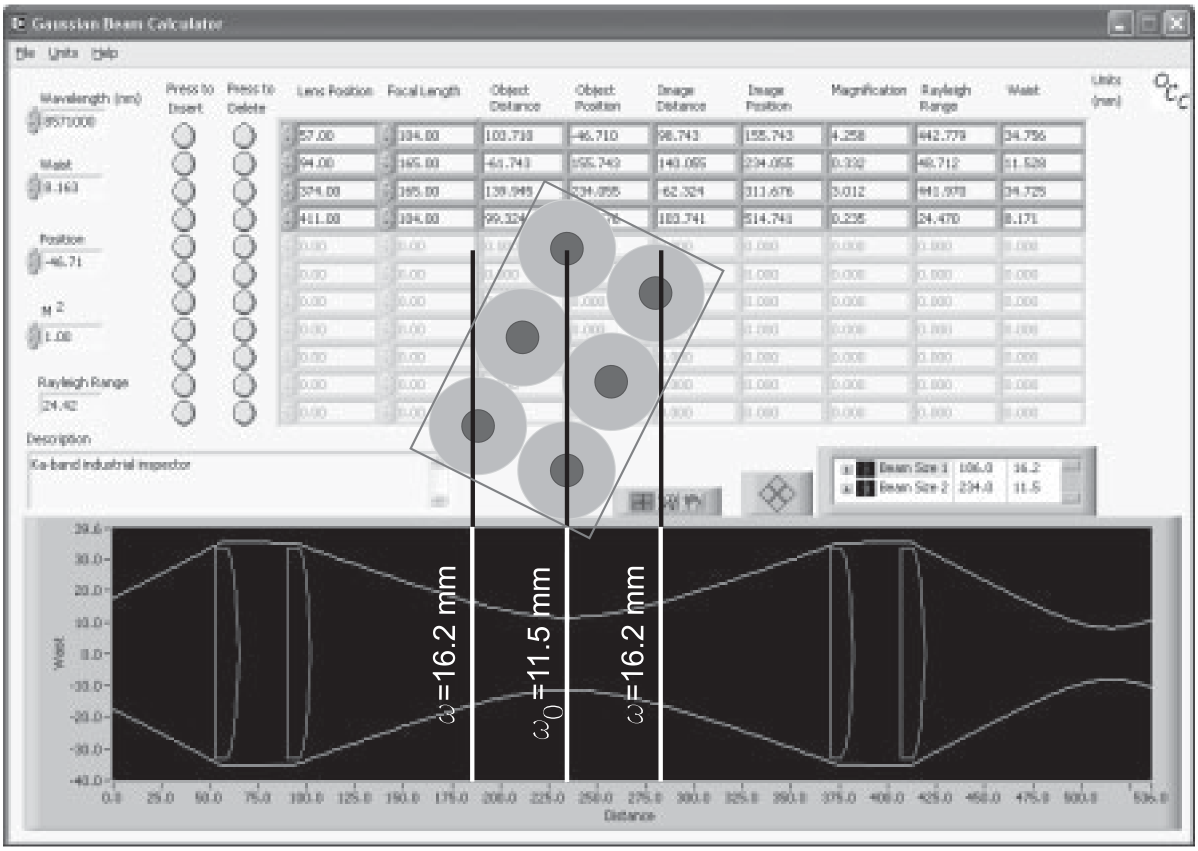

Wavelength (nm): 8571000

Waist: 8.163

Position: -46.71

M 2: 1.00

Rayleigh Range: 24.42

Description: Ka-band industrial inspector

Lens Position	Focal Length	Object Distance	Object Position	Image Distance	Image Position	Magnification	Rayleigh Range	Waist
57.00	104.00	103.710	-46.710	98.743	155.743	4.258	442.779	34.756
94.00	165.00	-61.743	155.743	140.055	234.055	0.332	48.712	11.520
374.00	165.00	139.945	234.055	-62.324	311.676	3.012	441.970	34.725
411.00	104.00	99.324	[illegible]	103.741	514.741	0.235	24.470	8.171

Beam Size 1	106.0	16.2
Beam Size 2	234.0	11.5

Figure 6.3: Simulation of the optical path for the Ka-band industrial inspector.

The analysis of the equation (6.7) leads to the conclusion that for the beam waist given by

$$\omega_0 = \sqrt[4]{N} = \sqrt{\frac{b\lambda}{\pi}} \tag{6.8}$$

the beam size at the distance b has its minimum. Assuming an operation frequency of 35 GHz and distance between the bottles $a = 62$ mm, the beam waist calculated employing equation (6.8) is $\omega_0 = 11.5$ mm. For this value of the beam waist, the beam radius at the distance b equals to $\omega\big|_{b=48.5mm} = 16.3$ mm.

For the design of the optical system, the parameters of the beam exiting the antenna have to be obtained. The beam parameters are defined by the type and the geometrical dimensions of the antennas used. The conical horn antennas (type JXTXYLB-28-20) used in this experiment have a gain of 20 dB. By inserting the antennas' dimensions: aperture diameter $D = 46$ mm and slant length $R_H = 59.4$ mm (refer to section 3.2.1) into equations (3.27) and (3.28) the calculated beam parameters for the frequency $f = 35$ GHz are: $\omega_0 = 8.16$ mm and $z_T = 46.7$ mm. Using the GBC, the optical system is optimized. As presented in Fig. 6.3, using aspherical lenses with focal lengths $F = 104$ mm and $F = 165$ mm, aperture diameter 80 mm, the simulated beam radius in the focus is $\omega_{0sim} = 11.5$ mm, whereas the beam radius at the distance $b = 48.5$ mm from the focus is $\omega\big|_{b=48.5mm} = 16.2$ mm. The distance between the second and the third lens is set to 280 mm to achieve a proper spatial separation between the transmitter and the emitter which is determined by the width of the industrial conveyor belt. The graph 6.3 also includes a sketch of the six-pack. As can be seen, the beam radius within the six-pack is always below 16.2 mm.

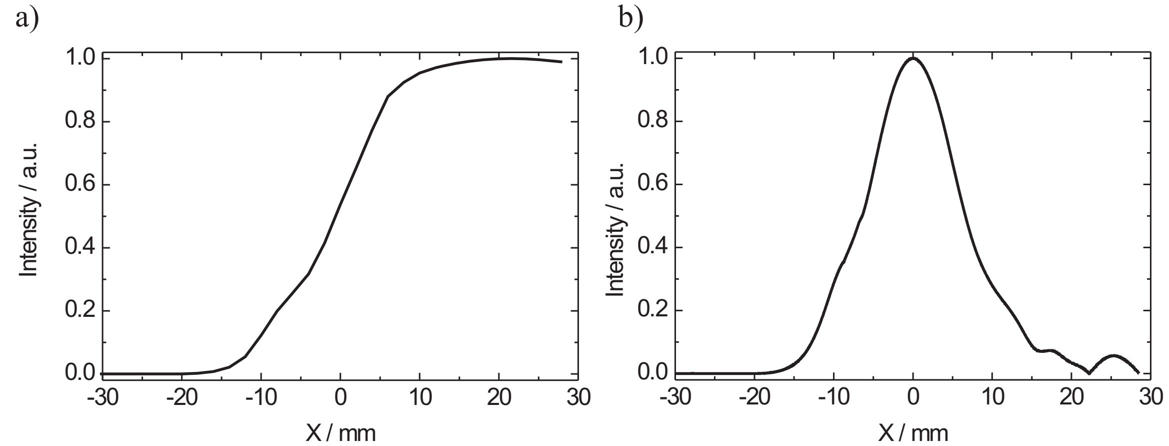

Figure 6.4: Ka-band industrial inspector focus diameter measurement: a) blade measurement characteristics, b) deconvoluted beam profile at the focus.

To validate the calculations and simulations, the beam profile at the focus is measured. For the evaluation of the radius size, a measurement employing the blade edge is performed. The obtained profile is presented in Fig. 6.4 a), whereas the extracted beam profile is depicted in Fig. 6.4 b). Based on the measured beam profile, the beam diameter at the focus is $\omega_{0meas} = 13.0$ mm. Therefore, the beam propagation ratio is $M^2 = 1.13$. The discrepancy between the measured and the simulated value of the beam radius arises due to the relatively big relation of the beam size to the geometrical dimensions of the optical components. As can be seen in Fig. 6.3, the beam diameter of the wave illuminating the second lens is 70 mm. It has to be taken into account that this value is referred to the transversal distance in which the radiation intensity falls to e^{-2} of the initial value. Practically, it means that 90% of the radiation intensity [196] is transferred by the aperture which has the diameter of 70 mm. As a result, the beam leaving the lens does not have a perfect Gaussian shape, as can be seen in Fig. 6.4 b). The profile asymmetry is partially attributed to the imperfect alignment of the optical components.

6.3 Six pack profiles

After getting promising measurements on single bottles, the profile of the six-pack is measured. For this reason, the optical setup presented in Fig. 6.3 is employed. The Gunn oscillator type OGL-28350110-32 operating at the centre frequency of 35 GHz and delivering up to 15 dBm of microwave power is supplied with constant voltage. The broadband Schottky diode detector type DETR-X offering a sensitivity of 3000 mV/mW is connected to a home-made, 12-bit data acquisition board. The six-pack arranged as shown in Fig. 6.2 b) is moved by the translation stage in a plane perpendicular to the optical path. To obtain a reasonable compromise between the measurement time and accuracy a step size of 1 mm is chosen. A personal computer drives the translation stage and stores the data.

In the first step measurements on incomplete six-packs are performed. First of all, the scan height is optimized to achieve maximal contrast between a full bottle and an empty bottle. If the scan height is set too low, the bottles overlap for the screening beam and detection is not possible. On the other hand, if the height is set too high, no information about the filling status can be obtained because of the aluminium foil covering the bottleneck. In this thesis it was

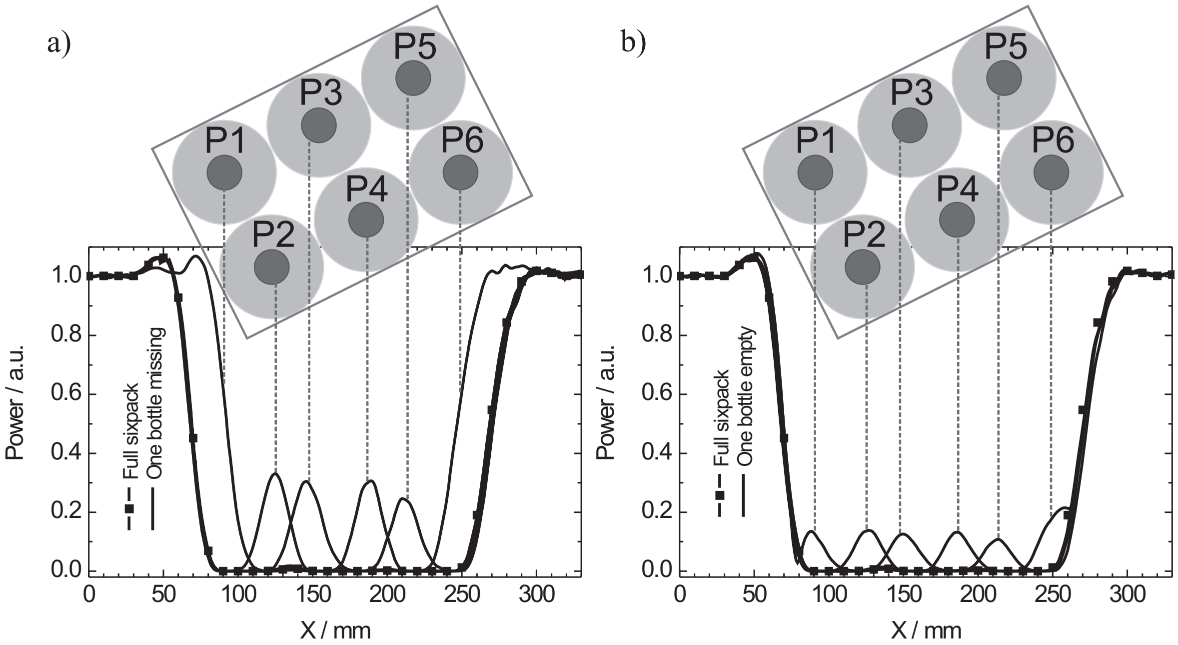

Figure 6.5: One dimensional scans of six pack including a) one missing bottle, b) one empty bottle.

found that the optimum scan height for the 0.33 l beer bottle is 170 mm. The measurement results are depicted in Fig. 6.5 a). In case the six-pack is complete, the millimeter wave signal is totally attenuated for 100 mm $< X <$ 250 mm, as shown in the graph. It is remarkable that for the coordinates $X =$ 45 mm and $X =$ 290 mm the detected signal is increased. Again, this effect can be explained by diffraction of the wave. Figure 6.5 a) also includes the results on the six-pack in which one bottle is missing. The six curves presented in the graph correspond to six measurements. For every measurement, one bottle is removed from its initial position denoted by P1, P2, . . . P6. It is clearly seen that the absence of the bottle leads to an increase of the detected signal. Since bottles 1 and 6 are placed at the edges of the six-pack, their absence corresponds to a considerable signal growth to the initial value. Nevertheless the lack of bottles at the positions P2, P3, P4 and P5 is also clearly noticeable in the graph. Here the signal increase is less pronounced because of the influence of the neighbouring bottles. On average, the signal reaches 30% of the initial intensity. To sum up, the absence of the bottle is pronounced as the increase of the detected signal.
In the second step the possibility of detection of an empty bottle is demonstrated. Therefore, the measurements are repeated; however, this time one empty bottle is placed at the positions P1, P2, . . . P6. The results are depicted in Fig. 6.5 b). Since the absorption of the empty bottle is significantly lower than that of the full one, the detected signal increases at every position at which the empty bottle is placed. Because of the absorption of the microwaves by the glass, the signal increase is not as significant as it was in the case of the missing bottle. However, the average value of the peaks reaches 14% of the initial intensity. This is a significantly higher value than the maximum of the signal measured with a full six-pack, which reaches 1% of the initial value. Therefore, it can be concluded that the evaluated system is capable of detecting the empty bottle.

Analysing the graphs presented in Fig. 6.5 it can be summed up that the absence of the bottle, or the presence of the empty bottle is detectable. Moreover, based on the measurements' results it is possible to find the number of nonconforming parts. Additionally, the position of the faulty part(s) in the six-pack can be obtained.

6.4 Ka-band industrial inspector design

The main parts of the industrial inspector are microwave components described in section 6.3. However, there is a need for a control device, which can make the decision about the six-pack status. Basically, a computer or a microcontroller can be employed. Contemporary microcontrollers offer high calculation power and therefore, they are a good alternative to systems based on the computers. Additionally, systems employing microcontrollers are compact, stand-alone and much more price-attractive. Since the complete, application-oriented firmware for the microcontroller can be written by the designer, this solution is more reliable than software written for the specific operational system of the computer. For these reasons, a control unit of the developed industrial inspector will be based on a microcontroller.

Hardware of the industrial inspector

The main task of the control unit is to digitalize and analyse the signal obtained from the microwave detector. Based on the programmed routines, the control unit has to supply the user with the evaluation results. As an example, if the six-pack contains one or more nonconforming parts, the control unit has to activate the line rejector which removes the six-pack from the conveyor belt. Moreover, information about the number of nonconforming parts and about their positions in the six-pack should be given. Other tasks of the control unit include human interfaces support (keyboard, display) and digital interfacing to the optional external device (e.g. computer).

The key part of the control unit is the microcontroller. It is advantageous if the microcontroller includes a precise Analog-to-Digital Converter (ADC) since it simplifies the design process. Moreover, the microcontroller has to provide the interfaces to the real world. On the one hand, human interfaces like the keyboard and the display are needed. On the other hand, a digital link with other optional external devices is beneficial.

Since the conveyor belt's speed is not constant, the control unit must be capable of measuring the current speed at which the components to be tested travel. For this reason the laser barrier operating at the wavelength 630 nm is employed. To ensure the immunity of the light barrier to the environmental conditions like background or ambient light, the laser current is modulated at a frequency of 180 kHz. The detector circuit following the photodiode is tuned to the centre frequency of the transmitter. Therefore, the influence of the external light sources is minimized. Since the length of the component travelling on the conveyor belt is known, the actual speed can be calculated from the time period in which the laser beam is blocked by the moving part.

It has been stated that contemporary 8-bit microcontrollers can fulfil the given requirements for the control unit. From the giant 8-bit microcontrollers family, a model ADuC842 based on the 8052 core manufactured by Analog Devices is chosen. The core of the microcontroller runs at a frequency of 16.8 MHz. The microcontroller is supplied with an 8-channel ADC running

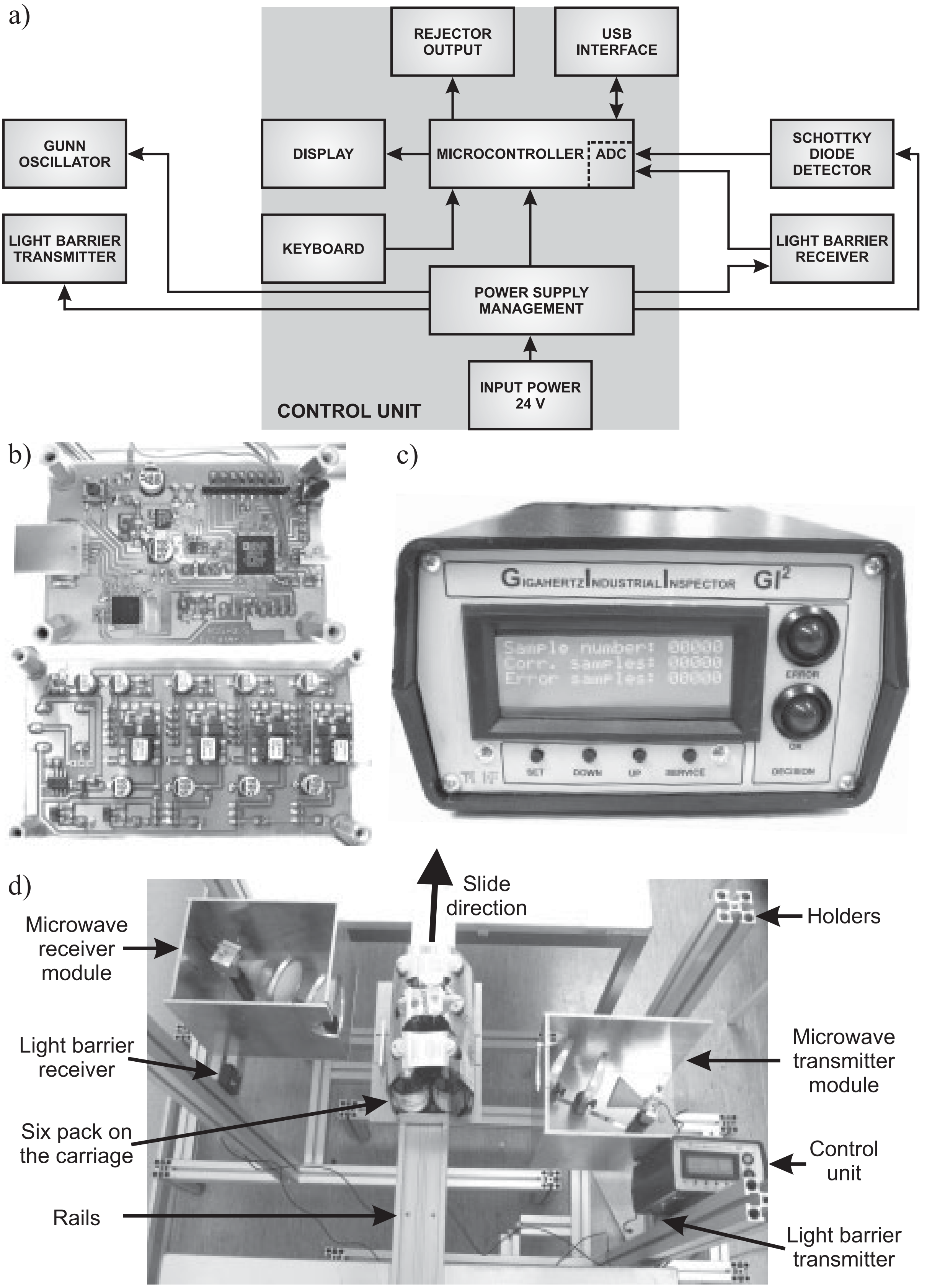

Figure 6.6: The hardware of the Ka-band industrial inspector: a) block diagram, b) a photograph of the microcontroller board and the power management system, c) a photograph of the control unit, d) a photograph of the complete system during the six-pack scan.

at the maximum speed of 420 kilo samples per second (kSPS), and two Digital-to-Analog Converters (DACs). The capacity of the program memory is 62 kB, the RAM is 2304 B and the non-volatile memory is 4 kB. The device is supplied with four 8-bit parallel ports and interfaces including Universal Asynchronous Receiver and Transmitter (UART), Inter-Integrated Circuit (I^2C) and Serial Peripheral Interface (SPI). The chosen microcontroller can be programmed in target system using UART, which extends the design flexibility. Using an external integrated circuit FT232BL, a translation from UART into the Universal Serial Bus (USB) 2.0 full speed protocol is assured. As a result, the programming of the microcontroller as well as the interfacing to the optional external device is performed over the USB link. The block diagram of the Ka-band industrial inspector hardware is shown in Fig. 6.6 a). The power management supplies all the components with appropriate voltages. In order to increase the efficiency of the power conversion, hybrid power modules manufactured by Texas Instruments are employed. The microcontroller acquires the analogue signals from the microwave detector and the light barrier detector. The six-pack evaluation results are presented on the display. If a nonconforming part is detected, a signal to the rejector is sent. Additionally, the data including the number of missing or empty bottles and their positions are transferred over the USB link to the computer. In the current version of the firmware, the microcontroller is capable of storing the measurement data of 99999 items. The number of conforming and nonconforming six-packs is presented on the display. Using the keyboard, these values can be re-set if necessary. The keyboard can also be used to input the parameters for the detection routine described in the following subsection. Figures 6.6 b) and c) present the photographs of the control unit.

In order to be able to perform the tests of the industrial inspector, the housing and holders are built. In the design stage two options of the holders were considered: holders attached to the conveyor belt and stand-alone holders. Generally, it is easier to fabricate the former type. However, the observations made in a real industrial conditions have lead to the conclusion that the vibrations originating from the belt movement can cause permanent misaligning of the microwave scanning path. Additionally, the amplitude of the vibrations can affect the proper functioning of the light barrier. For these reasons, stand-alone holders based on the profiles manufactured by MiniTec are built. The employed aluminium profiles offer high flexibility for different applications, since the height and the separation between the transmitter and the receiver can be easily adjusted. Additionally, this solution offers easy integration with existing conveyor belts. To ensure faultless operation of the microwave components in a harsh industrial environment, housings made of aluminium are fabricated. The additional function of housing is protection against the misalignment of the system. A photograph of the complete Ka-band industrial inspector during the six-pack scan in the laboratory is shown in Fig. 6.6 d). In order to perform laboratory measurements, a manually-driven conveyor belt model based on the linear slide system manufactured by Igus is employed. By using dedicated rails and carriage, the target velocity of 3 m/s of the six-packs can be obtained.

Firmware for the industrial inspector

Typical signals measured in X-coordinate domain of the full six-pack, the six-pack with empty or missing bottles have been presented in Fig. 6.5. In section 6.3 it is concluded that the absence

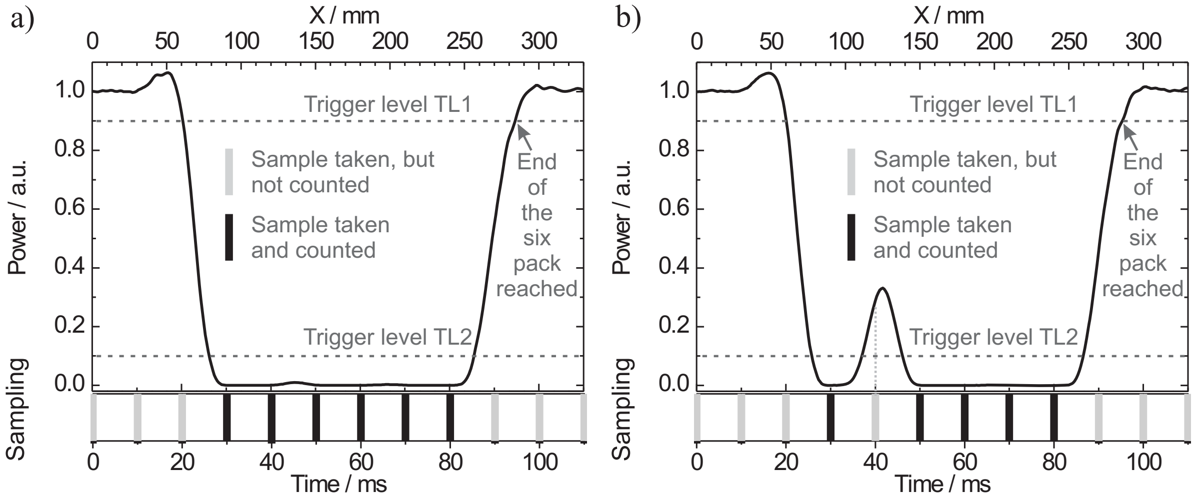

Figure 6.7: The detection routine of the Ka-band industrial imager: a) complete six-pack, b) incomplete six-pack.

of the bottle or the presence of the empty bottle contributes to the microwave signal increase.

In the following subsection, the detection routine will be explained. Figure 6.7 presents again the signal given by the full six-pack (a), and obtained from the six-pack in which the bottle at the position P3 is missing (b). In the first step, the maximum level of the microwave signal is measured after powering on the system. This value is stored as a reference value. For the detection routine, two trigger levels are set. The first trigger lever (TL1) is set at 90% of the reference value. The value of the second trigger level (TL2) is a variable and it can be set in a range from 0% to 20% of the reference value with a resolution of 0.1%. The microwave signal rectified by the Schottky diode detector is sampled continuously by the ADC at the speed of 1 kSPS. As soon as the signal drops to the value given by the TL2, the number of samples, whose values are below TL2, are counted. In contrast, the samples whose value is greater than TL2 are ignored. Finally, the counting process ends if the value TL1 is exceeded, which corresponds to the situation in which the six-pack leaves the scanning beam. For the sake of clarity the sampling speed is reduced to 100 SPS in Fig. 6.7. In this example the level TL2 is set to 10%. The bottom axis of the graph presents the time domain. The values on the time axis correspond to the conveyor speed of 3 m/s. As can be seen in case the six-pack is complete, the number of counted samples is 6. In contrast, if one bottle is missing, 5 samples are counted. In order to make the detection algorithm insensitive to the speed of the conveyor belt, the number of counted samples is divided by the time needed to screen a single six-pack. The required time period is obtained directly from the duration at which the photodiode is not illuminated by the laser. As a result of division, a new parameter called the factor is obtained. It is clear that the factor will have lower values for the six-packs in which a bigger number of bottles is missing or empty. Therefore, by evaluating the factor value, the information about the number of nonconforming parts can be obtained.

By testing the time periods for which the detected signal exceeds the TL2 the position of faulty elements in the six-pack can be determined. In the current version of the firmware a variable set-point is implemented and it is subtracted from the factor. If the subtraction result is positive, the six-pack is classified as full. Otherwise, a negative value corresponds to incomplete six-pack content. The described detection routine is implemented in C programming language. For the correct functioning of the system, a careful setting of the level TL2 and the set-point is necessary.

6.5 Measurement results

This section describes the measurement results on 0.33 litre beer bottles packaged in the six-pack, which were obtained with the Ka-band industrial inspector. After alignment of the microwave and the laser path, the level TL2 (refer to section 6.4) is optimized. Based on 20 measurements on the full six-pack the TL2 is set to a value which is higher than any of the measured signals in the time period 25 ms $< t <$85 ms (refer to Fig. 6.7). For all measurements presented here TL2 = 1.1%. In the following subsections the results on a six-pack with a single missing and single empty bottle will be presented. Additionally, the measurement results on a greater number of missing bottles will be shown.

Measurements on the six-packs with a missing bottle

The measurements are conducted in the configuration depicted in Fig. 6.6 d). In the first step, a complete six-pack is measured. Further, one bottle is removed from the six-pack. In order to check the system sensitivity to the absence of the bottle at the arbitrary position, the bottles are removed from one position P1, P2, . . . P6 for every measurement. To ensure proper adjustment and proper operation of the inspector, as well as to check the system reproducibility, each of the 7 configurations is measured 20 times. Every graph presented in Fig. 6.8 a) - f) depicts the count number (frequency) of the particular factor plotted on the horizontal axis for the full six-pack and the six-pack without one bottle at the corresponding position. Figure 6.8 g) summarizes all results presented in the former graphs.

Analysing the measurement results, it is remarkable that the factors of the complete six-pack are significantly higher than the case in which one bottle is missing. It is noticeable that no factor value representing the full six-pack is lower than the highest value obtained for the nonconforming six-pack. By setting the set-point to 716, a correct evaluation of the six-pack content can be ensured, since the factor of the conforming package is always greater than the set-point value.

Measurements on the six-packs containing one empty bottle

To check the ability of the industrial inspector to detect empty bottles, the measurement scenario described in the previous subsection is repeated. Here, one empty bottle is placed at one of the positions P1, P2, . . . P6 for every measurement. The graphs 6.9 a) - f) show the results obtained for the corresponding positions, at which the empty bottle is placed. Also in this case, the measurements are repeated 20 times for every position, at which the empty bottle is put. Figure 6.9 g) summarizes all results. Again it is notable that the factors of nonconforming

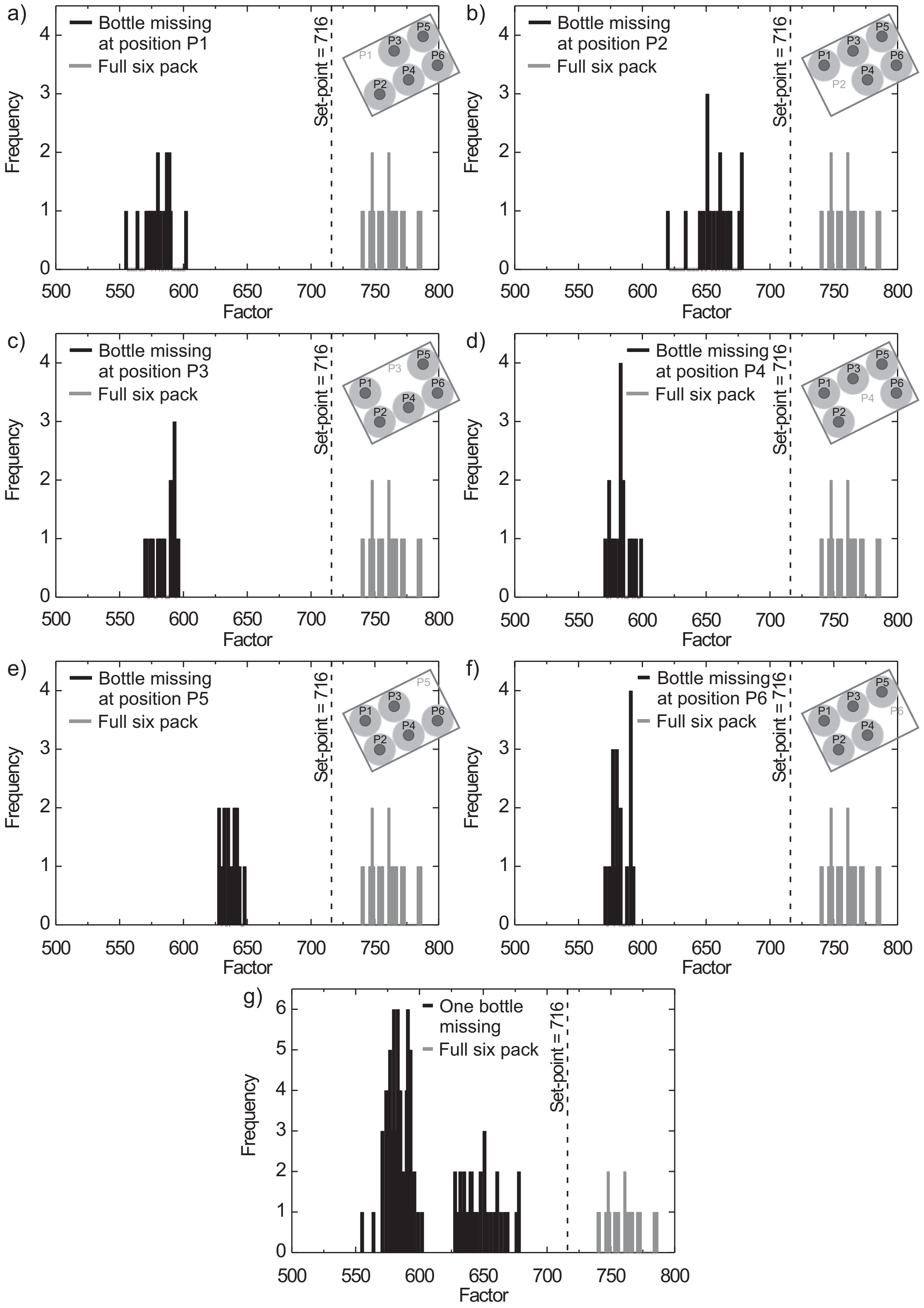

Figure 6.8: The detection of one missing bottle in the six-pack. Graphs a) … f) present the results obtained for corresponding positions at which the bottle is missing. Graph g) encloses all results presented in Figures a) … f).

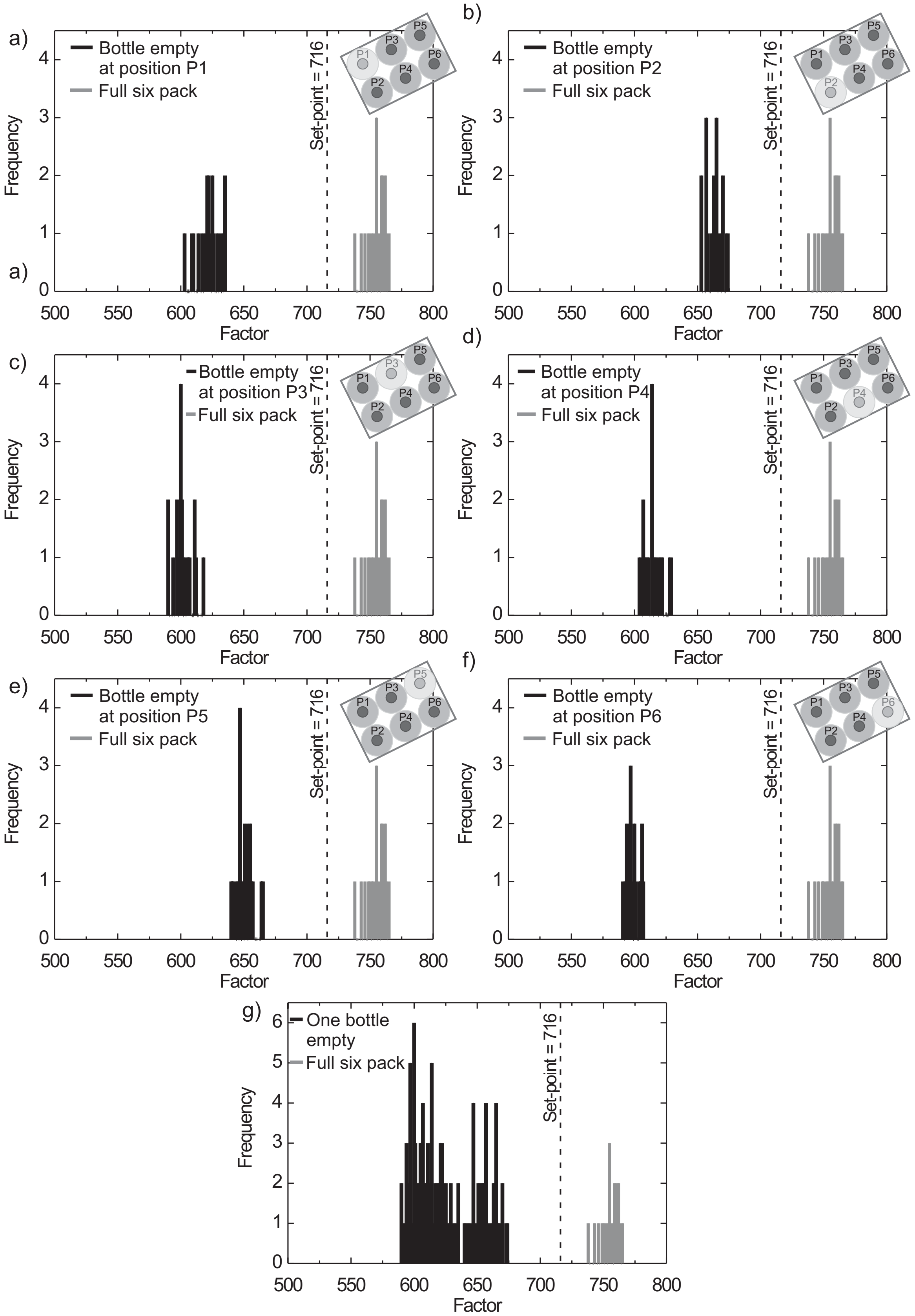

Figure 6.9: The detection of one empty bottle in the six-pack. Graphs a) . . . f) depicts the measurmenet results for the positions at which the empty bottle is placed. Graph g) encloses all results presented in Figures a) . . . f).

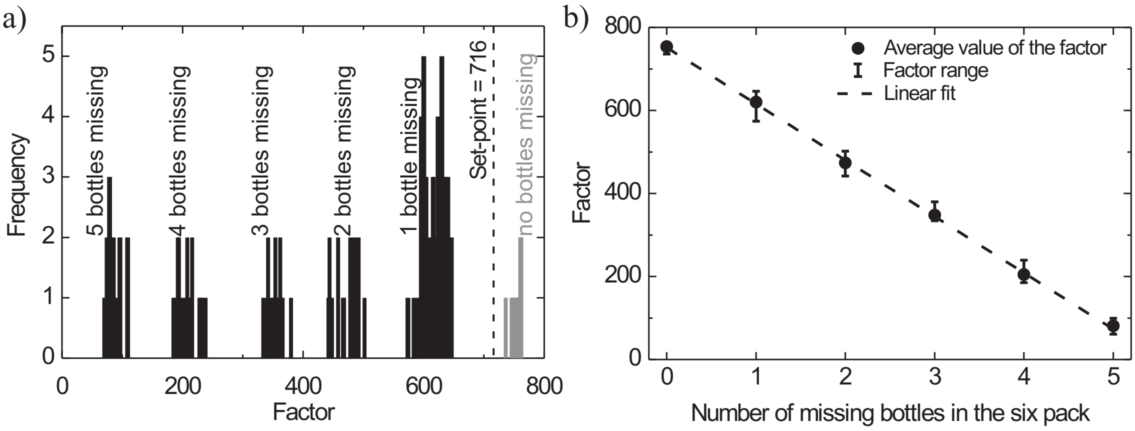

Figure 6.10: The detection of number of bottles missing in the six-pack.

packages are lower than those of the full six-pack. By setting the set-point value to 716, the nonconforming six-packs can be separated from the conforming ones.

Measurements on the six-packs containing missing bottles

As shown, using the Ka-band industrial inspector, the position of the missing and empty bottle can be determined. In this subsection the tests on the greater number of missing bottles will be described. The measurement results are presented in Fig. 6.10 a). In the first step, 10 measurements on the full six-pack are conducted. Then a bottle is removed. Here, the factors at all six possible places in the six-pack are tested. For every configuration, 10 measurements are performed. In the third step, two bottles are removed from the six-pack. Because of the big number of possible combinations, two of them are chosen and are measured. In the next steps, three, four and five bottles are removed from the pack. For every number of missing bottles, two random positions of missing bottles are chosen. As can be seen in Fig. 6.10 a) for every specific number of missing bottles a factor range can be defined. It is also noticeable that the factors of neighbouring constellations do not overlap. Therefore, a reliable determination of the number of missing bottles is achieved by observing the factor value. Figure 6.10 b) presents the average value of the factor for the corresponding number of bottles which are absent in the six-pack. Additionally, the error bars present the factor range for every number of missing bottles. The dashed line presents the linear fit based on the factor's average values.

6.6 Conclusions

This section presents the design of the 35 GHz, Ka-band industrial inspector. In particular the design of the hardware and the firmware principles is discussed. The inspector is optimized for the quality and completeness testing of the opaque-to-visible light beverage containers. The developed system offers safe, non-ionising screening of the products. Its spatial resolution is sufficient to determine the positions of the nonconforming bottle in the six-pack. Based on the series of measurements, it has been proven that the inspector detects missing bottles as well as empty bottles. Additionally, the system identifies the number of bottles which are missing.

This gives the user full information about the nonconforming drink bottles. By analysing the results supplied by the inspector, the positions which have the highest error ratio can be determined. This is valuable information for the optimization of the fabrication plants. The presented evaluation method is contact-free and nondestructive. The system can be integrated with most types of contemporary conveyor belts. In the end, it has to be emphasized that the price of the Ka-band industrial inspector is significantly lower than that of other competitive industrial screening systems.

The developed industrial inspector was successfully tested in a real industrial environment. The tests conducted in one of the German breweries on 0.33 l six-packs have proven the system's feasibility for the detection of the nonconforming drink containers.

7 Towards a MMIC-based GI^2 Gigahertz Industrial Inspector

After the promising results obtained with the Ka-band industrial inspector, a new design based on a different generation and detection approach is developed. The Ka-band industrial inspector which was described in chapter 6 is based on commercially available millimeter wave components like oscillator, detector and horn antennas. In order to achieve a further integration of the microwave path, the transmitter and the receiver are newly designed employing MMICs. Additionally, new antennas are calculated and fabricated by the mechanical workshop of our institute. The new approach contributes to the cost reduction of the system, which is a critical issue in the current economical situation.

Figure 7.1 presents the block diagram of the new system. The MMICs are used for the excitation and for the detection of the millimeter waves. Signals propagating in the planar structures have to be transformed into the waveguide elements. This can be accomplished by using a microstrip-to-rectangular waveguide transition. Finally, for the coupling of signals to free space, horn antennas are used.

In the following subsections the design of the components building the home-made Ka-band transmitter and receiver will be presented. Furthermore, the results on the completeness testing in the food industry with the Gigahertz Industrial Inspector (GI^2) will be shown.

7.1 Microstrip to waveguide transition design

The practical employment of MMICs requires the use of planar technology. However, horn antennas, which offer high gain at low HPBW, involve the use of waveguide technology. Therefore, in order to combine required horn antenna's parameters with MMICs, a transition between planar and waveguide technology is designed.

A number of microstrip-to-waveguide transitions is described in the literature. Existing solutions can be divided into two groups. The first group includes the transitions fabricated in planar

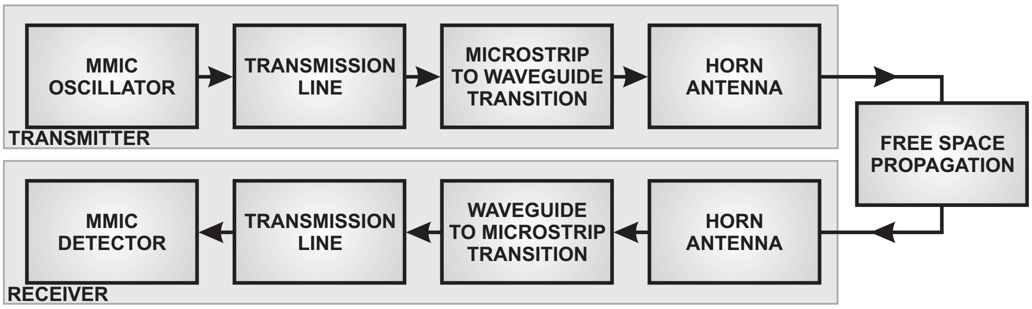

Figure 7.1: Gigahertz industrial inspector block diagram.

technology. Three-dimensional structures are representatives of the second group. Published solutions belonging to the latter group include ridged waveguides, microstrip and coaxial probe transitions, or antipodal fin line structures. The transitions based on the ridged structures use transformers that have a variable height [219]. Other approaches employ microstrip [220] or coaxial probes [221] to achieve energy coupling into the waveguide. The practical realisations use printed circuits board inserted into the waveguide along the E-plane. Finally, the transition can be realized as a tapered transmission line with coupled resonant circuits [222]. However, all the approaches presented so far require complicated mechanical processing of the waveguides. In contrast, transitions based on the planar structures are easy to fabricate, since standard and mature photolithography techniques can be employed. Among such approaches, transitions based on slot-fed microstrip antennas are the most common. Here, the coupling between the microstrip and the waveguide is assured through a slot in the ground plane. To enhance the coupling characteristics, an additional patch antenna can be used inside the waveguide [223]. However, this solution requires an additional layer, which complicates the fabrication process. The transition presented in [224] is based on a single layer dielectric substrate, but through holes are needed. In order to ease the fabrication procedure, the structure should be produced in one dielectric substrate, whereas the vertical interconnect access technology should be avoided. These requirements are fulfilled by the transition proposed in [225]. Therefore this design will be adapted to the Ka-band.

Prior to the transition design, a substrate is chosen. Here, the following aspects have to be considered: a) dielectric losses, b) mechanical properties, and c) thickness of the substrate. It is obvious that the dielectric losses have to be minimized. Therefore a low loss substrate, Rogers RO3003 which has a dissipation factor of $\tan\delta = 0.0013$ at 10 GHz is well suited for the Ka-band. However, it was shown in [191] that another substrate, Rogers RO4003C, can also be successfully employed in the Ka-band, since the dissipation factor does not exceed $\tan\delta = 0.004$ for frequencies below 94 GHz, while the dielectric constant meets the specification given by the manufacturer over an extended frequency range. The mechanical properties of the substrate have to allow for easy processing. In particular, it is advantageous if the substrate is not too fragile as it eliminates the risk of breaking during the mechanical processing. Finally, the thickness of the substrate has to be minimized, since it reduces insertion losses of the transition. Based on the trade-off between criteria discussed above, a 203 µm thick RO4003C substrate is chosen. The dielectric constant used for the design is $\epsilon_r = 3.55$, whereas the conductor thickness is 17.5 µm at each side of the dielectric.

The transition is presented in Fig. 7.2. The principle of operation is the wave coupling between the microstrip and the waveguide employing a slot in the ground plane. In order to maintain the compatibility with standard microwave components operating in Ka-band, typical dimensions of the waveguide WR-28 are adapted for the transition design. The top layer of the transition includes the microstrip and the radial stub. The role of the radial stub is to enhance the bandwidth. Even though the GI^2 is supposed to work at a single frequency, a broadband transition is beneficial, since the final frequency of the MMIC oscillator can be tuned in a wider range. Additionally, the wideband structure is less sensitive to fabrication errors. The ground plane of the transition is connected with the waveguide. To enable the coupling, a slot is etched into the ground plane. By introducing the H-shaped structure instead of a simple slot, the band-

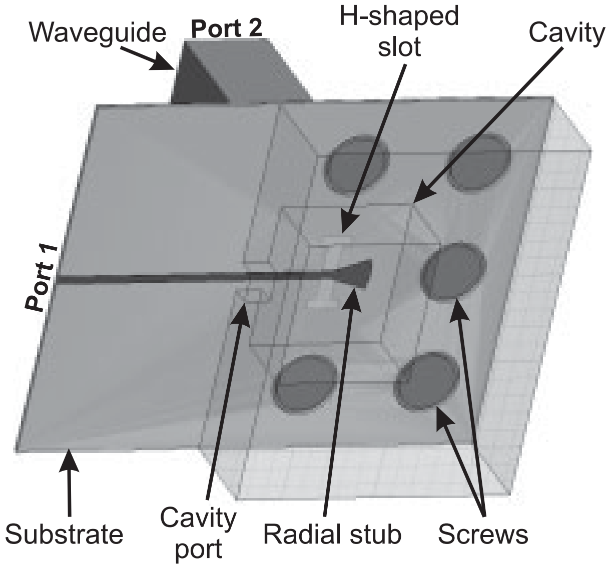

Microstrip width:	0.41 mm
Stub radius:	2.81 mm
Stub open angle:	35°
Slot length:	4.20 mm
Slot width:	0.84 mm
Cavity length:	8.0 mm
Cavity width:	7.2 mm
Cavity height:	3.8 mm
Cavity port width:	1.6 mm
Cavity port height:	1.1 mm

Figure 7.2: Ka-band transition and the optimised parameters.

width of the transition can be broadened [225]. In order to avoid losses which could appear as a result of energy radiation in the direction opposite to the waveguide, a cavity presented in Fig. 7.2 is employed. For the material of the waveguide and the cavity, brass is chosen. The width of the microstrip is tuned to achieve 50Ω characteristic impedance. For the calculations of the microstrip line, the Agilent Technologies AppCAD software is employed.

The design is verified with 3-D full-wave electromagnetic field simulator Ansoft High Frequency Structural Simulator (HFSS). Using HFSS, the complete structure is optimised for the frequency $f = 38.25$ GHz. The choice of the design frequency will be discussed in section 7.3. In the first step, the radius of the stub and the length of the slot are tuned to meet the design frequency. Then, other parameters of the H-shaped slot are optimised for the target frequency. In the final step, the cavity parameters are tuned for the optimal performance of the transition. The final parameters which characterise the designed transition are presented in Fig. 7.2. The simulated scattering parameters are shown in Fig. 7.3. The insertion loss for the design fre-

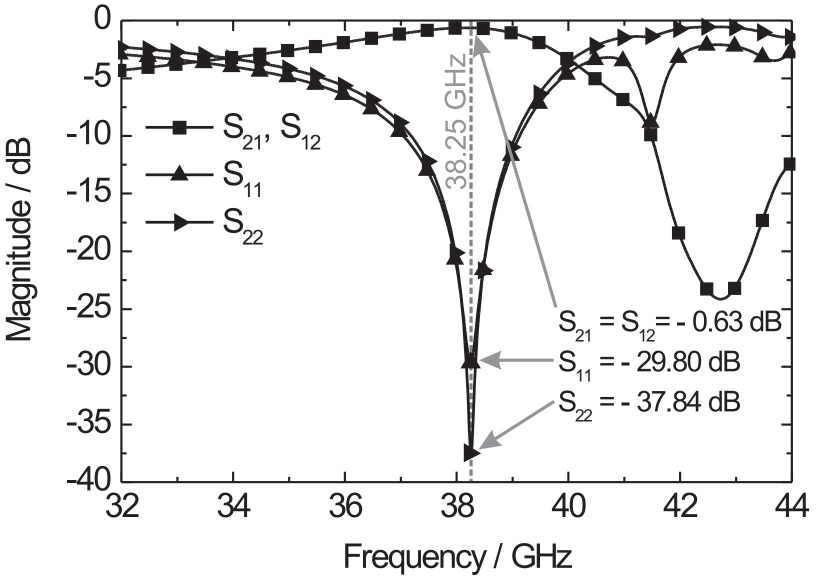

Figure 7.3: Simulation results of the Ka-band transition.

quency is 0.63 dB. The return loss seen from the planar structure is $S_{11} =$ -29.80 dB. The return loss seen from the waveguide port is as low as $S_{22} =$ -37.84 dB.

The structure is fabricated using a standard photolithography process. To compensate for over-etching the structure's dimensions were oversized. However, this procedure does not remove the fabrication errors completely, since the etching process is not 100% reproducible. Therefore, a bigger number of transitions was fabricated and every structure was measured under the microscope. The obtained results are inserted again to the simulation as parameters. Based on the simulation results, two structures which have the best overlap with the initial design were selected for the GI^2. However, actual parameters of the fabricated transitions could not be measured because of the lack of instrumentation.

7.2 Rectangular horn antenna design

To achieve efficient radiation of energy in the desired direction, horn antennas are used. Since the machining of the rectangular horn is much easier than of the conical one, in the following section the design of the rectangular horn antenna will be presented.

In the construction of horn antennas a compromise between the gain and the antenna size has to be found, since high gain antennas require high volumes. For the design of the GI^2 it is estimated that a 22 dB gain antenna will fulfil the system requirements. The centre frequency of the antenna has to be 38.25 GHz. In order to achieve a symmetric beam for which the beam sizes in the E-plane and H-plane are equal, the quadratic phase distributions S_E in the E-plane and S_H in the H-plane have to be set to $S_E =$ 0.26 and $S_H =$ 0.40 [226]. It was shown in [226] that in case that the -3dB beamwidths in both planes are equal, then $B/A =$ 0.68, where B is the aperture size in the E-plane and A denotes the aperture size in the H-plane. Based on the equations presented in [226], the aperture sizes are determined by the gain and wavelength as shown:

$$\frac{A}{\lambda} = 0.489\sqrt{G}, \tag{7.1}$$

$$\frac{B}{\lambda} = 0.332\sqrt{G}. \tag{7.2}$$

Inserting the known variables into equations (7.1, 7.2), following geometrical dimensions of the antenna are obtained: $A =$ 48.3 mm and $B =$ 32.8 mm. The slant radii R_E in the E-plane and R_H in the H-plane can be estimated from [226]:

$$\frac{R_H}{\lambda} = 0.0746G, \tag{7.3}$$

$$\frac{R_E}{\lambda} = 0.0531G. \tag{7.4}$$

After inserting the wavelength and gain into the above equations yields $R_H =$ 92.7 mm and $R_E =$ 87.2 mm. The distance L which is measured between the waveguide and the aperture (see Fig. 7.4 for the details) can be written as:

$$L = \frac{A-a}{A}\sqrt{R_H^2 - \frac{A^2}{4}}, \tag{7.5}$$

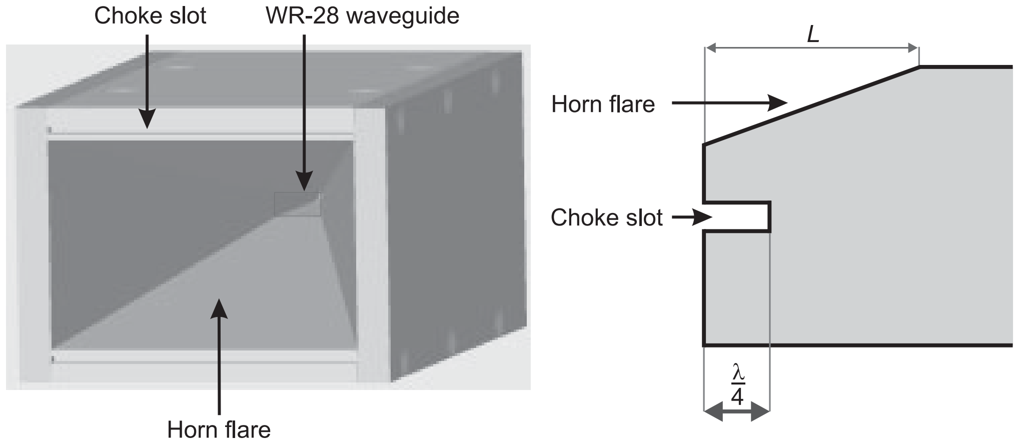

Figure 7.4: The design of the rectangular horn antenna.

where a is the longer wall of the waveguide. For the designed antenna $L = 76.3$ mm. However, for the obtained parameters, the calculated gain is $G = 22.43$ dB. Therefore, a second iteration process with a new temporary gain $G_T = 21.55$ dB was conducted. Following the presented scheme, the final dimensions of the antenna are obtained: $A = 45.9$ mm, $B = 31.2$ mm, $L = 68.1$ mm, $R_H = 83.8$ mm, $R_E = 78.5$ mm, $G = 22$ dB.

Since the wall thickness is 5 mm for the designed antenna, diffraction effects at the outer edges of the wall may appear. In order to minimize this undesirable phenomenon, a choke slot depicted in Fig. 7.4 can be employed [227]. The choke acts as an open circuit at the design frequency; therefore, the current flow at the outer edge is stopped.

As shown in Fig. 7.4, the antenna design includes a waveguide section in its structure. This enables for a direct mounting of the transition at the opposite side of the antenna. Therefore, a high degree of integration is obtained.

The antenna design is verified in HFSS. The obtained beam patterns are presented in Fig. 7.5 a) and b). Figure 7.5 a) presents the radiation patterns in the E- and H-plane. The -3dB beamwidths are equal and the simulated gain is $G_{simulated} = 22$ dB. Figure 7.5 b) presents the effect of the choke slot. Comparing the results obtained with and without the choke it can be concluded, that choke somewhat decreases the level of the side lobes.

The antennas were fabricated by the mechanical workshop of the institute. As material, brass is employed. In order to verify the simulation results, the measurement of the antenna

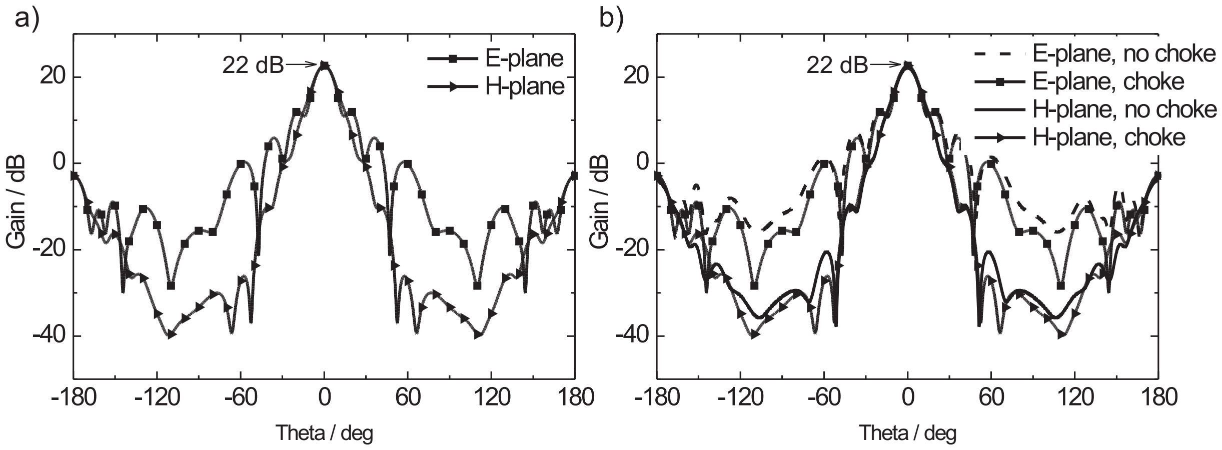

Figure 7.5: Simulated radiation patterns of the designed horn antenna.

gains based on a three-antenna gain measurement method is performed. For the measurement, three horn antennas with unknown gains, an oscillator and a detector are employed. Two antennas having gains G_1 and G_2 will be used in GI^2, whereas the third antenna with the gain G_3 is the commercially available model JXTXYLB-28-20. Using three antennas, three configurations employing a pair of antennas are built. For each configuration, the total gain of the pair of antennas, G_{12}, G_{13}, and G_{23} is measured. Based on the equation (2.15), under assumption the transmitter power is $P_{TdBm} = 15$ dBm, simultaneous equations can be written:

$$\begin{cases} 61.92\text{ dB} = 25.12\text{ dB} + G_1 + G_2 \\ 61.92\text{ dB} = 22.70\text{ dB} + G_1 + G_3 \\ 62.01\text{ dB} = 23.45\text{ dB} + G_2 + G_3 \end{cases} . \tag{7.6}$$

After solving, the gains of the individual antennas yield $G_1 = 18.73$ dB, $G_2 = 18.07$ dB, and $G_3 = 20.50$ dB. It is noticeable that the measured gain of the fabricated antennas is lower by approximately 3.5 dB comparing with the design values. The discrepancy emerges mainly from non a perfect fabrication quality. Additionally, the antenna walls were fabricated as separate parts. This has negative effect on the conductivity of the antenna. However, as it will be shown in subchapter 7.5, the fabricated horn antennas have sufficient gain for the application in the industrial inspector.

7.3 Monolithic microwave integrated circuits

Monolithic microwave integrated circuits (MMICs) offer a high design flexibility in the development of microwave circuits at relatively low cost. Compared to solutions based on waveguide technology, MMICs are more reliable and more compact.

Currently, MMIC integrated oscillators are available from several manufacturers including Eudyna, Hittite, Mimix and United Monolithic Semiconductors (UMS). The requirements for the GI^2 oscillator are: centre frequency $\sim$35 GHz, output power $\sim$10 dBm. Based on the products spectrum and the components availability from the manufacturers, the model CHV2243a produced by UMS is chosen. The centre frequency is 38.25 GHz and it can be tuned by $\pm$1.5 GHz. The typical output power is 8 dBm. The advantage of this oscillator is the fact, that it generates directly the target frequency. Therefore, no additional mixers complicating the design are required. The only components that are necessary are standard single layer capacitors (SLCs) which decouple the power supply lines as well as the tuning input of the oscillator. After the design of the power supply for the oscillator, a chip is integrated with the substrate. Generally, two techniques exist for mounting of MMICs. The direct placing of MMIC on a substrate simplifies the fabrication. However, the length of the bond wires is increased because of the height difference between the chip surface and the substrate. Since long bond connections have negative influence on the system performance at millimeter wave frequencies, a second technique based on the mounting the MMIC in the cavity is employed. In this method, the chip is placed in the cavity, which is cut in the substrate. In order to equalize the height of the substrate and that of the chip, a 100 µm thick socket made of molybdenum is employed. To assure appropriate mechanical and electrical properties of the connection between the brass carrier, the socket and the MMIC, a dedicated conducting epoxy glue Epo-Tek H20E is used. A photograph of the

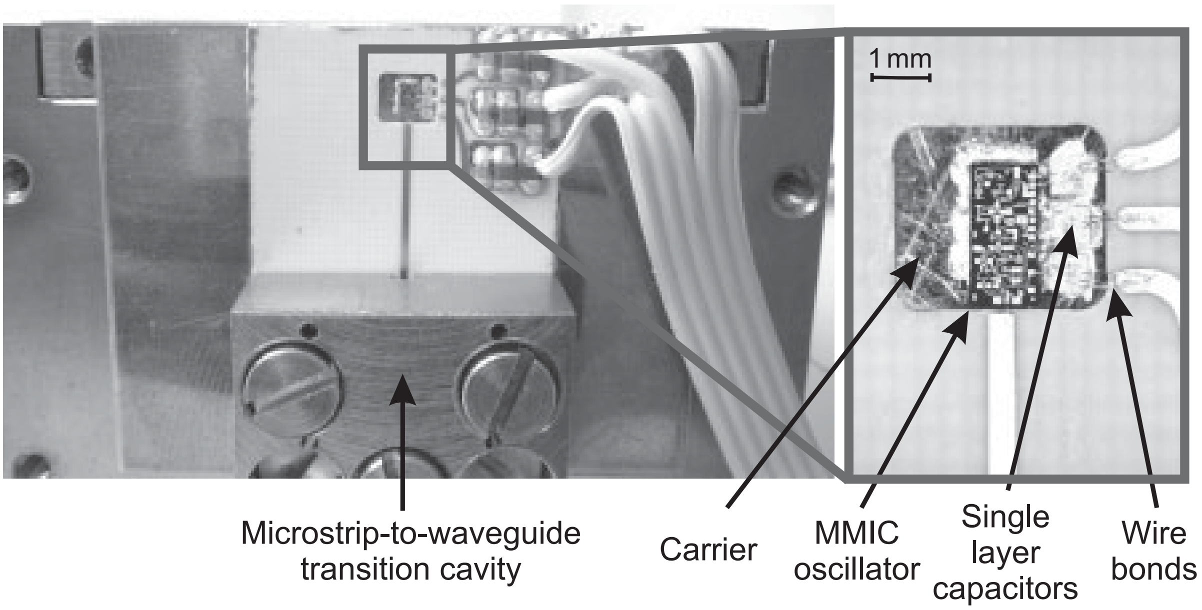

Figure 7.6: GI^2 transmitter.

oscillator chip mounted in the cavity is presented in Fig. 7.6. The main figure presents the back of the developed horn antenna including the microstrip-to-waveguide transition.

The GI^2 receiver is based on a wideband detector CHE1270a fabricated by UMS. The detector employs a matched detection diode and a reference diode to be used in differential mode. The MMIC is specified for the frequency range from 12 GHz to 40 GHz and it is capable to detect microwave signals that have power levels between -15 dBm and 15 dBm. To assure proper operation of the transmitter and the receiver, the power budget calculation based on equation (2.16) is performed. For the calculation of free space losses, the distance of 700 mm between the transmitter and the receiver is assumed. Including transition losses $L_{RdB} = L_{TdB} = 1$ dB, and the minimum power level that can be generated by the oscillator $P_{RdBm} = 4$ dBm, the calculated power at the receiver is $P_{RdBm} = -22.2$ dBm. Given the measured gain of the lenses $G_{Lens} = 9.4$ dB, the expected power at the detector is $P_{RdBm} = -12.8$ dBm. Since this value is only marginally higher than the minimum detectable signal of the detector chip, the use of an additional high frequency amplifier is required. In order to obtain maximum design flexibility of the receiver, a variable gain amplifier is employed. From a group of MMIC amplifiers, a chip with high maximal gain and low noise figure is chosen. The gain of the amplifier CHA2294 manufactured by UMS can be tuned in the range from 0 dB to 24 dB by the control voltage, whereas the noise figure does not exceed 4 dB. Since high gain amplifiers employ a bigger number of amplification stages, an advanced power supply incorporating two fixed and three variable output voltages had to be developed. Figure 7.7 presents the receiver module which incorporates the amplifier and the detector mounted in the cavities, as well as the waveguide-to-microstrip transition.

After the assembling of the transmitter and receiver module and separating them by the distance 700 mm, the detected signal is measured. The DC-component at the MMIC detector is 600 mV, which corresponds to the input power $P_{Rdet} = 7$ dBm according to the detector calibration characteristics. Therefore it can be calculated, that the amplifier gain G_{Amp} is $G_{Amp} = P_{Rdet} - P_{RdBm} = 19.8$ dB. Additionally the noise is measured. Based on the measure-

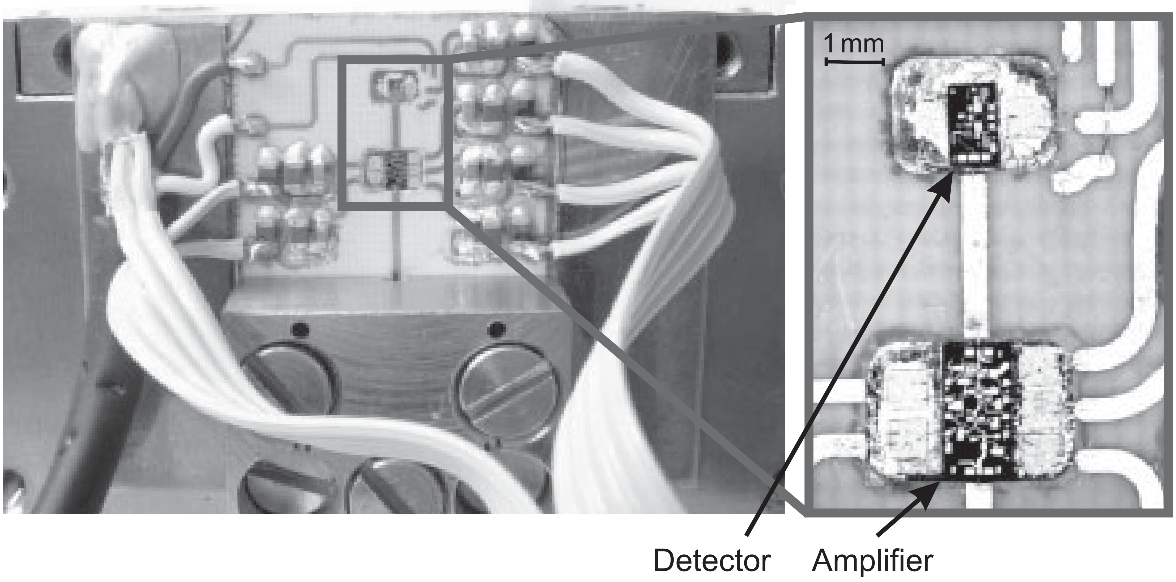

Figure 7.7: GI^2 receiver.

ments it can be concluded that the system dynamics exceeds 20 dB, which is sufficient for the industrial testing applications.

7.4 GI^2 design

After the design of the transitions, antennas and the MMIC assembly, the optical path of the GI^2 is optimised. In the first step, beam parameters are calculated. For this purpose, a set of equations (3.27, 3.28) is employed. However, since the maximum coupling efficiency of the fundamental mode to a Gaussian beam with beam waist ω_0 is achieved for $\omega = 0.175D$ in the case of rectangular antennas [196], the equations are correspondingly modified. Finally, the obtained beam parameters are $\omega_0 = 7.8$ mm and $z_T = 8.7$ mm. Since the GI^2 is optimized for scanning of the sausage bars presented in Fig. 7.8 a), it is advantageous that the beam diameter does not exceed the diameter of a single bar to be scanned. As presented in the photograph, one complete package contains 24 bars arranged in four rows and six columns. Since the diameter of the bar is 47 mm, the position of the lenses is tuned to obtain a beam with a diameter size lower

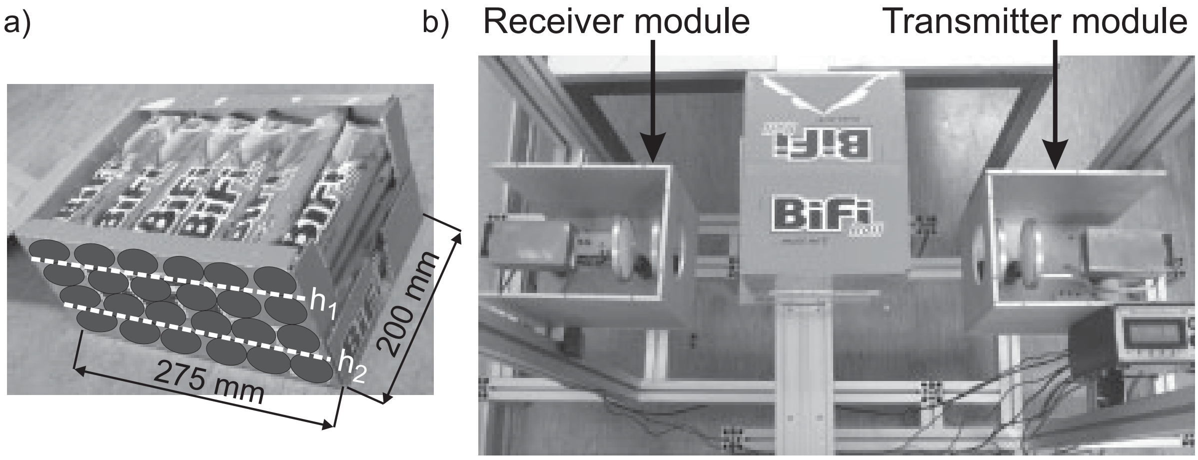

Figure 7.8: Screened object (a) and the complete GI^2 system (b).

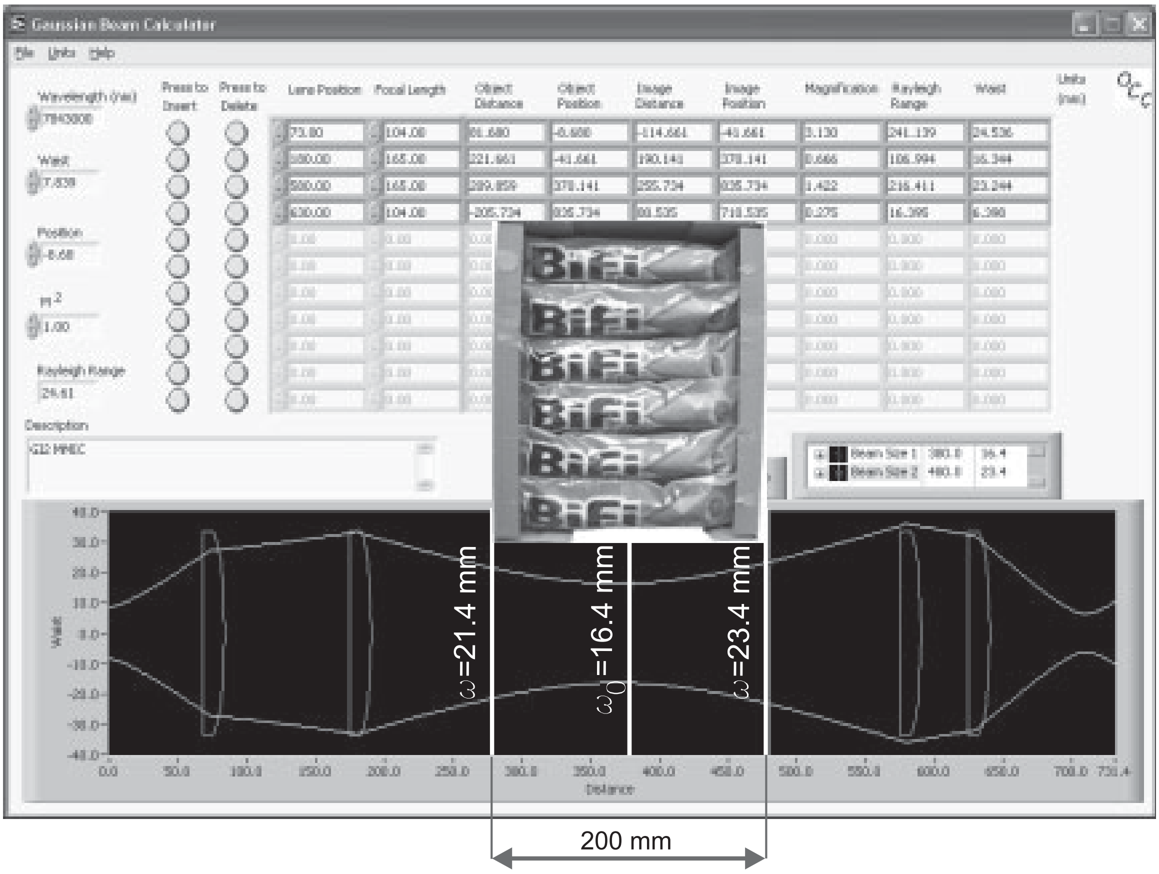

Figure 7.9: GI^2 optical design using GBC.

than 47 mm along the package width of 200 mm. For the optical design, GBC is used. As can be seen, using the configuration shown in Fig. 7.9, the beam has a waist radius of $\omega_{0sim} = 16.4$ mm. Simultaneously, the beam diameter does not exceed the value $2\omega\big|_{b=100\text{mm}} = 47$ mm over the package width 200 mm. To verify the simulation results, beam profile measurements employing the edge method are performed. The results are presented in Fig. 7.10. The raw profile is shown in Fig. 7.10 a) and the extracted beam profile in Fig. 7.10 b). It is noticeable the beam profile does not have a perfect Gaussian shape. This is attributed to misalignment between the transition structure and the waveguide and the possible asymmetry of the antennas. However, the measured beam radius $\omega_{0meas} = 16.5$ mm agrees well with the calculated value.

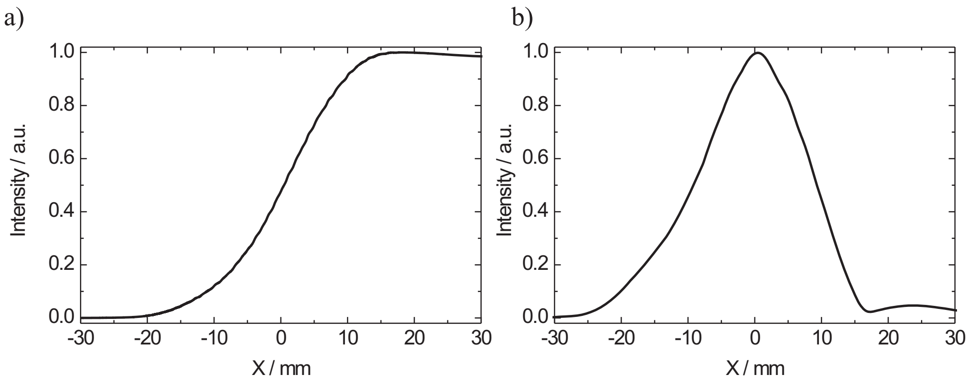

Figure 7.10: GI^2 focus diameter measurement: a) blade measurement characteristics, b) deconvoluted beam profile at the focus.

7.5 Measurement results

This section concentrates on the results obtained with the GI^2. The main task for the inspector is to check the completeness of the opaque-to-visible light package including the sausage bars.

In the first step, package profiles, showing the distribution of the detected signal in the coordinate perpendicular to the optical path, are measured. The measurement results are supplied directly by the GI^2, which worked in the data acquisition mode. For the data processing and control of the 1-dimensional translation stage, a computer is used.

Since the beam diameter corresponds to the diameter of the single bar, for the first set of measurements the beam height h_1 is adjusted to hit the space between row 1 and row 2 (refer to Fig. 7.8 a). It is presumed that this alignment enables for a simultaneous detection of the missing object in both rows. The measurement results are presented in Fig. 7.11. Here, 12 different positions of the missing bar are investigated. The graphs 7.11 a) - f) show the results obtained by removing one item from column 1 to 6. Every graph presents three curves: a reference curve which was recorded for the complete package, and two curves which correspond to the scans of row 1 and 2.
In order to check the system feasibility of screening the rows 3 and 4, the measurements are repeated for the new adjustment of the beam height h_2 between the rows 3 and 4 (Fig. 7.8 a)). The measurement results are presented in Fig. 7.12. Analysing the data shown in Figures 7.11 and 7.12 it can be concluded that the signals obtained for the incomplete packages differ from those which originate from the full package. If the package is complete, then the attenuation of the millimeter waves appears because of the reflection and scattering on the metallic foil covering the sausage bars. In contrast, when the bar is absent the signal can propagate through the air, which results in its increased transmission to the $10 \ldots 30\%$ of the reference value. This principle can be employed for the detection of the missing items in the package.

In the second step the measurements with the stand-alone GI^2 system shown in Fig. 7.8 b) are performed. Based on the results presented in Figures 7.11 and 7.12 the trigger level TL2 is set to TL2 = 10%. To test the GI^2, one item is removed from the package and the measurement is repeated 3 times using the linear slide system. For every measurement the variable factor versus its frequency is plotted in Fig. 7.11 g) (rows 1 and 2) and in Fig. 7.12 g) (rows 3 and 4). As can be seen, full packages result in the factor greater than 850. However, if any of 24 parts is missing, the factor is clearly below 850. By setting the set-point to 850, a correct evaluation of the package content can be performed. Additionally, by analysing the time slots for which the signal is increased, localisation of the missing bar can be performed. However, in the current detection scheme it is not possible to distinguish between row 1 and 2, as well as between row 3 and 4.

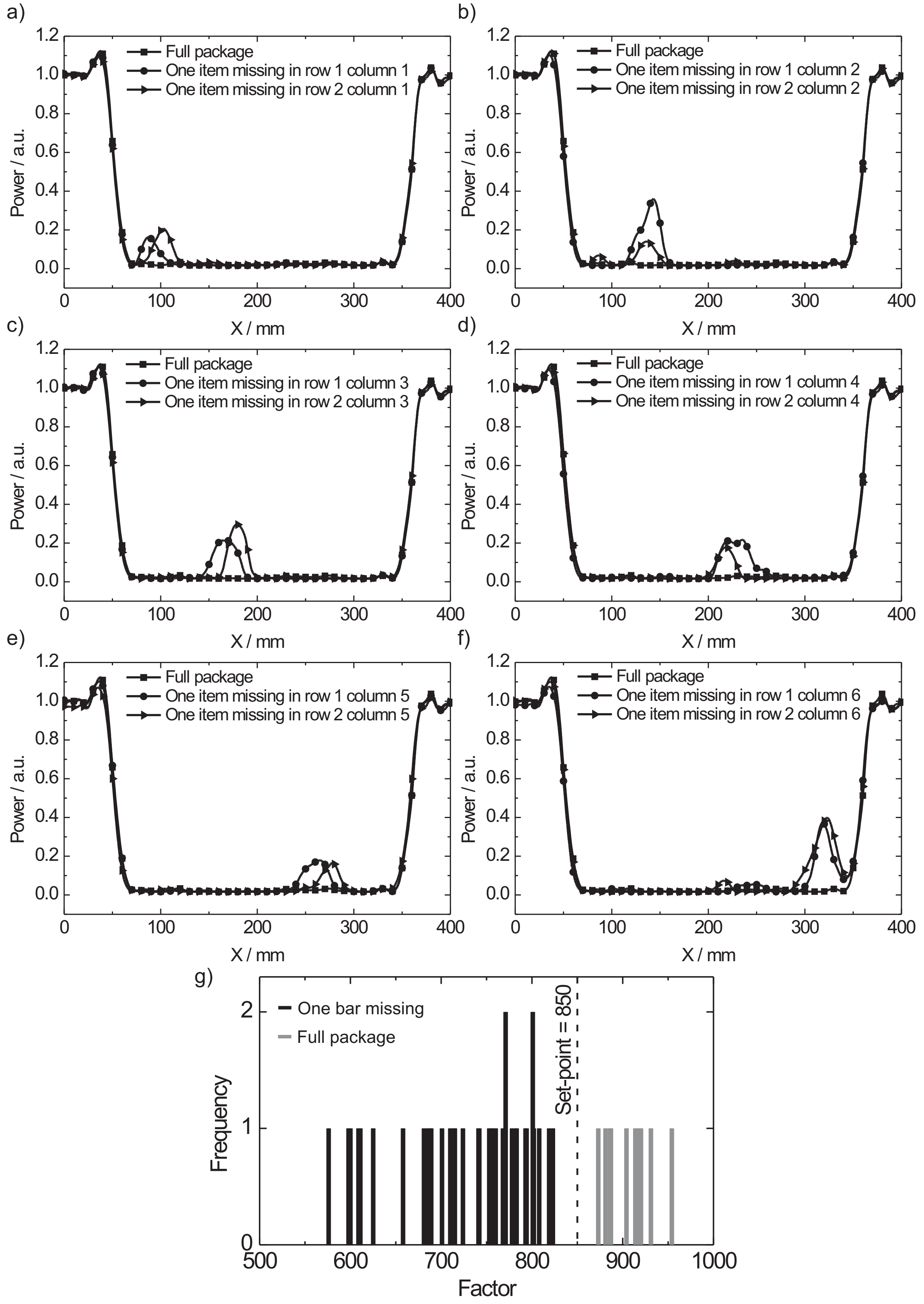

Figure 7.11: The detection of one missing bar in the package in the first and the second row. Graphs a) … f) present the results obtained for corresponding columns at which one part is missing. Graph g) presents the factor measurements.

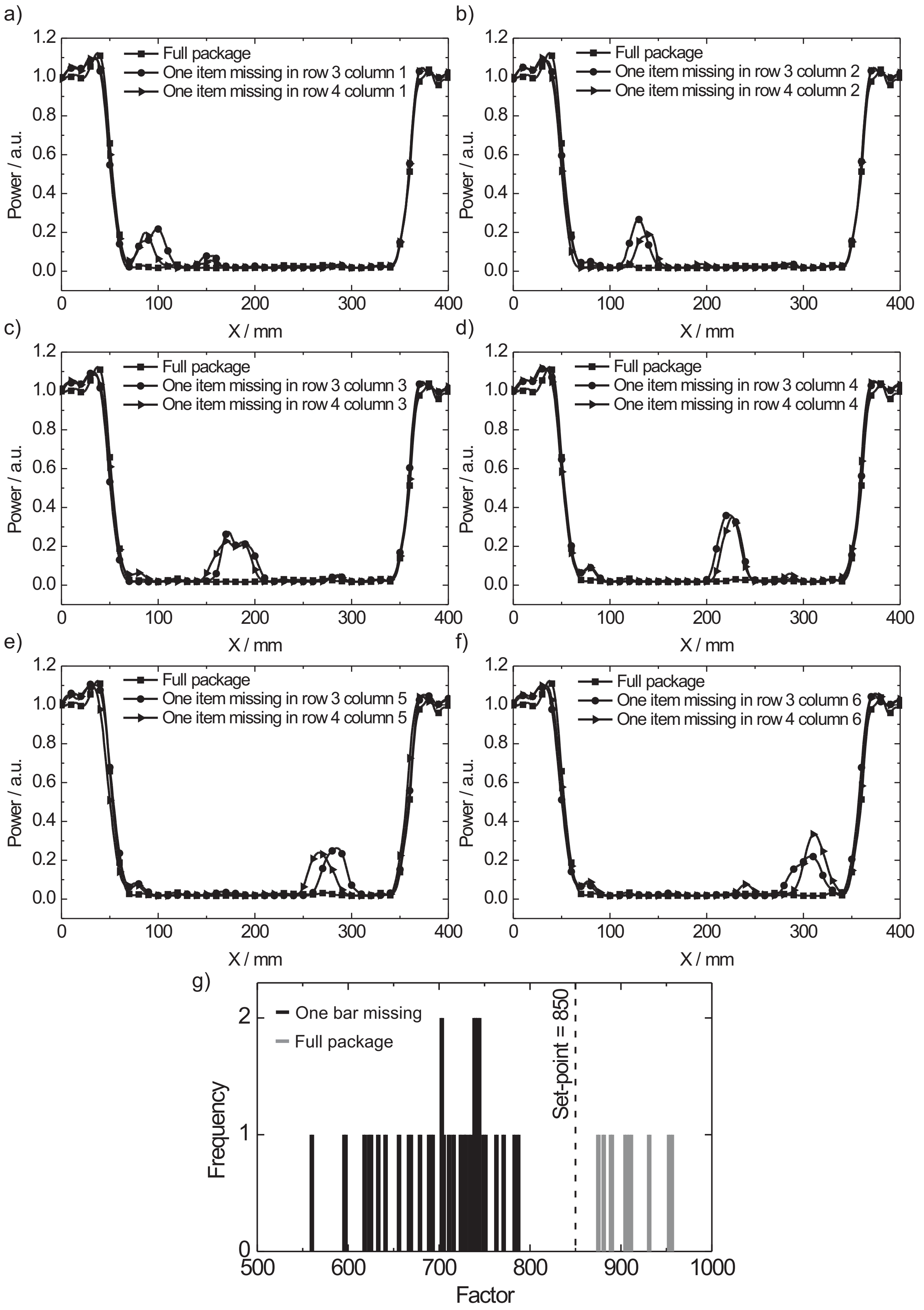

Figure 7.12: The detection of one missing bar in the package in the third and the fourth row. Graphs a) … f) present the results obtained for corresponding columns at which one item is missing. Graph g) presents the factor measurements.

7.6 Conclusions

In this section, the development and the measurement results obtained with the home-made gigahertz industrial inspector based on monolithic microwave circuits are presented. By employing MMICs the costs of the microwave components have been dramatically reduced by 85%. The tests on food products, which were also performed in a real production plant, confirm the system's feasibility for the screening of the package content. Besides of the advantages of the millimeter wave systems described in section 6.6, it can be concluded that the developed GI^2 is a reliable and cost-effective scanner.

Outlook

Microwave systems can be successfully used for product screening in many branches of industry. The presented systems were optimised for use in the food sector. In particular, two systems tested in the industry enable the screening of drink containers and food packages. However, millimeter wave systems can be also employed for the evaluation of products in other sectors. By modifying the detection routine the inspector can be adapted for other tasks. One possibility is the evaluation of the humidity of food products. On the other hand, testing of the number of paper sheets in a stack is promising for the papermaking industry. Another application is the testing of water content in plants. Since many materials can be screened with microwaves, the applications area of the technique is practically unlimited.

Furthermore, the systems' reliability and costs can be still improved by several hardware modifications as presented below.

In order to enhance the screening capability of the system, a multipath approach can be used. Here, a greater number of the transmitter-receiver pairs can scan the object at different heights simultaneously. This method is promising for the screening of packages that contain a higher number of products arranged at different heights. The practical realisation of this method requires the use of additional analog-to-digital converters and a powerful microcontroller for the processing of the signals. To avoid crosstalk between the channels, additional instrumentation for the signal modulation and demodulation needs to be developed.

Another approach leading to the enhancement of the scanning area is the use of moving mirrors that modify the spatial position of the microwave scanning path. This method involves the development of optical components; however, only one transmitter-receiver pair is needed. Here, the beam is continuously translated by the mirrors and it scans the product along the plane which is perpendicular to the movement direction of the products on the conveyor belt. For this method, a high-speed analog-to-digital converter is required, since the inspector must be capable of acquiring data in a short time. As a result, the microcontroller must have sufficient calculation capabilities for the processing of the data.

For further integration of the system, planar array antennas can be developed. It has been shown that these antennas can have gains as high as 28 dB. The employment of array antennas lowers the system complexity, since the microstrip-to-waveguide transition is not needed. Additionally, the antennas can be manufactured in one photolithographic process together with the transmission lines. To sum up, the use of planar antennas leads to the reduction of the weight, volume and the price of the system.

Finally, all components building the inspector can be integrated with the transmitter and receiver module. This can be accomplished by the placing of the antenna, the transmission lines and electronic circuits, including power supplies and the microcontroller, onto a single substrate. Such systems will improve the reliability, reduce the overall costs and are well suited for mass production.

Summary

The aim of the work was to investigate new application areas for millimeter wave imaging systems. Another important task was to realize the scanner for application in industrial plants.

Based on the setup employing a commercial vector network analyser equipped with a lens system, the feasibility for materials scanning was explored. As a result, a great potential for quality checking with microwaves was discovered. One of the application fields is the food industry. In particular, the use of millimeter wave systems for the detection of foreign objects and quality control is promising. It can be stated that dry, frozen and fat-rich products can be successfully examined for the presence of inclusions. In contrast, products containing water cannot be screened because of the high absorption factor of the water at millimeter frequencies. It is also crucial that the packaging material is relatively transparent for the scanning beam. This requirement is fulfilled for products that are packaged in polyethylene, polyethylene-terephthalate, polypropylene, glass and cardboard. However, goods enclosed in containers including metals or metal foils are not screenable in the investigated frequency range. It was shown that the applications of the millimeter wave scanner are not limited to the food sector exclusively. The employment of screening systems is of particular interest in the plastics industry. It has been proven that microwave imagers are well suited to the quality assessment of plastic weld joints and polymers. Typical problems appearing during the manufacturing of plastics including delaminations or the presence of inclusions can be detected. For plastics containing additives, a particle distribution map can be obtained. Since the millimeter waves are strongly attenuated by water, another application of this part of the electromagnetic spectrum is the control of rehydration process in plants. Finally, the employment of microwave systems for security scanning is possible, however it is limited to the recognition of relatively high volume items.
Based on promising results obtained with the network analyser, a 35 GHz system employing commercially available components was constructed. Together with the developed hardware and software, a fully stand-alone screening system for the completeness evaluation in the food industry was built. The inspector, which was successfully tested in an industrial plant, is capable of detecting a missing or an empty bottle in a drink container. For further integration and cost reduction, another screening system operating at the frequency of 38 GHz was developed. The gigahertz industrial inspector employs a home-made transmitter, receiver and antennas. The device was optimized for the completeness testing of packaged bars. The tests performed in a real industrial environment prove the inspector's feasibility for the detection of missing items.

The developed millimeter wave inspectors are a promising alternative or extension for existing quality control systems. Moreover, they surpass the contemporary screening devices in several aspects. First of all, microwaves are not ionising because of their low energy. This allows safe testing in the food and pharmaceutical industry. Furthermore, the evaluation method is noncontact and nondestructive. Therefore, it can be applied to 100% of the products. This assures the highest quality of manufactured goods. Finally, the developed inspectors are reliable and much more cost effective than the systems that exist in the market.

Bibliography

[1] E. P. Papadakis, *Financial justification of nondestructive testing: Cost of quality in manufacturing*. CRC, 2006.

[2] C. S. Brickenkamp, S. Hasko, and M. G. Natrella, *Checking the net contents of packaged goods*. U. S. Department of commerce / National bureau of standards, 1988.

[3] Weights and Measures, *The weights and measures (packaged goods), Regulations 2006 - Guidance note*. Department for innovation, universities and skills, 2007.

[4] C. J. Hellier, *Handbook of nondestructive evaluation*. McGraw-Hill, 2003.

[5] C. W. Kennedy and D. E. Andrews, *Inspection and gaging*. Industrial Press, 1977.

[6] G. B. Wetherill, *Sampling inspection and quality control*. Chapman & Hall, 1977.

[7] B. Smith, "Making war on defects: Six-sigma design," *IEEE Spectrum*, vol. 30, pp. 43–47, 1993.

[8] D. T. Pham and R. J. Alcock, *Smart inspection systems: Techniques and applications of intelligent vision*. Academic Press, 2003.

[9] H. Anglin, "MicroSeries - Machine vision part 1: Industrial inspection," *Circuit cellar INK: The computer applications journal*, vol. 83, pp. 66–72, 1997.

[10] M. Toledo, *Principles of checkweighing: A guide to the application and selection of checkweighers*. Hi-Speed Checkweigher Company, 1997.

[11] R. W. Kessler, *Prozessanalytik: Strategien und Fallbeispiele aus der Industriellen Praxis*. Wiley-VCH, 2006.

[12] R. Miller, *3-D Machine vision*. SEAI, Madison, GA and by Technical Insights, 1985.

[13] G. M. Mair, *Industrial robotics*. Prentice Hall, 1988.

[14] W. H. Organization, *Quality assurance of pharmaceuticals*. World Health Organization, 2004.

[15] M. Clute, *Food industry quality control systems*. CRC, 2008.

[16] E. Papadakis, "Future growth of NDE," *Materials Evaluation*, vol. 41, p. 1130, 1983.

[17] J. Juran, *Quality handbook*. McGraw-Hill, 1999.

[18] M. J. Chandra, *Statistical quality control*. CRC, 2001.

[19] P. G. Cielo, *Optical techniques for industrial inspection*. Academic Press, Inc., 1988.

[20] J. M. Juran and F. M. Gryna, *Juran's quality control handbook*. McGraw-Hill, 1988.

[21] I. 9001, "Quality management systems - Requirements International Standard ANSI / ISO / ASQ 9001-2000," 2008.

[22] A. V. Feigenbaum, *Total quality control*. McGraw-Hill, 2008.

[23] W. A. Shewhart, *Economic control of quality of manufactured product*. Van Nostrand, 1931.

[24] W. E. Co., *Statistical quality control handbook*. Western Electric Co., Newark, 1956.

[25] A. B. Mundel, “Achieving productivity and manufacturing excellence,” *Qualtest-2 Conference Proceedings*, 1983.

[26] W. E. Deming, *Quality productivity and competitive position*. Massachusetts Inst Technology, 1982.

[27] E. P. Papadakis, C. H. Stephan, M. T. McGinty, and W. B. Wall, “Inspection decision theory: Deming inspection criterion and time-adjusted rate-of-return compared,” *Engineering Costs and Production Economics*, vol. 13, pp. 111–124, 1988.

[28] E. P. Papadakis, “Quality, productivity, and cash flow,” 1996.

[29] T. Mason and M. Povey, *Ultrasound in food processing*. Springer, 1995.

[30] E. Marszalec, H. Kopola, and R. Myllyla, “Non-destructive testing of the quality of naturally white food products,” *Sensors and Actuators: B. Chemical*, vol. 11, no. 1-3, pp. 503–509, 1993.

[31] L. Rylander and J. Gustafsson, “Non-destructive examination of the primary system in ignalina nuclear power plant,” *Nuclear Engineer*, vol. 35, no. 6, pp. 182–184, 1994.

[32] K. Baaske, M. Salhi, F. Rutz, T. Hasek, R. Wilk, H. Richter, and M. Koch, “Mail inspection using THz imaging: a comparison of three different systems,” *Proc. SPIE Defence and Security Symposium*, vol. 6212, p. 62120U, 2006.

[33] R. Kazys, A. Demcenko, L. Mazeika, R. Sliteris, and E. Zukauskas, “Air-coupled ultrasonic non-destructive testing of aerospace components,” *Insight: Non-Destructive Testing and Condition Monitoring*, vol. 49, no. 4, pp. 195–199, 2007.

[34] N. P. Avdelidis, C. Ibarra-Castanedo, Z. P. Marioli-Riga, A. Bendada, and X. P. V. Maldague, “A study of active thermography approaches for the non-destructive testing and evaluation of aerospace structures,” *Proc. SPIE*, vol. 6939, pp. 693918.1–693918.6, 2008.

[35] K. G. Hall, “Non-destructive testing of axles fitted to railway wheelsets,” *Insight: Non-Destructive Testing and Condition Monitoring*, vol. 37, no. 4, pp. 268–274, 1995.

[36] R. Patel and J. Rudlin, “Analysis of corrosion/erosion incidents in offshore process plant and implications for non-destructive testing,” *Insight: Non-Destructive Testing and Condition Monitoring*, vol. 42, no. 1, pp. 17–21, 2000.

[37] G. A. Raine, “The development and the role of non-destructive testing in the UK offshore industry,” *Insight: Non-Destructive Testing and Condition Monitoring*, vol. 41, no. 12, pp. 772–777, 1999.

[38] P. Murphy, “A fibre-optic endoscope used for nasal intubation,” *Anaesthesia*, vol. 22, no. 3, pp. 489–491, 1967.

[39] Anonym, “CCD’s used in linear imaging device,” *Bell Laboratories Record*, vol. 49, no. 4, pp. 128–129, 1971.

[40] D. Kindred, “Extending boroscope applications,” *Turbomachinery International*, vol. 47, no. 3, pp. 26–27, 2006.

[41] B. G. Batchelor and P. F. Whelan, *Intelligent vision systems for industry*, vol. 457. Springer-Verlag Telos, 1997.

[42] K. Isoda and Y. Nakagawa, *International encyclopedia of robotics applications and automation*. Wiley, 1988.

[43] H. H. Poole, *Fundamentals of robotic engineering*. Van Nostrand Reinhold, 1989.

[44] P. K. Wright and D. A. Bourne, *Manufacturing Intelligence*. Addison-Wesley Educational Publishers Inc, 1988.

[45] K. Hedenren, *Advances in machine Vision: Methodology for automatic image-based inspection of industrial objects*. Springer-Verlag, 1989.

[46] C. Yan, S. Dawei, H. Xueming, Y. Hailan, and W. Yixiong, “Study on surface defects recognition of circumferential laser weld based on visual inspection technology,” *Welding in the World*, vol. 52, no. SPEC. ISS., pp. 743–747, 2008.

[47] O. Oyeleye and E. A. Lehtihet, “Automatic visual inspection of surface mount solder joint defects,” *International Journal of Production Research*, vol. 37, no. 6, pp. 1217–1242, 1999.

[48] B. A. Pelligrino, “Remote visual testing for internal pressure vessel inspection,” *Materials Evaluation*, vol. 56, no. 5, pp. 606–609, 1998.

[49] E. Hoeft, “Visual inspection method for recurrent tests of weld seams at the reactor-tank and double-tank walls of the reactor SNR-300,” *Atomkernenergie, Kerntechnik*, vol. 47, no. 1, pp. 17–19, 1985.

[50] M. Piazza and M. Riggio, “Visual strength-grading and NDT of timber in traditional structures,” *Journal of building appraisal*, vol. 3, no. 4, pp. 267–296, 2008.

[51] M. M. Valentin, P. Dan, and C. Gabriel, “Automated optical inspection tool using the LPKF PCB mechanical prototyping machine,” in *Proceedings - 2008 2nd Electronics Systemintegration Technology Conference, ESTC*, pp. 1359–1362, 2008.

[52] S. S. Martinez, G. J. Ortega, G. J. García, and S. A. Garcia, “A sensor planning system for automated headlamp lens inspection,” *Expert Systems with Applications*, vol. 36, no. 5, pp. 8768–8777, 2009.

[53] T. Min, Z. Zuxun, and Z. Jianqing, “Visual inspection of industrial sheet metal part with CAD data,” in *Proceedings of SPIE - The International Society for Optical Engineering*, vol. 6788, 2007.

[54] G. A. Ruz, P. A. Estevez, and P. A. Ramirez, “Automated visual inspection system for wood defect classification using computational intelligence techniques,” *International Journal of Systems Science*, vol. 40, no. 2, pp. 163–172, 2009.

[55] P. Tantaswadi, J. Vilainatre, N. Tamaree, and P. Viraivan, “Machine vision for automated

visual inspection of cotton quality in textile industries using color isodiscrimination contour," *Computers and Industrial Engineering*, vol. 37, no. 1, pp. 347–350, 1999.

[56] C. K. Huang, C. W. Liao, A. P. Huang, and Y. S. Tarng, "An automatic optical inspection of drill point defects for micro-drilling," *International Journal of Advanced Manufacturing Technology*, vol. 37, no. 11-12, pp. 1133–1145, 2008.

[57] S. H. Ong, X. Han, and Q. Z. Ye, "3D visual inspection of IC bonding wires," in *Proc. SPIE Automatic Inspection and Novel Instrumentation*, vol. 3185, pp. 77–86, 1997.

[58] T. H. Kim, T. H. Cho, Y. S. Moon, and S. H. Park, "An automated visual inspection of solder joints using 2D and 3D features," in *Proceedings 3rd IEEE workshop on applications of computer vision*, pp. 110–115, 1996.

[59] W. Balachandran, Y. M. Enab, M. Halimic, and M. Tariq, "Intelligent robot-based dynamic weighing system," *Proceedings of SPIE - The International Society for Optical Engineering*, vol. 2353, pp. 398–409, 1994.

[60] N. P. Grigg, J. Daly, and M. Stewart, "Case study: The use of statistical process control in fish product packaging," *Food Control*, vol. 9, no. 5, pp. 289–297, 1998.

[61] M. Halimic, W. Balachandran, F. Cecelja, and M. Tariq, "Adaptive deconvolution approach for estimating the input of checkweighing systems," in *Conference Record - IEEE Instrumentation and Measurement Technology Conference 2*, vol. 2, pp. 1098–1101, 2003.

[62] T. Yamazaki, Y. Sakurai, S. Kurosu, H. Ohnishi, and M. Kobayashi, *Continuous mass measurement in checkweighers and conveyor belt scales*. No. 1685, VDI-Verlag GmbH, 2002.

[63] L. Schmerr and S. J. Song, *Ultrasonic nondestructive evaluation systems: Models and measurements*. Springer, 2007.

[64] K. S. Tan, R. Round, and B. Bridge, "Feasibility study in monitoring the setting process of aluminum orthophosphate bonded ceramics using through transmission ultrasound," *British ceramic.Transactions and journal*, vol. 88, no. 4, pp. 138–143, 1989.

[65] G. Baskaran, K. Balasubramaniam, C. V. Krishnamurthy, and C. L. Rao, "Ultrasonic TOFD flaw sizing and imaging in thin plates using embedded signal identification technique (ESIT)," *Insight: Non-Destructive Testing and Condition Monitoring*, vol. 46, no. 9, pp. 537–542, 2004.

[66] M. Schickert, M. Krause, and W. Mueller, "Ultrasonic imaging of concrete elements using reconstruction by synthetic aperture focusing technique," *Journal of Materials in Civil Engineering*, vol. 15, no. 3, pp. 235–246, 2003.

[67] M. Hirao, H. Ogi, and H. Fukuoka, "Resonance EMAT system for acoustoelastic stress measurement in sheet metals," *Review of Scientific Instruments*, vol. 64, no. 11, pp. 3198–3205, 1993.

[68] R. A. Kruger, P. Liu, Y. R. Fang, and C. R. Appledorn, "Photoacoustic ultrasound (PAUS) - Reconstruction tomography," *Medical Physics*, vol. 22, pp. 1605–1609, 1995.

[69] J. C. Berrios and P. C. Pedersen, “Ultrasonic measurement of forced diameter variations in an elastic tube,” *Ultrasonic imaging*, vol. 16, no. 2, pp. 124–142, 1994.

[70] R. Kazys and L. Svilainis, “Ultrasonic detection and characterization of delaminations in thin composite plates using signal processing techniques,” *Ultrasonics*, vol. 35, no. 5, pp. 367–383, 1997.

[71] D. Lian, V. Suga, G. Shou, and S. Kurihara, “An ultrasonic testing method for detecting delamination of sprayed ceramic coating,” *Journal of Thermal Spray Technology*, vol. 5, no. 2, pp. 128–133, 1996.

[72] D. R. Roberts, J. Mason, and C. Lewis, “Ultrasonic spot weld testing: Attenuation study,” *Insight: Non-Destructive Testing and Condition Monitoring*, vol. 42, no. 11, pp. 720–724, 2000.

[73] J. P. Sargent, “Corrosion detection in welds and heat-affected zones using ultrasonic Lamb waves,” *Insight: Non-Destructive Testing and Condition Monitoring*, vol. 48, no. 3, pp. 160–167, 2006.

[74] W. Grassi, E. Filippucci, A. Farina, F. Salaffi, and C. Cervini, “Ultrasonography in the evaluation of bone erosions,” *Annals of the Rheumatic Diseases*, vol. 60, no. 2, pp. 98–103, 2001.

[75] H. Austerlitz and M. Hewitt, “Ultrasonic fluid level sensor,” United states patent and trademark office pre-grant publication, 2006.

[76] J. P. Crane, M. L. LeFevre, R. C. Winborn, J. K. Evans, B. G. Ewigman, R. P. Bain, F. D. Frigoletto, and D. McNellis, “A randomized trial of prenatal ultrasonographic screening: Impact on the detection, management, and outcome of anomalous fetuses,” *American Journal of Obstetrics and Gynecology*, vol. 171, no. 2, pp. 392–399, 1994.

[77] S. Gonnelli, C. Cepollaro, D. Agnusdei, R. Palmieri, S. Rossi, and C. Gennari, “Diagnostic value of ultrasound analysis and bone densitometry as predictors of vertebral deformity in postmenopausal women,” *Osteoporosis International*, vol. 5, no. 6, pp. 413–418, 1995.

[78] H. L. Hedriana and T. R. Moore, “Ultrasonographic evaluation of human fetal urinary flow rate: Accuracy limits of bladder volume estimations,” *American Journal of Obstetrics and Gynecology*, vol. 170, no. 5 I, pp. 1250–1254, 1994.

[79] W. Browne, *Nuclear Technology International: Automated ultrasonic examination of primary circuit welds*. Sterling Publications Limited, 1988.

[80] J. R. Lilley, “Time-of-flight-diffraction (TOFD) techniques for crack detection and sizing in turbine rotor shafts,” *Proceedings of the 12th World Conference on Non-Destructive Testing*, vol. 2, pp. 1104 – 1106, 1989.

[81] P. Ashwin, “Time of flight diffraction technique and applications for retaining rings and turbine discs,” in *Steam Turbine/Generation NDE Workshop*, pp. 23 – 29, 1989.

[82] B. Shan, H. Wang, Y. Liang, Z. Duan, and J. Ou, “Ultrasonic phased array inspection imaging technology for NDT of offshore platform structures,” in *Proceedings of SPIE - The International Society for Optical Engineering*, vol. 6934, 2008.

[83] C. Mild, K. Nishikawa, H. Shirahata, and M. Takahashi, “Performance evaluation test of the time-of-flight diffraction technique for welded joints of steel bridges,” *Journal of Testing and Evaluation*, vol. 36, no. 3, pp. 213–221, 2008.

[84] M. J. Chen and Y. S. Sun, “Finite element prediction of possible application of pulse excitation in remote field eddy current nondestructive inspection devices,” *International journal of applied electromagnetics in materials*, vol. 2, no. 3, pp. 217–220, 1991.

[85] J. H. Yang and Y. S. Yoon, “Detection of metal defects on gas distribution pipeline by Remote Field Eddy Current (RFEC) using finite-element analysis,” *Oil and Gas Science and Technology*, vol. 56, no. 2, pp. 161–179, 2001.

[86] M. O’Connor, “Multifrequency eddy current iInstrumentation: Understanding the specifications,” *Materials Evaluation*, vol. 64, no. 4, pp. 391–393, 2006.

[87] N. Yusa, Z. Chen, K. Miya, T. Uchimoto, and T. Takagi, “Large-scale parallel computation for the reconstruction of natural stress corrosion cracks from eddy current testing signals,” *NDT and E International*, vol. 36, no. 7, pp. 449–459, 2003.

[88] R. Palanisamy, “Nondestructive inspection of kinetic bonding by eddy current method,” *Journal of Applied Physics*, vol. 55, no. 6, pp. 2626–2627, 1984.

[89] J. C. Moulder, E. Uzal, and J. H. Rose, “Thickness and conductivity of metallic layers from eddy current measurements,” *Review of Scientific Instruments*, vol. 63, no. 6, pp. 3455–3465, 1992.

[90] J. G. Thompson, “Subsurface corrosion detection in aircraft lap splices using a dual frequency eddy current inspection technique,” *Materials Evaluation*, vol. 51, no. 12, pp. 1398–1401, 1993.

[91] B. I. Volkov and V. M. Temryukh, “VAK-2 eddy current instrument for intermetallic corrosion damage estimation in tubes of superheaters of electric power plants,” *Defektoskopiya*, vol. -, no. 3, pp. 32–36, 1998.

[92] C. Bignon, C. Bedrin, and R. Weill, “Application of Eddy Currents to the In-Process Measurement of the Gap in E.C.M.,” *CIRP Annals - Manufacturing Technology*, vol. 31, no. 1, pp. 115–118, 1982.

[93] J. Hansen, “The eddy current inspection method. Part 4. Applications, practical testing and advanced concepts,” *Insight: Non-Destructive Testing and Condition Monitoring*, vol. 46, no. 8, pp. 480–483, 2004.

[94] K. Sauerland, F. Gockel, R. Mahnken, and F. Ferber, “Damage analysis under thermal shock loading using eddy current sensors,” *Nondestructive Testing and Evaluation*, vol. 24, no. 1-2, pp. 3–18, 2009.

[95] M. Graves, A. Smith, and B. Batchelor, “Approaches to foreign body detection in foods,” *Trends in Food Science and Technology*, vol. 9, no. 1, pp. 21–27, 1998.

[96] L. International, *The lock international metal detection handbook*. Lock International, 1991.

[97] R. V. Phadke and D. P. Rane, “All metal detector system for textile industry,” *Colourage*, vol. 44, no. 7, pp. 47–48, 1997.

[98] M. Bhuyan, *Measurement and control in food processing*. CRC, 2006.

[99] A. Royle and E. M. Unett, *Radiographic techniques and image evaluation*. Nelson Thornes, 1997.

[100] J. A. Pineault and M. E. Brauss, “Insitu measurements of residual and applied stresses in pressure vessels and pipelines using X-ray diffraction techniques,” in *American Society of Mechanical Engineers, Pressure Vessels and Piping Division*, vol. 276, pp. 145–148, 1994.

[101] S. Ganguly, M. E. Fitzpatrick, and L. Edwards, “Use of neutron and synchrotron X-ray diffraction for evaluation of residual stresses in a 2024-T351 aluminum alloy variable-polarity plasma-arc weld,” *Metallurgical and Materials Transactions A: Physical Metallurgy and Materials Science*, vol. 37, no. 2, pp. 411–420, 2006.

[102] H. Biermann, B. Von Grossmann, T. Ungar, S. Mechsner, A. Souvorov, M. Drakopoulos, A. Snigirev, and H. Mughrabi, “Determination of local strains in a monocrystalline turbine blade by microbeam X-ray diffraction with synchrotron radiation,” *Acta Materialia*, vol. 48, no. 9, pp. 2221–2230, 2000.

[103] C. Armentrout, T. Basinger, J. Beyer, B. Colesa, P. Olsztyn, K. Smith, C. Strandberg, D. Sullivan, and J. Thomson, “Inspection of small multi-layered plastic tubing during extrusion, using low-energy X-ray beams,” *Nuclear Instruments and Methods in Physics Research, Section A: Accelerators, Spectrometers, Detectors and Associated Equipment*, vol. 422, no. 1-3, pp. 964–968, 1999.

[104] M. Alvarez, J. Alvarado, A. R. Cristiano, L. M. Marco, and M. M. Perez, “Radioisotope X-ray fluorescence analysis of vanadium in petroleum coke samples,” *Journal of radioanalytical and nuclear chemistry*, vol. 144, no. 5, pp. 327–334, 1990.

[105] D. K. Lehmann, “X-ray systems for optimizing PCB inspection,” *Circuits Assembly*, vol. 13, no. 2, pp. 35–39, 2002.

[106] E. Ostman and S. Persson, “Application of X-ray Tomography in non-destructive testing of fibre reinforced plastics,” *Materials and Design*, vol. 9, no. 3, pp. 142–147, 1988.

[107] H. Yamada and R. Suryanarayanan, “Calculation of the penetration depth of X-rays in intact pharmaceutical film-coated tablets by microdiffractometry (Pharmaceutical Research),” *Pharmaceutical research*, vol. 25, no. 3, p. 709, 2008.

[108] K. Arunachalam, S. S. Udpa, and L. Udpa, “An X-ray security screening technique with limited field-of-view,” *International Journal of Applied Electromagnetics and Mechanics*, vol. 24, no. 1-2, pp. 79–89, 2006.

[109] C. Reh, *Nondestructive testing of food quality*. Wiley-Blackwell, 2008.

[110] C. Connolly, “X-ray systems for security and industrial inspection,” *Sensor Review*, vol. 28/3, pp. 194–198, 2008.

[111] N. A. Tracy and P. O. Moore, *Liquid penetrant testing (Nondestructive testing handbook, vol. 2)*. American Society for Nondestructive Testing, 1999.

[112] W. C. Morrey Jr., “Penetrant testing in the quality control of nuclear power plant construction,” *NDT International*, vol. 10, no. 1, pp. 9–12, 1977.

[113] D. C. Nielson and J. G. H. Thomson, "Evaluation of liquid penetrant systems," *Materials Evaluation*, vol. 33, no. 12, pp. 284–292, 1975.

[114] J. T. Schmidt, K. Skeie, and P. McIntire, *Magnetic particle testing (Nondestructive testing handbook, vol. 6)*. American Society for Nondestructive Testing, 1989.

[115] K. Berner and W. Rehme, "Magnetic Particle Crack Testing Device for Pipe End Inspection," *Materialpruefung/Materials Testing*, vol. 1, no. 9, pp. 374–376, 1998.

[116] L. M. Polentz, "Nondestructive testing of welds - Liquid - penetrant and magnetic-particle inspection techniques," *Plant Engineering (Barrington, Illinois)*, vol. 32, no. 4, pp. 177–178, 1978.

[117] R. Potter, "Magnetic particle testing of high tensile parts used in aerospace applications," *Materials Evaluation*, vol. 63, no. 8, pp. 790–792, 2005.

[118] J. Zheng, "Magnetic particle testing of a vane wheel hole for surface defects," *Wusun Jiance/Nondestructive Testing*, vol. 8, no. 6, pp. 157–159, 172, 1986.

[119] C. Allen, "Magnetic-particle testing pinpoints cracks in deaerator vessels," *Power*, vol. 129, no. 1, pp. 55–57, 1985.

[120] C. U. Grosse and M. Ohtsu, *Acoustic emission testing*. Springer, 2008.

[121] D. J. Holcomb, "General theory of the Kaiser effect," *International Journal of Rock Mechanics and Mining Sciences and*, vol. 30, no. 7, pp. 929–935, 1993.

[122] D. Racko, "Acoustic emission from welds as indicator of cracking," *Materials Science and Technology*, vol. 3, no. 12, pp. 1062–1066, 1986.

[123] P. Rossi, N. Godart, J. L. Robert, J. P. Gervais, and D. Bruhat, "Investigation of the basic creep of concrete by acoustic emission," *Materials and Structures*, vol. 27, no. 9, pp. 510–514, 1994.

[124] T. N. K. Titus, D. V. Reddy, S. E. Dunn, and W. H. Hartt, "Acoustic emission crack monitoring and prediction of remaining life of corroding reinforced concrete beams," *In: Non-destructive testing, Proc.4th european conf.*, vol. 2, pp. 1031–1040, 1988.

[125] H. Bathelemy, "Periodic inspection of compressed gas cylinders and tubes - flaw detection using acoustic emission testing," *Journal of Pressure Vessel Technology, Transactions of the ASME*, vol. 110, no. 2, pp. 161–167, 1988.

[126] S. Nambu and M. Enoki, "Analysis of acoustic emission behavior in graphite materials for solid rocket motor," *Key Engineering Materials*, vol. 270-273, no. I, pp. 479–484, 2004.

[127] R. M. Honeycutt, C. Skaar, and W. T. Simpson, "Use of acoustic emissions to control drying rate of red oak," *Forest Products Journal*, vol. 35, no. 1, pp. 48–50, 1985.

[128] D. E. Lee, B. Raeymaekers, and F. E. Talke, "In-situ monitoring of the brush/rotor interface in a homopolar motor with Acoustic Emission," *Australian Journal of Mechanical Engineering*, vol. 6, no. 1, pp. 53–60, 2008.

[129] M. A. Hamstad and J. D. McColskey, "Detectability of slow crack growth in bridge steels by acoustic emission," *Materials Evaluation*, vol. 57, no. 11, pp. 1165–1174, 1999.

[130] G. V. Barbosa-Canovas and P. Juliano, “Symposium 3 part 2: The food chain - Food processing and food safety. Adaptation of classical processes to new technical developments and quality requirements,” *Journal of Food Science*, vol. 69, no. 5, pp. E240–E250, 2004.

[131] D. R. Green, “Thermal and infrared nondestructive testing of composites and ceramics,” *Materials Evaluation*, vol. 29, no. 11, pp. 241–248, 1971.

[132] D. R. Green, “Experimental electro-thermal method for nondestructively testing welds in stainless steel pipes,” *Materials Evaluation*, vol. 37, no. 11, pp. 54–60, 1979.

[133] E. P. Papadakis, H. L. Chesney, and R. G. Hurley, “Quality assurance of aluminum radiators by infrared thermography,” *Materials Evaluation*, vol. 42, no. 3, pp. 333–336, 1984.

[134] B. P. Dooher and E. Elliott, “Dynamic thermal testing and winding temperature response of a 30-MVA transformer,” in *Proceedings of the American Power Conference 55 (pt 2)*, vol. 55, pp. 1652–1657, 1993.

[135] M. P. Wirick and H. A. Diede, “Infrared testing of printed circuit boards and hybrids,” *Proceedings of the Society of Photo-Optical Instrumentation Engineers*, vol. 220, pp. 124–129, 1980.

[136] M. D. Hudson, C. J. Brierley, A. J. Miller, and A. E. J. Wilson, “Fabrication and testing of diamond coatings on infrared windows for the harrier GR7 and AV8-B systems,” in *Proceedings of SPIE - The International Society for Optical Engineering*, vol. 3060, pp. 196–202, 1997.

[137] M. Mukherjee, N. Mazumder, S. K. Roy, and K. Goswami, “GaN IMPATT diode: A photo-sensitive high power terahertz source,” *Semiconductor Science and Technology*, vol. 22, no. 12, pp. 1258–1267, 2007.

[138] J. Faist, F. Capasso, D. L. Sivco, C. Sirtori, A. L. Hutchinson, and A. Y. Cho, “Quantum cascade laser,” *Science*, vol. 264, no. 5158, pp. 553–556, 1994.

[139] D. H. Auston, K. P. Cheung, and P. R. Smith, “Picosecond photoconducting Hertzian dipoles,” *Applied Physics Letters*, vol. 45, no. 3, pp. 284–286, 1984.

[140] A. Leitenstorfer, S. Hunsche, J. Shah, M. C. Nuss, and W. H. Knox, “Femtosecond charge transport in polar semiconductors,” *Physical Review Letters*, vol. 82, no. 25, pp. 5140–5143, 1999.

[141] A. Nahata, A. S. Weling, and T. F. Heinz, “A wideband coherent terahertz spectroscopy system using optical rectification and electro-optic sampling,” *Applied Physics Letters*, vol. 69, no. 16, pp. 2321–2323, 1996.

[142] Y. R. Shen, “Far-infrared generation by optical mixing,” *Progress in Quantum Electronics*, vol. 4, no. PART 3, pp. 207–232, 1976.

[143] E. R. Brown, K. A. McIntosh, F. W. Smith, M. J. Manfra, and C. L. Dennis, “Measurements of optical-heterodyne conversion in low-temperature-grown GaAs,” *Applied Physics Letters*, vol. 62, no. 11, pp. 1206–1208, 1993.

[144] L. O. Hocker, A. Javan, D. R. Rao, L. Frenkel, and T. Sullivan, “Absolute frequency mea-

surement and spectroscopy of gas laser transitions in the far infrared," *Applied Physics Letters*, vol. 10, no. 5, pp. 147–149, 1967.

[145] A. Nahata, J. T. Yardley, and T. F. Heinz, "Free-space electro-optic detection of continuous-wave terahertz radiation," *Applied Physics Letters*, vol. 75, no. 17, pp. 2524–2526, 1999.

[146] J. Struckmeier, A. Euteneuer, B. Smarsly, M. Breede, M. Born, M. Hofmann, L. Hildebrand, and J. Sacher, "Electronically tunable external-cavity laser diode," *Optics Letters*, vol. 24, no. 22, pp. 1573–1574, 1999.

[147] I. H. Libon, S. Baumgaertner, M. Hempel, N. E. Hecker, J. Feldmann, M. Koch, and P. Dawson, "An optically controllable terahertz filter," *Applied Physics Letters*, vol. 76, no. 20, pp. 2821–2823, 2000.

[148] T. Kleine-Ostmann, P. Dawson, K. Pierz, G. Hein, and M. Koch, "Room-temperature operation of an electrically driven terahertz modulator," *Applied Physics Letters*, vol. 84, no. 18, pp. 3555–3557, 2004.

[149] Z. Ghattan, T. Hasek, R. Wilk, M. Shahabadi, and M. Koch, "Sub-terahertz on-off switch based on a two-dimensional photonic crystal infiltrated by liquid crystals," *Optics Communications*, vol. 281, no. 18, pp. 4623–4625, 2008.

[150] T. Hasek, Z. Ghattan, R. Wilk, M. Shahabadi, and M. Koch, "Photonic crystals for on-off switching of sub-terahertz electromagnetic waves," in *33rd International Conference on Infrared and Millimeter Waves and the 16th International Conference on Terahertz Electronics, 2008, IRMMW-THz 2008*, 2008.

[151] R. Wilk, *Switchable THz Reflectors*. PhD thesis, Technische Universitaet Braunschweig, 2007.

[152] H. T. Chen, W. J. Padilla, M. J. Cich, A. K. Azad, R. D. Averitt, and A. J. Taylor, "A metamaterial solid-state terahertz phase modulator," *Nature Photonics*, vol. 3, no. 3, pp. 148–151, 2009.

[153] D. M. Mittleman, M. Gupta, R. Neelamani, R. G. Baraniuk, J. V. Rudd, and M. Koch, "Recent advances in terahertz imaging," *Applied Physics B: Lasers and Optics*, vol. 68, no. 6, pp. 1085–1094, 1999.

[154] Y. Shen and P. F. Taday, "Development and application of terahertz pulsed imaging for nondestructive inspection of pharmaceutical tablet," *IEEE Journal on Selected Topics in Quantum Electronics*, vol. 14, no. 2, pp. 407–415, 2008.

[155] F. Rutz, M. Koch, S. Khare, M. Moneke, H. Richter, and U. Ewert, "Terahertz quality control of polymeric products," *International Journal of Infrared and Millimeter Waves*, vol. 27, no. 4, pp. 547–556, 2006.

[156] S. Wietzke, C. Jansen, F. Rutz, D. M. Mittleman, and M. Koch, "Determination of additive content in polymeric compounds with terahertz time-domain spectroscopy," *Polymer Testing*, vol. 26, pp. 614–618, 8 2007.

[157] N. Krumbholz, T. Hochrein, N. Vieweg, T. Hasek, K. Kretschmer, M. Bastian, M. Mi-

kulics, and M. Koch, “Monitoring polymeric compounding processes inline with THz time-domain spectroscopy,” *Polymer Testing*, vol. 28, no. 1, pp. 30–35, 2009.

[158] S. Wietzke, C. Joerdens, N. Krumbholz, B. Baudrit, M. Bastian, and M. Koch, “Terahertz imaging: a new non-destructive technique for the quality control of plastic weld joints,” *Journal of the European Optical Society - Rapid Publications*, vol. 2, p. 07013, 2007.

[159] C. Joerdens and M. Koch, “Detection of foreign bodies in chocolate with pulsed terahertz spectroscopy,” *Optical Engineering*, vol. 47, no. 3, p. 037003, 2008.

[160] T. Kleine-Ostmann, P. Knobloch, M. Koch, S. Hoffmann, M. Breede, M. Hofmann, G. Hein, K. Pierz, M. Sperling, and K. Donhuijsen, “Continuous-wave THz imaging,” *Electronics Letters*, vol. 37, pp. 1461–1463, Nov 2001.

[161] N. N. Zinov’ev, C. D. Sudworth, E. Berry, S. M. Strafford, D. J. Wood, F. A. Carmichael, R. E. Miles, M. A. Smith, and J. M. Chamberlain, “Identification of tooth abnormalities using Terahertz imaging and spectroscopy,” in *Proceedings of SPIE - The International Society for Optical Engineering*, vol. 5141, pp. 196–201, 2003.

[162] M. Koch, S. Hunsche, P. Schuacher, M. C. Nuss, J. Feldmann, and J. Fromm, “THz-imaging: A new method for density mapping of wood,” *Wood Science and Technology*, vol. 32, no. 6, pp. 421–427, 1998.

[163] B. Fischer, M. Hoffmann, H. Helm, R. Wilk, F. Rutz, T. Kleine-Ostmann, M. Koch, and P. Jepsen, “Terahertz time-domain spectroscopy and imaging of artificial RNA,” *Opt. Express*, vol. 13, no. 14, pp. 5205–5215, 2005.

[164] M. Scheller, C. Joerdens, B. Breitenstein, D. Selmar, and M. Koch, “Effective permittivity and scattering model for the evaluation of the leaf water status,” in *33rd International Conference on Infrared and Millimeter Waves and the 16th International Conference on Terahertz Electronics*, 2008.

[165] D. Creeden, J. C. McCarthy, P. A. Ketteridge, P. G. Schunemann, T. Southward, J. J. Komiak, and E. P. Chicklis, “Compact, high average power, fiber-pumped terahertz source for active real-time imaging of concealed objects,” *Optics Express*, vol. 15, no. 10, pp. 6478–6483, 2007.

[166] R. Piesiewicz, M. Jacob, M. Koch, J. Schoebel, and T. Kuerner, “Performance analysis of future multigigabit wireless communication systems at THz frequencies with highly directive antennas in realistic indoor environments,” *IEEE Journal on Selected Topics in Quantum Electronics*, vol. 14, no. 2, pp. 421–430, 2008.

[167] N. Krumbholz, K. Gerlach, F. Rutz, M. Koch, R. Piesiewicz, T. Kuerner, and D. Mittleman, “Omnidirectional terahertz mirrors: A key element for future terahertz communication systems,” *Applied Physics Letters*, vol. 88, no. 20, p. 202905, 2006.

[168] A. Hirata, H. Takahashi, R. Yamaguchi, T. Kosugi, K. Murata, T. Nagatsuma, N. Kukutsu, and Y. Kado, “Transmission characteristics of 120 GHz band wireless link using radio-on-fiber technologies,” *Journal of Lightwave Technology*, vol. 26, no. 15, pp. 2338–2344, 2008.

[169] C. Jastrow, K. Muenter, R. Piesiewicz, T. Kuerner, M. Koch, and T. Kleine-Ostmann, “300 GHz transmission system,” *Electronics Letters*, vol. 44, no. 3, pp. 213–214, 2008.

[170] D. M. Pozar, *Microwave Engineering*. John Wiley and Sons, 2005.

[171] M. I. Skolnik, *Radar Handbook*. McGraw-Hill Professional, 2007.

[172] R. E. Collin, *Foundations for microwave engineering*. Wiley-IEEE Press, 2000.

[173] S. Kharkovsky, J. T. Case, M. A. Abou-Khousa, R. Zoughi, and F. L. Hepburn, “Millimeter-wave detection of localized anomalies in the space shuttle external fuel tank insulating foam,” *IEEE Transactions on Instrumentation and Measurement*, vol. 55, no. 4, pp. 1250–1257, 2006.

[174] M. Ando, K. Sakurai, N. Goto, K. Arimura, and Y. Ito, “Radial line slot antenna for 12 GHz satellite tv reception,” *IEEE Transactions on Antennas and Propagation*, vol. AP-33, no. 12, pp. 1347–1353, 1985.

[175] Y. S. Shin and S. O. Park, “A compact loop type antenna for Bluetooth, S-DMB, wibro, wimax and wlan applications,” *IEEE Antennas Wireless Propagation Letters*, vol. 6, pp. 320–323, 2008.

[176] C. Gan, N. Perng, P. Lin, and T. Kuo, “Time-division-based cyclic scheduling for UMTS high-speed downlink shared-channels,” *IEEE Transactions on Vehicular Technology*, vol. 56, no. 4 II, pp. 2086–2094, 2007.

[177] E. D. Kaplan, “Understanding GPS principles and applications,” *Publishing House of Electronics Industry*, vol. 1, p. 129, 2003.

[178] M. E. Lin, Z. F. Fan, Z. Ma, L. H. Allen, and H. Morkoc, “Reactive ion etching of GaN using BCl3,” *Applied Physics Letters*, vol. 64, no. 7, pp. 887–888, 1994.

[179] M. Mukherjee, N. Mazumder, and S. K. Roy, “Prospects of 4H-SiC double drift region IMPATT device as a photo-sensitive high-power source at 0.7 terahertz frequency regime,” *Active and Passive Electronic Components*, vol. 2008, p. 275357, 2008.

[180] M. Mizan and R. C. McGowan, “Extremely low-phase noise X-band field effect transistor dielectric resonator oscillator,” *IEEE MTTS Dig., Boston, MA, June*, vol. 2, pp. 891–894, 2006.

[181] J. Kinross-Wright, N. Butler, S. Normand, M. P. J. Gaudreau, and M. A. Kempkes, “High power solid-state magnetron transmitters,” in *2008 IEEE International Vacuum Electronics Conference*, pp. 320–321, 2008.

[182] Z. Zhou, D. Dong, and S. Wang, “Experimental studies on 45 MW high power klystron,” *Yuanzineng Kexue Jishu/Atomic Energy Science and Technology*, vol. 42, no. 5, pp. 396–399, 2008.

[183] Z. H. Li, “Investigation of an oversized backward wave oscillator as a high power microwave generator,” *Applied Physics Letters*, vol. 92, no. 5, p. 054102, 2008.

[184] T. Idehara, M. Kamada, H. Tsuchiya, T. Hayashi, L. Agusu, S. Mitsudo, I. Ogawa, V. N. Manuilov, K. Naito, T. Yuyama, W. Jiang, and K. Yatsui, “Development of an ultra high

frequency gyrotron with a pulsed magnet," in *AIP Conference Proceedings*, vol. 807, pp. 197–205, 2006.

[185] S. A. Maas, *The RF and microwave circuit design cookbook*. Artech House Publishers, 1998.

[186] A. W. Rudge, K. Milne, A. D. Olver, and P. Knight, *The handbook of antenna design*. Institution of Electrical Engineers, 1986.

[187] N. Blaunstein and C. Christodoulou, *Radio propagation and adaptive antennas for wireless communication links: terrestrial, atmospheric and ionospheric*. Wiley-Interscience, 2006.

[188] C. A. Balanis, *Antenna theory: Analysis and design*. Wiley-Interscience, 2005.

[189] M. I. Amanti, M. Fischer, C. Walther, G. Scalari, and J. Faist, "Horn antennas for terahertz quantum cascade lasers," *Electronics Letters*, vol. 43, no. 10, pp. 573–574, 2007.

[190] S. A. Schelkunoff and H. T. Friis, *Antenna theory and practice*. John Wiley & Sons, 1952.

[191] J. J. Wooldridge, "High density interconnect (HDI) packaging for microwave and millimeter wave circuits," in *IEEE Aerospace Applications Conference Proceedings*, vol. 1, pp. 369–376, 1998.

[192] I. D. Robertson and S. Lucyszyn, *RFIC and MMIC design and technology*. Institution of Engineering and Technology, 2001.

[193] W. Smith, *Modern optical engineering*. McGraw-Hill Professional, 2007.

[194] G. Litfin, *Technische Optik in der Praxis*. Springer, 2003.

[195] M. Bass, *Handbook of Optics*. McGraw-Hill Professional, 1994.

[196] P. F. Goldsmith, *Quasioptical systems: Gaussian beam quasioptical propogation and applications*. Wiley-IEEE Press, 1998.

[197] J. A. Murphy, "Aperture efficiencies of large axisymmetric reflector antennas fed by conical horns," *IEEE Transactions on Antennas and Propagation*, vol. 36, no. 4, pp. 570–575, 1988.

[198] S. A. Self, "Focusing of spherical Gaussian beams," *Applied Optics*, vol. 22, no. 5, pp. 658–661, 1983.

[199] A. E. Siegman, "New developments in laser resonators," in *Proceedings of SPIE - The International Society for Optical Engineering*, vol. 1224, pp. 2–14, 1990.

[200] H. A. Jones-Bey, "Choosing software: Different design paths lead to different solutions," *Laser Focus World*, vol. 42, pp. 97–104, 2006.

[201] W. J. Smith, *Modern lens design*. McGraw-Hill Professional, 2004.

[202] C. Jansen, "Anregung photoleitender Dipolantennen mittels optisch generierter Shiftstroeme in <110> orientiertem GaAs," Master's thesis, Technische Universitaet Braunschweig, 2007.

[203] C. R. Ditchfield and T. S. England, “Passive detection at Q-Band,” *RRE Memorandum*, vol. 1, p. 1124, 1955.

[204] D. M. Sheen, D. L. McMakin, and T. E. Hall, “Three-dimensional millimeter-wave imaging for concealed weapon detection,” *IEEE Transactions on Microwave Theory and Techniques*, vol. 49, no. 9, pp. 1581–1592, 2001.

[205] A. Tessmann, S. Kudszus, T. Feltgen, M. Riessle, C. Sklarczyk, and W. H. Haydl, “Compact single-chip W-band FMCW radar modules for commercial high-resolution sensor applications,” *IEEE Transactions on Microwave Theory and Techniques*, vol. 50, no. 12, pp. 2995–3001, 2002.

[206] N. Karpowicz, H. Zhong, C. Zhang, J. Lin, K.and Hwang, J. Xu, and X. Zhang, “Compact continuous-wave subterahertz system for inspection applications,” *Applied Physics Letters*, vol. 86, no. 5, pp. 1–3, 2005.

[207] F. Gumbmann, L. Schmidt, P. Tran, and J. Weinzierl, “Advanced broadbandmillimeter-wave characterization techniques of dielectrics,” in *9th European Conference on NDT*, 2006.

[208] W. M. Brown, “Synthetic aperture radar,” in *IEEE Trans. Aerosp. Electron*, vol. AES-3, pp. 217–229, 1967.

[209] B. R. Hunt, “Application of constrained Least Squares Estimation to image restoration by digital computer,” in *IEEE Transactions on Computers*, vol. C-22, pp. 805–812, 1973.

[210] Z. A. Maricevic, T. K. Sarkar, Y. Hua, and A. R. Djordejevic, “Time-domain measurements with the Hewlett-Packard network analyzer HP 8510 using the matrix pencil method,” *IEEE Transactions on Microwave Theory and Techniques*, vol. 39, no. 3, pp. 538–547, 1991.

[211] T. Roy, R. Kailath, “ESPRIT - Estimation of Signal Parameters via Rotational Invariance Techniques,” *IEEE Transactions on Acoustics, Speech, and Signal Processing*, vol. 37, no. 7, pp. 984–995, 1989.

[212] Y. Hua and T. K. Sarkar, “Generalized pencil-of-function method for extracting poles of an EM system from its transient response,” *IEEE Transactions on Antennas and Propagation*, vol. 37, no. 2, pp. 229–234, 1989.

[213] W. Saleh and N. Qaddoumi, “Potential of near-field microwave imaging in breast cancer detection utilizing tapered rectangular waveguide probes,” *Computers and Electrical Engineering*, vol. 35, no. 4, pp. 587–593, 2009.

[214] F. Rutz, T. Hasek, M. Koch, H. Richter, and U. Ewert, “Terahertz birefringence of liquid crystal polymers,” *Applied Physics Letters*, vol. 89, no. 22, p. 221911, 2006.

[215] M. Tomassetti, L. Campanella, and M. Delfini, “Determination of water in plant samples: A comparative thermogravimetric and nmr study on different species of seeds,” *Thermochimica Acta*, vol. 105, no. C, pp. 179–190, 1986.

[216] E. Schulze and W. Kuehn, “Kontinuierliche und zerstörungsfreie Messung des Wassergehalts in Pflanzen durch Absorption vom Mikrowellen,” *Angewandte Botanik*, vol. 58, pp. 1919–1994, 1984.

[217] C. Matzler, “Microwave (1-100 GHz) dielectric model of leaves,” *IEEE Transactions on Geoscience and Remote Sensing*, vol. 32, no. 4, pp. 947–949, 1994.

[218] L. Thrane, R. H. Jacobsen, P. U. Jepsen, and S. R. Keiding, “THz reflection spectroscopy of liquid water,” *Chem. Phys. Lett.*, vol. 240, no. 4, pp. 330–333, 1995.

[219] H. Kang, H. Choi, and J. Choi, “Analysis of a Ka-band microstrip-to-waveguide transition by the FDTD expanding-cell algorithm,” *Asia-Pacific Microwave Conference Proceedings, APMC*, vol. 3, pp. 674–677, 1999.

[220] T. Q. Ho and Y. C. Shih, “Spectral-domain analysis of E-plane waveguide to microstrip transitions,” *IEEE Transactions on Microwave Theory and Techniques*, vol. 37, no. 2, pp. 388–392, 1989.

[221] W. Kanghan, C. Zhihong, Z. Yumei, and H. Jinzhong, “A novel coaxial probe waveguide to microstrip transition,” in *Asia-Pacific Microwave Conference Proceedings*, vol. 1, 2005.

[222] G. E. Ponchak and A. N. Downey, “New model for broadband waveguide-to-microstrip transition design,” *Microwave Journal*, vol. 31, no. 5, pp. 333–335, 1988.

[223] W. Grabherr, B. Huder, and W. Menzel, “Microstrip to waveguide transition compatible with mm-wave integrated circuits,” *IEEE Transactions on Microwave Theory and Techniques*, vol. 42, no. 9, pp. 1842–1843, 1994.

[224] H. Iizuka, T. Watanabe, K. Sato, and K. Nishikawa, “Millimeter-wave microstrip line to waveguide transition fabricated on a single layer dielectric substrate,” *IEICE Transactions on Communications*, vol. E85-B, no. 6, pp. 1169–1177, 2002.

[225] P. Herrero and J. Schoebel, “A WR-6 rectangular waveguide to microstrip transition and patch antenna at 140 GHz using low-cost solutions,” *Radio and Wireless Symposium, 2008 IEEE*, vol. 1, pp. 355–358, 2008.

[226] T. A. Milligan, *Modern antenna design*. Wiley-IEEE Press, 2005.

[227] E. Holzman, *Essentials of RF and microwave grounding*. Artech House Publishers, 2006.

List of Publications

Original Journal Papers

- N. Krumbholz, T. Hochrein, N. Vieweg, T. Hasek, K. Kretschmer, M. Bastian, M. Mikulics, and M. Koch, “Monitoring polymeric compounding processes inline with THz time-domain spectroscopy,” *Polymer Testing*, vol. 28, no. 1, pp. 30-35, 2009.
- R. Wilk, N. Vieweg, O. Kopschinski, T. Hasek, and M. Koch, “THz spectroscopy of liquid crystals from the CB family,” *Journal of Infrared, Millimeter, and Terahertz Waves*, vol. 30, no. 11, pp. 1139-1147, 2009.
- C. Joerdens, N. Krumbholz, T. Hasek, N. Vieweg, B. Scherger, L. Baehr, M. Mikulics, and M. Koch, “Fibre-coupled terahertz transceiver head,” *Electronics Letters*, vol. 44, no. 25, pp. 1473-1475, 2008.
- Z. Ghattan, T. Hasek, M. Shahabadi, and M. Koch, “Coupling of free space sub-terahertz waves into dielectric slabs using PC waveguides,” *Optics Express*, vol. 16, no. 9, pp. 6112-6118, 2008.
- Z. Ghattan, T. Hasek, R. Wilk, M. Shahabadi, and M. Koch, “Sub-terahertz on-off switch based on a two-dimensional photonic crystal infiltrated by liquid crystals,” *Optics Communications*, vol. 281, no. 18, pp. 4623-4625, 2008.
- R. Wilk, A. Klehr, M. Mikulics, T. Hasek, M. Walther, and M. Koch, “Terahertz generation with 1064 nm DFB laser diode,” *Electronics Letters*, vol. 43, no. 2, pp. 108-110, 2007.
- F. Rutz, T. Hasek, M. Koch, H. Richter, and U. Ewert, “Terahertz birefringence of liquid crystal polymers,” *Applied Physics Letters*, vol. 89, no. 22, p. 221911, 2006.
- T. Hasek, H. Kurt, D. S. Citrin, and M. Koch, “Photonic crystals for fluid sensing in the subterahertz range,” *Applied Physics Letters*, vol. 89, no. 17, p. 17358, 2006.
- C. Joerdens, M. Salhi, T. Hasek, G. Thorwirth, U. Boettger, and M. Koch, “Micro-mirrors for a multifocus terahertz imaging system,” *Proceedings of the European Microwave Association*, vol. 2, pp. 300-304, 2006.

Conference Contributions

- N. Krumbholz, C. Joerdens, T. Probst, T. Hasek, and M. Koch, “Fiber-coupled terahertz transceiver heads for reflection measurements,” *34th International Conference on Infrared and Millimeter Waves (IRMMW-THz)*, Busan, South Korea, Sept. 2009.
- N. Krumbholz, C. Joerdens, T. Hasek, N. Vieweg, B. Scherger, L. Baehr, and M. Koch, “Fiber-coupled terahertz transceiver antenna,” *Optical Terahertz Science and Technology (OTST)*, Santa Barbara, USA, Mar. 2009.

- N. Krumbholz, T. Hochrein, N. Vieweg, T. Hasek, K. Kretschmer, M. Bastian, and M. Koch, "THz spectroscopy for the inline control of polymeric compounding processes," *33rd International Conference on Infrared and Millimeter Waves and the 16th International Conference on Terahertz Electronics (IRMMW-THz)*, Pasadena, USA, Sept. 2008.
- T. Hasek, Z. Ghattan, R. Wilk, M. Shahabadi, and M. Koch, "Photonic crystals for on-off switching of sub-terahertz electromagnetic waves," *33rd International Conference on Infrared and Millimeter Waves and the 16th International Conference on Terahertz Electronics (IRMMW-THz)*, Pasadena, USA, Sept. 2008.
- N. Krumbholz, M. Schwerdtfeger, T. Hasek, B. Scherger, and M. Koch, "A fiberstretcher operating as an optical delay line in a fiber-coupled THz spectrometer," *33rd International Conference on Infrared and Millimeter Waves and the 16th International Conference on Terahertz Electronics (IRMMW-THz)*, Pasadena, USA, Sept. 2008.
- C. Joerdens, N. Krumbholz, B. Scherger, D. Stanze, T. Hasek, M. Mikulics, and M. Koch, "Towards multi-channel THz imaging", *European Optical Society Annual Meeting 2008 (EOS)*, Paris, France, Sept. 2008.
- R. Wilk, N. Vieweg, T. Hasek, O. Kopschinski, and M. Koch, "THz spectroscopy on liquid crystals from the CB family," *32nd International Conference on Infrared and Millimeter Waves (IRMMW-THz)*, Cardiff, UK, Sept. 2007.
- N. Vieweg, N. Krumbholz, T. Hasek, R. Wilk, V. Bartels, C. Keseberg, V. Pethukov, M. Mikulics, L. Wetenkamp, and M. Koch, "A fibre-coupled THz spectroscopy system for monitoring polymeric compounding processes," *Proceedings SPIE European Symposium on Optical Metrology*, Munich, Germany, Jun. 2007.
- H. Kurt, T. Hasek, M. Koch, and D. S. Citrin "Photonic crystal waveguides for terahertz and sub-terahertz sensing," *Optical Terahertz Science and Technology (OTST)*, Orlando, USA, Mar. 2007.
- T. Hasek, H. Kurt, D. S. Citrin, and M. Koch, "A fluid sensor based on a sub-terahertz photonic crystal waveguide," *Proceedings of SPIE - The International Society for Optical Engineering (Photonics West)*, San Jose, USA, Jan. 2007.
- T. Hasek, R. Wilk, H. Kurt, D. S. Citrin, and M. Koch, "Sub-terahertz 2D photonic crystal waveguides for fluid sensing applications," *31st International Conference on Infrared and Millimeter Waves and 14th International Conference on Terahertz Electronics (IRMMW-THz)*, Shanghai, China, Sept. 2006.
- C. Joerdens, F. Rutz, T. Hasek, and M. Koch, "Towards real-time terahertz quality assurance of chocolate products," *31st International Conference on Infrared and Millimeter Waves and 14th International Conference on Terahertz Electronics (IRMMW-THz)*, Shanghai, China, Sept. 2006.
- K. Baaske, M. Salhi, F. Rutz, T. Hasek, R. Wilk, H. Richter, and M. Koch, "Mail inspection using THz imaging: A comparison of three different systems," *Optical Terahertz Science and Technology (OTST)*, Orlando, USA, Apr. 2006.
- M. Salhi, T. Hasek, and M. Koch, "Towards a con-focal THz laser microscope," *35th Workshop: Physics and Technology of THz Photonics*, Erice, Italy, Jul. 2005.